Ignition and extinction analyses of spray diffusion flames

Daniel Martínez Ruiz, PhD Dissertation

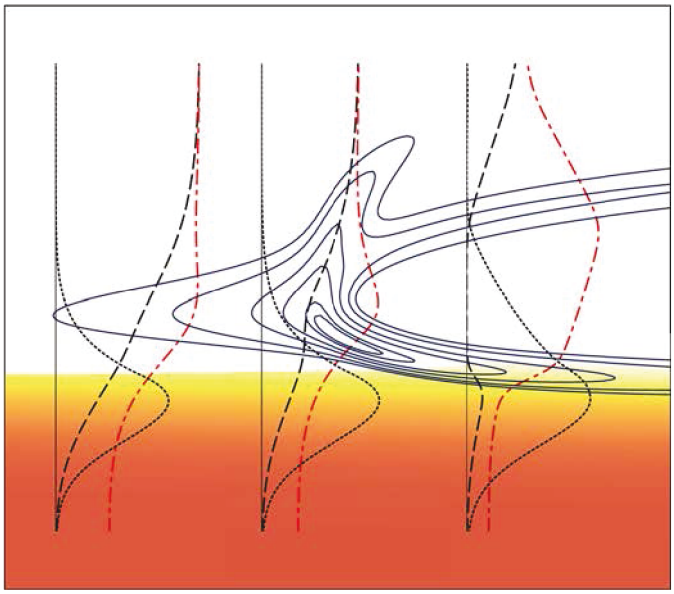

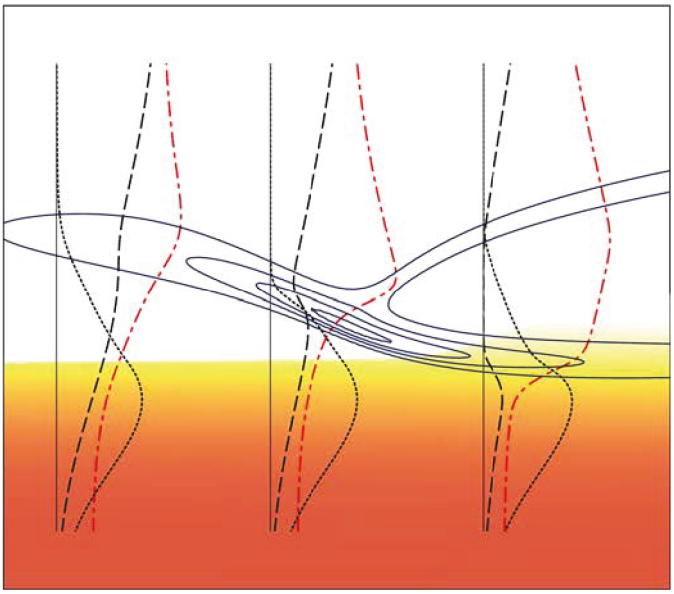

Universidad
Carlos III de Madrid
Departamento de Ingeniería Térmica y de Fluidos

UNIVERSIDAD CARLOS III DE MADRID

Escuela Politécnica Superior

Ignition and extinction analyses of spray diffusion flames

Tesis Doctoral

Autor
Daniel Martínez Ruiz

Directores
Antonio Luis Sánchez Pérez
Amable Liñán Martínez
Javier Urzay Lobo

DEPARTAMENTO DE INGENIERÍA TÉRMICA Y DE FLUIDOS

Leganés, Julio 2015

DEPARTAMENTO DE INGENIERÍA TÉRMICA Y DE FLUIDOS
Escuela Politécnica Superior

Ignition and extinction analyses of spray diffusion flames

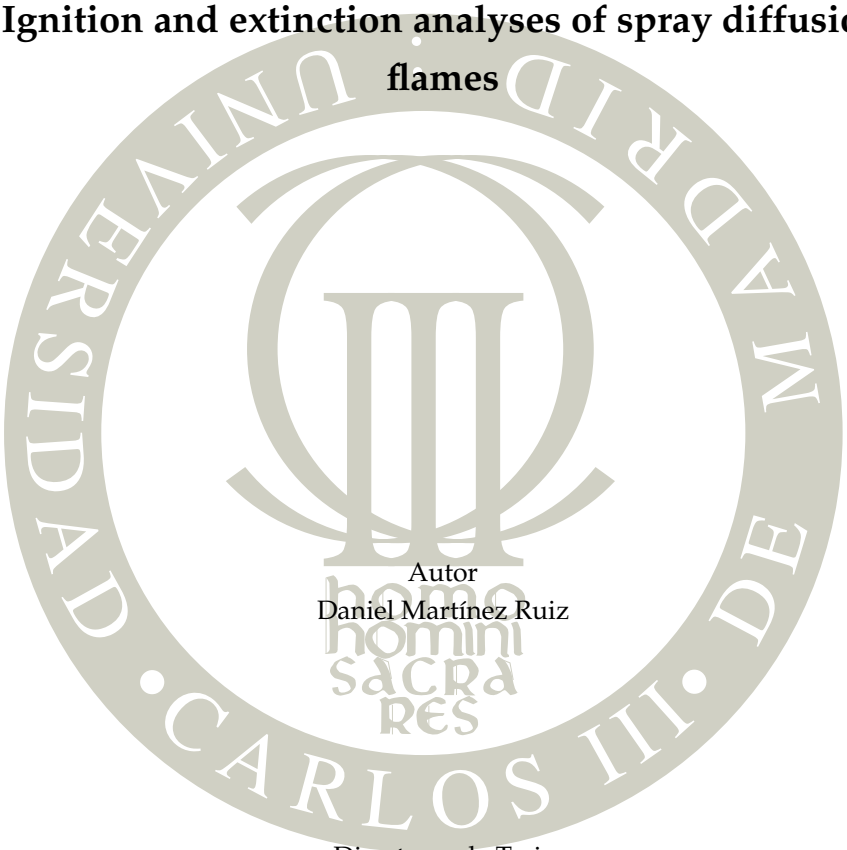

Autor
Daniel Martínez Ruiz

Directores de Tesis
Antonio Luis Sánchez Pérez Amable Liñán Martínez Javier Urzay Lobo

Leganés, Julio 2015

A las amistades

TESIS DOCTORAL

IGNITION AND EXTINCTION ANALYSES OF SPRAY DIFFUSION FLAMES

Autor
Daniel Martínez Ruiz

Directores de Tesis:
Antonio Luis Sánchez Pérez
Amable Liñán Martínez
Javier Urzay Lobo

Firma del Tribunal Calificador:

Firma

Presidente: D. Francisco Higuera Antón

Vocal: D. Luc Vervisch

Secretario: D. Eduardo Fernández Tarrazo

Suplente: D. Pedro Luis García Ybarra

Calificación:

Leganés, 9 de Julio de 2015

Agradecimientos

This work was supported by the Spanish MCINN through project # CSD2010-00010. The work on diffusion-flame extinction was completed during a fruitful five-month stay in the research group of Professor Forman A. Williams at the Department of Mechanical and Aerospace Engineering of University of California San Diego. His continuous advice on many different aspects of my research work is highly appreciated. Part of the investigation on ignition of sprays was completed during a two-month stay of the author in the Center for Turbulence Research at Stanford University, whose personnel is gratefully acknowledged for hospitality.

Me gustaría además agradecer en estas páginas a todas aquellas personas que me han acompañado durante esta fase de trabajo y aprendizaje, y que con su apoyo en lo personal y académico han hecho posible que esta tesis llegue a su fin.

En primer lugar a Antonio por la oportunidad, por su constante dedicación y empeño en producir un trabajo honesto y competitivo. Gracias a Amable por su magnífica guía y contagiarme con la ambición de comprender. A Javier Urzay por hacer de mí un investigador más competente y guiarme durante mi estancia en Palo Alto.

Gracias a Javier Rodríguez, Eduardo, Mario, Marcos, Alejandro, Inma y Wil como maestros de los que he aprendido y compañeros con los que he tenido el gusto de convivir. A los numerosos doctorandos y ya doctores con los que tanto he compartido durante mi etapa en Leganés en el departamento de ingeniería térmica y fluidos. Gracias a Jaime Carpio por su interés y por su colaboración. A Cristina, por el apoyo incansable en el trabajo y en lo personal.

En especial a Sergio, con la alegría de haber encontrado un amigo como un hermano. Gracias Miriam, por la vida y los proyectos que hemos construido juntas, siempre mostrando el camino del optimismo. Gracias César e Irene por ser mi familia allá donde vayamos y compartir tantos momentos. Matías y Paula porque me dieron la vuelta al mundo y se dejaron acompañar. A los excluidos Luis y Dani Pérez-Grande. Bego y Manu, gracias por vuestra bondad y generosidad mil veces demostrada. A Quino y Jorge, con mucho cariño por todas las risas y conversaciones compartidas. Gracias Elena.

A todos los amigos de largo recorrido, Pau, Adri, Luzi4, Paloma, Gloria, Isa, Edu G., Edu M., Germán, Victor, Mikel, MVP. Y por último, gracias a mi familia, Alfonso, Elvira y Lita.

Abstract

The present dissertation deals with the description of the interacting multiscale processes governing spray vaporization and combustion downstream from the near-injector atomization region in liquid-fueled burners. The analysis incorporates rationally derived simplifications based on the disparity of length and time scales present in the problem. In particular, it is shown how the disparity of the scales that correspond –with increasing values of their orders of magnitude– to the droplet size, interdroplet spacing, and width of the spray jets, ensures the validity of their homogenized description. The two-way coupling associated with exchanges of mass, momentum, and energy between the gas and the liquid phases is dominated by the homogenized exchanges with the gas provided collectively by the droplets, and not by the direct interaction between neighboring droplets. The resulting multicontinua formulation is used as a basis to investigate different aspects of spray combustion, including diffusion-flame structures and finite-rate effects. Specific attention is given to three laminar canonical problems, namely:

i) The laminar coflow mixing layer separating a hot-air stream from a monodisperse spray carried by either an inert gas or air is investigated numerically and analytically in an effort to increase understanding of the ignition process leading to stabilization of high-speed spray combustion. The problem is formulated in an Eulerian framework, with the conservation equations written in the boundary-layer approximation and with a one-step Arrhenius model adopted for the chemistry description. The numerical integrations unveil two different types of ignition behavior depending on the fuel availability in the reaction kernel, which in turn depends on the rates of droplet vaporization and fuel-vapor diffusion. When sufficient fuel is available near the hot boundary, as occurs when the thermochemical properties of heptane are employed for the fuel in the integrations, combustion is established through a precipitous temperature increase at a well-defined thermal-runaway location, a phenomenon that is amenable to a theoretical analysis based on activation-energy asymptotics, presented here, following earlier ideas developed in describing unsteady gaseous ignition in mixing layers. By way of contrast, when the amount of fuel vapor reaching the hot boundary is small, as is observed in the computations employing the thermochemical properties of methanol, the incipient chemical reaction gives rise to a slowly developing lean deflagration that consumes the available fuel as it propagates across the mixing layer towards the spray. The

flame structure that develops downstream from the ignition point depends on the fuel considered and also on the spray carrier gas, with fuel sprays carried by air displaying either a lean deflagration bounding a region of distributed reaction or a distinct double-flame structure with a rich premixed flame on the spray side and a diffusion flame on the air side. For fuels carried by an inert gas, a trailing diffusion flame develops downstream from the ignition region, approaching at large distances a Burke-Schumann solution that can be described in terms of coupling functions, as shown in an appendix.

ii) An axisymmetric opposed-jet configuration, involving a stream of hot air counterflowing against a stream of nitrogen carrying a spray of fuel droplets, is employed as a basis to address effects of droplet inertia on spray vaporization and combustion. The Reynolds numbers of the jets are assumed to be large, so that mixing of the two streams is restricted to a thin mixing layer that separates the counterflowing streams. The evolution of the droplets in their feed stream from the injection location is seen to depend fundamentally on the value of the droplet Stokes number St, defined as the ratio of the droplet acceleration time to the mixing-layer strain time close to the stagnation point. Two different regimes of spray vaporization and combustion can be identified depending on the value of St. For values of St below a critical value, which is seen to be equal to $1/4$ for dilute sprays with small values of the spray liquid mass-loading ratio, the droplets decelerate to approach the gas stagnation plane with a vanishing axial velocity. In this case, the droplets located initially near the axis reach the mixing layer, where they can vaporize due to the heat received from the hot air, producing fuel vapor that can burn with the oxygen in a diffusion flame, located on the air side of the mixing layer. The character of the spray combustion is different for values of St of order unity, because the droplets cross the stagnation plane and move into the opposing air stream, reaching distances that are much larger than the mixing-layer thickness before they turn around. The vaporization of these crossing droplets, and also the combustion of the fuel vapor generated by them, occur in the hot air stream, without significant effects of molecular diffusion, generating a vaporization-assisted nonpremixed flame that stands on the air side outside the mixing layer. Separate formulations will be given below for these two regimes of combustion, with attention restricted to the near-stagnation-point region, where the solution is self-similar and all variables are only dependent on the distance to the stagnation plane. The resulting formulations display a reduced number of controlling parameters that effectively embody dependences of the structure of the spray flame on spray dilution, droplet inertia, and fuel preferential diffusion. Sample solutions are given for the limiting cases of pure vaporization and of infinitely fast

chemistry, with the latter limit formulated in terms of chemistry-free coupling functions that allow for general nonunity Lewis numbers of the fuel vapor. For completeness, a complementary analysis is given in an appendix for the case of vaporization of a spherical droplet cloud, which is the canonical problem addressed in the initial theoretical analyses.

iii) The limit of large-activation energy is employed to investigate strain-induced extinction of counterflow spray diffusion flames. As in the case of gaseous flames, which is treated separately in an appendix, for near-extinction conditions the flame structure is in the first approximation that corresponding to the limit of infinitely fast reaction, i.e., two outer regions of equilibrium flow separated by an infinitesimally thin reaction layer where the fuel vapor generated outside by the vaporizing droplets reacts with the oxygen of the air at a diffusion-controlled rate. The computation of the leading-order equilibrium solution, including the flame-sheet location and the associated peak temperature, fuel-consumption rate, and temperature gradients on both sides, is facilitated by the introduction of chemistry-free coupling functions that allow for general non-unity Lewis numbers of the fuel vapor. The formal analysis of the extinction regime requires consideration of the small departures from equilibrium occurring both in the thin reaction layer, whose inner structure is in the first approximation identical to that encountered in gaseous nonpremixed flames, and also in the outer regions, where the corrections are associated with the reactants leaking through the flame, whose description involves the integration of a set of coupled linear equations on each side of the flame sheet. Appropriate matching of the solution in the different regions provides expressions for the critical extinction conditions. The results of the asymptotic analysis enable strain-rate dependences on spray dilution, fuel-vapor diffusivity, and droplet inertia to be investigated.

Resumen

La tesis doctoral que se presenta a continuación nace con el objetivo de describir los procesos interactivos multiescala que controlan la vaporización y la combustión de sprays en sistemas de combustibles líquidos cerca de la zona de atomización. El análisis que se ha realizado considera una serie de simplificaciones basadas en la disparidad de escalas temporales y espaciales presentes en el problema. En concreto, se muestra cómo las diferentes escalas que corresponden – en orden creciente de su orden de magnitud – al tamaño de las gotas, su interespaciado y el espesor del chorro de spray, permiten el empleo de una descripción homogeneizada de la fase dispersa. El acoplamiento entre las fases líquida y gaseosa asociado al intercambio de masa, cantidad de movimiento y energía está dominado por los efectos colectivos homogeneizados de las gotas en el medio gaseoso y no tanto por la interacción directa entre las mismas. Ambas fases son tratadas como medios continuos, lo que da lugar a una formulación general de la que se hace uso para investigar diferentes aspectos de la combustión de sprays. En particular, con el objetivo de ahondar en el entendimiento de los fenómenos físico-químicos que aparecen en configuraciones realistas, se identifican tres problemas canónicos laminares que permiten investigar aspectos específicos de interés. Los tres problemas que se han tratado se describen a continuación.

i) Como primer problema, se plantea el estudio del proceso espontáneo de ignición en una capa de mezcla laminar en coflujo que separa una corriente de aire caliente y un spray monodisperso. El objetivo es mejorar el entendimiento del proceso de estabilización de llama en la combustión de sprays inyectados a altas velocidades en cámaras de combustión continua. En el estudio se hace uso de una formulación Euleriana, donde las ecuaciones de conservación se escriben en la aproximación de capa límite, incluyendo un modelo químico de un paso de tipo Arrhenius. Se identifican mediante integraciones numéricas dos modos de ignición en función de la disponibilidad de combustible en la zona de reacción, lo cual depende de los procesos de vaporización y difusión del combustible. Para aquellos casos en los que aparece una cantidad apreciable de combustible en la cercanía de la corriente caliente de aire, tal y como se observa cuando se usan las propiedades del heptano en las simulaciones, el quemado se establece tras un incremento espontáneo de la temperatura en una posición localizada. El proceso asociado de explosión térmica se puede describir de manera teórica mediante el uso de métodos asintóticos basados

en el valor elevado de la energía de activación. Por otro lado, si la cantidad de combustible gaseoso es insuficiente cerca de la zona caliente, tal y como ocurre en el caso del metanol, la ignición se produce de forma gradual en forma de una deflagración pobre que consume el combustible en su camino hacia el interior del spray. La estructura que presenta la solución aguas abajo del punto de ignición depende del tipo de combustible y del gas presente en el lado del spray. Cuando el spray es transportado por aire, la solución evoluciona o bien hacia una deflagración pobre o bien hacia una estructura doble incluyendo una llama de premezcla en el lado del combustible y una llama de difusión en el lado del aire. Para combustibles transportados por un gas inerte, se observa el desarrollo de una llama de difusión de tipo Burke-Schumann, cuya descripción detallada se aborda en uno de los apéndices.

ii) El segundo estudio tiene como objetivo el análisis del efecto de la inercia de las gotas en los procesos de vaporización y combustión de sprays diluidos. Para ello, se considera la configuración de contraflujo axisimétrica que se establece entre una corriente de aire caliente y un spray de gotas de combustible líquido transportadas por una corriente de nitrógeno. El número de Reynolds de las corrientes se considera elevado, de forma que el proceso de mezclado se limita a una capa de mezcla delgada situada cerca del plano de remanso. La evolución de las gotas en su camino desde el punto de inyección hacia la zona de mezclado depende fundamentalmente del valor de su número de Stokes St, el cual se define como el cociente entre el tiempo de aceleración de las gotas y el tiempo fluidomecánico característico, dado por el inverso del ritmo de estiramiento. En función del citado parámetro se identifican dos regímenes bien diferenciados. Así, para valores de St inferiores a un valor crítico (1/4 en sprays diluidos), las gotas se desaceleran según se aproximan al plano de remanso, de forma que las gotas colocadas inicialmente cerca del eje de simetría se incorporan a la capa de mezcla cerca del punto de remanso central, donde reciben calor de la corriente caliente y se vaporizan, produciendo combustible gaseoso que reacciona con el aire caliente en una llama de difusión. Por otra parte, para valores supercríticos de St de orden unidad, aparece un régimen distinto en el que las gotas cruzan el plano de remanso y penetran en la corriente opuesta hasta distancias del orden de la distancia de inyección. En este caso, los efectos de transporte molecular en la vaporización de las gotas y en el quemado del combustible gaseoso que se genera son despreciables en primera aproximación. La combustión se produce en forma de una llama asistida por la vaporización que se sitúa en la corriente de aire lejos de la capa de mezcla. Los dos regímenes identificados requiren formulaciones matemáticas distintas, que incluyen parámetros adimensionales que miden en cada caso la dilución

del spray, la inercia de las gotas y la difusión preferencial del combustible. El análisis aborda en particular los casos límite correspondientes a vaporización pura sin reacción química y reacción química infinitamente rápida. Como complemento a este estudio, se recoge en un apéndice el problema clásico de la vaporización de nubes esféricas de gotas, lo que permite discutir los resultados de los análisis teóricos iniciales en el marco del tratamiento unificado que se propone en esta tesis.

iii) Por último, se hace de nuevo uso de la configuración de contracorriente para estudiar el proceso de extinción de llamas de spray inducido por el estiramiento aerodinámico. Al igual que en llamas gaseosas, que se estudian separadamente en uno de los apéndices, cuando la reacción química es muy sensible a los cambios de temperatura, la estructura de la llama cerca de la extinción está dada en primera aproximación por la solución de Burke-Schumann: en la que aparecen dos regiones externas en equilibrio químico separadas por una lámina infinitamente delgada de reacción donde reaccionan el combustible generado por la vaporización de las gotas y el oxígeno del aire a un ritmo controlado por la difusión de los reactantes. El cálculo de la citada solución proporciona la posición de la llama, la temperatura pico de la misma, el ritmo de quemado del combustible y los gradientes de temperatura a ambos lados de la zona de reacción. Estas cantidades son de interés para llevar a cabo el análisis de la extinción, para el que han de tenerse en cuenta las pequeñas perturbaciones a la solución de equilibrio químico tanto en la zona de reacción como en las regiones externas, estas últimas asociadas al sangrado de reactantes a través de la llama. La solución mediante expansiones asintóticas acopladas determina las condiciones críticas de extinción.

Contents

CHAPTER
ONE

Introduction

1.1 Motivation

The existence of length and time scales of very different magnitude is a complicating characteristic of many problems encountered in fluid mechanics and combustion. The mathematical description of the associated flows can be facilitated by accounting for the disparity of these scales. A renowned example of the success of this approach is the boundary-layer theory developed by Ludwig Prandtl over a century ago. Separation of scales has also been extensively used in connection with the description of combustion problems, where the disparity of time scales is often due to the strong temperature sensitivity of the chemical reactions. For spray combustion, additional length and time scales originate from the two-phase nature of the flow.

Over the past half century combustion modelers have successfully exploited the separation of the scales present in the vaporization and combustion of droplets and sprays to generate simplified equations for the description of reactive spray flows. The present work will begin with a discussion of the reasons for the validity, and also the shortcomings, of the continuum description of the gas and liquid phases in the vaporization and combustion of sprays. Because of the important role of the interphase exchange rates of mass, energy, and momentum, a summary of these rates is given, and then used in the conservation equations for the description of reacting sprays; this simplifies in the important extreme limiting cases of pure spray vaporization, without chemical reactions, and diffusion-controlled spray combustion. Simple laminar canonical problems, widely used in the past in fundamental investigations of spray combustion, are formulated in nondimensional form to identify the parameters that characterize the interplay of the different spray physicochemical phenomena.

In diesel engines, gas turbines, and rocket engines, liquid fuel is often delivered into the combustion chamber by means of atomizers that facilitate the breakup of the liquid vein and the dispersion of the resulting fuel spray. The understanding of the multi-scale phenomena involved in the turbulent reactive

flow associated with the burning of these fuel sprays is a challenging task. The additional complications associated with the presence of two different phases hinder the identification of the main phenomena and prevent the extraction of general conclusions. As a result, despite significant previous efforts, the current level of understanding of many aspects of spray flames is considerably lower than that of gaseous flames, a deficiency that limits necessarily the modeling strategies and associated predictive capabilities for spray combustion.

Substantial research efforts have been made in the past in connection with the problems of vaporization and combustion of droplets and droplet arrays [1–9], ignition of fuel sprays [10], and dynamics and modeling of turbulent sprays [11–13]. Related work on atomization of liquid jets [14–16], including recent modelling efforts for electrospray applications [17, 18], and on the dynamics of particle-laden turbulent flows [19–21] is relevant for understanding the generation and dispersion of sprays. A reference book including an updated comprehensive presentation of the current level of understanding of fluid dynamics and transport of droplets and sprays is available [22]. In addition, other relevant literature includes reference textbooks on atomization [23] and multiphase combustion [24], as well as research monographs [25, 26].

The design of liquid-fueled combustion systems is subject to a number of constraints stemming from the need to vaporize the droplets, mix the fuel vapor with the surrounding air, and ignite and burn completely the resulting mixture in the limited available residence time, with the scales and parameters of these different physicochemical processes entering in the determination of the combustor performance. An important consideration that must be taken into account when describing vaporization and combustion in diesel engines, and also in the primary combustion zone of gas turbines, is the large value of the liquid-to-gas density ratio, on the order of a few hundred in many applications. Also relevant for combustion is the large value, of order $S \sim 15$, of the mass of air required to burn in stoichiometric proportions the unit mass of fuel. Another basic consideration pertaining to the required dispersion of the droplets in the combustion chamber is that the heat needed for the vaporization of each droplet comes from the sensible heat of the gas within the spray, so that vaporization in the bulk of the spray can only start when sufficiently dilute conditions are reached; otherwise the amount of gas entrained by the spray is insufficient to provide the heat of vaporization. In assessing the coupling between the liquid and gas phases, one must also bear in mind that the heat released by burning the fuel is enough to lead to flame temperatures several times larger than the initial liquid temperature.

The large temperature sensitivity of the combustion reactions also enters

in a fundamental way. For instance, in continuous-combustion devices this temperature sensitivity explains the onset of ignition near the hot boundary in mixing layers separating the spray from the preheated air. An important consideration, relevant for the selection of the atomizer in a given application, is that the droplet size must be small enough to ensure their complete vaporization and prevent their impingement with the confining walls. In view of the above considerations, it is clear that spray combustion stands out as a very particular category within the general field of two-phase flows, one that cannot be understood without accounting for its distinctive attributes.

1.2 Outline of the dissertation

The remainder of the present document is organized as follows. Different aspects of fluid-mechanical phenomena relevant to spray combustion systems, including droplet atomization and dispersion and coupling of gaseous and liquid phases, are discussed in Chapter 2, along with approaches to the mathematical treatment of the resulting multiphase reactive flows and a qualitative description of spray-combustion phenomena occurring in practical combustion devices. This is followed, in Chapter 3, by the proposed homogenized formulation for spray combustion, to be used as mathematical framework thereafter, and the presentation of the main controlling parameters that serve to characterize the flow. Specific canonical configurations that serve to shed light on their underlying phenomena are identified, including coflow and counterflow laminar mixing layers. The former is employed in Chapter 4 to investigate spray autoignition processes downstream from high-speed fuel injectors in continuous-combustion systems while the latter is utilized in Chapter 5 as a basis to examine effects of droplet inertia on spray vaporization and on structures of spray diffusion flames. The laminar counterflow is also used to study effects of strain on extinction of spray flames when, as typically occurs in applications, the rate of heat release by chemical reaction has a strong temperature dependence. The associated analysis, presented in Chapter 6, parallels the classical large-activation-energy analysis developed over 40 years ago by Liñán for gaseous flames [27]. For completeness, aspects of the extinction problem for gaseous systems, not considered in previous works, such as effects of variable density and transport properties and comparisons with finite-rate numerical integrations, are included in an appendix. Finally, general conclusions and future prospects are delineated in Chapter 7.

References

[1] F. A. Williams, Combustion of droplets of liquid fuels: a review, Combust. Flame 21 (1973) 1–31.

[2] C. K. Law, Recent advances in droplet vaporization and combustion, Prog. Energy Combust. Sci. 8 (1982) 171–201.

[3] G. M. Faeth, Evaporation and combustion of sprays, Prog. Energy Combust. Sci. 9 (1983) 1–76.

[4] W. A. Sirignano, Fuel droplet vaporization and spray combustion theory, Prog. Energy Combust. Sci. 9 (1983) 291–322.

[5] J. Bellan, Supercritical (and subcritical) fluid behavior and modeling: drops, streams, shear and mixing layers, jets and sprays, Prog. Energy Combust. Sci. 26 (2000) 329–366.

[6] H. Chiu, Advances and challenges in droplet and spray combustion. i. toward a unified theory of droplet aerothermochemistry, Progress in Energy and Combustion Science 26 (4) (2000) 381–416.

[7] K. Annamalai, W. Ryan, Interactive processes in gasification and combustion. part i: Liquid drop arrays and clouds, Progress in energy and combustion science 18 (3) (1992) 221–295.

[8] A. Umemura, Interactive droplet vaporization and combustion: approach from asymptotics, Progress in energy and combustion science 20 (4) (1994) 325–372.

[9] W. A. Sirignano, Advances in droplet array combustion theory and modeling, Progress in Energy and Combustion Science 42 (2014) 54–86.

[10] S. K. Aggarwal, A review of spray ignition phenomena: present status and future research, Progress in Energy and Combustion Science 24 (6) (1998) 565–600.

[11] X. Jiang, G. Siamas, K. Jagus, T. Karayiannis, Physical modelling and advanced simulations of gas–liquid two-phase jet flows in atomization and sprays, Progress in Energy and Combustion Science 36 (2) (2010) 131–167.

[12] E. Gutheil, in: B. Merci, D. Roekaerts, A. Sadiki (Eds.), Experiments and numerical simulations of diluted spray turbulent combustion, Springer, 2011, pp. 1–39.

[13] P. Jenny, D. Roekaerts, N. Beishuizen, Modeling of turbulent dilute spray combustion, Progress in Energy and Combustion Science 38 (6) (2012) 846–887.

[14] S. Lin, R. Reitz, Drop and spray formation from a liquid jet, Annual Review of Fluid Mechanics 30 (1) (1998) 85–105.

[15] J. Lasheras, E. Hopfinger, Liquid jet instability and atomization in a coaxial gas stream, Annual Review of Fluid Mechanics 32 (1) (2000) 275–308.

[16] C. Dumouchel, On the experimental investigation on primary atomization of liquid streams, Experiments in fluids 45 (3) (2008) 371–422.

[17] F. J. Higuera, Eulerian model of a dilute spray of charged droplets, Journal of Aerosol Science 48 (2012) 34–45.

[18] F. J. Higuera, Multifluid eulerian model of an electrospray in a host gas, Journal of Fluid Mechanics 734 (2013) 363–386.

[19] C. Crowe, T. Troutt, J. Chung, Numerical models for two-phase turbulent flows, Annual Review of Fluid Mechanics 28 (1) (1996) 11–43.

[20] S. Balachandar, J. K. Eaton, Turbulent dispersed multiphase flow, Annual Review of Fluid Mechanics 42 (2010) 111–133.

[21] S. Subramaniam, Lagrangian–eulerian methods for multiphase flows, Progress in Energy and Combustion Science 39 (2) (2013) 215–245.

[22] W. A. Sirignano, Fluid dynamics and transport of droplets and sprays, 2nd edition, Cambridge University Press, Cambridge, UK., 2010.

[23] A. Lefebvre, Atomization and sprays, Hemisphere Publishing, 1989.

[24] K. K. Kuo, R. Acharya, Fundamentals of Turbulent and Multi-Phase Combustion, John Wiley & Sons, 2012.

[25] H. Chiu, N. Chigier, Mechanics and combustion of droplets and sprays, Begell House Publishers, 1995.

[26] K. K. Kuo, Recent advances in spray combustion: Spray atomization and drop burning phenomena, Vol. 1, AIAA, 1996.

[27] A. Liñán, The asymptotic structure of counterflow diffusion flames for large activation energies, Acta Astronautica 1 (7) (1974) 1007–1039.

CHAPTER
TWO

Preliminary considerations pertaining to spray flows in combustion systems

2.1 Atomization in spray-combustion systems

The spray length required by the limited size of the combustion chamber can only be accomplished when there exists a significant velocity difference between the liquid jet or sheet to be atomized and the surrounding coflowing gas [1]. This is the case if the liquid stream is injected at high velocity, as in pressure atomizers of diesel engines, or by exposing the liquid to a high-velocity air stream, the method used in air-assist and airblast atomizers. The hydrodynamic instabilities involved in the breakup process, different for pressure and airblast atomizers [2–6], lead to primary atomization of the liquid vein to form ligaments and droplets, which further break up downstream as a result of the interactions with the surrounding turbulent gaseous flow in the secondary atomization region.

To guide the following discussion, a sketch of the spray flow corresponding to a plain-orifice atomizer, used in diesel combustion engines and turbojet afterburners, is shown in Fig. 2.1. In this kind of pressure atomizer, the liquid is injected from a high-pressure chamber through small circular holes, forming high-velocity jets that disintegrate rapidly downstream to form a jet spray with a small cone angle, whose value may depend on the transverse velocities induced inside the injector by the instabilities of the cavitating flow [7]. The working principle of other pressure atomizers can be more complex. For instance, in pressure-swirl atomizers, considered in the schematic representation of a liquid-fueled combustor shown in Fig. 2.2, to be discussed later, the fuel is injected through tangential ports in the injector plenum. Because of angular-momentum conservation, the resulting swirling motion is transformed, near the injector orifice, into kinetic energy of the axial and radial motion of the liquid, generating a conical sheet that breaks up to give a hollow-cone spray [8, 9].

The design of the injection system must satisfy a number of constraints. To ensure that the penetration length L_s of the spray is comparable to the cylinder

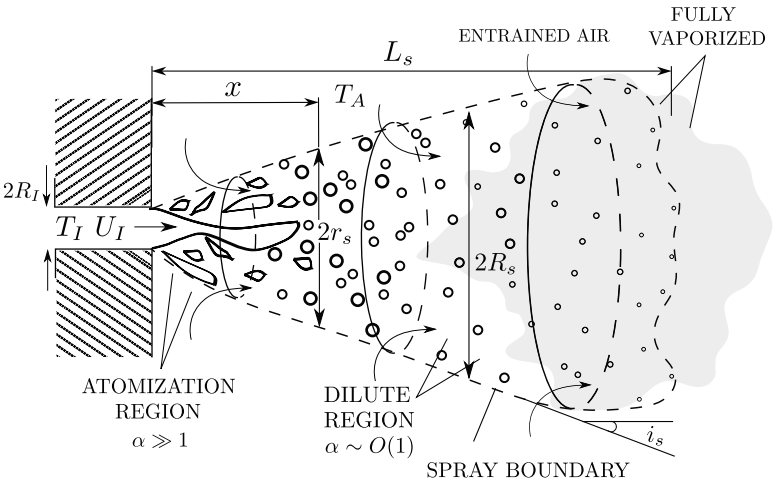

Figure 2.1. A schematic view of a vaporizing spray generated by a plain-orifice pressure atomizer, including characteristic scales and regions.

radius in diesel engines - or to the size of the primary combustion zone in gas turbines - the injection velocity U_I must be sufficiently large, while still giving time for the droplets to vaporize, thereby avoiding their collision with the walls of the combustor, an undesired phenomenon that would lead to increased unburnt hydrocarbon emissions. On the other hand, the orifice radius of the injector R_I must be small to lead, after atomization of the liquid jet or of the conical sheet issuing from pressure-swirl atomizers, to droplets with sizes small enough that they vaporize and simultaneously penetrate a distance L_s, of the order of the chamber size, before reaching the combustor wall.

The distribution of droplet radii is determined by the phenomena occurring in the atomization region, where the spray is still dense and its velocity and temperature do not differ substantially from their injection values U_I and T_I. In this atomization region, the droplets acquire a transverse velocity that, although small compared with U_I, is responsible for the initial transverse dispersion of the spray, which is further enhanced downstream by the turbulent motion acquired by the entrained air. The resulting spray jet is typically very slender. For instance, in plain-orifice atomizers, droplet dispersion results in small cone angles $2i_s$ that usually lie between 5° and 15° [1]. Similar considerations apply also to the slender conical sprays produced by pressure-swirl atomizers or by liquid atomizers assisted by swirling air flows.

Direct numerical simulations can be instrumental in revealing the highly

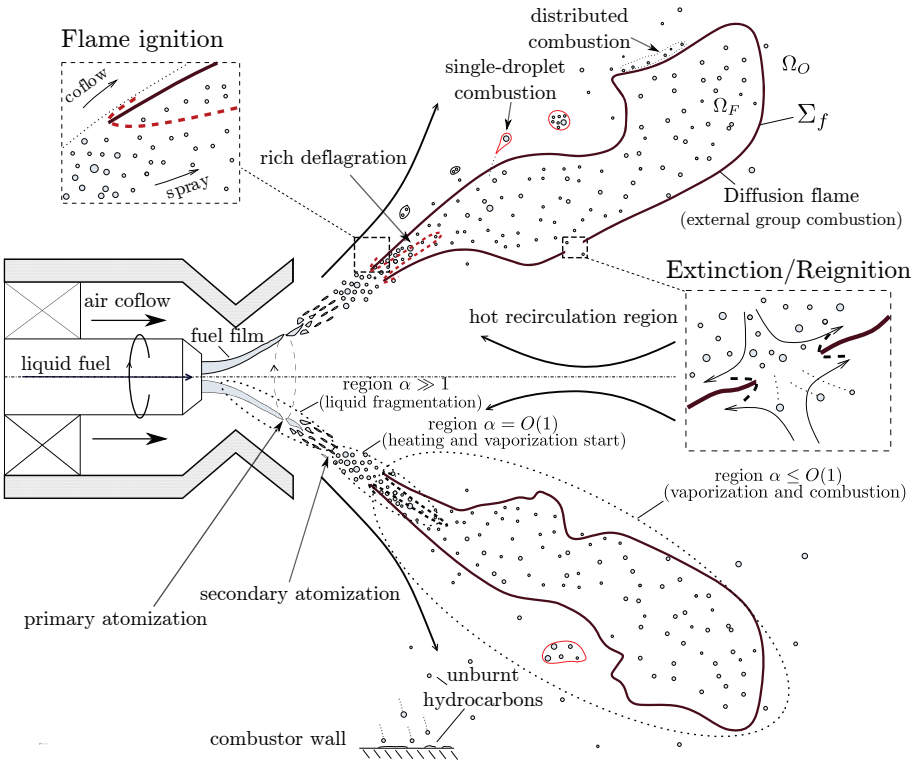

Figure 2.2. Sketch of fundamental spray-combustion processes in typical liquid-fueled continuous-combustion systems.

complex interactions occurring in the atomization region. Sample computations of the primary breakup region near the injection orifice as well as the subsequent downstream dispersion and mixing processes are available [10–15]. Future improvements in computational capabilities will enable extended computations of both primary and secondary atomization regions in transient and stationary jet configurations to be performed, thereby providing quantitative information for the parametric dependence of the downstream jet-spray characteristics.

Droplet heating and vaporization can only occur downstream from the atomization region, once droplet dispersion, due to ambient gas entrainment, causes the spray to become sufficiently dilute to allow for the droplets to receive significant energy from the entrained gas. As a consequence, the processes of liquid-jet atomization, leading to spray formation, and those of spray vaporization and combustion occur in separate spatial regions, which can be investigated independently. Attention will be paid below to the description of the different spray-combustion phenomena occurring in the dilute downstream

region where the volume fraction occupied by the liquid phase is small, so that direct droplet-droplet interactions are unimportant, while the associated liquid mass loading is comparable to that of the entrained gas, as is needed to provide the heat required for droplet vaporization.

2.2 Spray dispersion and mass-loading ratio

A measure of the monodisperse spray droplet population is the local number density n, i.e., number of droplets per unit volume, which decreases rapidly along the spray. Correspondingly, $l_d = n^{-1/3}$ is the characteristic interdroplet distance, to be compared with the characteristic droplet radius a. The analysis of the spray flow shall be limited to dilute regions where the liquid volume fraction $\phi = (4\pi/3)a^3 n$, of order $(2a/l_d)^3$, is small, such that the interdroplet distance l_d is significantly larger than a, resulting in negligible direct interaction between neighboring droplets. On average, each individual droplet can be envisioned as being centered in a cubic volume of gas of side length l_d. The ratio of the mass of the droplet, $(4\pi/3)\rho_l a^3$, to the mass of the corresponding surrounding gas, $\rho l_d^3(1-\phi)$, defines a mass-loading ratio $\alpha = (4\pi/3)a^3\rho_l n/[\rho(1-\phi)]$, where ρ_l and ρ represent the liquid and gas densities, respectively.

In most combustion systems, the gas and liquid densities are very different, the only exception being the conditions found in supercritical applications, for which $\rho \sim \rho_l$ in the vicinity of the droplets. For most of the other applications, the liquid-to-gas density ratio satisfies

$$\frac{\rho_l}{\rho} \gtrsim 10^2. \tag{2.1}$$

It shall be seen below that α is one of the two fundamental parameters characterizing the collective inter-phase coupling for momentum and energy in spray flows, the other being the Stokes number St defined later in (3.29). Effective two-way coupling occurring for values of $\alpha = O(1)$, corresponding to dilute sprays with small liquid volume fractions $\phi \sim \rho/\rho_l \ll 1$. Under these conditions the expression given above for α reduces to

$$\alpha = \phi\rho_l/\rho = \frac{(4\pi/3)a^3 n\rho_l}{\rho} = \frac{\pi}{6}\frac{\rho_l}{\rho}\left(\frac{2a}{l_d}\right)^3. \tag{2.2}$$

The distribution of α in the spray jet is nonuniform. Its value decreases due to droplet dispersion from very large values near the atomizer to small values sufficiently far downstream. A simple order-of-magnitude analysis for

the spray jet formed in the plain-orifice atomizer of Fig. 2.1 serves to illustrate the downstream evolution of α in the bulk of the spray jet and its effect on the spray-jet development. In this case, the injection velocity U_I and the contracted injector radius R_I determine the injected liquid volume flow rate $\pi R_I^2 U_I$. If, for simplicity, the spray formed upon atomization and breakup is considered to be monodisperse, with initial droplet radius a_o, then the number of droplets injected per unit time $\dot{N}$ from the atomization region into the combustion chamber is given simply by $\dot{N} = (\pi R_I^2 U_I)/(\frac{4}{3}\pi a_o^3)$. The flux number of droplets is conserved before complete vaporization, so that the flux of droplets across the jet at a given downstream location must be equal to the number of droplets injected. In order of magnitude, this conservation condition leads to a first relationship

$$n r_s^2 u_d \sim \pi R_I^2 U_I / \left(\tfrac{4}{3}\pi a_o^3\right) = \dot{N} \tag{2.3}$$

linking, at an axial distance x, the characteristic value of n with the corresponding values of the spray-jet radius r_s and droplet axial velocity u_d. If the injector is discharging into air at rest, the momentum flux of the jet must be equal to the injection value $\pi R_I^2 \rho_l U_I^2$, leading to a second relationship

$$(\rho u^2 + \rho_l \frac{4}{3}\pi a^3 n u_d^2) r_s^2 \sim \rho_l U_I^2 R_I^2, \tag{2.4}$$

involving the characteristic axial component of the gas velocity u as an additional quantity. In the initial region where α is still large compared with unity, the gas and droplet axial velocities u and u_d maintain a value close to U_I, imposed by the inertia of the liquid droplets. Droplet heating and vaporization are also negligible in this region because for $\alpha \gg 1$ the energy balance is dominated by the presence of the abundant cold liquid phase, with the result that the temperature of the entrained gas rapidly decreases to match the initial liquid temperature T_I, while the droplet temperature hardly increases. In the absence of droplet vaporization, the dispersion dynamics of the resulting two-phase jet can be expected to be in many respects identical to that observed in gaseous jets laden with solid particles. Due to air entrainment, the radius r_s increases continuously with the downstream distance x to the atomization region. If we consider for simplicity that the small spray angle i_s is constant, so that $r_s \simeq i_s x$, then (2.3) and (2.4) lead to

$$\phi = \alpha\rho/\rho_l \sim (R_I/r_s)^2 \sim [R_I/(i_s x)]^2 \tag{2.5}$$

for the streamwise evolution of the liquid volume fraction.

As indicated in (2.4), the injected momentum flux, which is initially imparted to the droplets, is shared by the entrained air as the jet develops. In the initial region $\alpha \gg 1$ (although for a cubic array of droplets it is bounded by $\rho\alpha/\rho_l < \pi/6$), and thus $u \simeq u_d \simeq U_I$, with most of the momentum flux still associated with the liquid phase. Significant droplet and gas deceleration starts to occur when the momentum flux of the entrained gas becomes comparable to that of the liquid phase, which, according to (2.4), occurs as the jet mass-loading ratio α decreases to values of order unity. It is also in this region, $\alpha = O(1)$, where significant droplet vaporization will occur in the combustion chamber.

In general, the liquid is initially cold and the heating and vaporization of the droplets rely on the sensible heat of the surrounding hot gas, which may include hot combustion products that recirculate in the combustion chamber and also preheated air. The extent of heat exchange between the liquid and gas phases depends on the local value of α. Since the specific heat of the liquid fuel c_l is comparable to the specific heat at constant pressure of the surrounding gas mixture c_p, significant liquid heating requires that the individual cold droplet be surrounded by a volume of hot gas of mass comparable to or larger than that of the droplet, corresponding to values of α of order unity or smaller. Likewise, droplet vaporization also necessitates $\alpha \lesssim 1$, because in practical applications the specific enthalpy of the hot gas is comparable to the latent heat of vaporization L_v. As a result, significant droplet heating and vaporization occur only when the mass loading ratio decreases to values of order unity.

According to (2.2) and (2.5), the mass-loading ratio α in the bulk of the spray decreases to values $\alpha = O(1)$ when the spray radius r_s increases to large values of order

$$R_s = \left(\frac{\rho_l}{\rho}\right)^{1/2} R_I \gg R_I, \tag{2.6}$$

corresponding to large distances $x \sim L_s \sim R_s/i_s$, where a most important role in determining L_s is played by the growth of r_s associated with the gas entrainment. The design of the combustion system must ensure that the associated residence time L_s/U_I is comparable to the characteristic droplet life time, defined below by (3.26), and also comparable to the characteristic ignition time. Under those conditions, droplet dispersion resulting from turbulent gas entrainment, droplet vaporization, and chemical reaction collaborate effectively to burn the spray.

2.3 Collective effects in spray combustion

As indicated in (2.1), in most combustion systems the liquid density is much larger than the characteristic gas density in the combustion chamber. As a consequence, in regions where $\alpha = O(1)$, which, as noted above, are the zones where spray heating, vaporization, and combustion start to occur, the characteristic interdroplet distance is significantly larger than the droplet diameter, i.e., $l_d/(2a) \sim [\rho_l/(2\alpha\rho)]^{1/3} \gg 1$, which corresponds to large gas-to-liquid volume fractions $\phi^{-1} = \rho_l/(\alpha\rho) \gtrsim 10^2$ according to (2.1). These length scales are to be compared with the relevant macroscopic length scale ℓ of the problem (e.g., the thickness of the spray), which in most configurations of interest satisfies the condition $\ell \gg l_d$. For instance, for the slender jet spray of Fig. 2.1, the relevant macroscopic length ℓ is the characteristic radius R_s corresponding to the region where the average mass loading ratio decreases to values of order unity, given in order of magnitude in (2.6). Using this last expression together with the condition $\alpha = O(1)$ provides $R_s/l_d \sim (R_I/a)(\rho_l/\rho)^{1/6}$. In typical plain-orifice atomizers, with values of R_I on the order of a fraction of a millimeter, values of a on the order of a a few tens of microns, and large values of ρ_l/ρ in the range indicated in (2.1), the condition $R_s \gg l_d$ clearly holds.

In most systems, therefore, the characteristic scales of the problem satisfy

$$\ell \gg l_d \gg a. \tag{2.7}$$

Because of the condition $a \ll l_d$, each droplet vaporizes and moves with no significant direct effects from neighboring droplets. The main effects on the vaporization of the droplets are not due to the direct influence of their neighbors, but are associated instead with their interaction with the mean gas-phase collective environment created by all the droplets. This is clearly the case in the important distinguished regime when the droplet Reynolds number Re_d (based on the droplet diameter, $2a$, and the slip velocity, $|\mathbf{v} - \mathbf{v}_d|$, between the droplet and the local mean gas environment) is of order unity. Then, each droplet produces in the gas relatively large variations of the composition and temperature that are felt only in the immediate vicinity of the droplet, decaying rapidly at distances of the order of a, although more slowly in their wake, where the exchanges of mass, energy, and momentum between the droplet and gas are incorporated, in such a way that in most of the gas phase between droplets the variations of the gas properties are much smaller, as sketched in Fig. 2.3. The vaporization rate of and the force acting on each individual droplet are to be computed as those of the isolated droplet moving quasi-steadily, with the slip

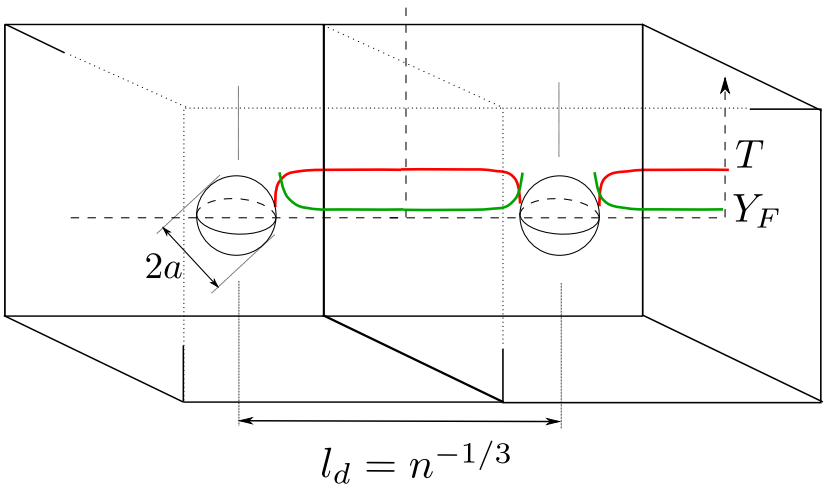

Figure 2.3. Droplets effect on collective temperature (red) and gaseous fuel concentration (green) profiles in a dilute region with $\alpha = O(1)$, where $a \ll l_d$ allows to neglect interactions between neighboring droplets. Pronounced changes of gas properties occur at near-droplet distances of order a, which ,in turn, are not accounted for in the bulk volume of the averaging cell.

velocity, in the mean local environment. The description of the slow variations of the different gas-phase variables, including the velocity, temperature, density, and relevant mass fractions, which occur over distances ℓ much larger than l_d, can be obtained at any spatial point by space-averaging over a neighborhood of that point of size d, with d in the range $\ell \gg d \gg l_d$. Since $d^3 \gg l_d^3$, each averaging cell includes many droplets, so that the corresponding point sources can be homogenized, as if they were homogeneously distributed, giving source terms that are proportional to the number of droplets per unit volume n. A noteworthy result of this homogenization process is that the intermediate length scale l_d only enters indirectly in the formulation (i.e., through the resulting value of n that appears as a factor in the sources).

In the distinguished regime $\mathrm{Re}_d \sim 1$, both molecular transport and convective transport contribute to the droplet-gas exchange rates and, after dumping these exchanges in the wakes, these contribute to the uniformized the local mean properties. These exchanges involve a diffusion time a^2/D_T, where D_T denotes the gas thermal diffusivity, and a residence time $a/|\mathbf{v} - \mathbf{v}_d|$, of the same order, both small compared with the characteristic droplet vaporization time $t_v \sim (a^2/D_T)(\rho_l/\rho)$, defined below in (3.26). Clearly, the wakes of the droplets randomly located upstream of each droplet, representing the mean convective transport, and the transverse diffusion both cooperate to uniformize the inter-

droplet atmosphere. Therefore, within the averaging cell, the gas properties can be taken as uniform. The pronounced gas-property changes occurring in the vicinity of each individual droplet (i.e., at distances of order a) can be neglected in the first approximation in the homogenized description, because the near-droplet regions occupy a negligible fraction $\phi \sim \rho/\rho_l \ll 1$ of the volume of the averaging cell.

While a single macroscopic scale ℓ can be often identified for laminar flows, a range of flow scales emerges in connection with the turbulent flow conditions found in practical applications, so that assessing the applicability of the criterion (2.7) is not straightforward. The integral scales of the turbulent flow, associated with the size ℓ' and velocity fluctuations v' of the largest eddies, are comparable to, although somewhat smaller than, the macroscopic scales of the jet. The condition $\ell' \gg l_d \gg a$ guarantees the validity of the multicontinua approach for the description of the interphase interactions occurring at these integral scales, including in particular the dispersion of the droplets, which is often dominated in shear flows by the large energetic eddies [16]. These large eddies coexist and interact with smaller vortices, of decreasing size down to the Kolmogorov length scale ℓ_k. The effects of the interaction of the droplets with the eddies of size below ℓ' can be expected to be weak, because their associated turnover time is typically much smaller than the droplet acceleration time, with the result that the droplets behave ballistically with respect to the smallest eddies. In other words, the small, rapid velocity fluctuations of the Kolmogorov eddies, which modify the instantaneous slip velocity seen by the droplet, do not change appreciably the associated drag force, whose value is determined instead by the average slip velocity, with leading-order corrections to the motion transverse to the spray arising mainly from the largest eddies. In that sense, therefore, the multicontinua description given in the following chapter can be expected to reproduce the main features of turbulent reacting sprays even when $\ell_k \sim l_d$, a condition often encountered in applications.

2.4 Spray-combustion phenomenology

The fuel vapor generated by the vaporizing droplets mixes with the surrounding hot air, enabling ignition to occur when a favorable equivalence ratio is encountered. Fuel sprays can be ignited using external sources such as electric sparks, torches or plasma jets, as is needed during the start and relight of jet engines and in the operation of gasoline direct-injection engines [17, 18]. Forced ignition is not needed during the normal steady operation of continuous-combustion systems, such as that depicted in Fig. 2.2, which represents the

typical arrangement found in gas turbines or industrial furnaces [18]. The manner in which combustion is stabilized downstream from the initial vaporization region is fundamentally dependent on the injection conditions. When the existing flow velocity is sufficiently low, combustion is established through partially premixed fronts that propagate along mixing layers in the nonuniform mixture created upstream by the vaporizing spray [19, 20]. In many systems, however, the injection velocities are much higher than the characteristic deflagration speed, thereby precluding upstream triple-flame propagation. In that case, combustion stabilization must rely instead on the autoignition of the fuel-air mixture, which is facilitated by the high temperature of the surrounding gas, with ignition often occurring near the edge of the spray jet, where the temperatures are higher.

The resulting ignition dynamics depends on the dispersion of the droplets in the presence of turbulent motion [21]. Optimal droplet dispersion is achieved for values of the droplet Stokes time, defined in (3.27), of the order of the integral time scale of the large vortices in the mixing layer [16, 22–24], under which conditions droplets may cross the mixing layer at vortex-braid regions to vaporize on the other side surrounded by hot air. On the other hand, droplets with sufficiently small Stokes times behave as flow tracers and become entrained in the large-scale turbulent eddies, where they come into contact with the high-temperature air. The lower strain rates found in these near-core regions facilitate ignition, whereas the larger strain rates found in the vortex-braid regions prevent ignition from occurring there by limiting fuel residence times.

As suggested earlier for purely gaseous ignition [25], the unsteady unstrained flamelet -and also the closely related problem of the laminar coflow mixing layer- may provide an adequate representation of the spray ignition dynamics occurring at the low-strain interfaces wrapped around the vortices. Numerical and asymptotic analyses of group ignition of heptane and methanol spray streams by coflowing hot air will be attempted in Chapter 4 (see also our recent publication [21]) with a simple one-step Arrhenius model adopted for the chemistry description. The two main controlling parameters will be seen to be the liquid mass-loading ratio α of the spray and the ratio of the droplet vaporization time t_v to the characteristic chemical time for ignition t_{ch}, evaluated at the air-side temperature, both assumed to be of order unity in the integrations. The solution is seen to depend strongly on the thermochemical properties of the selected fuel. Thus, because of its smaller latent heat of vaporization L_v, heptane droplets vaporize faster than methanol droplets. As a result, as the mixing layer develops, heptane vapor becomes available for reaction earlier than methanol vapor, thereby leading to smaller ignition distances, a

result in agreement with the ignition trends observed in previous numerical computations of ignition times in uniform spray mixtures [26]. Besides, the ignition of heptane is facilitated by its chemical heat release being more than twice that of methanol, resulting in a larger temperature increase per unit mass of fuel burnt that facilitates the self-acceleration of the chemical reaction rate, enabling a thermal runaway to take place. By way of contrast, the ignition of methanol proceeds gradually, in the form of a lean premixed flame that propagates slowly across the mixing layer from the hot air side. As shown in Chapter 4, the morphology of the ignition region is very sensitive to the specific values of the parameters selected. For instance, when air is employed as spray carrier, two-flame structures [27–31] are seen to emerge when the thermochemical properties of heptane are considered, but they are not observed for methanol.

As mentioned earlier, for all liquid fuels the mass of air needed to burn the unit mass of fuel, S, is a very large quantity (i.e., $S \simeq 15.2$ for heptane). As a result, in many applications, the partially premixed front originating at the ignition kernel burns completely the air that has been entrained upstream, while consuming only a limited fraction of the fuel available in the jet spray. The remaining gaseous fuel and accompanying fuel droplets burn downstream, in a diffusion flame that envelops the oxygen-starved spray jet. The resulting group-combustion configuration was envisioned as the predominant combustion regime in early theoretical analyses of droplet-cloud combustion. The extent to which the partially premixed region contributes to the overall combustion process depends on the specific configuration and may also change depending on the operating conditions, as observed in direct numerical simulations [31], which also reinforce the qualitative description given above.

Figure 2.2 depicts an external diffusion-flame configuration, often encountered in applications, in which the diffusion flame stands off the droplet cloud, burning the ambient oxygen with the fuel that originates from the vaporizing droplets. In many applications, the gas-phase chemical reactions are fast, in that the characteristic time for fuel oxidation is much shorter than both the characteristic fluid-mechanical time and the droplet-vaporization time. Under those conditions, the flame appears as a sheet, Σ_f, separating an internal oxygen-free region Ω_{F} from an external region Ω_{O} where no gaseous fuel is present in significant amounts.

For the high-Reynolds-number flows typically encountered in liquid-fueled burners, the diffusion flame is embedded in thin mixing layers bounding the spray-carrier stream. These mixing layers are distorted and strained by the turbulent flow. A canonical problem that helps to investigate effects of strain on

flames is the counterflow configuration [32], which will be used in Chapter 5 to examine the role of droplet inertia on the structure of spray flows, including the two extreme limits of chemically frozen (purely vaporizing) sprays and Burke-Schumann spray flames with infinitely fast reaction (see also our associated publication [33]).

Just as in the case of gaseous flames investigated by Liñán [34], sufficiently large values of the strain rate may lead to extinction of spray diffusion flames [35]. Since for typical liquid fuels the chemical-kinetic rate is strongly dependent on the temperature, the resulting flames near extinction display a thin reaction layer, whose inner structure is given by a reaction-diffusion balance. If a one-step reaction model is adopted for the chemistry description, then the extinction analysis of spray diffusion flames parallels that given by Liñán for gaseous flames [34]. In particular, as seen in Chapter 6, the inner structure of the reaction-diffusion layer is identical to that found by Liñán, while the presence of the droplets modifies the outer transport layers and must be correspondingly accounted for when describing the basic Burke-Schumann solution, including the resulting peak temperature, which is also affected by differential-diffusion effects associated with the small fuel-vapor diffusivity.

When extinction occurs, the flame surface develops an incipient hole with a bounding edge flame that propagates along the mixing layer. The dynamics of these edge flames under the action of the external strain determines whether the flame hole reheals, through a reignition triple flame, or whether the extinction hole continues to increase, as the edge flame further retreats. While there exists substantial knowledge of many aspects of edge flames and triple flames in gaseous combustion [36, 37], the associated spray problem has only been considered recently [38] and more work is needed to both clarify the structure of spray edge flames and quantify the dependences of their propagation velocity.

Large droplets with sufficient inertia may cross the mixing layers and move into the oxidizer stream, where they can possibly burn or vaporize individually or in small groups if favorable conditions are found. In principle, a closed diffusion flame may appear surrounding each individual droplet if their radius is large enough and favorable conditions for ignition are found as the droplet enters the oxidizer region [39]. The droplets in most practical combustion applications are however too small to sustain a flame in their vicinity. Therefore, as indicated in Fig. 2.2, many of the droplets that cross the spray diffusion flame can be expected to vaporize in Ω_O without a surrounding flame, generating fuel vapor that reacts with the existing oxygen in a distributed manner. Although the contribution of this distributed reaction to the total amount of heat released in the combustor can be expected to be negligible, these finite-rate effects are

of utmost importance, since partial oxidation of the fuel vapor generated by the crossing droplets, especially in the cold regions found near the combustor walls, results in augmented emissions of CO and unburnt hydrocarbons.

Before closing this overview, it is worth describing briefly the transient combustion phenomenology associated with the combustion cycle in diesel engines. Diesel-fuel injection into the cylinder begins shortly before top dead center. The spray starts to vaporize immediately as it mixes with the compressed hot air, creating a nonuniform mixture of fuel vapor and air, whose temperature continues to increase as a result of the homogeneous compression process that is occurring simultaneously, thereby enhancing the incipient chemical reaction. Autoignition occurs simultaneously at several near-stoichiometric hot spots in the bulk of the spray jet, where the most favorable conditions are met, leading to the formation of ignition fronts that sweep through the reactive mixture with a velocity of a few tens meters per second. This rapid process is accompanied by a significant increase of temperature and pressure in the cylinder that further accelerates the chemical reaction. The magnitude of these pressure and temperature increments depends on the fraction of the liquid fuel that was vaporized prior to ignition. As they propagate through the spray jet, the ignition fronts deplete the oxygen found in fuel-rich regions and the fuel vapor found in fuel-lean regions, leaving a diffusion flame at the instantaneous stoichiometric surface. As a result, an internal group combustion regime emerges following ignition, with the diffusion flame located within the spray, separating an inner oxygen-free region from an outer region free from gaseous fuel. In the subsequent evolution, the droplets found outside may burn individually or may vaporize, generating fuel vapor that mixes and reacts with the available air.

References

[1] A. Lefebvre, Atomization and sprays, Hemisphere Publishing, 1989.

[2] G. Taylor, The dynamics of thin sheets of fluid. iii. disintegration of fluid sheets, Proceedings of the Royal Society of London. Series A. Mathematical and Physical Sciences 253 (1959) 296–312.

[3] S. Lin, R. Reitz, Drop and spray formation from a liquid jet, Annual Review of Fluid Mechanics 30 (1) (1998) 85–105.

[4] J. Lasheras, E. Hopfinger, Liquid jet instability and atomization in a coaxial gas stream, Annual Review of Fluid Mechanics 32 (1) (2000) 275–308.

[5] C. Dumouchel, On the experimental investigation on primary atomization of liquid streams, Experiments in fluids 45 (3) (2008) 371–422.

[6] W. A. Sirignano, Fluid dynamics and transport of droplets and sprays, 2nd edition, Cambridge University Press, Cambridge, UK., 2010.

[7] E. Giannadakis, M. Gavaises, C. Arcoumanis, Modelling of cavitation in diesel injector nozzles, Journal of Fluid Mechanics 616 (2008) 153–193.

[8] G. Taylor, The mechanics of swirl atomizers, Proc. 7th Intl. Congress for Appl. Mech. 2 (1948) 280–285.

[9] G. Taylor, The dynamics of thin sheets of fluid. iii. disintegration of fluid sheets, Proceedings of the Royal Society of London. Series A. Mathematical and Physical Sciences 253 (1274) (1959) 313–321.

[10] O. Desjardins, H. Pitsch, Detailed numerical investigation of turbulent atomization of liquid jets, Atomization and Sprays 20 (4).

[11] J. Shinjo, A. Umemura, Simulation of liquid jet primary breakup: Dynamics of ligament and droplet formation, International Journal of Multiphase Flow 36 (7) (2010) 513–532.

[12] S. Rana, M. Herrmann, Primary atomization of a liquid jet in crossflow, Physics of Fluids 23.

[13] J. Shinjo, A. Umemura, Detailed simulation of primary atomization mechanisms in diesel jet sprays (isolated identification of liquid jet tip effects), Proceedings of the Combustion Institute 33 (2) (2011) 2089–2097.

[14] V. Le Chenadec, H. Pitsch, A monotonicity preserving conservative sharp interface flow solver for high density ratio two-phase flows, Journal of Computational Physics 249 (2013) 185–203.

[15] J. Reveillon, K. Bray, L. Vervisch, DNS study of spray vaporization and turbulent micro-mixing, in: 36th Aerospace Sciences Meeting and Exhibit, Reno NV, 1998, p. 72.

[16] E. K. Longmire, J. K. Eaton, Structure of a particle-laden round jet, Journal of Fluid Mechanics 236 (1992) 217–257.

[17] J. B. Heywood, Internal combustion engine fundamentals, Vol. 930, Mcgraw-hill New York, 1988.

[18] A. H. Lefebvre, Gas turbine combustion, CRC press, 1998.

[19] S. K. Marley, E. J. Welle, K. M. Lyons, Combustion structures in lifted ethanol spray flames, Journal of engineering for gas turbines and power 126 (2) (2004) 254–257.

[20] V. M. Reddy, D. Trivedi, S. Kumar, Experimental investigations on lifted spray flames for a range of coflow conditions, Combustion Science and Technology 184 (1) (2012) 44–63.

[21] D. Martínez-Ruiz, J. Urzay, A. L. Sánchez, A. Liñán, F. A. Williams, Dynamics of thermal ignition of spray flames in mixing layers, Journal of Fluid Mechanics 734 (2013) 387–423.

[22] B. Lazaro, J. Lasheras, Particle dispersion in the developing free shear layer. part 2. forced flow, Journal of Fluid Mechanics 235 (1992) 179–221.

[23] C. Crowe, T. Troutt, J. Chung, Numerical models for two-phase turbulent flows, Annual Review of Fluid Mechanics 28 (1) (1996) 11–43.

[24] C. Lacour, D. Durox, S. Ducruix, M. Massot, Interaction of a polydisperse spray with vortices, Experiments in fluids 51 (2) (2011) 295–311.

[25] N. Peters, Turbulent combustion, Cambridge university press, 2000.

[26] E. Gutheil, Numerical analysis of the autoignition of methanol, ethanol, n-heptane and n-octane sprays with detailed chemistry, Combustion science and technology 105 (4-6) (1995) 265–278.

[27] S. C. Li, F. A. Williams, Experimental and numerical studies of two-stage methanol flames, in: Symposium (International) on Combustion, Vol. 26, Elsevier, 1996, pp. 1017–1024.

[28] S. Marley, E. Welle, K. Lyons, W. Roberts, Effects of leading edge entrainment on the double flame structure in lifted ethanol spray flames, Experimental thermal and fluid science 29 (1) (2004) 23–31.

[29] J. Reveillon, L. Vervisch, Analysis of weakly turbulent dilute-spray flames and spray combustion regimes, Journal of Fluid Mechanics 537 (2005) 317–347.

[30] M. Mikami, Y. Mizuta, Y. Tsuchida, N. Kojima, Flame structure and stabilization of lean-premixed sprays in a counterflow with low-volatility fuel, Proceedings of the Combustion Institute 32 (2) (2009) 2223–2230.

[31] K. Luo, H. Pitsch, M. G. Pai, O. Desjardin, Direct numerical simulations and analysis of three-dimensional n-heptane spray flames in a model swirl combustor, Proc. Comb. Inst. 89 (2011) 1447–1460.

[32] S. C. Li, Spray stagnation flames, Progress in energy and combustion science 23 (4) (1997) 303–347.

[33] A. Liñán, D. Martínez-Ruiz, A. L. Sánchez, J. Urzay, Regimes of spray vaporization and combustion in counterflow configurations, Combustion Science and Technology 187 (1-2) (2015) 103–131.

[34] A. Liñán, The asymptotic structure of counterflow diffusion flames for large activation energies, Acta Astronautica 1 (7) (1974) 1007–1039.

[35] E. Gutheil, W. A. Sirignano, Counterflow spray combustion modeling with detailed transport and detailed chemistry, Combustion and Flame 113 (1) (1998) 92–105.

[36] J. Buckmaster, Edge-flames, Progress in Energy and Combustion Science 28 (5) (2002) 435–475.

[37] S. Chung, Stabilization, propagation and instability of tribrachial triple flames, Proceedings of the Combustion Institute 31 (1) (2007) 877–892.

[38] J. Greenberg, L. Kagan, G. Sivashinsky, A numerical study of polydisperse spray flame ignition and extinction fronts in a mixing layer, Combustion Theory and Modelling 17 (6) (2013) 1053–1066.

[39] M. Mikami, S. Miyamoto, N. Kojima, Counterflow diffusion flame with polydisperse sprays, Proceedings of the Combustion Institute 29 (1) (2002) 593–599.

CHAPTER

THREE

Multicontinua formulation for vaporization and combustion of dilute sprays

The disparity of scales typically present in practical spray-combustion applications enables a simplified description of the resulting flow to be performed in which the gas and liquid phases, when seen with a scale $\ell \gg l_d$, can be treated as continuum media, whose evolution is coupled through the interphase exchanges of mass, momentum, and energy [1]. The multicontinua formulation corresponding to a reactive polydisperse spray with N_c different droplet classes is given below, including the separate sets of equations needed to describe the homogenized gas phase and the evolution of each droplet class. To complete the formulation, expressions are provided for the different droplet source terms. The resulting equations, including a simple one-step description for the chemical reaction rate, are employed to identify, through appropriate order-of-magnitude analyses, the main controlling parameters and their role in the coupling between the liquid and gas phases in vaporizing and reacting spray flows.

3.1 Liquid-phase equations

In treating the droplets as moving point sources it seems natural to employ a Lagrangian approach in which each droplet is traced individually, with the ambient properties changing as the droplet traverses the flow field. The position of the droplet k is determined by integrating the kinematic equation

$$\frac{\mathrm{d}\mathbf{x}_d^k}{\mathrm{d}t} = \mathbf{v}_d^k. \tag{3.1}$$

Correspondingly, the evolution of the droplet velocity $\mathbf{v}_d^k$, droplet radius a^k, and droplet temperature T_d^k is obtained by integrating along the droplet trajectory

the evolution equations

$$\frac{4}{3}\pi\rho_l(a^k)^3\frac{\mathrm{d}\mathbf{v}_d^k}{\mathrm{d}t} = \mathbf{f}^k, \tag{3.2}$$

$$\frac{4}{3}\pi\rho_l\frac{\mathrm{d}(a^k)^3}{\mathrm{d}t} = -\dot{m}^k, \tag{3.3}$$

$$\frac{4}{3}\pi\rho_l(a^k)^3 c_l\frac{\mathrm{d}T_d^k}{\mathrm{d}t} = \dot{q}_d^k. \tag{3.4}$$

The source terms on the right-hand side account for the exchange rates of momentum, mass, and heat between the droplet and the surrounding gas environment. In particular, $\dot{m}^j$ and $\dot{q}_d^j$ are the vaporization and heating rates of the individual droplet and $\mathbf{f}^j$ is the force of the gas on the droplet. In writing (3.4), the temperature is assumed to be uniform inside the droplet, a valid approximation when the heat conduction in the liquid droplet (possibly assisted by internal convection) is sufficiently fast for the associated conduction time to be much smaller than the droplet heating time t_q from the injection temperature T_I to a value close to the boiling temperature. Using the expression $t_q = \frac{1}{3}(c_l/c_p)(\rho_l/\rho)(a^2/D_T)$ given after (3.28) together with the estimate $a^2/[\pi\kappa_l/(\rho_l c_l)]$ for the heat conduction time through the droplet (including in the denominator a factor π taken from the solution of heat conduction in the sphere [2]) indicates that this approximation of uniform droplet temperature is accurate when the thermal conductivity of the liquid fuel κ_l is much larger than the gas thermal conductivity κ [3], a condition satisfied in most situations (e.g., for methanol, $\kappa_l \simeq 0.2$ W/(J K) at its boiling temperature, whereas for air $\kappa \simeq 0.03$ W/(J K) at that same temperature). Clearly, this approximation of uniform droplet temperature becomes even more accurate in the presence of internal liquid circulation. For liquid fuels of low thermal conductivity equation (3.4) must be replaced during the fairly short heating period by a more complicated heating description accounting for the nonuniform temperature distribution inside the droplets [3], with consideration of the presence of recirculating liquid flow needed for increased accuracy [4].

In modeling combustion systems, the droplets are often introduced in the flow field at different entry ports, as required to mimic the injection characteristics of the system. Integrating with the given initial conditions provides the instantaneous distributions of a^k, $\mathbf{v}_d^k$, and T_d^k along the droplet trajectories. In order to simplify the Lagrangian description, the droplets may be classified into classes, according to their origin and velocity of penetration at the entrance surface to the computational domain. The computation is coupled to that of the gas phase through the source terms in the conservation equations for the gas

phase, which are to be evaluated in the numerical integration by accounting for the trajectories that traverse each averaging cell at a given time. This kind of tracking techniques is commonly employed in the particle-source-in-cell model [5] of typical turbulent combustion codes. Applications of this combined Eulerian-Lagrangian modeling strategy can be found, for instance, in computations of group combustion in pulverized coal furnaces [6–8] and of full-scale aeronautical combustors [9–11]. It should be noted, however, that the Lagrangian treatment of the liquid phase can lead to high computational costs and load-balancing issues in parallel computations with large numbers of droplets.

An alternative to this Eulerian-Lagrangian description is the so-called multi-continua formulation, in which the liquid phase is also treated as a continuum field including N_c different droplet classes, with the droplet population of each droplet class j described in terms of the number of droplets per unit volume n^j through the conservation equation

$$\frac{\partial n^j}{\partial t} + \nabla \cdot \left(n^j \mathbf{v}_d^j \right) = 0. \tag{3.5}$$

Correspondingly, in this Eulerian description the evolution equations along the trajectories (3.2)–(3.4) are expressed for each droplet class with use made of the Eulerian differential operator $\mathrm{d}()/\mathrm{d}t = \partial()/\partial t + \mathbf{v}_d^j \cdot \nabla()$. This continuum formulation is often simpler than formulations involving tracking of individual droplets and greatly facilitates analyses of laminar sprays. However, the continuum description of the liquid phase is known to be inadequate for addressing inertial sprays with multiple crossings of droplet trajectories, as occurs, for example, in turbulent flows or in the presence of recirculating flow regions when the particle size is not small enough. Although for some laminar flow configurations, such as those considered in Chapters 4, 5 and 6, introduction of specific modifications to the formulation renders the Eulerian description valid, methods based on Lagrangian descriptions of the liquid phase are in general needed in the presence of droplet crossings. A promising alternative approach for tackling the crossing of droplet trajectories in inertial sprays, based on field formulations of the liquid phase, employs quadrature methods of moments to solve the kinetic spray equation [12]. Despite the significant progress made recently in the development of these formulations [13, 14], more work remains to be done to warrant full applicability to spray-combustion problems [15].

3.2 Gas-phase conservation equations

The description shall be complemented by writing the homogenized gas-phase conservation equations, which include the continuity, species, and momentum equations

$$\frac{\partial \rho}{\partial t} + \nabla \cdot (\rho \mathbf{v}) = \sum_{j=1}^{N_c} n^j \dot{m}^j, \tag{3.6}$$

$$\frac{\partial}{\partial t}(\rho Y_i) + \nabla \cdot (\rho \mathbf{v} Y_i) + \nabla \cdot (\rho Y_i \mathbf{V}_i) = \dot{w}_i + \begin{cases} \sum_{j=1}^{N_c} n^j \dot{m}^j \text{ (if } i = \text{F)} \\ 0 \text{ (if } i \neq \text{F)} \end{cases}, \tag{3.7}$$

$$\frac{\partial}{\partial t}(\rho \mathbf{v}) + \nabla \cdot (\rho \mathbf{v}\mathbf{v}) = \nabla \cdot \overline{\tau} - \nabla p' + \sum_{j=1}^{N_c} n^j (\dot{m}^j \mathbf{v}_d^j - \mathbf{f}^j), \tag{3.8}$$

where $\mathbf{v}$ and $\overline{\tau}$ denote, respectively, the gas velocity and the viscous stress tensor. The gas composition is described in terms of the mass fraction Y_i of the N_s chemical species present in the mixture, with $\dot{w}_i$ representing the mass of species i generated by chemical reaction per unit volume per unit time. Note that, since the sum of the N_s conservation equations (3.7) leads to (3.6), the description of the gas phase requires the integration of $N_s - 1$ of the conservation equations for the chemical species, the mass fraction of the N_sth species (often N_2) being computed from the identity $\sum_{i=1}^{N_s} Y_i = 1$. For the conditions found in most spray-combustion applications, the prevailing Mach number is small, so that the relative spatial pressure variations are negligible. This is taken into account in the formulation by using in the momentum equation the variable $p' = p - p_o(t)$, defined as the difference of the pressure from the value $p_o(t)$ found at a fixed arbitrary point in the combustor, the ratio p'/p_o being a small quantity of the order of the Mach number squared.

The summations appearing on the right-hand sides of the above equations are the coupling terms accounting for the presence of the droplets, which appear as distributed sources. In the formulation, the expressions written for these source terms correspond to a continuum description of the liquid phase, with the superscript j used to indicate the properties of each one of the N_c droplet classes considered. Thus, the continuity equation (3.6) and the fuel-vapor conservation equation include the mass of fuel vapor produced per unit volume per unit time, $\sum_{j=1}^{N_c} n^j \dot{m}^j$, with n^j representing the number of droplets per unit volume. Similarly, momentum exchange between the liquid and gas phases is accounted for in writing (3.8). Note that, if a Lagrangian description

is employed instead for the liquid phase, then the source terms in the gas-phase equations would be calculated by evaluating the separate contributions of the different droplets present in each computational cell.

In the low-Mach-number limit, viscous dissipation can be neglected along with spatial pressure variations when writing the energy equation, thereby yielding

$$\frac{\partial}{\partial t}\left(\rho h\right)+\nabla\cdot\left(\rho\mathbf{v}h\right)=-\nabla\cdot\mathbf{q}-\sum_{j=1}^{N_c}n^j\left[\dot{m}^j\left(L_v-h_{\mathrm{F}_s}^j\right)+\dot{q}_d^j\right]+\frac{\mathrm{d}p_o}{\mathrm{d}t}, \tag{3.9}$$

where $h=\sum_{i=1}^{N_s}Y_ih_i=\sum_{i=1}^{N_s}Y_i(h_i^o+h_i^T)$ is the gas enthalpy, expressed here for a mixture with N_s different chemical species, with h_i, h_i^o, $h_i^T=\int^T c_{p_i}\mathrm{d}T$, and c_{p_i} representing the enthalpy, enthalpy of formation, thermal enthalpy, and specific heat at constant pressure of species i. The time variation of the pressure has been retained in (3.9), as it can be of importance for combustion in reciprocating engines. The expression for the heat-flux vector $\mathbf{q}=-\kappa\nabla T+\rho\sum_{i=1}^{N_s}h_iY_i\mathbf{V}_i+\mathbf{q}_R$ includes the Fourier heat-conduction term $-\kappa\nabla T$, where κ is the thermal conductivity and T is the gas temperature, along with the radiative heat flux $\mathbf{q}_R$ and the energy transferred by diffusive transport of chemical species, $\rho\sum_{i=1}^{N_s}h_iY_i\mathbf{V}_i$, where $\mathbf{V}_i$ is the diffusion velocity of species i. The droplet source term in (3.9) accounts for the heating and vaporization of the liquid fuel, with $h_{\mathrm{F}_s}^j=h_{\mathrm{F}}^o+\int^{T_d^j}c_{p\mathrm{F}}\mathrm{d}T$ representing the enthalpy of the fuel vapor at the droplet-surface temperature T_d^j. It is worth noting that the effect of the chemical reactions on the energy balance is clearly apparent when the summation over all species of the enthalpy of formation h_i^o times (3.7) is subtracted from (3.9) to give

$$\begin{aligned}&\frac{\partial}{\partial t}\left(\rho c_pT\right)+\nabla\cdot\left(\rho\mathbf{v}c_pT\right)-\nabla\cdot\left(\kappa\nabla T\right)=-\nabla\cdot\mathbf{q}_R\\&-\sum_{i=1}^{N_s}h_i^o\dot{w}_i-\sum_{j=1}^{N_c}n^j\left[\dot{m}^j\left(L_v-c_pT_d^j\right)+\dot{q}_d^j\right]+\frac{\mathrm{d}p_o}{\mathrm{d}t}.\end{aligned} \tag{3.10}$$

which is written explicitly in terms of the temperature T by neglecting differences of specific heats c_{p_i} from the mean value c_p.

The above equations for the gas and liquid phases must be supplemented with the equation of state

$$p_o=\rho R^oT\sum_{i=1}^{N_s}\frac{Y_i}{M_i}, \tag{3.11}$$

where R^o is the universal gas constant and $(\sum_{i=1}^{N_s} Y_i/M_i)^{-1}$ is the mean molecular mass of the gas mixture, with M_i representing the molecular mass of species i. Also, appropriate constitutive equations must be given for the viscous stress tensor $\overline{\tau}$ and for the diffusion velocities, the latter often expressed in terms of Fick's law $\mathbf{V}_i = -D_i \nabla Y_i$, with D_i representing the diffusion coefficient of the species i into the gas mixture. To complete the formulation, expressions must be provided for the chemical-reaction rates $\dot{w}_i$ and for the exchange rates of mass $\dot{m}$, heat $\dot{q}_d$, and momentum $\mathbf{f}$, between the gas and the droplets.

3.3 Exchange rates between the droplet and the local homogenized gas

To compute the exchange rates of mass, momentum, and energy between the individual droplet and the surrounding gas one needs to describe the flow field in the vicinity of the droplet, where the flow relative to the droplet is quasisteady at distances of the order a from the droplet surface, as indicated before. This is so because the residence time $a/|\mathbf{v} - \mathbf{v}_d|$ and the diffusive times, of order a^2/D_T, in that region are typically of the same order, very small compared with the characteristic droplet life time $t_v \sim (a^2/D_T)(\rho_l/\rho)$, given below in (3.26), a result of the disparity $\rho_l \gg \rho$ [16]. Two main nondimensional parameters play a significant role in determining the near-droplet distributions of temperature and fuel mass fraction. One is the Reynolds number,

$$\mathrm{Re}_d = \frac{\rho|\mathbf{v} - \mathbf{v}_d|2a}{\mu}, \tag{3.12}$$

defined in terms of the droplet diameter $2a$ and the values of the gas density and viscosity corresponding to the surrounding atmosphere, ρ and μ. The other, an eigenvalue of the problem, is the nondimensional vaporization rate

$$\lambda = \frac{\dot{m}}{4\pi\kappa a/c_p}, \tag{3.13}$$

which represents a Stefan-flow Peclet number based on the mean radial gas velocity at the droplet surface $\dot{m}/(4\pi a^2\rho)$. The value of λ is determined by the balance between convective transport and conductive and diffusive transport of heat and species, associated with the temperature and concentration differences between the gas and the droplet surface, which are represented by the Spalding transfer numbers $c_p(T - T_d)/L_v$ and $(Y_{\mathrm{F},S} - Y_{\mathrm{F}})/(1 - Y_{\mathrm{F},S})$, where $Y_{\mathrm{F},S}$ is the fuel-vapor mass fraction at the droplet surface. As seen below, for low Reynolds

numbers, λ is given by the algebraic equations (3.17) and (3.18).

3.3.1 Effects of droplet Reynolds number

In combustion applications, the resulting values of λ range from small, in the initial stages of droplet heating, to values at most of order unity during the main vaporization stage (note that the nondimensional vaporization rate λ can never be much larger than unity, because the associated strong blowing would prevent the needed transfer of heat from the atmosphere surrounding the droplet). As for the droplet Reynolds number, in regions where most of the spray vaporization occurs, the typical values of Re_d range from only moderately small compared with unity, for small droplet sizes, to values only moderately large compared with unity. For small Re_d the convective transport terms associated with the slip velocity are negligible in the gas-phase near-field region of the droplets, resulting in temperature and concentration fields with spherical symmetry. The convective transport due to slip flow becomes important in the non-spherico-symmetrical Oseen far-field region, scaled with a/Re_d, which does not need to be described when evaluating the near-field Stokes flow, because this matches directly with the first approximation given by the homogenized field.

In the relevant distinguished limit $\mathrm{Re}_d \sim 1$, the molecular-transport effects on the near-droplet flow field, and also the vorticity, are confined to radial distances $r \sim a$ from the droplet and to the droplet wake, where the exchanges between the particle and the gas are collected and transported downstream with the local mean gas slip velocity. At downstream distances of order l_d the width of the wake is of order $\sqrt{al_d}$, and the relative variations of temperature and fuel mass fraction across the wake, of order unity at distances of order a, have been reduced by a factor a/l_d. Similarly, at these distances $\sim l_d$ the spatial variations of velocity in the wake are of order $|\mathbf{v} - \mathbf{v}_d|a/l_d$, whereas the azimuthal vorticity, of order $|\mathbf{v} - \mathbf{v}_d|/a$ in the vicinity of the droplet, is reduced by a factor $(a/l_d)^{3/2}$ in the wake.

The vorticity in the wake determines the local distribution of the gas velocity relative to the homogenized gas, with a momentum flux (towards the droplet) equal to the difference between the droplet drag $\mathbf{f}$ and the momentum added to the gas phase by vaporization of the liquid fuel at the droplet surface $\dot{m}\mathbf{v}_d$. This is clearly visible in the droplet source term on the right-hand side of the momentum conservation equation of the gas phase (3.8). Correspondingly, since the fuel vapor generated at the droplet surface is convected to the trailing wake, the flux of the excess of fuel vapor across the wake equals the droplet vaporization

rate $\dot{m}$, as seen in the homogenized gas-phase continuity and species equations (3.6) and (3.7). Similarly, the flux of the defect of enthalpy in the droplet wake equals the rate of heat transferred to the droplet $\dot{m}L_v + \dot{q}_d$, corrected to account for the enthalpy of the fuel vapor added to the wake by vaporization $\dot{m}h_{\mathrm{F}_s}$, giving the contribution emerging in the energy equation (3.9).

The presentation shall now be continued by summarizing the expressions of the exchange rates, for values of Re_d small compared with unity, which, surprisingly, due to strong geometric effects remain fairly accurate as the Reynolds number increases to $\mathrm{Re}_d \sim 1$, so that the associated description provides sufficient accuracy for many spray-combustion applications. More complete droplet models, incorporating dependences on Re_d as well as influences of additional effects not contemplated in the derivation given below, are available for use in computations when increased accuracy is needed [1].

3.3.2 Exchange rates for $\mathrm{Re}_d \ll 1$

For values of Re_d much smaller than unity the flow is dominated by molecular transport, leading to well-known results, including the familiar Stokes formula

$$\mathbf{f} = 6\pi\mu a(\mathbf{v} - \mathbf{v}_d) \tag{3.14}$$

for the force acting on the droplet. This expression neglects the presence of the Stefan flow associated with vaporization, which gives a uniform radial mass flux equal to the droplet vaporization rate $\dot{m}$. Consideration of the Stefan flow due to gasification leads to quantitative modifications to Stokes law (3.14), including a correcting factor, a function of λ, fairly close to unity when $\lambda \sim 1$ [17].

In the limit of small Re_d associated with (3.14) the distributions of temperature and fuel mass fraction around the droplet are spherically symmetrical. The temperature distribution $\tilde{T}$ is obtained as a function of the radial coordinate scaled with the droplet radius $\tilde{r}$ by integrating the steady form of the energy equation subject to the boundary values T and T_d in the surrounding atmosphere and on the droplet surface, respectively. The integration is simplified by incorporating the commonly used assumption of constant gas thermal conductivity, although analyses are available that do not make use of this approximation [18–20]. The resulting problem

$$\frac{\mathrm{d}}{\mathrm{d}\tilde{r}}\left(\lambda\tilde{T} - \tilde{r}^2\frac{\mathrm{d}\tilde{T}}{\mathrm{d}\tilde{r}}\right) = 0 \begin{cases} \tilde{r} = 1: & \tilde{T} = T_d \\ \tilde{r} \to \infty & \tilde{T} = T \end{cases} \tag{3.15}$$

can be integrated to give $\tilde{T} = T - (T - T_d)(1 - e^{-\lambda/\tilde{r}})/(1 - e^{-\lambda})$, which can be used to compute the rate of heat transferred to the droplet by heat conduction from the gaseous atmosphere $\dot{q}_g = 4\pi a\kappa(\mathrm{d}\tilde{T}/\mathrm{d}\tilde{r})_{\tilde{r}=1}$, giving $\dot{q}_g = 4\pi\kappa a(T - T_d)\lambda/(e^{\lambda} - 1)$, where $\lambda/(e^{\lambda} - 1)$ is the Nusselt number accounting for the Stefan flow. According to the energy balance at the droplet surface, the heat transferred from the surrounding gas is employed to heat up the interior of the droplet and to vaporize the liquid fuel at the surface according to $\dot{q}_g = \dot{q}_d + L_v\dot{m}$, which can be rewritten in the form

$$4\pi\kappa a \left(\frac{T - T_d}{e^{\lambda} - 1} - \frac{L_v}{c_p} \right) \lambda = \dot{q}_d, \tag{3.16}$$

providing a relationship between λ and $\dot{q}_d$. Similarly, the fuel-vapor distribution around the droplet $\tilde{Y}_{\mathrm{F}} = Y_{\mathrm{F}} + (Y_{\mathrm{F},S} - Y_{\mathrm{F}})(1 - e^{-L_{\mathrm{F}}\lambda/\tilde{r}})/(1 - e^{-L_{\mathrm{F}}\lambda})$ is obtained by integrating the corresponding convection-diffusion conservation equation with boundary conditions $\tilde{Y}_{\mathrm{F}} = Y_{\mathrm{F}}$ as $\tilde{r} \to \infty$ and $\tilde{Y}_{\mathrm{F}} = Y_{\mathrm{F},S}$ at $\tilde{r} = 1$, where $Y_{\mathrm{F},S}$ is the fuel-vapor mass fraction at the droplet surface. Here, a binary description is adopted for the fuel-vapor diffusion velocity, with D_{F} representing the binary diffusion coefficient of the gaseous fuel and nitrogen –which is the dominant component of the gas mixture surrounding the droplet– and $L_{\mathrm{F}} = \kappa/(\rho c_p D_{\mathrm{F}})$ being the corresponding Lewis number. For a mono-component fuel droplet, for which the radial flux of fuel vapor is equal to $\dot{m}$, the fuel-vapor distribution $\tilde{Y}_{\mathrm{F}}(\tilde{r})$ can be used to obtain the relationship

$$\lambda = \frac{1}{L_{\mathrm{F}}} \ln \left(\frac{1 - Y_{\mathrm{F}}}{1 - Y_{\mathrm{F},S}} \right). \tag{3.17}$$

To close the problem, the condition of thermodynamic equilibrium at the droplet surface is applied again to compute the fuel surface mass fraction using the Clausius-Clapeyron relation for the partial pressure of the fuel vapor at the droplet surface

$$\frac{M_s}{M_{\mathrm{F}}} Y_{\mathrm{F},S} = \exp\left(\frac{L_v}{R_{\mathrm{F}} T_B} - \frac{L_v}{R_{\mathrm{F}} T_d} \right), \tag{3.18}$$

which has an Arrhenius-like dependence on T_d, with a constant heat of vaporization L_v per unit mass if the pressure in the chamber is not close to the critical pressure. Here, $R_{\mathrm{F}} = R^o/M_{\mathrm{F}}$ is the fuel gas constant and T_B is the boiling temperature of the fuel at the chamber pressure. The mean molecular mass of the gas at the droplet surface $M_s = (Y_{\mathrm{F},S}/M_{\mathrm{F}} + \sum_{i \neq \mathrm{F}}^{N_s} Y_{i,s}/M_i)^{-1}$ depends on $Y_{\mathrm{F},S}$ and also on the mass fractions of the other chemical species at the droplet surface $Y_{i,s}$. Their values can be obtained in terms of their corresponding ambi-

ent values Y_i by integrating the convection-diffusion balance equations for each species to give $Y_{i,s} = Y_i \exp(-\lambda L_i)$, where the Lewis numbers L_i are evaluated with the binary diffusion coefficients of the given species through nitrogen, whose mass fraction is determined in this approximation from the equation $\sum_{i=1}^{N_s} Y_i = 1$.

Equations (3.17) and (3.18), supplemented with the expressions $Y_{i,s} = Y_i \exp(-\lambda L_i)$ for the computation of M_s, determine the values of λ and $Y_{\mathrm{F},S}$ in terms of T_d and of the ambient mass fractions. For given values of a and T, the resulting value of λ can be used in (3.16) to determine $\dot{q}_d$ and in (3.13) to compute the associated droplet vaporization rate $\dot{m}$. The computation is simplified if the expression $M_{\mathrm{F}}/M_s = Y_{\mathrm{F},S} + (1 - Y_{\mathrm{F},S})M_{\mathrm{F}}/M_{\mathrm{N}_2}$ is employed, an approximation that accounts for the large differences of the molecular masses of the fuel vapor and N_2, while taking the molecular mass of all other species equal to that of nitrogen. In that case, equation (3.18) can be used to determine $Y_{\mathrm{F},S}$ as a function of T_d, while (3.17) gives explicitly λ in terms of $Y_{\mathrm{F},S}$ and Y_{F}.

The above expressions (3.16)–(3.18) involve a number of physicochemical properties that are different for different fuels, with representative values given below in Table 3.1. For the three different liquid fuels considered, straightforward evaluations using these properties indicate that the latent heat of vaporization satisfies $L_v \gg R_{\mathrm{F}} T_B$, which implies that the mass fraction of fuel vapor at the droplet surface, given by the Clausius-Clapeyron equation (3.18), remains exponentially small until the droplet temperature reaches values close to the boiling temperature. For those applications in which the injection temperature T_I is sufficiently below T_B, i.e., its value is such that $(T_B - T_I)/T_B \gg [L_v/(R_{\mathrm{F}} T_B)]^{-1}$, there exists necessarily an initial heat up period during which $Y_{\mathrm{F},S} \ll 1$, so that $Y_{\mathrm{F},S}$ can be neglected with respect to unity in (3.17). If the atmosphere surrounding the droplet contains fuel vapor, then during this initial period there exists condensation ($\lambda < 0$), as inferred by (3.17), while if $Y_{\mathrm{F}} = 0$ then $0 < \lambda \ll 1$. In this last case, the thermal power transferred from the gas is dedicated to increasing the temperature of the yet non-vaporizing droplet, with a rate that simplifies to $\dot{q}_d = 4\pi\kappa a(T - T_d)$, as follows from (3.16) when $\lambda \ll 1$. This heat-up period ends when the liquid temperature reaches values close to the boiling temperature, i.e., $(T_B - T_d)/T_B \sim [L_v/(R_{\mathrm{F}} T_B)]^{-1} \ll 1$, when vaporization starts with values of the fuel-vapor mass fraction of order unity at the droplet surface. In this vaporizing period the droplet temperature remains approximately constant, with a value $T_d \simeq T_B$, so that $\dot{q}_d \simeq 0$, while the vaporization rate reduces to the

	M_{F} [g/mol)]	ρ_l [kg/m^3]	c_l [kJ/kg]	L_v [kJ/kg]	T_B [K]	L_{F}	$L_v/(R_{\mathrm{F}}T_B)$
Heptane	100	679.5	2.250	0.34×10^3	371	2.6	11.02
Dodecane	170	750	2.212	0.36×10^3	489	3.6	15.05
Methanol	32	791	2.484	1.1×10^3	337	1.2	12.56

Table 3.1. Values of physicochemical properties relevant for droplet heating and vaporization.

well-known Spalding expression

$$\frac{\dot{m}}{4\pi\kappa a/c_p} = \lambda = \ln\left(1 + \frac{c_p(T - T_B)}{L_v}\right), \tag{3.19}$$

derived by computing λ from (3.16) with $\dot{q}_d = 0$. Clearly, the approximation $T_d = T_B$ used in (3.19) is inaccurate when the gas temperature in the environment surrounding the droplet is close to the boiling temperature, i.e., $(T - T_B)/T_B \sim [L_v/(R_{\mathrm{F}}T_B)]^{-1} \ll 1$.

Equations (3.14) and (3.16)–(3.18) provide a simplified description of the exchange sources for the computational modeling of evaporating sprays. More involved expressions are needed for slip flow with Re_d larger than unity or when increased accuracy is sought by incorporating physical phenomena that are not considered in the above derivation [1] (see also [21, 22] for summaries and assessments of different models). For instance, unsteady effects resulting from droplet acceleration can be accounted for, leading to corrections to the drag force and vaporization rate that have been computed by asymptotic methods [23].

As previously mentioned, effects of near-droplet convection associated with the slip velocity $\mathbf{v} - \mathbf{v}_d$ introduce corrections to the exchange rates that, surprisingly, remain moderately small as the Reynolds number increases, so that (3.14) and (3.16)–(3.18) provide sufficient accuracy for $\mathrm{Re}_d \sim 1$. For instance, although the expression given in (3.14) tends to underpredict the drag force on the droplet as the Reynolds number increases, the underpredictions are not severe, i.e., the relative errors are of the order of 12% for $\mathrm{Re}_d = 1$, increasing to 40% for $\mathrm{Re}_d = 5$ [24].

As a final comment, it should be mentioned that the flow around the droplet is modified for droplets burning individually in an oxidizing atmosphere with a surrounding flame. For droplets moving relative to the ambient gas with a

Reynolds number Re_d of order unity, the envelope diffusion flame around the droplet extinguishes when the droplet radius decreases below a critical value of the order of the thickness δ_L of the stoichiometric gaseous planar deflagration. For lower values of the droplet radius, the fuel vapor generated by the droplet will only burn in its wake, in a distributed manner. Conversely, a droplet may burn individually with a surrounding flame when its radius is larger than the critical extinction value, that being the case observed in the spray-deflagration experiments reported in [25], which consider large droplets with diameters exceeding 300 microns. When the droplet is surrounded by a flame, the expressions derived above for $\mathrm{Re}_d \ll 1$ should be modified. For instance, in the Spalding vaporization rate (3.19) the enthalpy difference $c_p(T - T_B)$ must incorporate an augmented effective ambient temperature that accounts for the presence of the flame. In the limit of infinitely fast reaction with the reasonable approximation of unity Lewis number adopted for O_2, the associated enthalpy increase can be shown to be equal to the ambient oxygen mass fraction Y_{O_2} times the amount of heat released per unit mass of oxygen consumed in the chemical reaction [12, 26]. The surrounding flame has been shown to affect also the force acting on the droplet [19]. Modifications would also be needed in the gas-phase equations, with the burning droplets appearing there as sources of heat and combustion products and as sinks for oxygen [20].

3.4 Simplified chemical kinetics description

The oxidation of typical gaseous hydrocarbons involves hundreds of elementary chemical reactions among dozens of short-lived intermediate chemical species. Detailed kinetic schemes containing the needed elementary reactions, resulting from direct molecular collisions, and their associated rate constants are now well established for a few simple fuels, including hydrogen [27] (of interest in rocket-propulsion applications), alcohols [28], and some hydrocarbons [29, 30]. For many purposes, however, a simpler chemistry description suffices to investigate many aspects of combustion flows. For the discussion that follows, focused on the fluid mechanic aspects of nonpremixed spray combustion, we adopt the overall reaction

$$\mathrm{F} + s\mathrm{O}_2 \rightarrow (1+s)\mathrm{P} + q', \tag{3.20}$$

as a representation of the underlying stoichiometry for the oxidation of a given saturated fuel. According to the one-step reaction, the unit mass of fuel reacts with a mass s of oxygen to give a mass $(1+s)$ of products, releasing in the process an amount of energy given by q'. The resulting values of these

parameters differ only by a small amount for hydrocarbons that share the same molecular structure, a characteristic that explains why their combustion properties are also very similar [e.g., $s = (3.52, 3.48)$ and $q' = (48.10, 44.56)$ kJ/g for heptane and dodecane, respectively. Alternatively, $s = (1.5, 2.08)$ and $q' = (22.6, 29.69)$ kJ/g for methanol and ethanol]. It is of interest that, the associated values of $q'/s \simeq 15$ kJ/g are found for the alcohols and $q'/s \simeq 13$ kJ/g in hydrocarbon combustion.

In nonpremixed spray flames the burning rate is diffusion controlled when the overall reaction given is sufficiently fast so that its chemical kinetic rate becomes inconsequential. This rate is, however, important in extinction and ignition processes, for which the strong temperature dependence of the reaction rate plays a central role. This strong temperature sensitivity can be described with use made of the simple irreversible Arrhenius rate expression

$$\omega_{\rm F} = B\rho Y_{\rm F} Y_{\rm O_2} \exp(-E_a/R^o T), \tag{3.21}$$

for the mass of fuel consumed per unit volume per unit time, which is a function of the temperature T and of the fuel and oxygen mass fractions $Y_{\rm F}$ and $Y_{\rm O_2}$. The rate parameters include the pre-exponential factor B and the activation energy E_a , which can be selected to reproduce the main combustion characteristics of a given fuel.

The simplified chemistry description defined in (3.20) and (3.21) will be employed below as a basis to analyze finite-rate effects in chemically reacting spray flows. Correspondingly, the conservation equations for reactant and species will be written in the simplified form

$$\frac{\partial}{\partial t}\left(\rho Y_{\rm F}\right) + \nabla\cdot\left(\rho \mathbf{v} Y_{\rm F}\right) - \nabla\cdot\left(\rho D_{\rm F}\nabla Y_{\rm F}\right) = -\omega_{\rm F} + \sum_{j=1}^{N_c} n^j \dot{m}^j, \tag{3.22}$$

$$\frac{\partial}{\partial t}\left(\rho \hat{Y}_{\rm O}\right) + \nabla\cdot\left(\rho \mathbf{v} \hat{Y}_{\rm O}\right) - \nabla\cdot\left(\rho D_{\rm O}\nabla \hat{Y}_{\rm O}\right) = -S\omega_{\rm F}, \tag{3.23}$$

$$\frac{\partial}{\partial t}\left(\rho c_p T\right) + \nabla\cdot\left(\rho \mathbf{v} c_p T\right) - \nabla\cdot\left(\kappa\nabla T\right) = q'\omega_{\rm F} - \sum_{j=1}^{N_c} n^j \left[\dot{m}^j\left(L_v - c_p T_d^j\right) + \dot{q}_d^j\right], \tag{3.24}$$

with a Fickian description adopted in (3.22) and (3.23) for the diffusion velocities, including the fuel and oxygen diffusivities $D_{\rm F}$ and $D_{\rm O}$. Here, $\hat{Y}_{\rm O} = Y_{\rm O_2}/Y_{\rm O_{2A}}$ is the oxidizer mass fraction normalized with its value in the air stream and $S = s/Y_{\rm O_{2A}}$ is the amount of air consumed per unit of fuel mass.

3.5 Characteristic times and controlling parameters

Using the expressions given above to evaluate $\dot{m}$, $\mathbf{f}$, and $\dot{q}_d$ in the droplet-balance equations (3.2)–(3.4) provides estimates for the characteristic times of droplet vaporization, droplet acceleration, and droplet heating. For instance, using (3.13) to evaluate $\dot{m}$ in (3.3) yields

$$-\frac{1}{a^3}\frac{\mathrm{d}a^3}{\mathrm{d}t} = 3\frac{D_T}{a^2}\frac{\rho}{\rho_l}\lambda = \frac{\lambda}{t_v}, \tag{3.25}$$

which defines a vaporization time

$$t_v = \tfrac{1}{3}(a^2/D_T)(\rho_l/\rho), \tag{3.26}$$

where $D_T = \kappa/(\rho c_p)$ denotes the gas thermal diffusivity. On the other hand, using Stokes law (3.14) for the drag force in (3.2) provides

$$\frac{\mathrm{d}\mathbf{v}_d}{\mathrm{d}t} = \frac{9}{2}\frac{\nu}{a^2}\frac{\rho}{\rho_l}(\mathbf{v}-\mathbf{v}_d) = \frac{\mathbf{v}-\mathbf{v}_d}{t_a}, \tag{3.27}$$

where

$$t_a = \tfrac{2}{9}(a^2/\nu)(\rho_l/\rho) \tag{3.28}$$

is the droplet acceleration (or accommodation) time, the so-called Stokes time, which can be alternatively expressed in the form $t_a = 2t_v/(3Pr)$ in terms of the Prandtl number $\mathrm{Pr} = \nu/D_T$. It is worth noting that, since $\mathrm{Pr} \simeq 0.7$ for air, the times t_v and t_a are practically identical. Similarly, the characteristic droplet heating time $t_q = (c_l/c_p)t_v$ involved in $\mathrm{d}T_d/\mathrm{d}t = (T-T_d)/t_q$, obtained by using the simplified rate $\dot{q}_d = 4\pi\kappa a(T-T_d)$ in (3.4), also is of order of the droplet vaporization time t_v, because the specific-heat ratio c_l/c_p is always of order unity.

The ratio of the droplet accommodation time t_a to the characteristic flow time ℓ/U_c defines the Stokes number

$$\mathrm{St} = t_a/(\ell/U_c), \tag{3.29}$$

which measures the coupling of the droplets with the gas phase, as can be

readily seen by rewriting (3.2)–(3.4) in the alternative form

$$-\frac{1}{a^3}\frac{\mathrm{d}a^3}{\mathrm{d}\tau} = \frac{2}{3\mathrm{Pr}}\frac{\lambda}{\mathrm{St}}, \tag{3.30}$$

$$\frac{\mathrm{d}\mathbf{v}_d}{\mathrm{d}\tau} = \frac{\mathbf{v}-\mathbf{v}_d}{\mathrm{St}}, \tag{3.31}$$

$$\frac{\mathrm{d}T_d}{\mathrm{d}\tau} = \frac{2c_p/c_l}{3\mathrm{Pr}}\frac{T-T_d}{\mathrm{St}}, \tag{3.32}$$

involving the dimensionless time $\tau = t/(\ell/U_c)$. Large values of the Stokes number correspond to ballistic droplets that are not influenced significantly by the surrounding gas flow. Their velocities, radii, and temperature are not modified in the available residence time ℓ/U_c, as follows from (3.30)–(3.32) in the limit $\mathrm{St} \gg 1$. Since these ballistic droplets cross the flow field without vaporizing, droplets with large Stokes numbers cannot be predominant in combustion applications, which require the complete vaporization of the liquid fuel in the available residence time. By way of contrast, droplets with small Stokes numbers have response times much smaller than the characteristic flow time, so that they readily adjust their velocity and temperature to that of the surrounding gas flow, as can be seen from (3.31) and (3.32), vaporizing rapidly before they penetrate a significant distance into the combustion chamber, as dictated by (3.30). In most liquid-fuel combustion devices droplet inertia plays a central role in ensuring droplet dispersion prior to droplet vaporization, which in turn guarantees effective fuel-air mixing, needed for reducing combustion times. Small droplets with $\mathrm{St} \ll 1$ are not desirable for this purpose in combustion applications, since they disappear as soon as they come into contact with the hot gas. These considerations indicate that in selecting the injector for a given combustion system (e.g, a gas-turbine combustor) one should target droplets with a size such that the resulting Stokes numbers are

$$\mathrm{St} \sim O(1), \tag{3.33}$$

under which conditions adequate droplet dispersion and complete vaporization can be simultaneously achieved.

While the above equations (3.30)–(3.32) clearly indicate that the Stokes number St governs the coupling of the droplets with the gas flow, with the distinguished regime $\mathrm{St} \sim O(1)$ identified as being especially relevant in combustion applications, a different nondimensional parameter is seen to control the gas-phase coupling with the droplets. This can be shown by estimating the influence of the exchanges of mass, momentum, and energy on the gas flow

through order-of-magnitude comparisons in the gas-phase conservation equations. For instance, according to (3.8), the interphase exchange of momentum results in an acceleration of the flow according to $\nabla \cdot (\rho \mathbf{v}\mathbf{v}) \sim -\sum_{j=1}^{N_c} n^j \mathbf{f}^j$, which can be used to give

$$|\Delta \mathbf{v}| \sim \left(\frac{\alpha}{\mathrm{St}}\right) |\mathbf{v} - \mathbf{v}_d|. \tag{3.34}$$

for the characteristic increment of gas velocity resulting from the presence of the droplets. As can be seen, rather than the Stokes number alone, the relevant parameter here is the ratio of the liquid mass-loading ratio to the Stokes number α/St. The resulting expression indicates that for $\alpha/\mathrm{St} \ll 1$ the gas phase is independent of the liquid phase, in that the variations in gas velocity owing to the presence of the droplets are negligibly small, and that in the opposite limit $\alpha/\mathrm{St} \gg 1$, corresponding to the dense-spray conditions found near the injectors, the velocity of the interstitial gas rapidly adjust to that of the droplets, whose inertia dominates the fluid motion (i.e., $\mathbf{v} = \mathbf{v}_d$).

Similarly, a straightforward order-of-magnitude balance between the convective transport term $\nabla \cdot (\rho \mathbf{v} Y_{\mathrm{F}})$ and the droplet-vaporization term $\sum_{j=1}^{N_c} n^j \dot{m}^j$ in the fuel-vapor conservation equation (3.22) indicates that the characteristic fuel-vapor mass fraction in the combustor arising from droplet vaporization is

$$Y_{\mathrm{F}} \sim \frac{2}{3\mathrm{Pr}} \frac{\alpha}{\mathrm{St}} \lambda, \tag{3.35}$$

whereas the corresponding estimate $\nabla \cdot (\rho \mathbf{v} c_p T) \sim -\sum_{j=1}^{N_c} n^j \dot{q}_d^j$ in (3.24) leads to

$$|\Delta T| \sim -\frac{2}{3\mathrm{Pr}} \frac{\alpha}{\mathrm{St}} (T - T_d) \tag{3.36}$$

for the gas-temperature variation due to heat transfer to the droplets. Clearly, for $\alpha/\mathrm{St} \ll 1$ we find negligible effects of droplet vaporization on the gas flow, in that the gas composition and the gas temperature do not change significantly in this limit. In the opposite limit $\alpha/\mathrm{St} \gg 1$, the vaporization rate λ remains negligibly small, because the gas rapidly adjusts its temperature to that of the droplets (i.e., $T = T_d$), as indicated by (3.36). Effective coupling of the gas flow with the droplets occurs therefore in the distinguished limit

$$\alpha/\mathrm{St} \sim O(1), \tag{3.37}$$

which can be anticipated to be the prevailing condition in applications.

The above considerations, pertaining to vaporizing sprays, indicate that effective two-way coupling is found in regions where $\mathrm{St} \sim 1$ and $\alpha \sim 1$, so

that both conditions (3.33) and (3.37) are simultaneously satisfied. In spray combustion applications the coupling is more pronounced in the presence of reaction, because the heat released by burning the fuel vapor is enough lo lead to flame temperatures several times larger than the spray feed temperatures. In analyzing the interphase coupling in burning sprays one should bear in mind that in the combustion of typical hydrocarbon fuels the air-to-fuel stoichiometric ratio S that appears as a factor in (3.23) (i.e., the mass of air needed to burn the unit mass of fuel) is a large quantity of order $S \sim 15$. As a result, very dilute sprays with small values of $\alpha \sim S^{-1} \ll 1$, often found in the main combustion region of near-stoichiometric combustion systems, generate diffusion-flame temperatures of the order of the stoichiometric adiabatic flame temperature, thereby producing a strong effect on the gas flow through the associated gas expansion. For these dilute conditions, the direct effects of droplet vaporization, heating, and acceleration on the gas motion are negligible, as can be inferred from observation of the droplet source terms in (3.8), (3.22), and (3.24), although significant interphase coupling still exists associated with the strong exothermicity of the chemical reaction. The limit $\alpha \sim S^{-1} \ll 1$ will be specifically considered below when analyzing structures of counterflow spray diffusion flames.

The above discussion illustrates the importance of group effects, with the mean gas-phase environment generated collectively by the droplets determining the overall vaporization and combustion dynamics of the spray. Elementary problems involving a limited number of competing phenomena serve to illustrate the interplay of the different physicochemical processes, including the coflow and counterflow mixing layers used in this dissertation. The early investigations were based on even simpler models. In particular, regimes of group vaporization and combustion of sprays were defined by considering quasisteady solutions to uniform, spherically symmetric, quiescent fuel-droplet clouds [31–37]. Under appropriate simplifying assumptions, a single dimensionless parameter, called the group combustion number [31], was reasoned to control the energy and mass transfer between the droplet cloud and the surrounding atmosphere. Since this number is widely used in applications, it is of interest to discuss its connection with the spray parameters α and St identified above by addressing the problem of transient vaporization of a monodisperse droplet cloud in a hot air environment at constant pressure. For completeness, this is done in Appendix A.

References

[1] W. A. Sirignano, Fluid dynamics and transport of droplets and sprays, 2nd edition, Cambridge University Press, Cambridge, UK., 2010.

[2] H. S. Carslaw, J. C. Jaeger, et al., Conduction of heat in solids, Vol. 2, Clarendon Press Oxford, 1959.

[3] C. K. Law, W. A. Sirignano, Unsteady droplet combustion with droplet heating - ii: Conduction limit, Combustion and Flame 28 (1977) 175–186.

[4] B. Abramzon, W. A. Sirignano, Droplet vaporization model for spray combustion calculations, International journal of heat and mass transfer 32 (9) (1989) 1605–1618.

[5] C. T. Crowe, M. P. Sharma, D. E. Stock, The particle-source-in cell (psi-cell) model for gas-droplet flows, Journal of Fluids Engineering 99 (2) (1977) 325–332.

[6] A. Bermúdez, J. L. Ferrín, A. Liñán, The modelling of the generation of volatiles, H_2 and CO, and their simultaneous diffusion controlled oxidation, in pulverized coal furnaces, Combus. Theor. Modell. 11 (2007) 949–976.

[7] A. Bermúdez, J. Ferrín, A. Liñán, L. Saavedra, Numerical simulation of group combustion of pulverized coal, Comb. Flame 158 (2011) 1852–1865.

[8] X. Y. Zhao, D. C. Haworth, Transported pdf modeling of pulverized coal jet flames, Combustion and Flame 161 (7) (2014) 1866–1882.

[9] P. Moin, S. Apte, Large-eddy simulation of realistic gas turbine combustors, AIAA Journal 44 (2006) 698–708.

[10] N. Patel, M. Kırtaş, V. Sankaran, S. Menon, Simulation of spray combustion in a lean-direct injection combustor, Proceedings of the Combustion Institute 31 (2) (2007) 2327–2334.

[11] G. Hannebique, P. Sierra, E. Riber, B. Cuenot, Large eddy simulation of reactive two-phase flow in an aeronautical multipoint burner, Flow, turbulence and combustion 90 (2) (2013) 449–469.

[12] F. A. Williams, Combustion Theory, Second ed., Benjaming Cummings, Menlo Park, CA., 1985.

[13] D. Kah, F. Laurent, L. Fréret, S. De Chaisemartin, R. O. Fox, J. Reveillon, M. Massot, Eulerian quadrature-based moment models for dilute polydisperse evaporating sprays, Flow, Turbulence and Combustion 85 (3-4) (2010) 649–676.

[14] C. Yuan, R. O. Fox, Conditional quadrature method of moments for kinetic equations, Journal of Computational Physics 230 (22) (2011) 8216–8246.

[15] R. O. Fox, Large-eddy-simulation tools for multiphase flows, Annual Review of Fluid Mechanics 44 (2012) 47–76.

[16] F. A. Williams, On the assumptions underlying droplet vaporization and combustion theories, The Journal of Chemical Physics 33 (1) (1960) 133–144.

[17] S. S. Sadhal, P. S. Ayyaswamy, Flow past a liquid drop with a large nonuniform radial velocity, Journal of Fluid Mechanics 133 (1983) 65–81.

[18] D. R. Kassoy, F. A. Williams, Variable property effects on liquid droplet combustion., AIAA Journal 6 (10) (1968) 1961–1965.

[19] M. Hermanns, High order numerical methods applied to the analysis of transport phenomena in combustion, PhD Dissertation, UPM, Madrid, 2006.

[20] J. Urzay, H. Pitsch, A. Liñán, Source terms for calculations of vaporizing and burning fuel sprays with non-unity lewis numbers in gases with temperature-dependent thermal conductivities, Annual Research Briefs, Center for Turbulence Research, Stanford University.

[21] R. Miller, K. Harstad, J. Bellan, Evaluation of equilibrium and non-equilibrium evaporation models for many-droplet gas-liquid flow simulations, International Journal of Multiphase Flow 24 (6) (1998) 1025–1055.

[22] E. K. Shashank, H. Pitsch, Spray evaporation model sensitivities, Annual Research Briefs, Center for Turbulence Research, Stanford University.

[23] G. Del Alamo, F. A. Williams, Theory of vaporization of a rigid spherical droplet in slowly varying rectilinear flow at low reynolds numbers, Journal of Fluid Mechanics 580 (2007) 219–249.

[24] S. Dennis, J. Walker, Calculation of the steady flow past a sphere at low and moderate reynolds numbers, Journal of Fluid Mechanics 48 (04) (1971) 771–789.

[25] M. Queiroz, S. C. Yao, A parametric exploration of the dynamic behavior of flame propagation in planar sprays, Combustion and flame 76 (3) (1989) 351–368.

[26] A. Liñán, Theory of droplet vaporization and combustion, in: R. Borghi, P. Clavin, A. Liñán, P. Pelcé, G. I. e. Sivashinsky (Eds.), Modélisation des phénoménes de combustion, Editions Eyrolles, 1985, pp. 73–103.

[27] A. L. Sánchez, F. A. Williams, Recent advances in understanding of flammability characteristics of hydrogen, Progress in Energy and Combustion Science 41 (2014) 1–55.

[28] S. M. Sarathy, P. Oßwald, N. Hansen, K. Kohse-Höinghaus, Alcohol combustion chemistry, Progress in Energy and Combustion Science 44 (2014) 40–102.

[29] S. Palle, C. Nolan, R. S. Miller, On molecular transport effects in real gas laminar diffusion flames at large pressure, Physics of Fluids (1994-present) 17 (10) (2005) 103601.

[30] J. M. Simmie, Detailed chemical kinetic models for the combustion of hydrocarbon fuels, Progress in energy and combustion science 29 (6) (2003) 599–634.

[31] T. Suzuki, H. H. Chiu, Multi-droplet combustion of liquid propellants, Proceedings of 9th International on Space Technology Science (1971) 145–153.

[32] H. H. Chiu, T. Liu, Group combustion of liquid droplets, Combust. Sci. Tech. 17 (1977) 127–142.

[33] M. Labowsky, D. E. Rosner, Group combustion of droplets in fuel clouds, i. quasi-steady predictions, in: J. T. Zung (Ed.), Evaporation-Combustion of Fuels, Americal Chemical Society, 1978, pp. 63–79.

[34] H. H. Chiu, H. Kim, E. J. Croke, Internal group combustion of liquid droplets, Proc. Combust. Inst. 19 (1982) 971–980.

[35] S. M. Correa, M. Sichel, The group combustion of a spherical cloud of monodisperse fuel droplets, Proc. Combust. Inst. 19 (1982) 981–991.

[36] S. M. Correa, M. Sichel, The boundary layer structure of a vaporizing fuel cloud, Combust. Sci. Tech. 28 (1982) 121–130.

[37] M. Yang, M. Sichel, Spherical droplet clouds, AIAA paper (1990) 90–3060.

CHAPTER
FOUR

Dynamics of thermal ignition of spray flames in mixing layers

4.1 Introduction

Spray flames are ubiquitous in piston engines and in the combustors of jet engines, liquid-propellant rockets, and helicopters [1, 2]. Of particular relevance for ensuring stable combustion in technological applications is the ignition dynamics of high-speed fuel sprays. Contrary to the advanced knowledge available on ignition in non-premixed gaseous flames, the ignition of fuel sprays is still not thoroughly understood, as revealed by recent studies and reviews [3–6], which point out a number of key aspects of the problem in need of additional investigation.

In typical liquid-fueled burners the fuel is injected as a high-velocity liquid jet that breaks up to form the spray. The initial heating and vaporization of the liquid fuel rely on the relatively large temperatures of the surrounding gas, which may include hot combustion products and preheated air. The heat exchange between the liquid and the gas phases is enhanced by droplet dispersion arising from the predominant turbulent motion. Chemical reaction takes place once molecular mixing between the fuel vapor and the oxidizer has occurred in mixing layers separating the spray flow from the hot air stream. Since in most applications the injection velocities are much larger than the premixed-flame propagation velocity, combustion stabilization relies on autoignition of the fuel-oxygen mixture, with the combustion stand-off distance being controlled by the interaction of turbulent transport, droplet heating and vaporization, and gas-phase chemical reactions.

Studies of laminar mixing-layer configurations have been found to be instrumental in developing understanding of turbulent combustion [7], including the ignition of turbulent gaseous diffusion flames [6]. For the spray problem at hand, the configuration selected, shown in Fig. 4.1, involves a coflow mixing layer formed between a stream of hot air moving at velocity U_A and a monodisperse spray moving at velocity $U_S \sim U_A$. The boundary-layer approximation

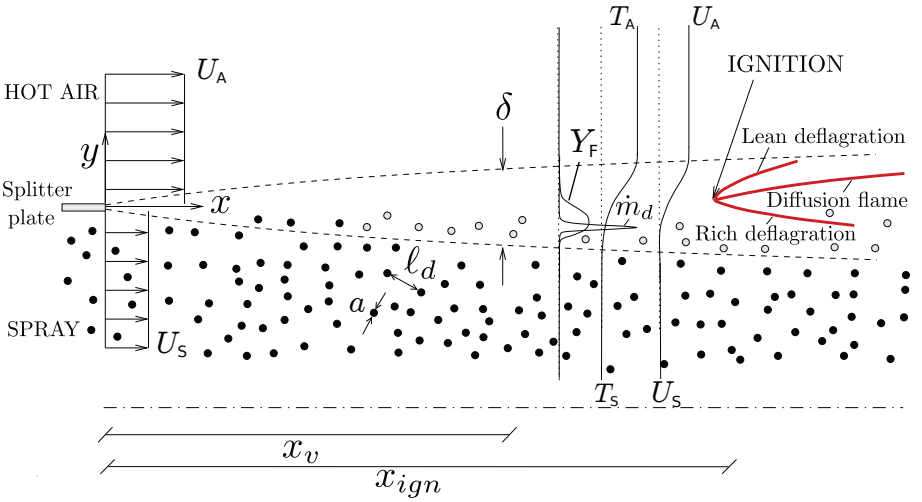

Figure 4.1. Sketch of the model problem: The thermal ignition of a fuel spray in a two-dimensional laminar mixing layer. Here, the black dots indicate fuel droplets, with grey-color droplets corresponding to vaporizing droplets. The dashed lines represent the edges mixing-layer.

will be used below to describe the resulting slender flow, which exhibits different igniting behaviors depending on the characteristics of the fuel. In this approximation, consideration of the case $U_A = U_S$ enables laminar ignition distances to be related to ignition times of unstrained spray flamelets, thereby providing quantitative information of direct applicability in regions of low scalar dissipation-rate in turbulent reactive flows (see, e.g., the discussion in pp. 181–186 of [7]).

4.2 Droplet dispersion and ignition in turbulent mixing layers

Before proceeding with the analysis, it is of interest to discuss in greater detail the relevance of the laminar problem investigated below in the context of spray ignition in turbulent mixing layers. The discussion requires consideration of the transport of droplets in the presence of turbulent motion. The dynamics of the large vortices in the mixing layer is characterized by the integral time scale

$$t_\ell = \ell/U, \tag{4.1}$$

with ℓ being the integral length (i.e., the characteristic thickness of the turbulent mixing layer) and U being related to the mean streamwise velocity. This time is to be compared with the characteristic acceleration time of the droplets. When

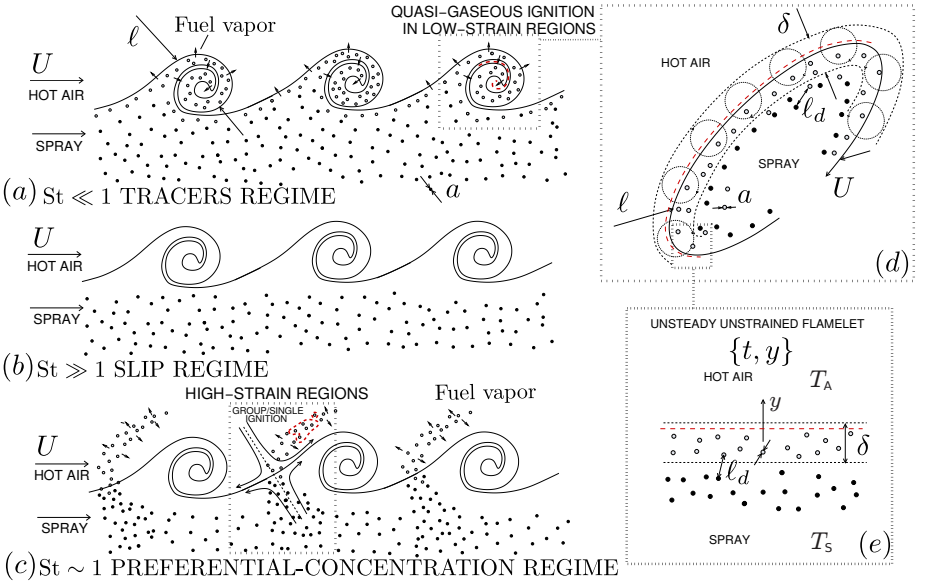

Figure 4.2. Spray-laden turbulent mixing layers at (a) small Stokes numbers (tracers regime), (b) large Stokes numbers (slip regime) and (c) order-unity Stokes numbers (preferential-concentration regime). Figure (d) shows a sketch of the large turbulent eddies entraining the fuel spray, and (e) depicts the unsteady unstrained flamelet model of spray ignition at low Stokes numbers. Igniting regions are sketched with thick-dashed lines (red color).

the motion around the droplet is dominated by molecular transport, as occurs when the droplets are sufficiently small, this acceleration time (or Stokes time) is of the order of the droplet vaporization time, defined in (3.26), which can be therefore used to define an integral-scale Stokes number

$$\mathrm{St} = t_v/t_\ell, \tag{4.2}$$

the parameter controlling the overall dispersion characteristics in particle-laden turbulent mixing layers [8]. Different values of St are associated with different regimes of droplet dispersion, as depicted in Fig. 4.2(a-c).

For $\mathrm{St} \gg 1$ the droplets on the spray side of the mixing layer are insensitive to the velocity perturbations induced by the large vortical motion and therefore continue in straight trajectories, as sketched in Fig. 4.2(b). In this slip regime, the droplets remain surrounded by the cold carrier gas, thereby hindering droplet vaporization.

An increasing interaction of the droplets with the turbulent eddies occurs as the Stokes number decreases, with droplet dispersion becoming optimal for

$\mathrm{St} = O(1)$, when the compression strain effect acting in times of order t_ℓ enables the droplets to be ejected from the spray side through the high-strain vortex-braid regions, resulting in non-uniform droplet distributions. Experimental evidence for these preferential-concentration effects has been reported in earlier work (see for instance [8]). In this scenario, the droplets cross the mixing layer to vaporize on the other side surrounded by hot air. Individual-droplet ignition is seldom observed for droplets in the sub-millimeter diameter range, because at the air temperatures typically found in applications the characteristic chemical time for ignition is much larger than the diffusion time around the droplet. Instead, the fuel vapor generated by droplet vaporization mixes with the surrounding air to form reactive pockets that are convected downstream. If the fuel concentration in these pockets is sufficiently high for the resulting mixture to be flammable, ignition occurs downstream, at a location such that the residence time becomes comparable to the chemical time for homogeneous ignition.

The description of ignition for $\mathrm{St} = O(1)$ is not readily amenable to a simple Eulerian modeling of the type used here because of the existence of crossing droplet trajectories as the droplets traverse the mixing layer through the vortex braids. These crossing trajectories have been observed, for instance, in counterflow configurations [4]. Additional studies of ignition of counterflow sprays, including large inertial droplets crossing the stagnation plane, would be clearly beneficial in clarifying spray-ignition characteristics in turbulent mixing layers for $\mathrm{St} = O(1)$. The present work, however, is not relevant for $\mathrm{St} = O(1)$ or larger, under which conditions individual-droplet combustion or droplet-cloud combustion may occur, the latter been favored by large mass-loading ratios [9–11].

For $\mathrm{St} \ll 1$, the droplets behave as flow tracers and become entrained in the large-scale turbulent eddies, where they come into contact with the high-temperature air, thereby promoting vaporization and ignition of the fuel spray in the resulting mixing layers. This regime is depicted in Fig. 4.2(a). The strain in the vortex-braid regions promotes the transport of the fuel vapor towards the interior of the rollers, where ignition occurs more readily as a result of the existing lower strain [6, 12], while the larger strain rates found in the vortex-braid regions prevent ignition from occurring there by limiting fuel residence times. As suggested earlier for purely gaseous ignition [7], the unstrained flamelet, achieved in Fig. 4.1 by setting U_S equal to U_A, may provide an adequate representation of the ignition dynamics in the low-strain mixing regions wrapped around the core of such large vortices. As a consequence, associated ignition times, as those computed below, are relevant for quantifying

ignition distances in these turbulent mixing layers.

The above discussion revolves around the effect of the large eddies associated with the integral scales of the turbulent mixing layer, which dominate the dispersion of the droplets. These large eddies coexist and interact with smaller eddies, with the smallest size corresponding to the Kolmogorov length scale ℓ_k, which can be anticipated to be comparable with the laminar mixing-layer thickness δ in the model of Fig. 4.1, both lengths being influenced by molecular-transport effects. Although these smaller turbulent eddies may also affect mixing and reaction, their effect on ignition is less prominent than that of the large vortices, in that the cores of the large rollers correspond to regions of low strain, where ignition should occur sooner and where the unstrained laminar flamelet provides a good representation for the local flow.

4.3 Characteristic scales

As previously discussed in Chapter 2, in combustion applications involving liquid-fuel injection, appreciable liquid heating and vaporization resulting from heat transfer from the gas carrier occurs only downstream from the atomization region, once the droplet distribution becomes sufficiently dilute for the mass-loading ratio to decay to values of order unity. When this condition $\alpha \sim O(1)$ is used in (2.2) the relationship

$$l_d \sim (\rho_l/\rho_A)^{1/3} a_o \gg a_o \tag{4.3}$$

is obtained for the order of magnitude of the initial inter-droplet distance $l_d = n_o^{-1/3}$, with the typical ratio of liquid-to-gas densities found in (2.1) for the conditions encountered in propulsion applications.

The scales l_d and $a_o \ll l_d$ are to be compared with those of the spray-air mixing layer, associated with the acceleration, heating and vaporization of the droplets, all three processes having comparable time scales, of the order of the droplet vaporization time defined from (3.26). Since the chemical reaction cannot begin until after the gaseous fuel is generated, the vaporization time t_v naturally defines the scales of the igniting mixing layer, in that ignition occurs at distances downstream from the splitter plate that are of the order of or larger than $x_v = U_A t_v$. At these streamwise distances, the characteristic thickness of the mixing layer is

$$\delta \sim (D_{T_A} t_v)^{1/2} \sim (\rho_l/\rho_A)^{1/2}\, a_o, \tag{4.4}$$

which is smaller than x_v by a factor equal to the square root of the characteristic Péclet number

$$\mathrm{Pe} = (x_v/\delta)^2 = U_A^2 t_v / D_{T,A}. \tag{4.5}$$

For the large values of Pe typically found in applications, the resulting flow is slender and correspondingly can be described in the boundary-layer approximation.

As follows from (4.3) and (4.4) with $\rho_l/\rho_A \gg 1$, the inequalities

$$\delta \gg l_d \gg a_o \tag{4.6}$$

can be expected to hold for mixing-layer ignition of spray flows, where the mixing-layer thickness δ is the characteristic flow length in (2.7). As explained in Chapter 2, this disparity enables a two-continua description of the spray ignition problem to be adopted, in which the different gas-phase variables are described at any spatial point by space-averaging over a neighborhood of that point of size d, with d in the range $\delta \gg d \gg l_d$. Irrespective of the inaccuracy of the most stringent condition $(\rho_A/\rho_l)^{1/6} \gg 1$ needed to justify $\delta \gg l_d$, the inequality $d \gg l_d$ facilitates understanding by assuring that each averaging cell includes many droplets, so that the corresponding point sources can be homogenized, as if they were homogeneously distributed. This gives source terms that are proportional to the number of droplets per unit volume, which is the natural variable to describe in the continuum limit the droplet population of monodisperse sprays. Recent applications of this type of two-continua descriptions include analyses of spray-jet vaporization [13] and derivations of coupling-function formulations for spray-flame computation [14].

For simplicity, the chemistry describing the ignition process will be modeled with an irreversible reaction between the oxygen of the air and the fuel vapor to produce combustion products according to $\mathrm{F} + s\mathrm{O}_2 \rightarrow (1+s)\mathrm{P} + q'$, involving the mass of oxygen consumed s and the amount of heat released q' per unit mass of fuel burnt. The reaction rate (mass of fuel consumed per unit volume per unit time) is assumed to be given by the Arrhenius law $\omega_{\mathrm{F}} = B\rho Y_{\mathrm{F}} Y_{\mathrm{O}_2} \exp(-E_a/R^oT)$, given above in (3.21), including the frequency factor B and the activation energy E_a as the only rate parameters, with the ratio E_a/R^o of the activation energy to the universal gas constant R^o representing an activation temperature. In the formulation, Y_{F} and $\hat{Y}_{\mathrm{O}} = Y_{\mathrm{O}_2}/Y_{\mathrm{O}_{2A}}$ represent the fuel-vapor and oxygen mass fractions, respectively, the latter normalized with its air-side value $Y_{\mathrm{O}_{2A}}$. The rate (3.21) defines a characteristic temperature-dependent chemical time for fuel oxidation $B^{-1}\exp(E_a/R^oT)$ that

can be evaluated with the air-side temperature to give the value

$$t_c = B^{-1} \exp[E_a/(R^o T_A)]. \tag{4.7}$$

The ratio of this chemical time to the vaporization time defined in (3.26) gives the Damköhler number

$$\Delta = t_v/t_c, \tag{4.8}$$

which enters as a prominent parameter in the problem. Autoignition data often are fitted to (3.21) to provide values of B and E_a for different fuels, but since the intention of the present work is to explore influences of spray properties rather than variations of gas-phase chemical-kinetic properties, only representative orders of magnitude of the nondimensional gas-phase chemical-kinetic properties will be employed.

Characteristic values of Δ corresponding to realistic fuels can be evaluated by using the homogeneous ignition delay time for stoichiometric fuel-air mixtures as an estimate for t_c. For instance, for heptane at elevated pressure, the shock-wave experiments reported by [15] give values of ignition delay times on the order of 2×10^{-3} s at a temperature of 1000 K. This value can be used for t_c in evaluating (4.8) with the vaporization time t_v obtained from (3.26) with the density of liquid heptane and with the values of the air properties at $T_A = 1000$ K. The resulting Damköhler number, which depends strongly on the droplet size through the square of the droplet radius a_o^2, can be seen to become unity for $a_o \simeq 23$ μm, a value on the order of those found in applications, indicating that the distinguished limit $\Delta \sim O(1)$ must be considered in addressing spray ignition. Clearly, extreme values of Δ can also be of interest, as they may appear in configurations with either higher air-side temperatures or larger droplets ($\Delta \gg 1$) or in configurations with smaller temperatures or smaller droplet radii ($\Delta \ll 1$).

4.4 Formulation

The vaporization time given in (3.26) will be used to define length scales for the longitudinal and transverse coordinates, x and y, giving the dimensionless variables $x' = x/(U_A t_v)$ and $y' = y/(D_{T_A} t_v)^{1/2}$. Correspondingly, the velocity of the gas and that of the droplets will be scaled to give $u' = u/U_A$ and $u'_d = u_d/U_A$ for the longitudinal components and $v' = v/(D_{T_A}/t_v)^{1/2}$ and $v'_d = v_d/(D_{T_A}/t_v)^{1/2}$ for the transverse components.

The characteristic properties of the air stream will be used to scale the

gas and droplet temperatures, $T' = T/T_A$ and $T'_d = T_d/T_A$, as well as the gas density, viscosity and thermal conductivity, $\rho' = \rho/\rho_A$, $\mu' = \mu/\mu_A$, and $\kappa' = \kappa/\kappa_A$, respectively. Variations of the specific heat of the gas mixture will be neglected. A Fickian description will be adopted for the diffusion velocities of all species, with the binary diffusivity of species i into the mixture D'_i scaled with its air-side value to give $D'_i = D_i/D_{iA}$. The primes used above to denote non-dimensional variables are dropped in what follows.

A presumed power-law dependence is introduced for the transport properties,

$$\rho D_i = \mu = \kappa = T^\sigma, \tag{4.9}$$

with $\sigma = 0.7$. It is assumed that the molecular mass of the inert gas in the spray stream is close to that of air, so that prior-to-ignition changes in mean molecular weight of the gas mixture are only associated with the presence of fuel vapor. As a result, the equation of state (3.11) can be written in terms of the mass fraction of fuel $Y_{\rm F}$ in the form

$$\rho T \left[1 - Y_{\rm F}\left(1 - \frac{M_A}{M_F}\right)\right] = 1, \tag{4.10}$$

with M_A and M_F representing, respectively, the molecular mass of the air and the fuel.

In terms of the above dimensionless variables, the gas-phase conservation equations (3.6)–(3.8) and (3.10) reduce to

$$\frac{\partial(\rho u)}{\partial x} + \frac{\partial(\rho v)}{\partial y} = \alpha n \dot{m}_d, \tag{4.11}$$

$$\frac{\partial(\rho u u)}{\partial x} + \frac{\partial(\rho v u)}{\partial y} = {\rm Pr}\frac{\partial}{\partial y}\left(T^\sigma \frac{\partial u}{\partial y}\right) + \alpha n \dot{m}_d u_d - \alpha n f_x, \tag{4.12}$$

$$\frac{\partial(\rho u Y_{\rm F})}{\partial x} + \frac{\partial(\rho v Y_{\rm F})}{\partial y} = \frac{1}{L_{\rm F}}\frac{\partial}{\partial y}\left(T^\sigma \frac{\partial Y_{\rm F}}{\partial y}\right) + \alpha n \dot{m}_d - \Delta\Omega, \tag{4.13}$$

$$\frac{\partial(\rho u \hat{Y}_{\rm O})}{\partial x} + \frac{\partial(\rho v \hat{Y}_{\rm O})}{\partial y} = \frac{\partial}{\partial y}\left(T^\sigma \frac{\partial \hat{Y}_{\rm O}}{\partial y}\right) - S\Delta\Omega, \tag{4.14}$$

$$\frac{\partial(\rho u T)}{\partial x} + \frac{\partial(\rho v T)}{\partial y} = \frac{\partial}{\partial y}\left(T^\sigma \frac{\partial T}{\partial y}\right) - \alpha n[\dot{m}_d(l_v - T_d) + \dot{q}_d] + q\Delta\Omega, \tag{4.15}$$

where Pr represents the Prandtl number, $S = s/Y_{{\rm O}_2 A}$ is the mass of air consumed per unit mass of fuel burnt, and $q = q'/(c_p T_A)$ and $l_v = L_v/(c_p T_A)$ are the dimensionless values of the heat of combustion (lower heating value) and latent heat of vaporization, respectively, of the fuel. While a unity Lewis number is assumed for oxygen in writing (4.14), an excellent approximation

under most combustion conditions, the formulation considers a fuel-vapor Lewis number L_{F} different in general from unity, as is necessary to account for the low diffusivity of most spray fuels. The above gas-phase equations include source terms associated with the presence of the droplets in the flow, all being proportional to the number of droplets per unit volume n and involving the interphase exchange rates f_x, f_y, $\dot{q}_d$, and $\dot{m}_d$, which can be evaluated with the expressions presented in Chapter 3. The dimensionless chemical reaction rate in (4.13)–(4.15) is given by

$$\Omega = \rho \hat{Y}_{\text{O}} Y_{\text{F}} \exp[T_a(T-1)/T], \tag{4.16}$$

with

$$T_a = E_a/(R^o T_A) \tag{4.17}$$

denoting the nondimensional activation temperature.

The accompanying equations for the liquid phase include the conservation of droplets

$$\frac{\partial(nu_d)}{\partial x} + \frac{\partial(nv_d)}{\partial y} = 0, \tag{4.18}$$

along with equations following their trajectories for the evolution of the droplet radius, droplet temperature, and droplet velocity

$$ca^3\left(u_d\frac{\partial T_d}{\partial x} + v_d\frac{\partial T_d}{\partial y}\right) = \dot{q}_d, \tag{4.19}$$

$$u_d\frac{\partial a^3}{\partial x} + v_d\frac{\partial a^3}{\partial y} = -\dot{m}_d, \tag{4.20}$$

$$a^3\left(u_d\frac{\partial u_d}{\partial x} + v_d\frac{\partial u_d}{\partial y}\right) = f_x, \tag{4.21}$$

$$a^3\left(u_d\frac{\partial v_d}{\partial x} + v_d\frac{\partial v_d}{\partial y}\right) = f_y, \tag{4.22}$$

where $c = c_l/c_p$ is the ratio of the specific heats for the two phases. These equations may be derived from the spray equation and associated conservation equations [16], for example, by integrating over the droplet size-distribution function, which becomes a delta function for monodisperse sprays.

The values of f_x and f_y are evaluated from

$$f_x = \frac{3}{2}\text{Pr}T^\sigma a(u-u_d), \tag{4.23}$$

$$f_y = \frac{3}{2}\text{Pr}T^\sigma a(v-v_d). \tag{4.24}$$

corresponding to the nondimensional form of Stokes law (3.14). Similarly, we shall employ the expressions

$$\dot{q}_d = aT^{\sigma}(T - T_d) \quad \text{and} \quad \dot{m}_d = 0 \quad \text{if} \quad T_d < T_B \tag{4.25}$$

and

$$\dot{q}_d = 0 \quad \text{and} \quad \dot{m}_d = aT^{\sigma} \ln\left(1 + \frac{T - T_B}{l_v}\right) \quad \text{if} \quad T_d = T_B \tag{4.26}$$

for the droplet heating and vaporization rates, where T_B represents the boiling temperature nondimensionalized with T_A. As explained earlier in Chapter 3, these simplified equations apply for fuels whose latent heat of vaporization is much larger than the fuel thermal energy, as occurs for instance for heptane and methanol, for which $L_v/(R^o T_B/M_F) = 11.02$ and $L_v/(R^o T_B/M_F) = 12.30$, respectively. These expression would need to be modified to describe the burning of isolated droplets [17, 18], as may occur in some situations following ignition when the gas carrier contains oxygen and the droplet radii are sufficiently large for the droplets to sustain a surrounding flame. The possibility of ignition and burning of individual droplets is not considered further in the analysis below, which focuses on group ignition instead, the case more often encountered in applications.

Equations (4.11)–(4.15) and (4.18)–(4.22) supplemented with (4.10), (4.16), and (4.23)–(4.26), must be integrated with initial conditions at $x = 0$

$$u - 1 = Y_{\mathrm{F}} = \hat{Y}_{\mathrm{O}} - 1 = T - 1 = n = 0 \tag{4.27}$$

for $y > 0$, and

$$\begin{aligned} &u - u_S = Y_{\mathrm{F}} = T - T_S = n - 1 = T_d - T_S = a - 1 \\ &= u_d - u_S = v_d = \hat{Y}_{\mathrm{O}} - \hat{Y}_{\mathrm{O}_S} = 0 \end{aligned} \tag{4.28}$$

for $y < 0$, and with boundary conditions for $x > 0$ given by

$$u - 1 = Y_{\mathrm{F}} = \hat{Y}_{\mathrm{O}} - 1 = T - 1 = 0 \tag{4.29}$$

as $y \to +\infty$, and

$$u - u_S = Y_{\mathrm{F}} = \hat{Y}_{\mathrm{O}} - \hat{Y}_{\mathrm{O}_S} = T - T_S = v = 0 \tag{4.30}$$

as $y \to -\infty$, where $\hat{Y}_{\mathrm{O}_S} = 0$ when the spray is carried by an inert and $\hat{Y}_{\mathrm{O}_S} = 1$

when the spray is carried by air. The effect of the boundary layers developing upstream on both sides of the splitter plate has been neglected in defining the initial profiles of streamwise velocity and temperature, as is appropriate when the length of the splitter plate is much smaller than the characteristic mixing-layer length $U_A t_v$. An arbitrary condition of zero entrainment velocity on the spray side is included in writing (4.30), as applies when the mixing layer surrounds a spray jet, but this condition is inconsequential for determining the ignition distance, because of the transverse translational invariance of the problem. For $x \ll 1$, corresponding to residence times much smaller than the vaporization time, there is no appreciable coupling between the gas and liquid phases, i.e., the effect of the source terms appearing on the right-hand-side of (4.11)–(4.22) is negligible in the first approximation. As a result, the initial gaseous mixing occurs according to the classical self-similar mixing-layer solution for two parallel streams [19, 20], while the droplets initially maintain their velocity, temperature, and radius.

It is worth mentioning that, since the mixing-layer problem lacks a characteristic length scale, and therefore a characteristic flow time, the Stokes number St does not appear explicitly as a parameter in the formulation. Before proceeding with the analysis, it is therefore worth discussing the role of this parameter in the context of the laminar problem considered here. For spray flow, the time scales for droplet acceleration and droplet vaporization are comparable. For instance, when the relative flow around the droplet is dominated by molecular transport, the assumption adopted in writing (4.24)–(4.26), the acceleration time (or Stokes time) is given as $2/(3\mathrm{Pr})$ times the vaporization time t_v. For the mixing layer, the only relevant flow time is the local residence time, so that the associated Stokes number becomes $\mathrm{St} = 2/(3\mathrm{Pr}\, x)$ in terms of the dimensionless streamwise distance. This decaying function is such that at distances from the splitter plate of order x_v, i.e., dimensionless values $x \sim O(1)$, where ignition is anticipated to occur when $\Delta \gtrsim O(1)$, the resulting Stokes number is of order unity, so that in this region the gaseous streamlines generally differ from the droplet trajectories. For small values of the Damköhler number, however, ignition occurs at distances much larger than x_v, where the local Stokes number is very small, causing the droplet trajectories to follow closely the stream lines up to the ignition point. Nevertheless, regardless of the ignition location, the thermal expansion following the ignition of the fuel-air mixture induces large transverse velocities in a nonslender region where droplets cannot follow the gas flow, as will be seen in the plots below.

	q	l_v	T_B	c	$\frac{M_A}{M_F}$	L_F	S
Heptane	39.5	0.34	0.37	2.2	0.29	2.6	15.2
Methanol	18.6	1.09	0.34	2.5	0.91	1.2	6.5

Table 4.1. Values of the dimensionless parameters used in the numerical simulations for the two liquid fuels considered.

4.5 Spray ignition in coflow laminar mixing layers

The reactive spray in the laminar mixing layer was computed by numerical integration of (4.11)–(4.15) and (4.18)–(4.22), supplemented with (4.10), (4.16), and (4.23)–(4.26) and with the initial and boundary conditions given in (4.27)–(4.30). A Crank-Nicholson numerical scheme was used to integrate the parabolic gas-phase equations by marching in the x direction. The liquid-phase equations were integrated by using a third-order Runge-Kutta method.

The solution depends on the thermochemical and transport properties of the fuel through the values of q, l_v, T_B, c, S, M_A/M_F and L_F, which are listed in Table 4.1, where the first four values are evaluated assuming $T_A = 1000$ K for the air-side temperature. The remaining parameters are kept fixed at representative practical values for the simulations unless mentioned otherwise, with values given by $\alpha = 1$, $\mathrm{Pr} = 0.7$, $\Delta = 1$, $T_a = 10$, and $T_S = T_B$, the latter implying that the droplets in the spray are in equilibrium with the carrier gas, where no fuel vapor is present. The integrations considered cases with $\hat{Y}_{O_S} = 0$ and with $\hat{Y}_{O_S} = 1$, corresponding, respectively, to sprays carried by an inert gas and by air. Although the isovelocity case $u_S = 1.0$ is to be considered separately in Section 4.5.5, much of the discussion below is based on computations for a spray with velocity $u_S = 0.8$.

Sample results of the numerical integrations are shown in Fig. 4.3. In all cases, the spray mixes initially with the coflowing stream of hot air without appreciable chemical reaction. The hot air stream provides the heat needed for droplet vaporization, which, with the scales selected, occurs over distances of order unity. The fuel vapor diffuses into the air stream, and it begins to react with the oxygen as it reaches the high-temperature boundary, located far away from the spray. Different ignition behaviors are observed in Fig. 4.3 depending on the set of parameters selected in the integrations.

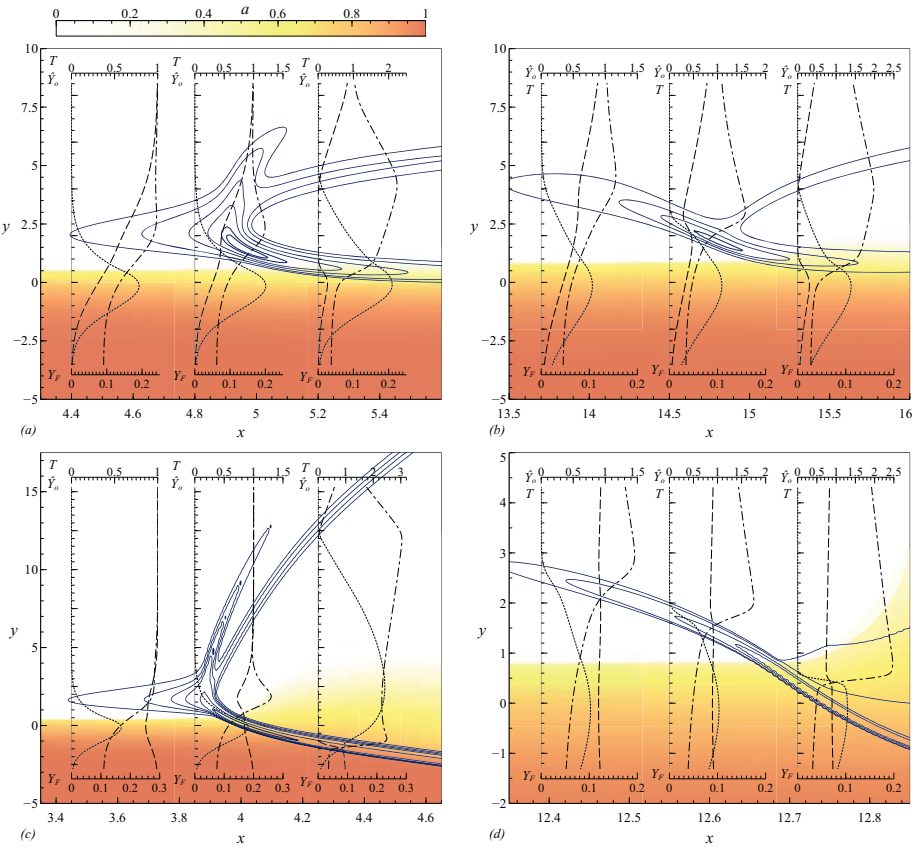

Figure 4.3. Ignition kernels of (a,c) heptane and (b,d) methanol sprays as obtained from integration of (4.11)-(4.22), with q, l_v, T_B, c, S, M_A/M_F and L_F given in Table 4.1 for each fuel, and $\alpha = 1$, $T_S = T_B$, $u_S = 0.8$, Pr $= 0.7$, $\Delta = 1$ and $T_a = 10$. The calculations are performed with sprays carried by (a,b) inert and (c,d) air. The figures show dimensionless reaction-rate contours (solid lines), with contour lines given by (a) $\Omega = [0.01, 0.02, 0.05, 0.1, 0.2, 0.25]$, (b) $\Omega = [0.02, 0.1, 0.25, 0.5]$, (c) $\Omega = [0.01, 0.025, 0.05, 0.1, 0.5, 2.0]$ and (d) $\Omega = [0.25, 0.5, 2.0, 5.0]$. Shaded contours of the droplet radius a are shown, with red and white color indicating $a = 1$ and $a = 0$, respectively. Temperature (dot-dashed lines), fuel mass fraction (dotted lines) and oxygen mass fraction (dashed lines) are shown in the insets for different x locations.

4.5.1 Sprays carried by an inert, $\hat{Y}_{O_S} = 0$ (nonpremixed systems)

Plots of the ignition zone for sprays carried by an inert, shown in Fig. 4.3(a) (heptane) and Fig. 4.3(b) (methanol), display important morphological differences (independent of chemical-kinetic properties) depending on the fuel considered, with heptane ignition occurring earlier and in a more abrupt way. Differences in the thermochemical properties of the two fuels explain the different ignition

behaviors observed. Thus, because of its smaller latent heat of vaporization ℓ_v, heptane droplets tend to vaporize faster than methanol droplets. As a result, as the mixing layer develops, heptane vapor becomes available for reaction earlier than methanol vapor, thereby explaining the occurrence of ignition at smaller streamwise distances. For example, for the parametric values used in Fig. 4.3(a,b), the resulting ignition distance, identified by the local maximum of the reaction rate, is $x_{ign} \simeq 4.95$ for heptane and $x_{ign} \simeq 14.8$ for methanol.

The ignition of heptane is facilitated by its chemical heat release being more than twice that of methanol, resulting in a larger temperature increase per unit mass of fuel burnt that facilitates the self-acceleration of the chemical reaction rate, enabling a thermal runaway to take place. The ignition kernel develops rapidly to produce a diffusion flame surrounded on the sides by lean and rich deflagration waves that burn the excess reactants, a tribrachial structure that is clearly apparent in the reaction-rate contours of Fig. 4.3(a). These results agree with ignition structures found in DNS simulations of spray reacting flows [21, 22]. Additional computations, not shown in the figure, indicate that the same type of sudden thermal-runaway event leading to a tribrachial structure characterizes the ignition of heptane when the initial spray temperature is below the boiling value. The main difference in that case is that, as a consequence of the existence of a heating stage preceding the vaporization of the droplets, the resulting ignition distance becomes larger for smaller values of T_s, so that, for example, $x_{ign} \simeq 22$ for $T_s = 0.28$, all other parameters being those used in Fig. 4.3(a).

The ignition of methanol proceeds in a more gradual form. As a result of the smaller chemical heat release of methanol, when the fuel vapor reaches the hot boundary and reacts with the oxygen of the air, the associated temperature increase is not sufficient to accelerate the chemical reaction locally to produce a thermal runaway. Instead, the fuel is seen to burn in a lean premixed flame that propagates slowly across the mixing layer into richer regions of lower initial temperature. Upon crossing stoichiometric conditions, this slow deflagration wave gives rise to a trailing diffusion flame and to a rich premixed flame, as shown in Fig. 4.3(b). The rich premixed flame increases the rate of spray vaporization as it burns the oxygen pocket that has diffused earlier into the spray side of the mixing layer. This rich flame eventually extinguishes at distances of order unity downstream from the ignition kernel as the oxidizer is depleted.

The two ignition modes identified here, i.e., a thermal runaway and a slow deflagration propagation, were also encountered in the analysis of ignition in gaseous mixing layers [23]. In particular, the prevalence of one mode of ignition

over the other was found in that case to depend only on the value of the ratio of the temperature difference between the two streams to the temperature increase associated with adiabatic combustion of the stoichiometric mixture, which emerges as the main controlling parameter in the equidiffusional case considered by [23]. A thermal-runaway regime, similar to that found here for heptane, occurs when this ratio takes values smaller than 1. By way of contrast, when its value exceeds unity, the steep temperature gradient found at the ignition kernel prevents the self-acceleration of the chemical reaction from taking place, leading instead to the establishment of a slow lean deflagration, similar to that observed for methanol in Fig. 4.3(b).

The effect of fuel diffusivity was addressed in [24] by introducing the fuel Lewis number as a parameter in the analysis, with the nondimensional heat of reaction assumed to be of order unity. It was found that for diffusive fuels with Lewis numbers smaller than one a thermal runaway occurs, and the amount of fuel reaching the hot boundary is so large compared with that required to sustain the thermal runaway that fuel consumption can be neglected altogether in analyzing ignition, that situation applying, for example, to hydrogen [25]. By way of contrast, when the Lewis number was larger than one, it was found [24] that the amount of fuel available for reaction at the hot boundary was so small that its reaction produced a temperature increase much too small for the chemical reaction to undergo self-acceleration, and a slow deflagration emerged instead.

These observations would suggest that the behavior seen in Fig. 4.3 would require the Lewis number of methanol to exceed that of heptane, but Table 4.1 shows the opposite to be true. In spray ignition, however, the amount of fuel reaching the hot boundary depends not only on the Lewis number but also on the fuel volatility through the heat capacity and latent heat of vaporization of the liquid fuel c and l_v, with the smaller values corresponding to heptane increasing the fuel supply rate. Besides, as noted previously [26], the self-acceleration of the chemical reaction is facilitated by the large value of q typical of liquid fuels, so that a thermal runaway can still be the prevailing mode of mixing-layer ignition for fuels with Lewis numbers larger than unity, provided that the heat of reaction is sufficiently large. The results in Fig. 4.3 indicate that, for heptane, the combined effect of the relatively small values of c and l_v and the large value of q counterbalance its low diffusivity in such a way that ignition proceeds through a thermal runaway, whereas for methanol the larger values of c and l_v and the smaller value of q prevent the sudden temperature rise from taking place, with the result that a gradual ignition mode through deflagration propagation emerges instead. Therefore, as the mixing layer de-

velops, heptane vapor becomes available for reaction earlier than methanol vapor, thereby leading to smaller ignition distances, a result in agreement with the ignition trends observed in previous numerical computations of ignition times in uniform spray mixtures [27]. The role of the different parameters is to be discussed further below in connection with the theoretical analysis of the thermal-runaway regime.

4.5.2 Downstream development of the diffusion flame

The ignition-kernel plots in Figs. 4.3(a,b) show an emerging diffusion flame accompanied by lean and rich deflagrative waves on the sides. These deflagrations, which propagate in the mixture formed by vaporization and reactant inter-diffusion upstream from the ignition point, vanish after depleting the deficient reactants on both sides, so that in the solution encountered downstream the chemical reactions occur only in a diffusion flame burning the fuel vapor generated by the vaporizing spray with the oxygen of the air stream.

As seen in the plots, the diffusion flame emerging from the ignition kernel is very thin. This can be explained by noting that, as a result of the high temperature sensitivity of the reaction rate (3.21), the associated reaction coefficient in (4.16) becomes exponentially large as the temperature increases by chemical heat release. Consideration of the solution of (4.13)–(4.15) for large values of the effective flame Damköhler number $\Delta \exp[T_a(T-1)/T]$ leads to the well-known Burke-Schumann condition $\hat{Y}_{\rm O} Y_{\rm F} = 0$, indicating that the reactants cannot coexist, so that the diffusion flame appears in the first approximation as a thin sheet separating a region without fuel vapor from a region without oxygen, a behavior clearly seen in the reactant profiles of Figs. 4.3(a,b).

The reactants reach the flame in stoichiometric proportions by diffusion from the sides. Because of the relatively large values of S corresponding to liquid fuels, the resulting nonpremixed flame lies far on the air side of the mixing layer. In the solution established for $x \gg x_{ign}$, part of the heat released at the diffusion flame is transferred by heat conduction towards the spray, where it is employed to vaporize the droplets. For $\alpha \sim O(1)$, vaporization occurs in a layer of characteristic thickness $(D_{T_A} t_v)^{1/2}$, corresponding to a nondimensional thickness of order unity. Since the mixing layer thickness increases downstream with the square root of the distance $x^{1/2}$, for $x \gg 1$ the vaporization layer appears as a thin front or sheath [11, 13].

The above considerations indicate that the reactive spray in the mixing layer approaches for large distances a solution including a diffusion flame located on the air side and a thin vaporization layer at the spray edge. This structure is

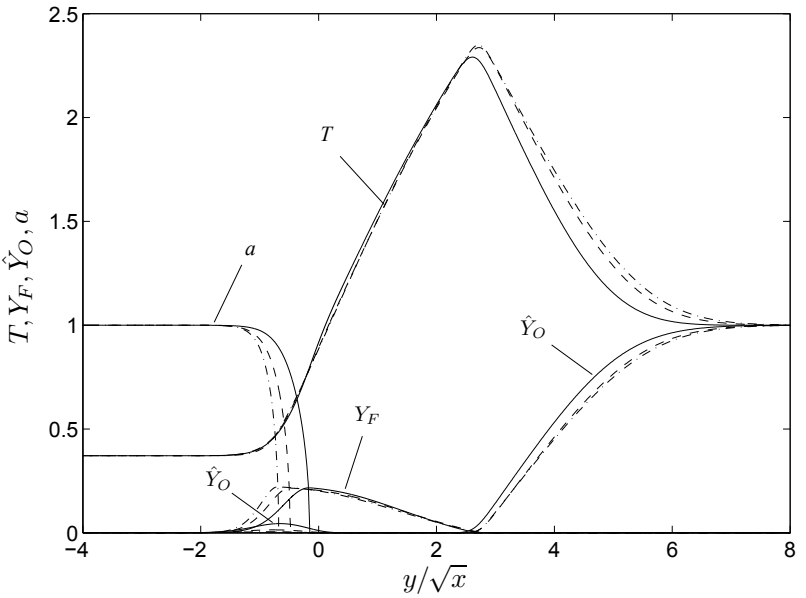

Figure 4.4. Profiles of $Y_{\rm F}$, $\hat{Y}_{\rm O}$, T, and a obtained at $x = 10$ (solid curves), $x = 20$ (dashed curves), and $x = 40$ (dot-dashed curves) from integration of (4.11)-(4.22) for the conditions of Fig. 4.3(a).

clearly exhibited by the profiles of temperature and reactants shown in Fig. 4.4, obtained by extending to large values of x the numerical integration of the heptane configuration of Fig. 4.3(a). Since both the flame and the vaporization layer are much thinner than the mixing layer, the asymptotic solution in the limit $x \to \infty$ is selfsimilar, so that the profiles obtained numerically at different values of $x \gg 1$ collapse when expressed in terms of the rescaled similarity coordinate $y/\sqrt{x}$ employed in Fig. 4.4. To clearly display the region where droplets are vaporizing, the plot includes the profile of droplet radius a, with the transition from $a = 1$ to $a = 0$ indicating the extent of the vaporization layer, whose relative thickness decreases with distance. The plot reveals also that the pocket of unburnt oxygen trapped on the spray side after ignition, which is still noticeable at $x = 10$, is almost completely burnt at $x = 20$, leaving the diffusion flame as the only reactive region across the mixing layer. The resulting trailing diffusion flame is further investigated in Appendix B by considering the limit of infinitely fast reaction, with attention restricted to the case of isovelocity mixing layers (i.e., $u = u_d = 1$).

4.5.3 Sprays carried by air, $\hat{Y}_{O_S} = 1$ (partially premixed systems)

Computations of heptane and methanol sprays carried by air were also considered. For heptane, ignition was also seen to occur in this case through a sudden temperature increase, leading to the formation of a triple flame, clearly visible in Fig. 4.3(c). The main difference from Fig. 4.3(a) pertains to the solution that emerges downstream. In Fig. 4.3(a), both premixed branches extinguish at a distance of order unity downstream from the ignition point, as the corresponding deficient reactant is depleted on each side. On the other hand, when air is employed as spray carrier, the deflagration wave developing on the rich side can propagate continuously into the spray cloud, consuming in a thin reaction layer the oxygen of the air with a fraction of the existing fuel vapor, which is generated on the spray side of the deflagration by heat conduction from the reaction region. The droplets crossing the deflagration vaporize in an oxidizer-free region, producing a large pocket of fuel vapor that has been expanded by the heat release and that diffuses to the air side to burn in a non-premixed flame, and their trajectories now move towards the oxidizer, as can be seen by the expansion of the shaded region. This two-flame structure, resembling that observed in earlier numerical simulations of spray jet flames [28, 29], is seen to persist downstream from the ignition kernel. The ultimate constant slope of the fuel-rich reaction zone is a measure of the premixed spray deflagration velocity.

A key ingredient for the existence of the two flames depicted in Fig. 4.3(c) is the relatively low value of the heat of vaporization of heptane, which facilitates the generation of large amount of fuel vapor by droplet vaporization ahead of the deflagration, sufficient to deplete the oxygen of the spray stream, so that an intermediate oxygen-free region appears between the rich deflagration and the diffusion flame. Methanol is less volatile than heptane, and sometimes it does not develop any multiple-flame solution. For instance, in the computation of Fig. 4.3(d), the premixed flame originating near the hot edge of the mixing layer continues burning under lean conditions as it propagates into the spray side, because heat conduction ahead of the front can generate only a limited amount of fuel vapor, as a consequence of the relatively large heat of vaporization of methanol. The partly vaporized fuel droplets then cross the deflagration and continue to vaporize in the post-flame region, where the fuel vapor reacts with the surrounding oxidizer in a distributed manner, never establishing a diffusion flame. Under these conditions the structure of the solution downstream from the ignition point is very sensitive to the specific set of boundary conditions, so that, depending on the values selected, both heptane and methanol can, in principle, support either a single lean deflagration followed by a region of dis-

tributed reaction or, ultimately, a double-flame structure with an intermediate oxygen-free region. These calculated behaviors apply for the representative reaction-rate parameters $\Delta = 1$ and $T_a = 10$ selected here, while different structures could arise if values of these and other parameters were very different, thus further emphasizing the remarkable variations that may occur, especially in partially premixed spray combustion.

4.5.4 Interaction of the spray cloud and the deflagration

In understanding the leakage of the droplets across the deflagration propagating into the spray in Figs. 4.3(c,d) one should keep in mind that the characteristic residence time across the flame can be expected to be proportional to (although somewhat larger than) the chemical-reaction time associated with the peak flame temperature, reached at the reaction layer. This chemical time for the deflagration is much smaller than the characteristic chemical time for ignition t_c, defined in (4.7), because the latter is based on the air-side temperature of the mixing layer, which is significantly smaller than the peak flame temperature, as can be seen in the profiles of Figs. 4.3(c,d). As a consequence, with the Damköhler number $\Delta = t_v/t_c$ assumed to be of order unity, the resulting residence time across the flame is smaller than the characteristic vaporization time, so that only a relatively small fraction of the liquid fuel vaporizes as the droplets cross the flame. Most of the droplet vaporization occurs instead either upstream in the mixing layer or in the post-flame region, resulting in the distribution of droplet radii shown in the figures. As previously discussed, depending on the value of ℓ_v the associated deflagration can be either rich, as occurs for heptane in Fig. 4.3(c) or lean, as occurs for methanol in Fig. 4.3(d).

To better display the characteristic features of the spray-deflagration interaction, a detailed view of the solution near the front corresponding to the flow conditions of Fig. 4.3(d) is given in Fig. 4.5. As the mixing layer develops upstream from the ignition region, the droplets vaporize partially through the heat flux coming from the hot air stream, creating a mixture that, for methanol droplets, is lean everywhere. This is illustrated in Fig. 4.5 by plotting the contours of the gaseous equivalence ratio $\phi_g = SY_F/\hat{Y}_O$. The fuel accumulates towards the middle of the mixing layer, where a maximum value $\phi_g \simeq 0.76$ is achieved. At that intermediate location, the transverse propagation velocity of the deflagration peaks, as indicated by the existence of an inflection point in the curved flame front. Because of the lean conditions, all of the fuel vapor available is consumed across the flame front. The droplets keep vaporizing as they cross the deflagration, and the fuel vapor generated by these droplets

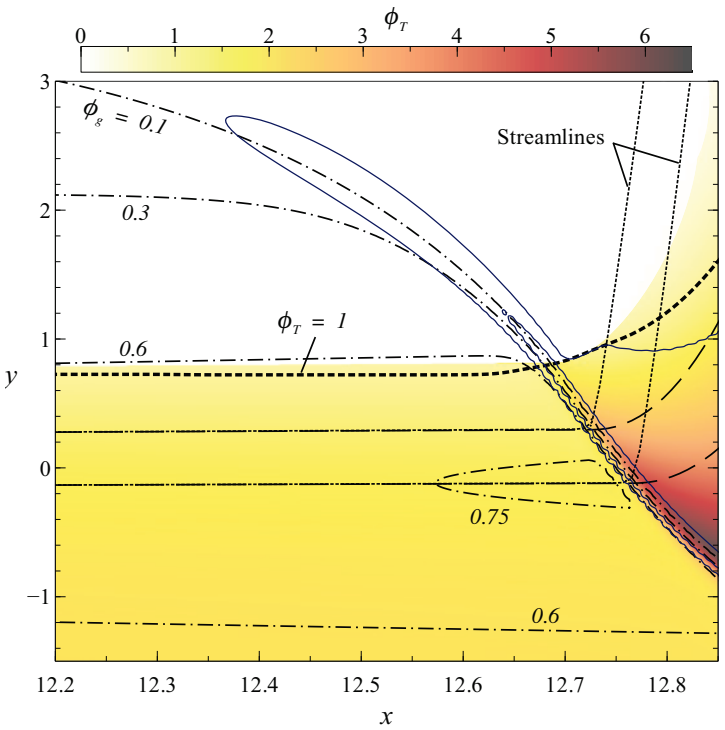

Figure 4.5. Close-up view of the spray-side deflagration wave of Fig. 4.3(d), including droplet trajectories (long-dashed lines), gaseous streamlines (dotted lines), reaction-rate contours $\Omega = 0.1$ and 5 (solid lines), contours of the gaseous equivalence ratio ϕ_g (dot-dashed lines), and a graded shade to indicate levels of global equivalence ratio ϕ_T.

burns in a distributed manner in the high-temperature post-flame region with the excess of oxygen that has leaked through the front.

Besides the standard gaseous-fuel equivalence ratio $\phi_g = SY_F/\hat{Y}_O$, in studying spray flames, it is convenient to introduce the liquid-based equivalence ratio $\phi_\ell = S\alpha n a^3/(\rho\hat{Y}_O)$. The resulting global equivalence ratio $\phi_T = \phi_\ell + \phi_g$, accounting for all of the fuel present in the flow, is represented by use of a graded shade in the plot as well as a thick dotted line indicating the region where $\phi_T = 1$. The initial value of ϕ_T in the fuel stream was $\phi_T = 2.21$ in these calculations, while it was $\phi_T = 5.17$ for the heptane spray in Fig. 4.3(c). In the region where $\phi_T < 1$ the local gaseous mixture is unconditionally lean, in that, even if all the liquid fuel were instantaneoulsy vaporized, the resulting gas mixture would still be lean. The sharp increase in ϕ_T observed in the post-flame region is a result of the thermal expansion across the flame, which reduces drastically the density, inducing accompanying large transverse velocities and

associated streamlines deflecting sharply at the flame front. The local mass-loading ratio increases, because the droplets cannot follow the gaseous flow, causing droplet trajectories to depart from streamlines as the flow crosses the deflagration, as shown in Fig. 4.5.

4.5.5 Ignition of unstrained spray flamelets

The solution for the mixing layer simplifies when the two coflowing streams have equal velocities, in which case, integration of (4.12) and (4.21) provides the uniform distribution $u = u_d = 1$ for the streamwise velocity components of the gas and liquid phases everywhere in the flowfield, a simplification that can be incorporated when writing the remaining equations (4.11), (4.13)–(4.15), (4.18)–(4.20), and (4.22). Besides describing the evolution with x of the isovelocity coflow mixing layer, the resulting mathematical problem provides the temporal evolution of the mixing layer formed by putting into contact at a given time a semi-infinite space of hot air with a semi-infinite spray suspension, with x being equivalent in that case to the dimensionless time t obtained with use made of the characteristic vaporization time t_v. The problem formulated here thus provides the solution for ignition of unsteady, unstrained spray flamelets, indicated earlier to have been considered relevant for studies of turbulent spray ignition for low Stokes numbers.

Sample results of the numerical integrations including both an inert gas and air as spray carriers are shown in Fig. 4.6 for heptane and in Fig. 4.7 for methanol. The values of the different parameters are those employed earlier for the integrations shown in Fig. 4.3. Profiles of temperature and fuel and oxygen mass fractions are represented at four different instants of times, which are selected to illustrate the ignition behavior. Corresponding curves from the problems whose solutions are shown in Fig. 4.3 would not be greatly different if x there were replaced by t.

Observation of the evolution of the temperature profiles in Fig. 4.6 reveals a sudden temperature increase a a given location, corresponding to a thermal-runaway mode of ignition characteristic of heptane, while the temperature profiles in Fig. 4.7 for methanol correspond to a deflagration front progressing from the hot boundary across the mixing layer. When the spray carrier is an inert, the case shown in Fig. 4.6(a-c) for heptane and in Fig. 4.7(a-c) for methanol, the solution at the last instant considered includes a central region free from oxygen bounded by a diffusion flame on the air side and a rich deflagration on the spray side, the latter front disappearing subsequently following the depletion of the oxygen pocket found on the left-hand side of Fig. 4.6(c)

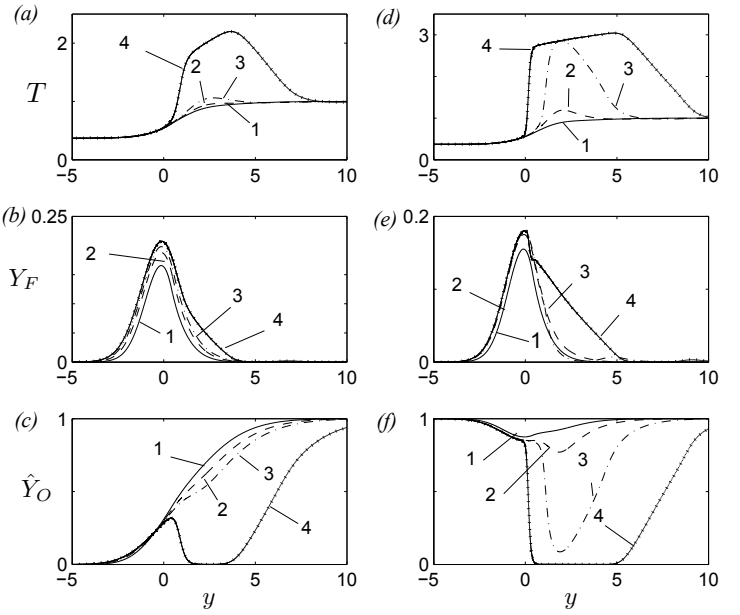

Figure 4.6. Temporal evolution of temperature, fuel and oxidizer mass fractions in a mixing layer of air and heptane spray carried by (a-c) inert and by (d-f) air. The time instants 1,2,3 and 4 correspond, respectively, to t =4.5, 5.5, 6.0 and 6.5 for (a-c), and to t =4.0, 4.8, 4.9 and 5.0 for (d-f).

and 4.7(c).

When air is present in the spray stream, the solution at the last instant of time considered is also similar for heptane and methanol. In this isovelocity case, both fuels develop downstream the double-flame solution previously observed in Fig. 4.3(c) for heptane. Observation of the evolution of the profiles in Fig. 4.7(d-e) indicates that the deflagration, initially lean, becomes rich at a given instant, leading to the emergence of large intermediate fuel pocket that burns on the air side in an emerging diffusion flame. The dramatic change in the flow structure for methanol is apparent by comparing the profiles at $t = 15.5$ and $t = 16.0$, which would correspond to proceeding to values of x greater than 12.8 in Fig. 4.3(d).

4.6 The thermal-runaway mode of spray ignition

Let us now focus attention on the type of autoignition process that occurs in Figs. 4.3(a,c), corresponding to Fig. 4.6. During this type of spray ignition

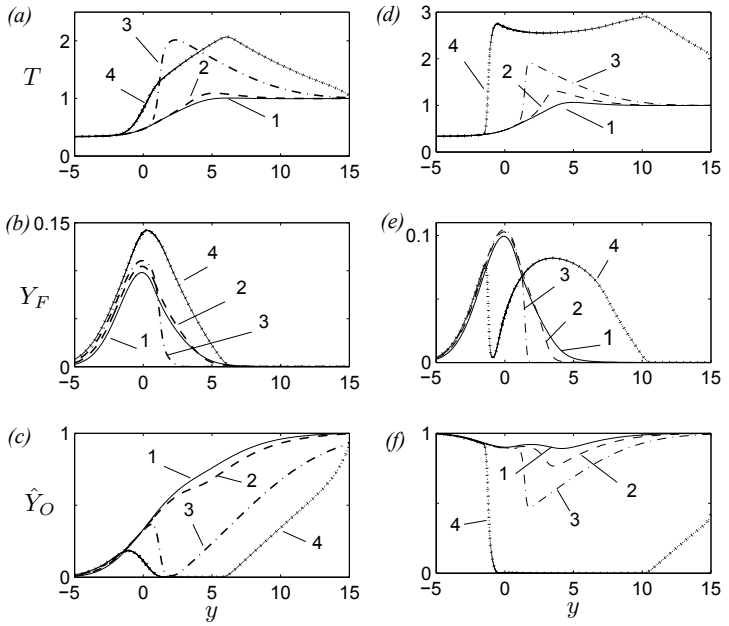

Figure 4.7. Temporal evolution of temperature, fuel and oxidizer mass fractions in a mixing layer of air and methanol spray carried by (a-c) inert and by (d-f) air. The time instants 1,2,3 and 4 correspond, respectively, to t =14.0, 16.0, 18.0 and 20.0 for (a-c), and to t =14.0, 15.0, 15.5 and 16.0 for (d-f).

by a hot coflow the chemical reaction occurs initially near the hot boundary, where the fuel mass fraction is a small quantity of order $Y_{\mathrm{F_R}} \ll 1$. It can be expected from (4.16) that because of the large activation energy the chemical reaction rate increases by a factor of order unity when the heat release causes the temperature to increase by a small relative amount, of order T_a^{-1}, giving rise to a self-accelerating reacting process that may lead to a local thermal runaway if sufficient fuel is available. It can be concluded by comparing the reaction terms in (4.13) and (4.15) that a nondimensional temperature increase of order T_a^{-1} is associated with fuel consumption that decreases the fuel mass fraction by an amount of order $(qT_a)^{-1}$. Therefore, a sustained self-acceleration of the chemical reaction is possible only when

$$Y_{\mathrm{F_R}} \gg (qT_a)^{-1}. \tag{4.31}$$

This condition is examined ahead and the associated ignition problem is formulated.

Because of the large value of the activation energy, during the weakly reactive stage prior to ignition, the temperature and reactant profiles are in the first approximation those resulting from the chemically frozen interaction of the spray with the hot air, to be determined by numerical integration of (4.11)–(4.22) with $\Delta = 0$. The solution at distances $y \gg 1$ takes up a simplified form that can be described by noticing that the streamwise velocity and density approach there their boundary values $u = \rho = 1$, so that the continuity equation (4.11) reduces to $\partial v/\partial y = 0$, indicating that the transverse velocity is given simply by the entrainment distribution $v = v_\infty(x)$. The temperature variations from the boundary value $T = 1$ are obtained by integrating the energy equation (4.15) written in the form

$$\frac{\partial T_f}{\partial x} + v_\infty \frac{\partial T_f}{\partial y} = \frac{\partial^2 T_f}{\partial y^2} \tag{4.32}$$

for the chemically frozen temperature T_f, which further reduces to the heat equation by introduction of the alternative transverse coordinate $y + y_T - \int_0^x v_\infty \mathrm{d}x$ involving an unknown translation y_T along with the displacement $-\int_0^x v_\infty \mathrm{d}x$ associated with the amount of gas entrained by the mixing layer. For $y \gg 1$, the equation admits a self-similar description in terms of the similarity diffusion variable obtained by scaling the alternative transverse coordinate with $(x - x_T)^{1/2}$, where x_T is an appropriate virtual origin. The solution to the heat equation then leads to the well-known representation

$$1 - T_f = A_T \operatorname{erfc}\left(\frac{y + y_T - \int_0^x v_\infty \mathrm{d}x}{2(x - x_T)^{1/2}} \right) \tag{4.33}$$

in terms of the complementary error function. Similarly, the same procedure applied to (4.13) yields

$$Y_\mathrm{F} = A_F \operatorname{erfc}\left(\frac{\sqrt{L_\mathrm{F}}(y + y_F - \int_0^x v_\infty \mathrm{d}x)}{2(x - x_F)^{1/2}} \right) \tag{4.34}$$

for the small value of the fuel mass fraction near the air boundary. The factors A_T and A_F, the transverse translations y_T and y_F, and the virtual origins x_T and x_F have values that may be determined by inspection of the numerical results corresponding to the vaporizing mixing layer in a given intermediate range of values of x, to provide through (4.33) and (4.34) a universal description of the temperature and fuel fields far from the spray. For instance, for the parametric values considered for heptane in Fig. 4.3(a), the values $A_T = 0.2689$,

$A_F = 1.7482$, $y_T = -0.6209$ and $y_F = 3.8177$, $x_T = 0.5321$, and $x_F = -2.2994$ are obtained at distances x of order unity, whereas for the parametric values considered for methanol in Fig. 4.3(b) one obtains the values $A_T = 0.5184$, $A_F = 0.0612$, $y_T = 0.8268$ and $y_F = 1.0665$, $x_T = -0.383$, and $x_F = 1.2229$. As can be seen, the virtual origins for the temperature and fuel fields are different. In particular, for given boundary conditions the value of x_F is seen to be significantly influenced by the latent heat of vaporization l_v and specific-heat ratio c of the fuel at hand, with vaporization being facilitated by smaller values of l_v and c, giving rise to values of the virtual origin x_F that are smaller for heptane than they are for methanol. Note that the description given in (4.33) and (4.34) for $x \sim O(1)$ is consistent with the self-similar solution emerging for $x \gg 1$, where $v_\infty = V_\infty/\sqrt{x}$ with V_∞ being a constant, with the temperature and fuel mass fraction taking self-similar solutions in terms of $\eta = y/\sqrt{x}$, such that $1-T_f \simeq A_T \operatorname{erfc}[(\eta-2V_\infty)/2]$ and $Y_\mathrm{F} \simeq A_F \operatorname{erfc}[\sqrt{L_\mathrm{F}}(\eta-2V_\infty)/2]$ for $\eta \gg 1$.

In the limit of large activation energy $T_a \gg 1$ chemical reaction occurs in a thin layer centered at a transverse location $y_\mathrm{R}(x) \gg 1$ such that the frozen temperature T_f differs from the air temperature by a small amount of order T_a^{-1}, a condition that can be expressed in the form

$$T_a^{-1} = A_T \operatorname{erfc}\left(\frac{y_\mathrm{R} + y_T - \int_0^x v_\infty \mathrm{d}x}{2(x-x_T)^{1/2}}\right), \tag{4.35}$$

which serves to define y_R for a given value of x. The corresponding fuel mass fraction $Y_{\mathrm{F_R}}$ at $y = y_\mathrm{R}$ can be evaluated from (4.34) to give

$$Y_{\mathrm{F_R}} = A_F \operatorname{erfc}\left(\frac{\sqrt{L_\mathrm{F}}(y_\mathrm{R} + y_F - \int_0^x v_\infty \mathrm{d}x)}{2(x-x_F)^{1/2}}\right). \tag{4.36}$$

Using the asymptotic expansion for large y of the complementary error functions in (4.35) and (4.36) it is easy to see that

$$y_\mathrm{R} \sim 2(x-x_T)^{1/2} \ln^{1/2}(T_a) \tag{4.37}$$

and that

$$Y_{\mathrm{F_R}} \sim T_a^{-l_\mathrm{F}}, \tag{4.38}$$

where

$$l_\mathrm{F} = L_\mathrm{F}(x-x_T)/(x-x_F) \tag{4.39}$$

is an effective fuel Lewis number. According to (4.38), the amount of fuel available at the reaction layer depends not only on the fuel diffusivity but also

on its heating and vaporization characteristics, which determine through l_v and c the virtual origins appearing in (4.39). In terms of the estimate (4.38), the criterion (4.31), determining whether sufficient fuel is available for a local thermal runaway to occur, becomes

$$qT_a^{1-l_{\rm F}} \gg 1. \tag{4.40}$$

For heptane, the value of q is quite large (i.e., $q = 39.5$ when the air temperature is taken to be 1000 K) and the values of c and l_v are sufficiently small that $x_{_F} < x_{_T}$, thereby resulting in a small enough value of $l_{\rm F} < L_{\rm F}$ such that the criterion (4.40) is satisfied under most conditions. The opposite is observed for methanol ignition, because, although the value of $L_{\rm F}$ is smaller than that of heptane, the associated heat of reaction q is smaller and the values of c and l_v are much larger.

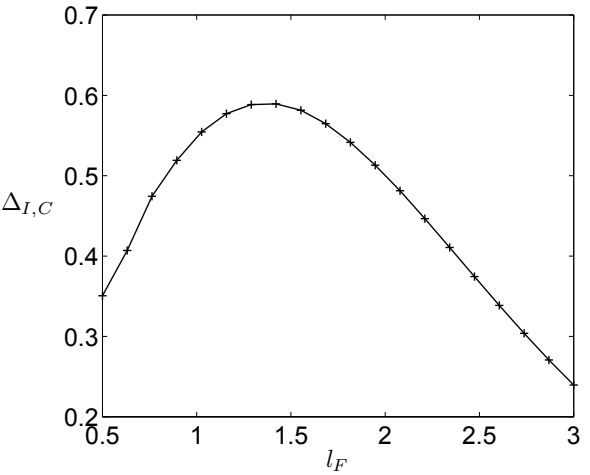

Figure 4.8. The variation of the critical Damköhler number for ignition $\Delta_{\rm I,C}$ with $l_{\rm F}$ as obtained from integrations of (4.43).

For conditions under which the criterion (4.40) is satisfied ignition can be expected to take place as a local thermal explosion centered at $y = y_{\rm R}$ at a given ignition location $x_{\rm I}$. Using the asymptotic expansion for large y of the complementary error functions in (4.35) and (4.36) indicates that the characteristic thickness of the reaction layer scales with $y_{\rm R}^{-1} \ll 1$, so that introduction of the normalized coordinate

$$\xi = \exp\left(-\frac{y_{\rm R}(y - y_{\rm R})}{2(x - x_{_T})}\right). \tag{4.41}$$

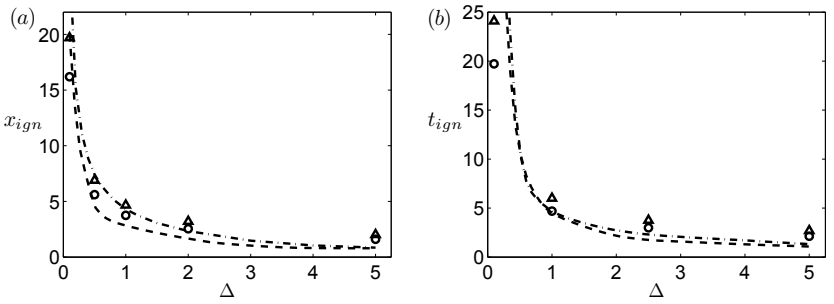

Figure 4.9. The variation with the Damköhler number Δ of the (a) ignition distance x_{ign} for the coflow mixing layer with $u_s = 0.8$ and (b) ignition time t_{ign} for the unstrained mixing layer (i.e., $u_s = 1.0$) as obtained for a heptane spray from numerical integration of the original problem (4.10)–(4.30) (symbols) and from the asymptotic prediction obtained by evaluating (4.35), (4.36), (4.39), and (4.44) (lines), for sprays carried by air (circles and dashed lines) and inert (triangles and dot-dashed lines).

simplifies the frozen temperature and fuel mass fractions to

$$T_a(1 - T_f) = \xi \qquad \text{and} \qquad Y_{\mathrm{F}} = Y_{\mathrm{F_R}} \xi^{l_{\mathrm{F}}} \tag{4.42}$$

with the modified fuel Lewis number l_{F} appearing as a exponent in the fuel mass fraction. Ignition can be described by writing (4.15) for the rescaled temperature increment $\theta = T_a(T - T_f)$ with fuel consumption neglected, an appropriate simplification when (4.40) holds. The accumulation term is seen to be a factor y_{R}^2 smaller than the conduction term, so that the problem reduces to a balance between conduction and chemical reaction according to

$$\frac{\mathrm{d}^2\theta}{\mathrm{d}\xi^2} = \Delta_{\mathrm{I}} \xi^{l_{\mathrm{F}}-2} e^{\theta-\xi}; \quad \theta(0) = \frac{\mathrm{d}\theta}{\mathrm{d}\xi}(\infty) = 0, \tag{4.43}$$

where

$$\Delta_{\mathrm{I}} = 4(x - x_T)^2 \Delta T_a q Y_{\mathrm{F_R}} / y_{\mathrm{R}}^2 \tag{4.44}$$

is the ignition Damköhler number.

As shown by [26], the problem (4.43) has two solutions for a value of Δ_{I} smaller than a critical value $\Delta_{\mathrm{I,C}}$ and no solution for $\Delta_{\mathrm{I}} > \Delta_{\mathrm{I,C}}$. The dependence of $\Delta_{\mathrm{I,C}}$ on l_{F} is shown in Fig. 4.8. This figure, together with (4.35), (4.36), (4.39), and (4.44) provide a coupled system of equations that determine the ignition location x_{ign} as well as the corresponding values of y_{R}, $Y_{\mathrm{F_R}}$, l_{F}, and $\Delta_{\mathrm{I,C}}$. Note that, because of the quasisteady approximation adopted in deriving (4.43), the asymptotic development necessarily contains errors that are of order $y_{\mathrm{R}}^2 \sim$

$1/\ln T_a$, to be kept in mind when assessing the comparison shown in Fig. 4.9(a) between the predictions of the asymptotic analysis and those of the numerical integrations. As can be seen, despite its inherent logarithmic errors, the level of accuracy displayed by the asymptotic prediction is satisfactory.

Straightforward replacement of x with t in (4.32)–(4.44) provides formulae for the evaluation of the ignition-delay time t_{ign} of unstrained spray flamelets. The chemically frozen evolution prior to ignition needs to be considered to determine the parameters entering in (4.35), (4.36), (4.39), and (4.44), including the values of A_T, A_F, y_T and y_F, along with the virtual origins t_T and t_F that replace x_T and x_F in the temporal description. The results of the asymptotic analysis so obtained are compared with the numerical simulations in Fig. 4.9(b), which shows a level of agreement similar to that displayed in Fig. 4.9(a) for the coflow mixing layer. The closeness of the values of x_{ign} and t_{ign} in the two figures in indicative of the similarity of the two problems, with x_{ign} being slightly less than t_{ign} because of the somewhat lower velocity in the spray streams.

4.7 Distributions of mixture fraction and scalar dissipation rate

Mixture fractions and magnitudes of their gradients, called scalar-dissipation rates or, more briefly, scalar dissipation (based on appearance in conservation equations for averages) are widely used in computations, analyses, and modeling of turbulent combustion [7]. It is important to recognize that there are many different definitions of mixture-fraction fields. They are introduced most readily for two-stream problems, that is, for problems in which inlet streams are of only two distinct types, typically one containing fuel and the other oxidizer, all fuel streams having identical compositions, and similarly for all oxidizer streams. The most basic definition of a mixture-fraction field is the fraction of mass of the material at any given position and time that originated in one of the two streams (by convention, the fuel stream). Such a definition can even be applied to partially premixed two-stream gaseous combustion problems, although that generally is not done because it requires treating the same chemical species in different streams as different species, augmenting the set of differential conservation equations by equations containing coefficients of self-diffusion, and extending the augmented system to a similar treatment of all combustion intermediaries and products.

The same fuel-stream-related definition can also be introduced for multiphase systems, such as the present spray-combustion problems, including the partially premixed case in which the droplets are transported in an air stream.

Just as for mixture-fraction definitions based on element mass fractions, any such definition results in a conserved scalar, in the sense that source terms in principle cannot appear in any differential equation for such a mixture fraction, in this case simply as a consequence of mass conservation. In spray-combustion problems, however, such a definition encounters the severe difficulty that fundamentally a differential conservation equation for this mixture-fraction field does not exist. Any such equation would, for example, be different in the liquid phase and in the gas phase. Moreover, this mixture fraction would, in general, be discontinuous at liquid-gas interfaces. Even when it can be measured in principle, its direct numerical simulation would be prohibitively complex. Unless modeling hypotheses are introduced at the outset, it is not a useful definition for spray-combustion analyses. Nevertheless, some progress in modeling spray combustion has been made with this approach [30, 31].

4.7.1 The gas-phase mixture fraction

An alternative definition of a mixture fraction in spray combustion that is more useful in many respects is one that focuses only on the gas phase. This makes good sense because a mixture fraction would be irrelevant in the liquid phase. This mixture fraction and its corresponding conservation equation can be derived, as was done for gaseous combustion by [32], by considering a linear combination of the conservation equations for oxygen and fuel vapor that is free from the chemical source term [14]. The essential results can be illustrated by taking the Lewis number of the fuel to be unity, which simplifies the equations. With this simplification, adding (4.14) and (4.13) times S leads, after use is made of (4.11), to the conservation equation

$$\frac{\partial(\rho u Z)}{\partial x} + \frac{\partial(\rho v Z)}{\partial y} = \frac{\partial}{\partial y}\left(T^{\sigma}\frac{\partial Z}{\partial y}\right) + \alpha n \dot{m}_d, \tag{4.45}$$

for the gas-phase mixture-fraction variable

$$Z = \frac{S Y_{_F} - \hat{Y}_{_O} + 1}{S + 1} \tag{4.46}$$

commonly employed in combustion. Equation (4.45) clearly demonstrates that, for spray combustion, this mixture-fraction variable fundamentally is not a conserved scalar, in the sense that it has a source associated with droplet vaporization.

While equation (4.45) is sufficiently accurate for methanol, for which the associated Lewis number is close to unity, it is inaccurate for most of the other

spray fuels, which typically have vapors with mass diffusivities much smaller than the thermal diffusivity, resulting in Lewis numbers significantly larger than unity, as seen for heptane in Table 3.1. When a nonunity fuel Lewis number is taken into account, the linear combination corresponding to that leading to (4.45) gives instead the equation

$$\frac{\partial(\rho u Z)}{\partial x}+\frac{\partial(\rho v Z)}{\partial y}=\frac{S/L_{\mathrm{F}}+1}{S+1}\frac{\partial}{\partial y}\left(T^{\sigma}\frac{\partial \tilde{Z}}{\partial y}\right)+\alpha n\dot{m}_{d}, \tag{4.47}$$

involving a diffusion-weighted mixture-fraction variable $\tilde{Z}=(SY_{F}/L_{\mathrm{F}}-\hat{Y}_{O}+1)/(S/L_{\mathrm{F}}+1)$ besides the unweighted mixture-fraction variable defined in (4.46). An accompanying coupling function free from chemistry effects can be derived for the temperature by combining linearly (4.14) with (4.15) to give

$$\frac{\partial(\rho u H)}{\partial x}+\frac{\partial(\rho v H)}{\partial y}=\frac{\partial}{\partial y}\left(T^{\sigma}\frac{\partial H}{\partial y}\right)-\alpha n[\dot{m}_{d}(q/S+l_{v}-T_{B}+1)+\dot{q}_{d}], \tag{4.48}$$

for the total enthalpy

$$H=T-1+(\hat{Y}_{O}-1)q/S, \tag{4.49}$$

which, just as the mixture fraction, is not a conserved scalar as a result of the presence of source terms, involving in this case the heat transfered from the gas to the droplets. In writing (4.48) the droplet temperature T_{d} has been replaced by the boiling temperature T_{B}, in agreement with the simplified description defined in (4.25) and (4.26). If the Lewis number of the oxidizer were not unity, then a diffusion-weighted H, analogous to $\tilde{Z}$, would also have to be introduced.

For numerical integrations one may in general replace two of the three equations (4.13)–(4.15) by (4.47) and (4.48). The analysis simplifies further in the Burke-Schumann limit of infinitely fast reaction rate, which arises when the reaction time is much smaller than the characteristic fluid mechanical times in the problem. Under those conditions, the chemical reaction is confined to a thin flame, which becomes a sheet when the limit of infinitely fast reaction is considered, separating a region free from oxidizer from a region free from fuel vapor. The flame is located where both Y_{F} and $\hat{Y}_{O}$ are simultaneously zero, corresponding to the stoichiometric values $Z=Z_{st}=1/(S+1)$ and $\tilde{Z}=\tilde{Z}_{st}=1/(S/L_{\mathrm{F}}+1)$ of the ordinary and diffusion-weighted mixture fractions. The condition that the reactants cannot coexist can be used to derive

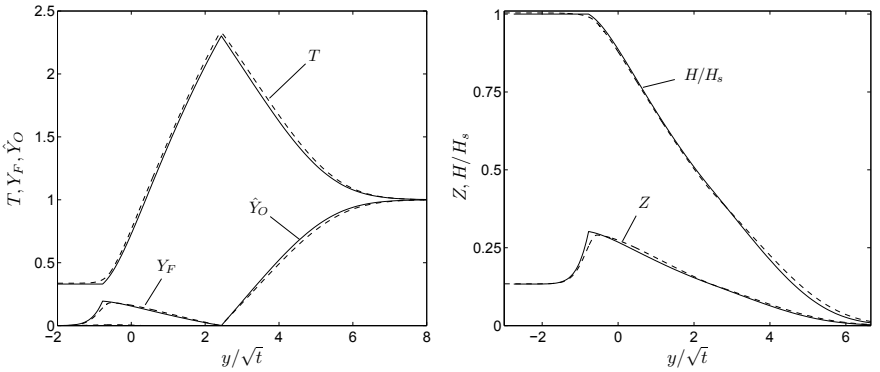

Figure 4.10. Profiles of Z, H, $\hat{Y}_{\rm O}$, $Y_{\rm F}$, and T across the unstrained unsteady mixing layer obtained from integration of the coupling-function equations (4.45) and (4.48) (solid curves) and from extending to $t = 65$ the numerical integrations of the methanol spray of Figs. 4.7(a-c) (dashed curves).

the equations

$$Z \geq Z_{st}: \quad \hat{Y}_{\rm O} = 0, \quad Y_{\rm F} = \frac{Z - Z_{st}}{1 - Z_{st}} = \frac{\tilde{Z} - \tilde{Z}_{st}}{1 - \tilde{Z}_{st}}, \; T = 1 + H + q/S$$
$$Z \leq Z_{st}: \quad Y_{\rm F} = 0, \quad \hat{Y}_{\rm O} = 1 - \frac{Z}{Z_{st}} = 1 - \frac{\tilde{Z}}{\tilde{Z}_{st}}, \; T = 1 + H + (Z/Z_{st})(q/S) \tag{4.50}$$

linking the values of Z, $\tilde{Z}$, and H everywhere in the flow field. This enables the integration of (4.47) and (4.48) to be performed and provides the mass fractions of reactants and the temperature in terms of the coupling-function variables.

The mixture fraction Z and the total enthalpy H defined in (4.46) and (4.49) can be used to describe the solution that appears in nonpremixed spray mixing layers far downstream from the ignition point, i.e., at distances $x \gg x_{ign}$. As shown in Fig. 4.4 for heptane, the flowfield structure includes a droplet-vaporization layer, whose characteristic thickness is of order unity with the scales selected here, embedded in a thick mixing layer of characteristic thickness $\sqrt{x}$. The mixture fraction Z peaks within the vaporization layer, where the temperature differs from the boiling value by a small amount $T - T_{_B} \sim 1/\sqrt{x} \ll 1$. No vaporization takes place outside the vaporization layer, because $a = 0$ on the air side and $T \leq T_{_B}$ on the spray side. The flame lies on the oxidizer side of the mixing layer at a location to be determined as part of the integration. The corresponding sheath-vaporization solution, similar to that encountered in previous works [13, 14], can be described by considering the asymptotic

limit $x \gg 1$ and introducing the similarity variables of order unity $\eta = y/\sqrt{x}$ and $V = \sqrt{x}v$. Integrating the conservation equations in the vaporization-free streams with appropriate jump conditions at the separating vaporization sheet provides a free-boundary parabolic problem that determines the locations of the vaporization and flame sheets, $\eta_V = y_V/\sqrt{x}$ and $\eta_f = y_f/\sqrt{x}$, along the peak value $Z = Z_V$ of the mixture fraction at $\eta = \eta_V$.

As in the computations for Figs. 4.6 and 4.7, an equivelocity mixing layer with $T_S = T_B$ will be considered below. For simplicity, the analysis also assumes that the Lewis number of the fuel is unity, thereby enabling (4.45) to be used in the computation. Under these conditions, the solution for the gas phase in the outer non-vaporizing stream for $\eta > \eta_V$ is determined by integration of (4.11), (4.45), and (4.48) written in the similarity form

$$(\rho V)_\eta - \eta\rho_\eta/2 = 0, \tag{4.51}$$

$$\left(T^\sigma Z_\eta\right)_\eta + \rho(\eta/2 - V)Z_\eta = 0, \tag{4.52}$$

$$\left(T^\sigma H_\eta\right)_\eta + \rho(\eta/2 - V)H_\eta = 0, \tag{4.53}$$

with the subscript η denoting differentiation with respect to this variable. The equations must be supplemented with the equation of state (4.10) and with the coupling-function relationships (4.50), which enable the computation of ρ and T as functions of Z and H. The solution is simpler for $\eta < \eta_V$ because with $T = T_B$ and $\hat{Y}_O = 0$ the total enthalpy on the spray side of the vaporization layer remains equal to its spray-side boundary value $H = H_S = -(q/S + 1 - T_B)$. For the development below, it is of interest that in this low-Stokes-number region the velocity of the droplets v_d differs by a small amount of order x^{-1} from the gas-phase velocity v, as follows from the limiting form of (4.22) for $x \gg 1$. This condition can be used to combine (4.11) with (4.18) to yield $\partial(n/\rho)/\partial x + v\partial(n/\rho)/\partial y = 0$, which can be integrated along the trajectories to give

$$n = \rho/\rho_S, \tag{4.54}$$

where $\rho_S = T_B^{-1}$ is the known value of the gas-phase density in the unperturbed spray stream.

The integration of (4.51)–(4.53) requires consideration of the jumps of V, Z_η, and H_η at $\eta = \eta_V$, to be determined by investigating the vaporization layer in terms of the translated coordinate $\xi = y - y_V = y - \eta_V x^{1/2}$ and the rescaled coupling functions $\mathcal{H} = (H - H_S)x^{1/2} = (T - T_B)x^{1/2}$ and $\mathcal{Z} = (Z - Z_V)x^{1/2}$.

The computation begins by integrating the reduced form (4.18),

$$-\frac{1}{2}\eta_V n_\xi + (nV)_\xi = 0, \tag{4.55}$$

with the boundary conditions $n - n^- = V - V^- = 0$ as $\xi \to -\infty$ to give

$$n\left(V - \frac{\eta_V}{2}\right) = n^-\left(V^- - \frac{\eta_V}{2}\right). \tag{4.56}$$

In this notation, the subscript ξ is used to indicate differentiation with respect to this variable, and the superscripts $+$ and $-$ denote values on the upper and lower sides of the vaporization layer, respectively. In particular, the boundary value of the number density appearing in (4.56) can be evaluated from (4.54) to give

$$n^- = \frac{\rho_V}{\rho_S}, \tag{4.57}$$

where

$$\rho_V = T_B^{-1}\left[1 - \frac{Z_V - Z_{st}}{1 - Z_{st}}\left(1 - \frac{M_A}{M_F}\right)\right]^{-1} \tag{4.58}$$

is the gas density at the vaporization layer, expressed here in terms of the unknown peak mixture fraction Z_V by virtue of (4.10) and (4.50). Using (4.56) and (4.57) in writing (4.11) and (4.20) in terms of the rescaled variables yields

$$V_\xi = \frac{\alpha}{\rho_S}\left(\frac{\eta_V}{2} - V^-\right)(a^3)_\xi = \frac{\alpha n a T_B^\sigma \mathcal{H}}{\rho_V l_v}. \tag{4.59}$$

On the other hand, the conservation equations for the coupling functions in the vaporization layer can be written as

$$-\frac{\mathcal{Z}_{\xi\xi}}{(1 - Z_V)} = \frac{\mathcal{H}_{\xi\xi}}{l_v} = \frac{\alpha n a \mathcal{H}}{l_v}. \tag{4.60}$$

Combining (4.59) and (4.60) to eliminate the vaporization term and integrating the result across the layer provides the equations

$$V^+ - V^- = \frac{\alpha}{\rho_S}\left(V^- - \frac{\eta_V}{2}\right) = -\frac{T_B^\sigma(Z_\eta^+ - Z_\eta^-)}{\rho_V(1 - Z_V)} = \frac{T_B^\sigma H_\eta^+}{\rho_V l_v}, \tag{4.61}$$

when use is made of the identities $Z_\eta = \mathcal{Z}_\xi$ and $H_\eta = \mathcal{H}_\xi$.

Integrating (4.51)–(4.53) for $\eta > \eta_V$ with boundary conditions $Z = H = 0$ as $\eta \to \infty$ and $Z - Z_V = H - H_S = V - V^+ = 0$ at $\eta = \eta_V^+$ and (4.51) and (4.52) with boundary conditions $Z - Z_{st} = V = 0$ as $\eta \to -\infty$ and $Z - Z_V = V - V^- = 0$ at $\eta = \eta_V^-$, subject to the jump conditions given in (4.61), provide the profiles of V,

Z, and H across the mixing layer, along with the values of $\eta_{\rm V}$, $Z_{\rm V}$, V^+, and V^-. The solution obtained with the values $T_B = 0.34$, $M_A/M_F = 0.91$, $Z_{st} = 0.133$, and $H_S = 3.52$, consistent with the parameters given for methanol in Table 3.1, is shown as solid curves in Fig. 4.10. The resulting selfsimilar solution therefore corresponds, approximately, to that approached by the unsteady methanol flamelet of Figs. 4.7(a-c) for $t \gg t_{ign}$. This is verified by including in the plots of Fig. 4.10 the methanol profiles of $\hat{Y}_{\rm O}$, $Y_{\rm F}$, and T determined numerically at $t = 65$ and also the accompanying functions Z and H computed by using these profiles to evaluate (4.46) and (4.49). The degree of agreement of the finite-rate-chemistry results with the coupling-function results is seen to be quite satisfactory. This simple example therefore serves to illustrate the predictive capability of the mixture-fraction formalism in computations of spray diffusion flames with fast chemistry, when appropriate account is taken of the spray-source terms affecting Z and H in their conservation equations.

Nevertheless, gas-phase mixture fractions analogous to (4.46) have been used widely in turbulent spray flames for analyses of DNS results [28, 33, 34] and for flamelet combustion modeling with finite-rate chemistry [35, 36]. Often in numerical approaches an approximate differential equation for Z, free from source terms, is assumed and solved, along with other conservation equations, to determine the Z field [37–39], sometimes accompanied by a progress-variable equation to account for partial premixing [7, 38]. Such a source-free conservation equation is more attractive computationally than (4.45) (or (4.47)) because the latter requires closure modeling for the spray-vaporization term in both the filtered equation and the associated conservation equation for the subgrid variance. The results, however, may miss essential physics in spray flames, associated with the source terms.

These source terms in the mixture-fraction equation associated with droplet vaporization have been shown to be important in some previous studies addressing flamelet models [40]. Also of interest in this context is the work of Pera et al. [41], who correctly accounted for the mixture-fraction source terms in their LES computations, which identified the need for closure models for the scalar-dissipation rate and vaporization sources. Results of our computations can be used to test the accuracies of the approximations for Z that have been introduced in the literature. The following observations emphasize computed characteristics of the Z fields and their scalar-dissipation counterparts that bear on such tests and that were not initially expected.

4.7.2 Multivalued mixture-fraction fields

The mixture fraction is a non-monotonic function of the transverse coordinate in the mixing layer of the spray. This is clearly shown in Fig. 4.10 for the downstream methanol diffusion flame and also in Figs. 4.11 and 4.12 for the flow field near the ignition kernel. In particular, Fig. 4.11 shows the contours of Z calculated by using (4.46) for the strained mixing layer of Fig. 2.2(a), which corresponds to a heptane spray carried by an inert. It is observed that Z varies from small, near-stoichiometric conditions in the spray stream ($y \to -\infty$) because of the absence of fuel vapor there, reaches a maximum within the vaporization zone, and then decays to $Z = 0$ in the hot-air stream ($y \to +\infty$). In this case since none of the fuel is vaporized in the feed stream of the spray, $Z = Z_{st} = 1/(1 + S)$ there according to (4.46). For sprays carried by air, the mixture fraction actually decays to $Z = 0$ in the spray stream, thus producing a bell-shaped spatial distribution. Additionally, in the combustion of sprays the dimensionless scalar dissipation rate χ nondimensionalized with ρ_A/t_v, which is defined here as

$$\chi = T^{\sigma} \left(\frac{\partial Z}{\partial y} \right)^2 \tag{4.62}$$

(to leading order in $1/\mathrm{Pe}$ for strained mixing layers), reaches zero within the vaporization region $y \simeq 0$ as shown by the colored contours of Fig. 4.11. This is because of the bell-shaped Z distribution, in which the maximum of Z clearly enforces $\chi = 0$ at that location. It is also observed in Fig. 4.11 that ignition by thermal runaway occurs in regions of low scalar dissipation rate immediately above the vaporization region, where fuel vapor is available in a high-temperature region in a manner made possible by (4.31). The low-χ promoting ignition is quite different from the nearby low-χ in the vaporizing layer.

Similar trends are observed in Fig. 4.12 for the temporal evolution of Z and χ in the same unstrained mixing layer of the heptane spray carried by inert that was shown in Fig. 4.6(a-c). In particular, the ignition by thermal runaway occurs at $y \sim 3$ in a region of low scalar dissipation rate. Two sharp peaks in the scalar dissipation rate occur on both sides of the vaporization layer, which here sits near the centerline of the mixing layer and occupies spatial scales of order unity, the value $\chi = 0$ being reached within the vaporization layer as in Fig. 4.11. The resulting dependence of χ on Z is shown in Fig. 4.12(c). By way of contrast, in laminar gaseous diffusion flames the scalar dissipation rate is a bell-shaped curve with $\chi = 0$ only at the two free streams $Z = 0$ and $Z = 1$, quite different from Fig. 4.12(c) [7]. This provides a one-to-one transform from physical space

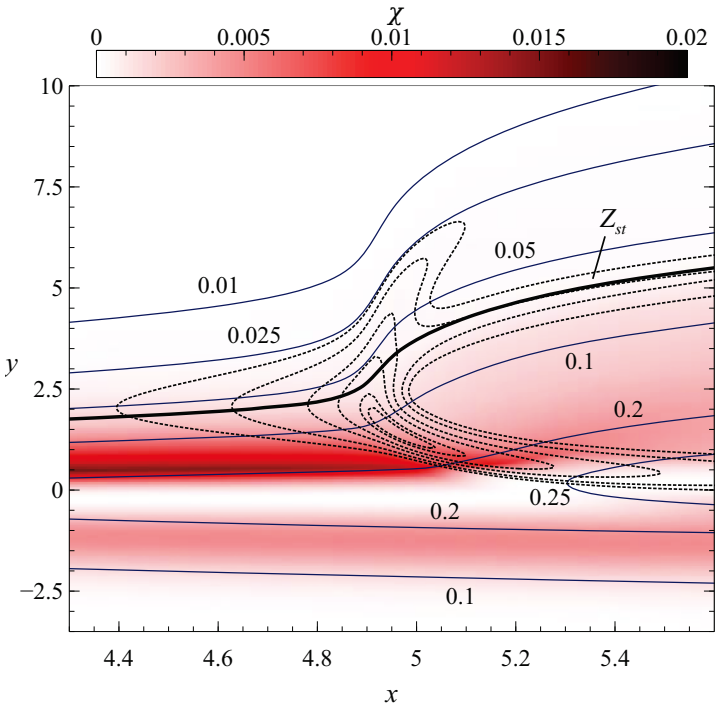

Figure 4.11. Contours of the mixture fraction Z (solid lines) overlaid on reaction rate isocontours (dashed lines) and filled contours of the scalar dissipation rate χ, for ignition in a strained mixing layer of heptane carried by inert, in the same conditions as in Fig. 2.2(a).

to Z space, which is lost in the combustion of sprays. The dual-peak χ profiles (Fig. 4.12) are a direct consequence of the bell-shaped Z profiles for the sprays and are unavoidable with the definition (4.46).

The complex behavior of this mixture fraction may be understood most easily by assuming that the mass diffusivities of all reactants are equal to the thermal diffusivity (unity Lewis numbers) and deriving a transport equation for Z by combining linearly the fuel and oxidizer transport equations (4.13) and (4.14), which gives (4.45). As previously remarked, this now simply and explicitly shows that Z no longer is a conserved scalar. In (4.45), the source term $\dot{m}_d$ is non-zero only in regions where fuel vapor is generated, which suggests that Z behaves as a conserved scalar on both sides of the vaporization layer. The source term $\dot{m}_d$ becomes localized in space in the sheath-vaporization limit that is approached sufficiently far downstream, as shown in Figs. 4.4 and 4.10. Near the ignition kernel, however, the thickness of the vaporization layer is

comparable to the mixing-layer thickness, with the consequence that typically there is no localization of $\dot{m}_d$ in mixture-fraction space, as will be illustrated in Section 4.7.4.

4.7.3 Mixture fraction and scalar dissipation in the gaseous region

Simplifications occur when attention is restricted to the gaseous region far from the vaporization layer, $y \gg 1$. This region is relevant here for analyzing the distribution of Z near the flame when $Z_{st} \ll 1$, and in this region (4.45) becomes

$$\frac{\partial Z}{\partial x} + v_\infty \frac{\partial Z}{\partial y} = \frac{\partial^2 Z}{\partial y^2}, \tag{4.63}$$

subject to $Z = 0$ at $y \to +\infty$. A procedure for solving (4.63) can be followed here which is similar to that described in Section 6 to derive (4.33) and (4.34). The result is

$$Z = \frac{A_Z}{2} \mathrm{erfc}\left(\frac{(y + y_Z - \int_0^x v_\infty \mathrm{d}x)}{2(x - x_Z)^{1/2}} \right), \tag{4.64}$$

where A_Z is a numerical constant, and y_Z and x_Z are virtual origins for the mixture fraction, the values of which are obtained by numerical integration. The values of A_Z, y_Z, and x_Z depend on the parameters appearing in Section 4, in particular on the spray parameters in Table 3.1 and on the velocity ratio $u_S = U_S/U_A$ between the spray and the air streams, which is representative of an applied strain rate. From (4.64) the tail of the scalar dissipation is obtained as

$$\chi = \frac{A_Z^2}{2\pi(x - x_Z)} \exp\left\{ -2 \left[\mathrm{erfc}^{-1}(2Z/A_Z) \right]^2 \right\} \tag{4.65}$$

for $y \gg 1$. For strained mixing layers, the effective strain-rate $\partial u/\partial y|_{y \gg 1}$ nondimensionalized with $1/t_v$ affects the prefactor $A_Z^2/(x - x_Z)$ in (4.65). For unstrained mixing layers this prefactor corresponds to the factor t^{-1} in the scalar dissipation rate in purely gaseous flows (see Eq. (3.56) in [7]) which describes its decay with time. These considerations show approximate analogies between purely gaseous ignition and spray ignition at low Stokes numbers, up to factors and time translations, in scalar dissipation near the ignition region and in the flame far from the vaporization layer. This is where flamelet modeling of ignition may apply at low Stokes numbers. The results for sprays depend on the spray dynamics, in that the constants A_Z and x_Z, affecting the shape of χ, depend on the spray parameters α, St, ℓ_v, c, M_F/M_A and T_B.

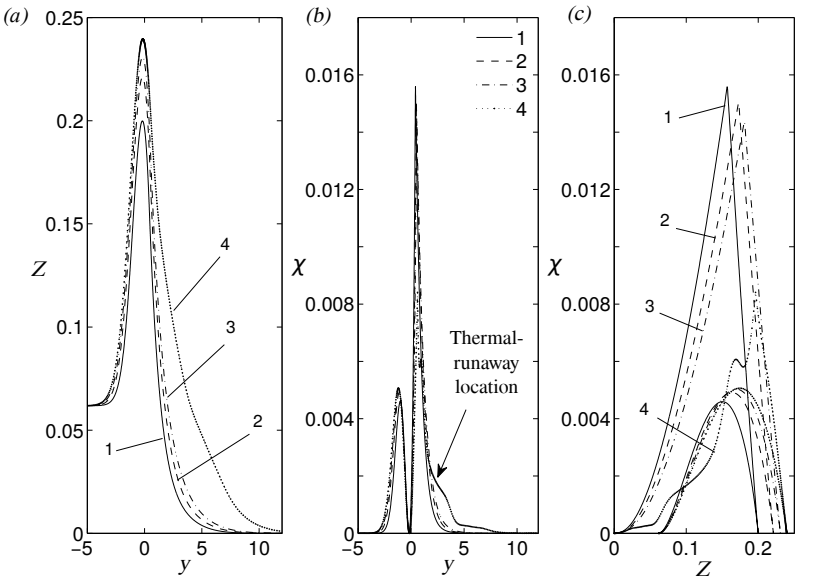

Figure 4.12. Temporal evolutions of (a) mixture fraction Z, (b) dimensionless scalar dissipation rate χ in physical space, and (c) dimensionless scalar dissipation rate χ in mixture-fraction space, for an unstrained mixing layer of a heptane spray carried by an inert gas, in the same conditions as in Fig. 4.6(a-c). The time instants 1, 2, 3 and 4 correspond, respectively, to $t = 4.5$, 5.5, 6.0 and 6.5.

4.7.4 Flamelet equations for the igniting mixing layer

Ignition in unstrained mixing layers may be addressed in Z space by expressing the conservation equations (4.13)-(4.15) as

$$\rho\frac{\partial Y_{_F}}{\partial t} + \alpha n\dot{m}_d\left\{\frac{\partial Y_{_F}}{\partial Z}(1-Z) - (1-Y_{_F})\right\} = \chi\frac{\partial^2 Y_{_F}}{\partial Z^2} - \Delta\Omega, \tag{4.66}$$

$$\rho\frac{\partial \hat{Y}_{_O}}{\partial t} + \alpha n\dot{m}_d\left\{\frac{\partial \hat{Y}_{_O}}{\partial Z}(1-Z) + \hat{Y}_{_O})\right\} = \chi\frac{\partial^2 \hat{Y}_{_O}}{\partial Z^2} - S\Delta\Omega, \tag{4.67}$$

$$\rho\frac{\partial T}{\partial t} + \alpha n\left\{\dot{q}_d + \dot{m}_d\left[\ell_v + T - T_d + +(1-Z)\frac{\partial T}{\partial Z}\right]\right\}$$
$$= \chi\frac{\partial^2 T}{\partial Z^2} + q\Delta\Omega, \tag{4.68}$$

in which unity Lewis numbers have been assumed and in which the change of variables $x \rightarrow t$ has been performed. Generalizations to remove these restrictions should be evident from the preceding development but are not

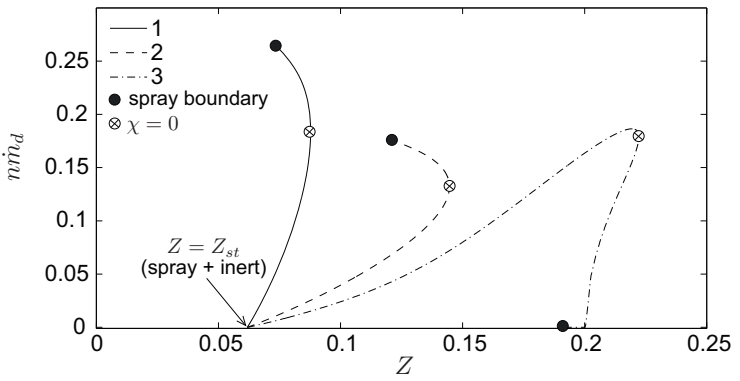

Figure 4.13. Distributions of the dimensionless spray vaporization rate per unit volume $n\dot{m}_d$ in Z space for an unstrained mixing layer of heptane carried by inert with unity Lewis numbers. The time instants 1, 2 and 3 correspond, respectively, to $t = 1.1$, 3.5 and 5.2.

exhibited here because their greater complexity serves only to obscure the essential conclusions. The presence of the additional terms within curly brackets in (4.66)–(4.68) is due to the vaporization of the spray. The form of (4.66)-(4.68) is independent of the flow configuration to the extent that Z-field curvature effects are negligible. These particular equations represent the flamelet equations for the combustion of equidiffusive monodisperse sprays with finite-rate chemistry at low Stokes number.

Use of flamelet equations for gaseous fuels generally involves modeling of $\chi(Z)$. Equations (4.66)-(4.68) indicate that, for sprays, models for the distributions $n(Z)$, $\dot{m}_d(Z)$, $\dot{q}_d(Z)$, and $T_d(Z)$ also are needed. An example of these distributions is given in Fig. 4.13 for the product $n(Z)\dot{m}_d(Z)$. The portions of the curves between $Z = Z_{st}$ and $\chi = 0$ should be excluded in flamelet modeling for the case plotted here because they lie within the spray where chemical reactions do not occur. The curves end at the spray boundary, which often is encountered before Z decreases again towards Z_{st}, reaching the region where ignition is most likely. For sufficiently volatile fuels, the additional terms might have little influence on the flamelet modeling in that they may not affect the tail of χ significantly near $Z = Z_{st}$, except for the spray corrections shown in equation (7.6); this has been found to be approximately true by comparing the curves in Fig. 4.12(c) with Z-field computations that ignore these source terms. However, for non-volatile sprays, combustion may occur near or within the spray cloud, and associated flamelet calculations would then necessarily involve modeling of these terms, which surely would be an ambitious task.

4.8 Conclusions

Ignition of nonpremixed and partially premixed spray flames in laminar mixing layers separating a monodisperse spray stream from a hot-air stream have been investigated both numerically and theoretically. This laminar configuration is reasoned to be representative of the reactive flow found in the mixing layers wrapped around the cores of the large convective eddies that develop in turbulent spray mixing layers, where the low-Stokes-number droplets tend to accumulate. Two different ignition modes are encountered depending on the thermochemical properties of the fuel, namely, i) a thermal-runaway mode in which ignition occurs through a rapid temperature increase and ii) a more gradual ignition mode in which the small amount of fuel vapor reaching the hot boundary burns in a lean premixed flame that propagates across the mixing layer towards the spray side. The former type of ignition, found when the thermochemical properties of heptane are employed in the integrations, can be anticipated to be the preferred mode of ignition for highly volatile liquid fuels with large values of the heat of combustion, whereas fuels of lower volatility and with smaller chemical heat release will have a more pronounced tendency to ignite in the slow-deflagration-wave mode, which is observed to occur in our numerical integrations when the properties of methanol are employed for the fuel. Activation-energy asymptotics is used to derive analytical predictions for ignition distances associated with thermal-runaway events, giving quantitative results in good agreement with the numerical integrations for heptane.

The numerical integrations serve to clarify different aspects of the igniting solution. For nonpremixed configurations, in which the spray is carried by an inert gas, ignition eventually leads to the formation of a trailing diffusion flame that sits far on the air side of the mixing layer at a location such that the fuel vapor generated by the vaporizing spray and the oxygen of the air stream meet in stoichiometric proportions. For the partially premixed configurations corresponding to sprays carried by air, depending on the specific boundary conditions considered, the numerical integrations give either solutions including a lean deflagration propagating into the spray followed by a region of distributed reaction or a double-flame configuration including a rich deflagration and a diffusion flame bounding an intermediate oxygen-free region where the droplets vaporize to generate a large fuel-vapor pocket.

The results of the integrations are used to evaluate mixture-fraction and scalar dissipation fields in spray mixing layers. Differences between spray and purely gaseous mixture-fraction-based models of combustion are highlighted. Also emphasized are the complexity of the resulting scalar dissipation rate and

the possible need for modeling additional vaporization terms arising in the augmented flamelet equations for spray combustion. It would be of interest to extend the monodisperse-spray results given here to polydisperse sprays by accounting for different droplet classes as indicated in the general formulation of Chapter 3.

References

[1] D. Harrje, Liquid propellant rockets, NASA monograph.

[2] A. H. Lefebvre, Gas turbine combustion, CRC press, 1998.

[3] W. A. Sirignano, Fluid dynamics and transport of droplets and sprays, 2nd edition, Cambridge University Press, Cambridge, UK., 2010.

[4] S. C. Li, Spray stagnation flames, Progress in energy and combustion science 23 (4) (1997) 303–347.

[5] Y. Huang, V. Yang, Dynamics and stability of lean-premixed swirl-stabilized combustion, Progress in Energy and Combustion Science 35 (4) (2009) 293–364.

[6] E. Mastorakos, Ignition of turbulent non-premixed flames, Progress in Energy and Combustion Science 35 (1) (2009) 57–97.

[7] N. Peters, Turbulent combustion, Cambridge university press, 2000.

[8] E. K. Longmire, J. K. Eaton, Structure of a particle-laden round jet, Journal of Fluid Mechanics 236 (1992) 217–257.

[9] H. H. Chiu, T. Liu, Group combustion of liquid droplets, Combust. Sci. Tech. 17 (1977) 127–142.

[10] M. Labowsky, D. E. Rosner, Group combustion of droplets in fuel clouds, i. quasi-steady predictions, in: J. T. Zung (Ed.), Evaporation-Combustion of Fuels, Americal Chemical Society, 1978, pp. 63–79.

[11] S. M. Correa, M. Sichel, The group combustion of a spherical cloud of monodisperse fuel droplets, Proc. Combust. Inst. 19 (1982) 981–991.

[12] Y. Wang, C. Rutland, Direct numerical simulation of ignition in turbulent n-heptane liquid-fuel spray jets, Combustion and flame 149 (4) (2007) 353–365.

[13] J. Arrieta-Sanagustín, A. L. Sánchez, A. Liñán, F. A. Wiliams, The sheath vaporization of a monodisperse fuel-spray jet, J. Fluid Mech. 675 (2011) 435–464.

[14] J. Arrieta-Sanagustín, A. L. Sánchez, A. Liñán, F. A. Williams, Coupling-function formulation for monodisperse spray diffusion flames with infinitely fast chemistry, Fuel Processing Technology 107 (2013) 81–92.

[15] H. Ciezki, G. Adomeit, Shock-tube investigation of self-ignition of n-heptane-air mixtures under engine relevant conditions, Combustion and Flame 93 (4) (1993) 421–433.

[16] F. A. Williams, Combustion Theory, Second ed., Benjaming Cummings, Menlo Park, CA., 1985.

[17] A. Liñán, Theory of droplet vaporization and combustion, in: R. Borghi, P. Clavin, A. Liñán, P. Pelcé, G. I. e. Sivashinsky (Eds.), Modélisation des phénoménes de combustion, Editions Eyrolles, 1985, pp. 73–103.

[18] J. Urzay, H. Pitsch, A. Liñán, Source terms for calculations of vaporizing and burning fuel sprays with non-unity lewis numbers in gases with temperature-dependent thermal conductivities, Annual Research Briefs, Center for Turbulence Research, Stanford University.

[19] D. R. Chapman, Laminar mixing of a compressible fluid, NACA-TN -1800.

[20] M. Lessen, On the stability of the laminar free boundary between parallel streams, Tech. rep., NACA-R-979 (1950).

[21] P. Domingo, L. Vervisch, J. Réveillon, Dns analysis of partially premixed combustion in spray and gaseous turbulent flame-bases stabilized in hot air, Combustion and Flame 140 (3) (2005) 172–195.

[22] J. Reveillon, L. Vervisch, Analysis of weakly turbulent dilute-spray flames and spray combustion regimes, J. Fluid Mech. 537 (2005) 317–347.

[23] A. Liñán, A. Crespo, An asymptotic analysis of unsteady diffusion flames for large activation energies, Combustion science and technology 14 (1-3) (1976) 95–117.

[24] A. L. Sánchez, Nonpremixed spontaneous ignition in the laminar wake of a splitter plate, Physics of Fluids 9 (7) (1997) 2032–2044.

[25] E. Fernández-Tarrazo, A. L. Sánchez, F. A. Williams, Hydrogen-air mixing-layer ignition at temperatures below crossover, Combustion and Flame 160 (10) (2013) 1981–1989.

[26] A. Liñán, F. A. Williams, Ignition in an unsteady mixing layer subject to strain and variable pressure, Combustion and flame 95 (1) (1993) 31–46.

[27] E. Gutheil, Numerical analysis of the autoignition of methanol, ethanol, n-heptane and n-octane sprays with detailed chemistry, Combustion science and technology 105 (4-6) (1995) 265–278.

[28] J. Reveillon, L. Vervisch, Analysis of weakly turbulent dilute-spray flames and spray combustion regimes, Journal of Fluid Mechanics 537 (2005) 317–347.

[29] L. P. Domingo, Vervisch, J. Reveillon, DNS analysis of partially premixed combustion in spray and gaseous turbulent flame-bases stabilized in hot air, Combust. and Flame 140 (2005) 172–195.

[30] R. W. Bilger, A mixture fraction framework for the theory and modeling of droplets and sprays, Combustion and Flame 158 (2) (2011) 191–202.

[31] S. De, K. Lakshmisha, R. W. Bilger, Modeling of nonreacting and reacting turbulent spray jets using a fully stochastic separated flow approach, Combustion and Flame 158 (10) (2011) 1992–2008.

[32] A. Liñán, F. A. Williams, Fundamental aspects of combustion, Oxford University Press, New York, 1993.

[33] J. Reveillon, L. Vervisch, Spray vaporization in nonpremixed turbulent combustion modeling: a single droplet model, Combustion and flame 121 (1) (2000) 75–90.

[34] K. Luo, H. Pitsch, M. G. Pai, O. Desjardin, Direct numerical simulations and analysis of three-dimensional n-heptane spray flames in a model swirl combustor, Proc. Comb. Inst. 89 (2011) 1447–1460.

[35] Y. Baba, R. Kurose, Analysis and flamelet modelling for spray combustion, Journal of Fluid Mechanics 612 (2008) 45–79.

[36] B. Franzelli, B. Fiorina, N. Darabiha, A tabulated chemistry method for spray combustion, Proceedings of the Combustion Institute 34 (1) (2013) 1659–1666.

[37] H. Pitsch, N. Peters, A consistent flamelet formulation for non-premixed combustion considering differential diffusion effects, Combustion and Flame 114 (1) (1998) 26–40.

[38] E. Knudsen, H. Pitsch, Large eddy simulation of a spray combustor using a multi-regime flamelet approach, Annual Research Briefs (2010) 337–350.

[39] Shashank, High-fidelity simulations of reactive liquid-fuel jets, PhD thesis, Stanford University.

[40] C. Hollmann, E. Gutheil, Modeling of turbulent spray diffusion flames including detailed chemistry, in: Symposium (international) on combustion, Vol. 26, Elsevier, 1996, pp. 1731–1738.

[41] C. Pera, J. Réveillon, L. Vervisch, P. Domingo, Modeling subgrid scale mixture fraction variance in les of evaporating spray, Combustion and Flame 146 (4) (2006) 635–648.

CHAPTER
FIVE

Regimes of spray vaporization and combustion in counterflow configurations

5.1 Introduction

For the high Reynolds numbers typically encountered in combustion applications the flow is turbulent and the flames appear embedded in thin mixing layers that are locally distorted and strained by the turbulent motion [1]. In applications involving spray combustion, the interactions of the flame with the flow are also dependent on the presence of the fuel droplets [2]. These interactions can be investigated by consideration of simple laminar problems, an example being the counterflow mixing layer, which has been widely used to represent local flow conditions in strained mixing layers [1]. Counterflow structures that move with the mean velocity can be abstracted from the interface dynamics of shear and mixing layers [3]. Local counterflow spray configurations are encountered in typical combustion chambers around the stagnation point that forms near the injector exit as a result of vortex breakdown of the swirling air-feed stream [4].

Counterflow configurations have been employed in previous experimental analyses of spray diffusion flames, with numerous fundamental contributions originating from the combustion laboratories at UCSD [5–8] and at Yale university [9–13]. Numerical analyses were developed in parallel efforts. Continillo and Sirignano [14] provided for the first time a two-continua formulation for spray flames in counterflow mixing layers and the conditions needed for the solution to remain self-similar in the vicinity of the stagnation point, where fluid properties are functions of the distance to the stagnation plane. The two-continua description applies to the dilute spray conditions typically found in the main vaporization and combustion region of practical liquid-fueled combustion devices [2], when the interdroplet distances are significantly larger than the droplet diameter and, for the counterflow configuration, smaller than the mixing-layer thickness. Then, as previously stated in Chapter 2, each droplet moves and vaporizes individually in the gas environment provided collectively

by the droplets, which includes the statistically smoothed effect of the wakes of the neighboring droplets, where the exchanges of fuel, energy, and momentum with the gas have been dumped. This allows us to use a homogenized treatment of the dispersed phase, in which the droplets appear as distributed point sources, resulting in source terms in the gas-phase equations that are proportional to the number of droplets per unit volume n.

The two-continua formulation, termed multicontinua formulation when used for the analysis of polydisperse sprays by incorporation of several droplet classes in the computation, has been used to explore different aspects of counterflow spray diffusion flames. The computation is simplified when the droplets are sufficiently small that they vaporize completely before crossing the stagnation plane [15–19]. However, as noted in early work [5, 20], sufficiently large droplets may cross the stagnation plane and even undergo oscillatory trajectories, a general complicating characteristic of particle-laden stagnation-point flows [21, 22]. As shown in [23], this can be successfully handled in the self-similar counterflow formulation by consideration of what they call "different sheets of solutions", and we shall call different droplet classes, thereby enabling computations that may account for oscillatory droplet trajectories [24–26]. The multicontinua formulation can be extended to the treatment of realistic droplet-size distributions by consideration of a large number of droplet classes (or "sectionals"). A different sectional approach is followed by other authors [10, 11], who used as starting point the spray equation originally derived by Williams [27].

5.2 Description of the counterflow problem

Vaporization and combustion of sprays in axisymmetric counterflow arrangements involving two high-Reynolds-number opposing streams, one of air and the other containing a polydisperse fuel spray carried by nitrogen is analyzed. Figure 5.1 represents the typical setup used in experimental studies, which involves two opposing nozzles of radius R whose exits are located a distance $2H$ apart. The resulting axisymmetric coaxial counterflowing jets are separated by a laminar stagnation-point mixing layer, to be described in terms of the radial and axial coordinates r and z measured from the stagnation point. The Reynolds number $\mathrm{Re} = U_s R/\nu_s$, based on the characteristic velocity U_s and kinematic viscosity ν_s of the spray-carrier gas, and the accompanying Reynolds number of the hotter air stream, are moderately large in typical applications. Under those conditions, the flow of the counterflowing streams is nearly inviscid and includes a potential region near the stagnation point where the gas

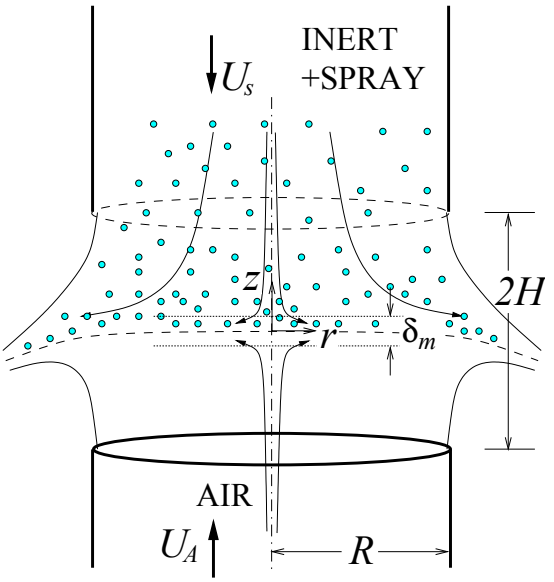

Figure 5.1. Schematic view of the typical experimental arrangement employed in experimental studies of counterflow spray flames.

velocity $\mathbf{v} = (u, v)$ is determined by the uniform strain rate found on each side of the stagnation plane. On the spray side the flow is given by

$$u = -A_s z \quad \text{and} \quad v = A_s r/2 \tag{5.1}$$

in terms of the spray-side strain rate A_s, a quantity of order U_s/R. The corresponding strain rate found on the air side is in general different, with a value $A_A = A_s\sqrt{\rho_s/\rho_A}$ dictated in terms of the inert-to-air density ratio by the condition of negligible pressure variation across the mixing layer. Because of the prevailing large-Reynolds-number flow, mixing between both streams occurs only in a thin layer around the separating surface, whose characteristic thickness is $\delta_m \sim (\nu_s/A_s)^{1/2} \sim R/\mathrm{Re}^{1/2} \ll R$. In the vicinity of the central stagnation point, the mixing layer exhibits a self-similar structure in terms of the strain rate A_s in which v/r and the other variables are a function of the distance z to the stagnation plane.

Typically in experiments the droplets are injected at a distance z_I from the stagnation plane much larger than the mixing-layer thickness. The initial temperatures of the droplets and of the inert gas are often sufficiently lower than the boiling temperature of the liquid fuel for droplet vaporization in the spray stream to be negligible. The description of the motion of the nonvaporizing

droplets in the nearly-inviscid inert stream is given below. Because of their diverging radial motion, only the droplets initially located near the axis, where $r \ll R$, eventually enter the self-similar region of the mixing-layer around the stagnation point.

As previously pointed out, two important parameters, dependent on the droplet size, govern the coupling between the liquid and gas phases in vaporizing sprays, namely, the Stokes number $\mathrm{St} = t_a A_s$, the ratio of the acceleration time $t_a = \frac{2}{9}(a^2/\nu)(\rho_l/\rho)$ and the strain time A_s^{-1}, and the ratio α of the liquid mass per unit volume to the mass of gas, defined in (2.2) for each droplet class (based on their radius at injection) [28]. The Stokes number, which for the counterflow is the ratio of the droplet acceleration time (which is of the order of its vaporization time) to the characteristic strain time A_s^{-1} of the counterflow mixing layer, measures the coupling of the droplets with the gas flow, whereas the ratio α/St measures the coupling of the gas phase with the droplets. As discussed in Section 3.5, in vaporizing sprays, effective two-way coupling occurs in the double distinguished limit $\mathrm{St} = O(1)$ and $\alpha = O(1)$, but the coupling is more pronounced in the presence of combustion, because small values of $\alpha \sim S^{-1} \ll 1$ are sufficient to generate flame temperatures several times larger than the spray feed temperatures, thereby affecting significantly the flow through the associated density differences.

The analysis focuses on values of the Stokes number of order unity and values of the liquid mass-loading ratio α of order S^{-1}. Since $\alpha \ll 1$, one-way coupling of the droplets in the spray stream is found, but strong two-way coupling in regions affected by the fuel-vapor combustion if the gas-phase reaction has been ignited. For these dilute sprays, the computation of the droplet motion downstream from the injection plane, given in the following section, reveals different behaviors depending on the value of St. For $\mathrm{St} < 1/4$, the droplets are seen to approach the stagnation plane with a vanishing transverse velocity, whereas for $\mathrm{St} > 1/4$ they cross the stagnation plane and move into the opposing air stream. These two behaviors lead to two distinct regimes of spray vaporization and combustion, which are analyzed separately below. For $\mathrm{St} < 1/4$, the droplets are trapped in the mixing layer, where droplet vaporization and gas-phase chemical reactions occur. For $\mathrm{St} > 1/4$, on the other hand, the droplets traverse the stagnation plane with a crossing velocity that is much larger than the transverse gas velocity in the mixing layer, penetrating large distances of the order of the initial injection distance into the counterflowing stream before they turn around. Droplet vaporization occurs in this case on the air side, with the inertial droplets distributing the fuel vapor over transverse distances much larger than the mixing-layer thickness.

Correspondingly, when this fuel vapor reacts with the oxygen of the air, the diffusion flame that forms stands away from the mixing layer, with a structure that is markedly different from that found for $\mathrm{St} < 1/4$.

5.3 Droplet dynamics in opposed-jet configurations

For the opposed-jet configuration, the computation of the inviscid flow in the outer streams involves the integration of the Euler equations for the gas phase coupled to the solution of the liquid phase, with the outer jet boundaries and the interface separating the two jets appearing as free surfaces to be obtained as part of the solution. The calculation is simplified for small values of the liquid mass-loading ratio α, such that there is one-way coupling of the droplets in the spray stream. Under these conditions, the gas velocity can be computed independently of the liquid phase, and then used to determine the droplet velocity $\mathbf{v}_d = (u_d, v_d)$ and associated droplet number density n of the droplets.

5.3.1 Computation of the gas flow in the nearly-inviscid region

The nearly inviscid flow found outside the mixing layer between the counterflowing streams and the jet-boundary shear layers with the outer stagnant gas depends on the values of the inter-nozzle separation H/R and of the inert-to-air density and velocity ratios ρ_s/ρ_A and U_s/U_A. The calculation can be carried out using the Navier-Stokes equations for large values of Re. Outside the mixing-layer and the jet-boundary shear layers, the solution evolves for $\mathrm{Re} \gg 1$ towards the inviscid unsteady solution. The integration provides in particular the distribution of gas velocity along the axis $u_a(z)$ and the associated near-axis radial velocity v_a, both components being related through the continuity equation according to $v_a = -(\mathrm{d}u_a/\mathrm{d}z)r/2$. This gas-velocity distribution $\mathbf{v} = (u_a, v_a)$ is to be used below in computing the near-axis droplet evolution.

Results of integrations of the axisymmetric Navier-Stokes equations are shown in Fig. 5.2 for the symmetric configuration $\rho_s/\rho_A = 1$ and $U_s/U_A = 1$, for which $u_a(z) = -u_a(-z)$. The computations consider a configuration with internozzle separation $H/R = 0.5$. The instantaneous isocontours of inert mass fraction shown in the upper plot mark the location of the jet-boundary shear layer, which becomes unstable as it evolves after the nozzle rim. These flow instabilities do not have a strong effect on the velocity distribution along the axis $u = u_a(z)$, which remains almost steady, as can be seen in the sample profiles shown in the intermediate plot for different values of the Reynolds number Re. The value of u_a evolves from $u_a = U_s$, assumed for z moderately

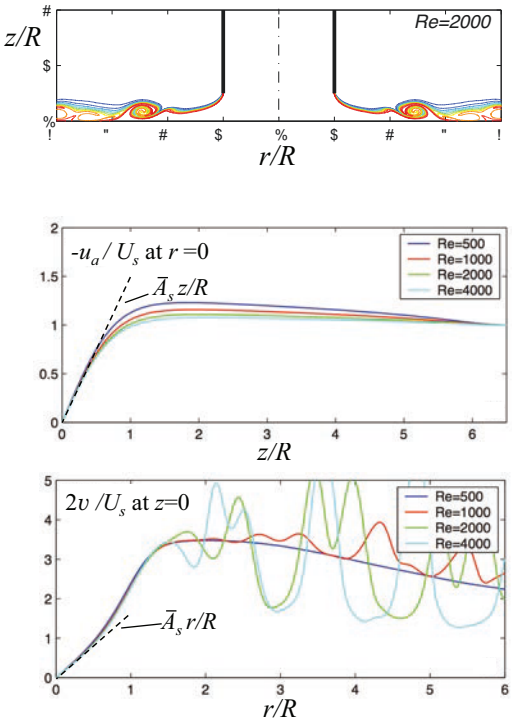

Figure 5.2. Results of integrations of the axisymmetric Navier-Stokes equations for $\rho_s/\rho_A = 1$, $U_s/U_A = 1$, $H/R = 0.5$ and different values of the Reynolds number $\mathrm{Re} = U_s R/\nu_s$. The color contours in the upper plot gives a snapshot of the distribution of inert mass fraction for $\mathrm{Re} = 2000$. The intermediate and lower plot show, respectively, the variations of the transverse velocity u with z/R along the axis and the variation of the radial velocity v with r in the stagnation plane for $\mathrm{Re} = (500, 1000, 2000, 4000)$. Figure courtesy of Dr. Jaime Carpio.

large compared with R, to approach the linear decay rate $u_a = -A_s z$ as $z \to 0$, where A_s is the stagnation-point strain rate. As can be seen, the growth of the boundary layer on the injector wall results in an initial acceleration of the near-axis flow, which is less pronounced for larger values of Re. The corresponding value of the strain rate A_s is seen to approach for $\mathrm{Re} \gg 1$ a constant value, given by $\bar{A}_s = A_s/(U_s/R) = 1.51$ for the particular case considered in Fig. 5.2.

As indicated in (5.1), the velocity near the stagnation point has the self-similar form $u = -A_s z$ and $v = A_s r/2$. This local description is tested in the intermediate and lower plots of Fig. 5.2, with the latter showing the instantaneous distributions of the radial velocity along the stagnation plane. As can be seen, although the flow instabilities cause the radial velocity to be unsteady at large radial distances, the solution remains steady, nearly unperturbed, in the

near-stagnation-point region. The integrations indicates that the linear variation of the axial and radial velocity components with the distance to the stagnation point applies in a fairly large region. For instance, for the case $H/R = 0.5$ considered in Fig. 5.2, equation (5.1) provides an accurate representation for the velocity field at distances to the stagnation point as large as half of the nozzle radius.

5.3.2 Droplet motion in the spray stream

To calculate the motion of the near-axis droplets, which ultimately determines the droplet velocity and droplet population outside the mixing layer, the gas-velocity distribution $\mathbf{v} = (u_a, v_a)$ previously computed is to be used to evaluate the drag force, which is assumed to be given by Stokes law $\mathbf{f} = 6\pi\mu_s a_o(\mathbf{v} - \mathbf{v}_d)$, where μ_s is the viscosity of the spray carrier gas and a_o is the initial droplet radius. The droplet axial velocity $u_d(z)$ is given by the solution of the autonomous system

$$\frac{\mathrm{d}u_d}{\mathrm{d}t} = \frac{u_a - u_d}{t_a}, \qquad \frac{\mathrm{d}z}{\mathrm{d}t} = u_d \tag{5.2}$$

with the near-axis initial conditions $u_d = u_I$ and $z = z_I$. Here, $t_a = \frac{2}{9}a_o^2\rho_l/\mu_s$ is the droplet acceleration time corresponding to the Stokes drag force, with ρ_l denoting the density of the liquid fuel. Introducing R and A_sR as length and velocity scales for z and u_d provides the alternative problem

$$\frac{\mathrm{d}\bar{u}_d}{\mathrm{d}\tau} = \frac{\bar{u}_a - \bar{u}_d}{\mathrm{St}}, \qquad \frac{\mathrm{d}\bar{z}}{\mathrm{d}\tau} = \bar{u}_d; \qquad \bar{u}_d(0) - \bar{u}_I = \bar{z}(0) - \bar{z}_I = 0 \tag{5.3}$$

for the axial velocity $\bar{u}_d = u_d/(A_sR)$, where $\bar{z} = z/R$ and $\tau = t/t_a$. The solution, involving the local stagnation-point Stokes number

$$\mathrm{St} = \frac{2}{9}A_s a_o^2\rho_l/\mu_s, \tag{5.4}$$

depends on the variation of the axial gas velocity $\bar{u}_a(\bar{z}) = u_a/(A_sR)$ and on the injection velocity and injection distance $\bar{u}_I = u_I/(A_sR)$ and $\bar{z}_I = z_I/R$. In the sample computations shown below the gas velocity is approximated by $\bar{u}_a = -\bar{A}_s^{-1}\mathrm{erf}[(\sqrt{\pi}/2)\bar{A}_s\bar{z}]$, with $\bar{A}_s = 1.51$, a convenient analytical representation of the results of the Navier-Stokes integrations shown in Fig. 5.2 for $\mathrm{Re} \gg 1$.

Figure 5.3 shows sample trajectories in the phase plane $(\bar{z}, -\bar{u}_d)$. Along the curve $\bar{u}_d = \bar{u}_a$, represented in blue color, the droplets experience a vanishing drag force and the associated trajectories correspondingly exhibit a zero slope,

as dictated by the first equation in (5.3). Qualitatively different behaviors appear depending on the form of the solution near the origin, which is a critical point of (5.3), with $\bar{u}_a = -\bar{z}$. The local solution there is of the form $\bar{z} = \bar{u}_d/\Lambda \propto \exp(\Lambda\tau)$, as determined by the roots

$$\Lambda^{\pm} = \frac{\pm\sqrt{1-4\mathrm{St}}-1}{2\mathrm{St}} \tag{5.5}$$

of the characteristic polynomial $\Lambda^2 + \Lambda/\mathrm{St} + 1/\mathrm{St}$. For $\mathrm{St} < 1/4$ both roots are real and negative, so that the origin of the phase plane is a stable node, while for $\mathrm{St} > 1/4$ both roots are complex and the origin is a stable spiral point. Both types of solutions are shown in Fig. 5.3 associated with the values $\mathrm{St} = 0.2$ (stable node) and $\mathrm{St} = 1.0$ (stable spiral).

The plot for $\mathrm{St} = 1.0$ in Fig. 5.3 is representative of the counterflow dynamics of large droplets with $\mathrm{St} > 1/4$, which are seen to reach the stagnation plane with a nonzero crossing velocity $\bar{u}_d$ of order unity. The trajectories are seen to spiral around the origin, indicating that nonvaporizing droplets with $\mathrm{St} > 1/4$ may undergo multiple stagnation-plane crossings, with velocities that depend on the injection conditions. Clearly, for nonsymmetric counterflow configurations with $\rho_s \neq \rho_A$, the gas velocity $\bar{u}_a$ used in (5.3) to compute $\bar{u}_d$ should be modified each time the droplet crosses the stagnation plane. The plot includes the separating trajectory that originates at $z/R \to \infty$ with $\bar{u}_d = \bar{u}_a$, corresponding to droplets injected far upstream with the local gas velocity. This trajectory shows a first intersection with the vertical axis $\bar{z} = 0$ at $-\bar{u}_d \simeq 0.3$, which is the maximum velocity with which droplets released with $u_I < u_a$ cross the stagnation plane for the first time.

The solution for $\mathrm{St} = 0.2$ includes as red curves the distinguished separating trajectories that originate at the critical point with slopes $\Lambda^{\pm}$. For injection conditions $(\bar{z}_I, -\bar{u}_I)$ that place the droplet initially below the upper separating trajectory, corresponding to droplets with initial injection velocities that are comparable to or smaller than the local gas velocity $\bar{u}_a$, the resulting droplet trajectory evolves to approach the origin of the phase plane along the critical trajectory associated with Λ^+, which acts as an attractor. These trajectories are associated with droplets that do not cross the stagnation plane. Instead they enter the mixing layer with a vanishing velocity

$$\bar{u}_d = \Lambda^+ \bar{z} = -\frac{1-\sqrt{1-4\mathrm{St}}}{2\mathrm{St}}\bar{z}. \tag{5.6}$$

This expression reduces to $\bar{u}_d = -\bar{z}$ for $\mathrm{St} \ll 1$, corresponding to tracing

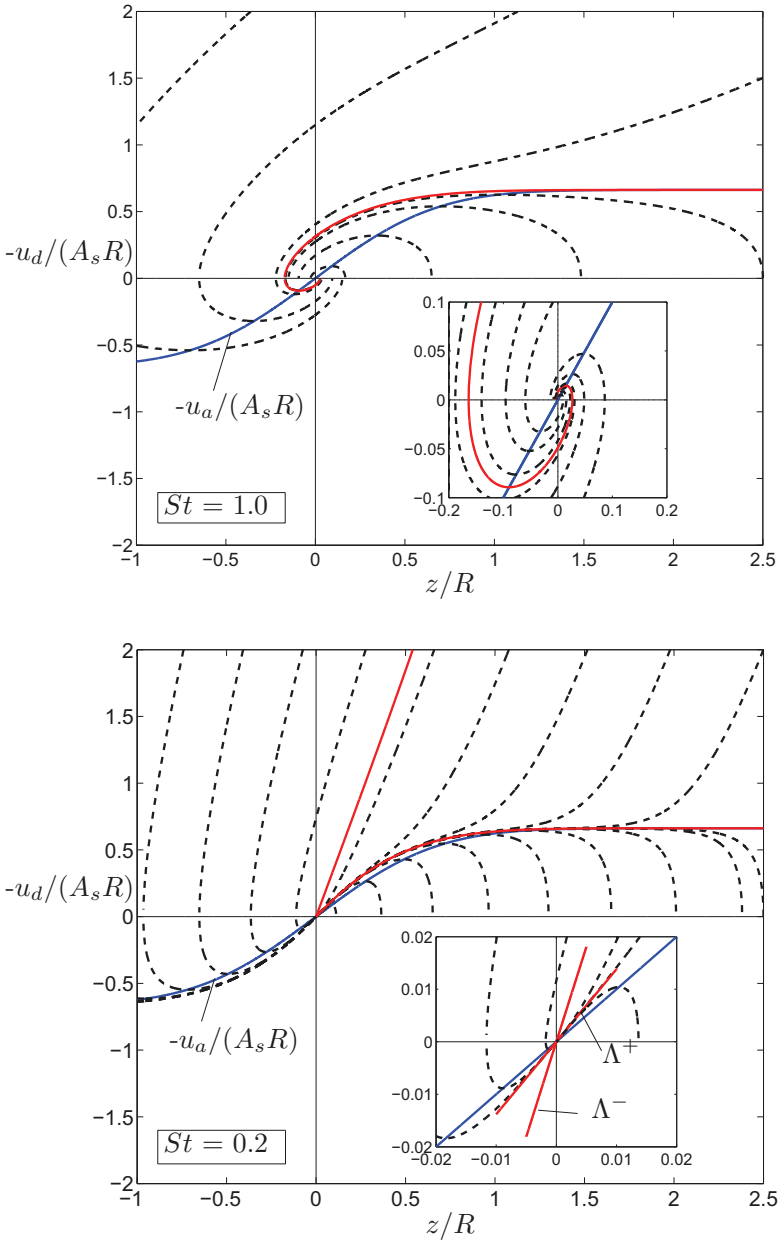

Figure 5.3. The phase plane $u_d - z$ obtained with the approximated gas velocity profile $\bar{u}_a = -\bar{A}_s^{-1}\mathrm{erf}[(\sqrt{\pi}/2)\bar{A}_s\bar{z}]$ by integration of (5.3) for $\mathrm{St} = 1.0$ (upper plot) and for $\mathrm{St} = 0.2$ (lower plot)

droplets with $u_d = u_a$. As seen in the plot, for small droplets with $\mathrm{St} < 1/4$ to cross the stagnation plane, their initial velocity at the injection point has to be much larger than the local gas velocity. As expected, since the upper separating trajectory becomes steeper for smaller values of the Stokes number (i.e., its initial slope becomes $\Lambda^- = \mathrm{St}^{-1}$ for $\mathrm{St} \ll 1$), the minimum injection velocity required to achieve droplet crossing becomes larger for smaller droplets. For most cases of practical interest, therefore, the simple criterion $\mathrm{St} < 1/4$ can be used to identify droplets that approach the stagnation plane with the linearly decreasing velocity (5.6), independent of the injection conditions, whereas for $\mathrm{St} > 1/4$ the droplets cross the stagnation plane with a crossing velocity of order $A_s R$, comparable to the injection velocity.

The droplet radial motion follows from integration of

$$\frac{\mathrm{d}v_d}{\mathrm{d}t} = \frac{v_a - v_d}{t_a}, \qquad \frac{\mathrm{d}r}{\mathrm{d}t} = v_d \tag{5.7}$$

with initial conditions $v_d = v_I$ and $r = r_I$. In the axisymmetric flow considered here, the droplet radial velocity near the axis is linearly proportional to the radial distance, and can be therefore represented in the form $v_d = A_d(z)r/2$, with initial distribution $v_I = A_I r/2$ at . Substituting this expression together with the near-axis velocity distribution $v_a = -(\mathrm{d}u_a/\mathrm{d}z)r/2$ into (5.7) and writing the problem in dimensionless form leads to

$$\bar{u}_d \frac{\mathrm{d}\bar{A}_d}{\mathrm{d}\bar{z}} = -\frac{1}{\mathrm{St}}\left(\frac{\mathrm{d}\bar{u}_a}{\mathrm{d}\bar{z}} + \bar{A}_d\right) - \frac{\bar{A}_d^2}{2}; \qquad \bar{A}_d = \bar{A}_I \text{ at } \bar{z} = \bar{z}_I, \tag{5.8}$$

after eliminating the time with use made of the second equation in (5.3). Here, $\bar{A}_d = A_d/A_s$ and $\bar{A}_I = A_I/A_s$. The integration determines the distribution of $\bar{A}_d(\bar{z})$ for the approaching droplets. For droplets crossing the stagnation plane, the integration gives a value of $\bar{A}_d(0)$ of order unity that depends on the initial injection conditions, whereas for droplets with $\mathrm{St} < 1/4$, whose axial velocity vanishes at the stagnation plane as dictated by (5.6), it is seen that

$$\bar{A}_d = \frac{\sqrt{2\mathrm{St} + 1} - 1}{\mathrm{St}} \tag{5.9}$$

as $\bar{z} \to 0$, as is required for the right-hand side of (5.8) to vanish as the stagnation plane is approached (note that $\mathrm{d}\bar{u}_a/\mathrm{d}\bar{z} = -1$ at $\bar{z} \ll 1$). As expected, for $\mathrm{St} \ll 1$ equation (5.9) simplifies to $\bar{A}_d = 1$, corresponding to droplets closely following the gas with radial velocity $v_d = v$.

The evolution of the droplet number density near the axis $n(z)$ from its

injection value n_I is determined by integrating the steady droplet conservation equation $\nabla \cdot (n\mathbf{v}_d) = 0$ written in the dimensionless form

$$\frac{\mathrm{d}}{\mathrm{d}\bar{z}}(\bar{n}\bar{u}_d) + \bar{n}\bar{A}_d = 0; \qquad \bar{n} = 1 \text{ at } \bar{z} = \bar{z}_I, \tag{5.10}$$

where $\bar{n} = n/n_I$, with $\bar{u}_d(\bar{z})$ and $\bar{A}_d(\bar{z})$ obtained from (5.3) and (5.8), respectively. Because of their slip motion, the droplets tend to accumulate, so that the value of $\bar{n}$ is always larger than unity for $\bar{z} < \bar{z}_I$. For $\mathrm{St} > 1/4$, the integration yields a finite value $\bar{n}(0) > 1$ as $\bar{z} \to 0$. By way of contrast, for $\mathrm{St} < 1/4$, the vanishing axial velocity (5.6) leads to a diverging droplet number density

$$\bar{n} = B\bar{z}^{-\mathcal{C}}, \tag{5.11}$$

as $\bar{z} \to 0$, where the exponent

$$\mathcal{C} = 1 - \frac{2[\sqrt{2\mathrm{St}+1}-1]}{1-\sqrt{1-4\mathrm{St}}} \tag{5.12}$$

can be easily determined by using in (5.10) the asymptotic droplet velocity distributions given in (5.6) and (5.9). The limiting values for this exponent are $\mathcal{C} \simeq \frac{3}{2}\mathrm{St}$ for $\mathrm{St} \ll 1$ and $\mathcal{C} = 3 - \sqrt{6} \simeq 0.55$ for $\mathrm{St} = 1/4$. The computation of the multiplying factor B in (5.11) requires integration of (5.10), giving a value of order unity that depends on the injection boundary conditions. According to the expression (5.11), the accumulation of droplets near the stagnation plane leads to large droplet densities n_m of order

$$n_m/n_I = B(R/\delta_m)^{\mathcal{C}} \sim \Re^{\mathcal{C}/2} \gg 1 \tag{5.13}$$

at distances z of the order of the mixing-layer thickness δ_m.

5.4 Spray vaporization and combustion in the mixing layer

The droplet velocity $\mathbf{v}_d = (u_d, v_d)$ and the droplet number density found near the stagnation plane outside the mixing layer are determined by the evolution of the near-axis droplets as they move from $z = z_I$ until they finally reach the stagnation plane $z = 0$. As shown above, for dilute sprays with small values of the liquid mass-loading ratio, the droplets with Stokes number $\mathrm{St} < 1/4$ approach the stagnation-point region with axial and radial velocity components

$$u_d = -\frac{1-\sqrt{1-4\mathrm{St}}}{2\mathrm{St}} A_s z \tag{5.14}$$

and

$$v_d = \frac{\sqrt{2\mathrm{St}+1}-1}{\mathrm{St}} A_s r/2, \tag{5.15}$$

both independent of the injection conditions. Because of their vanishing axial velocity, instead of crossing to the air side, these droplets remain in the mixing-layer region, corresponding to small axial distances z of the order of the mixing-layer thickness δ_m, where they vaporize when encountering the hot air.

The multi-continua formulation for spray vaporization and combustion in the counterflow mixing layer, the relevant regime for droplets with $\mathrm{St} < 1/4$, is given in this section. Attention is restricted to the near-stagnation-point region, where the flow has a self-similar structure determined by the strain rate A_s, in which the gas phase is described in terms of the radial and axial velocity components $v = A(z)r/2$ and $u(z)$, temperature and density $T(z)$ and $\rho(z)$, and mass fractions $Y_i(z)$. A polydisperse spray with N_c different droplet classes is considered. For each droplet class j, the continuum solution is given in terms of the droplet number density $n^j(z)$, droplet radial and axial velocity components $v_d^j = A_d^j(z)r/2$ and $u_d^j(z)$, and droplet radius $a^j(z)$ and temperature $T_d^j(z)$, the latter assumed to be uniform inside the droplet. The formulation, based on the conservation equations and interphase exchange rates, presented in Chapter 3, includes in the boundary conditions for the liquid phase the droplet velocity distributions given in (5.14) and (5.15) and the accompanying droplet number density given in (5.11), which hold at intermediate distances $\delta_m \ll z \ll R$. Together with the case of pure spray vaporization, specific consideration will be given below to the limit of infinitely fast reaction and its formulation in terms of coupling functions [28, 29].

5.4.1 Droplet submodels

The drag force $\mathbf{f}^j$ acting on the individual droplet of each class, its rate of vaporization $\dot{m}^j$, and heating rate $\dot{q}_d^j$, which depend in general on the droplet-gas slip motion, are evaluated below for the case of droplet Reynolds numbers small compared with unity, leading to the set of compact expressions (3.14) and (3.16)–(3.18). As discussed earlier, effects of near-droplet convection associated with the slip velocity introduce corrections to the exchange rates that, surprisingly, remain moderately small as the slip-flow Reynolds number increases to values of order unity, so that the given description provides sufficient accuracy under most conditions of interest. More complete droplet models, incorporating dependences on droplet Reynolds number as well as influences of additional effects not contemplated in the derivation given below are available [30] and

could be incorporated in the counterflow formulation.

5.4.2 Dimensionless formulation

The spray-side value of the strain rate A_s and the associated characteristic mixing-layer thickness $\delta_m = (D_{T_s}/A_s)^{1/2}$, where D_{T_s} is the thermal diffusivity of the unperturbed carrier gas, will be used as scales in defining the dimensionless variables $\tilde{z} = z/\delta_m$, $\tilde{A} = A/A_s$, $\tilde{u} = u/(A_s\delta_m)$, $\tilde{A}_d^j = A_d^j/A_s$, $\tilde{u}_d^j = u_d^j/(A_s\delta_m)$. Similarly, the unperturbed density ρ_s and temperature T_s of the carrier gas will be used to scale $\tilde{\rho} = \rho/\rho_s$, $\tilde{T} = T/T_s$, and $\tilde{T}_d^j = T_d^j/T_s$. The initial radius of each droplet class at the injection location a_I^j will be used to define the dimensionless value of the droplet radius $\tilde{a}^j = a^j/a_I^j$. The number of droplets per unit volume, has a characteristic value in the mixing layer n_m^j much larger than the value at the injection plane n_I^j according to $n_m^j/n_I^j = B(R/\delta_m)^{\mathcal{C}^j} \sim Re^{\mathcal{C}^j/2}$. Hence, to investigate the solution in the mixing layer, n_m^j is used to scale the number density according to $\tilde{n}^j = n^j/n_m^j$. For each droplet class, the droplet radius at injection a_I^j and the characteristic number density n_m^j will be seen to appear in the resulting formulation through the Stokes number $\mathrm{St}^j = \frac{2}{9}A_s(a_I^j)^2\rho_l/\mu_s$ and the liquid mass-loading ratio $\alpha^j = (4\pi/3)(a_I^j)^3(n_m^j)\rho_l/\rho_s$. For simplicity, the tilde denoting nondimensional quantities is removed in the remainder of the present chapter.

Given the gas-phase distributions of temperature and velocity, the evolution of each droplet class j requires integration of the equations following the droplet trajectories

$$u_d^j \frac{\mathrm{d}u_d^j}{\mathrm{d}z} = \frac{1}{\mathrm{St}^j}\frac{T^\sigma}{(a^j)^2}(u - u_d^j), \tag{5.16}$$

$$\frac{(A_d^j)^2}{2} + u_d^j \frac{\mathrm{d}A_d^j}{\mathrm{d}z} = \frac{1}{\mathrm{St}^j}\frac{T^\sigma}{(a^j)^2}(A - A_d^j), \tag{5.17}$$

$$u_d^j \frac{\mathrm{d}(a^j)^3}{\mathrm{d}z} = -\frac{2}{3\mathrm{Pr}\mathrm{St}^j} a^j T^\sigma \lambda^j, \tag{5.18}$$

$$u_d^j \frac{\mathrm{d}T_d^j}{\mathrm{d}z} = \frac{2c_p/c_l}{3\mathrm{Pr}\mathrm{St}^j}\frac{T^\sigma}{(a^j)^2}\left(\frac{T - T_d^j}{e^{\lambda^j} - 1} - \frac{L_v}{c_p T_s}\right)\lambda^j \tag{5.19}$$

$$\frac{\mathrm{d}}{\mathrm{d}z}(n^j u_d^j) + n^j A_d^j = 0 \tag{5.20}$$

supplemented with the expressions (3.17) and (3.18), needed to compute the dimensionless vaporization rate λ^j. For droplets with $\mathrm{St} < 1/4$, the initial conditions as $z \to \infty$, consistent with the solution found at intermediate distances

$\delta_m \ll z \ll R$, given in (5.11), (5.14), and (5.15), are

$$a^j - 1 = u_d^j + \frac{1-\sqrt{1-4\mathrm{St}^j}}{2\mathrm{St}^j} z = A_d^j - \frac{\sqrt{2\mathrm{St}^j+1}-1}{\mathrm{St}^j} = T_d^j - 1 = n^j - z^{-\mathcal{C}^j} = 0, \tag{5.21}$$

yielding a convenient description independent of the specific injection conditions. In writing (5.21), droplet vaporization prior to entering the mixing layer has been neglected along with differences of the droplet temperature from that of the carrier gas.

To complete the formulation using the nondimensional variables defined above, the gas-phase conservation equations are given, beginning with the continuity and radial momentum equations

$$\frac{\mathrm{d}}{\mathrm{d}z}(\rho u) + \rho A = \frac{2}{3\mathrm{Pr}} \sum_{j=1}^{N_c} \frac{\alpha^j}{\mathrm{St}^j} n^j a^j T^\sigma \lambda^j, \tag{5.22}$$

$$\begin{aligned} \frac{\rho A^2}{2} + \rho u \frac{\mathrm{d}A}{\mathrm{d}z} &= \frac{1}{2} + \mathrm{Pr} \frac{\mathrm{d}}{\mathrm{d}z}\left(T^\sigma \frac{\mathrm{d}A}{\mathrm{d}z}\right) \\ &+ \sum_{j=1}^{N_c} \frac{\alpha^j}{\mathrm{St}^j} n^j a^j T^\sigma (A_d^j - A)\left(1 + \frac{2}{3\mathrm{Pr}}\lambda^j\right). \end{aligned} \tag{5.23}$$

If the chemical reaction between the oxygen of the air and the fuel vapor is assumed to occur according to the global irreversible step $\mathrm{F} + s\mathrm{O}_2 \rightarrow (1+s)\mathrm{P} + q'$, then the equations for energy and reactants become

$$\begin{aligned} \frac{\mathrm{d}}{\mathrm{d}z}(\rho u T) + \rho A T &= \frac{\mathrm{d}}{\mathrm{d}z}\left(T^\sigma \frac{\mathrm{d}T}{\mathrm{d}z}\right) + \frac{q}{S}\left(\frac{S\omega_{\mathrm{F}}}{\rho_s A_s}\right) \\ &+ \frac{2}{3\mathrm{Pr}} \sum_{j=1}^{N_c} \frac{\alpha^j}{\mathrm{St}^j} n^j a^j T^\sigma \lambda^j \left(T_d^j - \frac{T - T_d^j}{e^{\lambda^j} - 1}\right), \end{aligned} \tag{5.24}$$

$$\begin{aligned} \frac{\mathrm{d}}{\mathrm{d}z}(\rho u Y_{\mathrm{F}}) + \rho A Y_{\mathrm{F}} &= \frac{1}{L_{\mathrm{F}}} \frac{\mathrm{d}}{\mathrm{d}z}\left(T^\sigma \frac{\mathrm{d}Y_{\mathrm{F}}}{\mathrm{d}z}\right) - \frac{1}{S}\left(\frac{S\omega_{\mathrm{F}}}{\rho_s A_s}\right) \\ &+ \frac{2}{3\mathrm{Pr}} \sum_{j=1}^{N_c} \frac{\alpha^j}{\mathrm{St}^j} n^j a^j T^\sigma \lambda^j, \end{aligned} \tag{5.25}$$

$$\frac{\mathrm{d}}{\mathrm{d}z}(\rho u \hat{Y}_{\mathrm{O}}) + \rho A \hat{Y}_{\mathrm{O}} = \frac{\mathrm{d}}{\mathrm{d}z}\left(T^\sigma \frac{\mathrm{d}\hat{Y}_{\mathrm{O}}}{\mathrm{d}z}\right) - \left(\frac{S\omega_{\mathrm{F}}}{\rho_s A_s}\right), \tag{5.26}$$

which naturally correspond to the dimensionless form of (3.22)–(3.24), with L_{F} and Pr denoting the Lewis number of the fuel vapor and the gas Prandtl number, the latter taken to be $\mathrm{Pr} = 0.7$ in the integrations. As in the previous

ignition analysis, a simple power-law $\propto T^{\sigma}$ with exponent $\sigma = 0.7$ has been assumed for the temperature dependence of the different transport coefficients.

The chemical-reaction terms appear written in (5.24)–(5.26) in terms of the dimensionless oxygen-consumption rate $(S\omega_{\mathrm{F}})/(\rho_s A_s)$, which introduces changes of order unity in $\hat{Y}_{\mathrm{O}}$, as can be inferred from (5.26). The same dimensionless factor is multiplied by q/S in (5.24), thereby introducing changes in the dimensionless temperature T of order q/S, and by S^{-1} in (5.25), generating changes in Y_{F} of order S^{-1}. This fuel mass fraction will be provided by the last term in (5.25) if α^j is of order S^{-1}, as it is in the distinguished regime $\alpha^j \sim S^{-1}$ considered below.

The above equations (5.22)–(5.26) are to be integrated with the boundary conditions

$$\begin{cases} u + z = A - 1 = T - 1 = Y_{\mathrm{F}} = \hat{Y}_{\mathrm{O}} = 0 & \text{as} \quad z \to +\infty \\ A - \sqrt{T_A} = T - T_A = Y_{\mathrm{F}} = \hat{Y}_{\mathrm{O}} - 1 = 0 & \text{as} \quad z \to -\infty. \end{cases} \tag{5.27}$$

Differences in molecular weight between the two feed streams have been neglected in writing the boundary condition for the strain rate on the air side, so that the value $A_A = A_s\sqrt{\rho_s/\rho_A}$ simplifies to $\sqrt{T_A}$ when expressed in dimensionless form. Note that an arbitrary zero displacement of the spray stream is assumed in writing the boundary condition $u + z = 0$ as $z \to +\infty$. The location $z = z_0$ of the stagnation plane, where $u = 0$, is obtained as part of the integration. The above equations must be supplemented with the equation of state written in the nondimensional form,

$$\rho T = [1 - Y_{\mathrm{F}}(1 - M_{\mathrm{N}_2}/M_{\mathrm{F}})]^{-1}. \tag{5.28}$$

To complete the formulation, an expression must be provided for the fuel-consumption rate ω_{F}. In this chapter, focused on the analysis of effects of droplet inertia on the resulting flow structure, the description will be limited to the two extreme cases of negligible and infinitely fast reaction rate, described by setting $\omega_{\mathrm{F}} = 0$ and $\omega_{\mathrm{F}} = \infty$ in (5.24)–(5.26).

5.4.3 Governing parameters

The dimensionless formulation given above serves to identify the parameters that control the structure of spray diffusion flames. Some of the parameters are related to the properties of the fuel, including its specific heat c_l and molecular mass M_{F}, which appear through the ratios c_p/c_l and $M_{\mathrm{N}_2}/M_{\mathrm{F}}$ in (5.19) and (5.28), respectively, the boiling temperature T_B, which enters in the Clasius-

Clapeyron relation (3.18), the latent heat of vaporization L_v, which appears in dimensionless form in (3.18) and (5.19) and the fuel Lewis number L_{F}, present in (3.17) and (5.25). The main thermochemical parameters involved in the chemical reaction, i.e., the mass S of air needed to burn the unit mass of fuel vapor and the dimensionless heat of reaction $q = q'/(c_p T_s)$, are also fuel dependent, although the differences are only small between fuels that share the same molecular structure, such as saturated hydrocarbons. For instance, for heptane and dodecane $S \simeq (15.2, 15)$ and $q' = (48.1, 44.56)$ kJ/g, giving a characteristic dimensionless temperature increase $q/S = q'/(Sc_pT_s) = (8.79, 8.24)$ when evaluated at the normal temperature $T_s = 300$ K with the average specific heat $c_p = 1200$ J/(kg K).

For each droplet class, the inertia of the droplets and the dilution of the spray are characterized by the Stokes number St^j and the liquid mass-loading ratio α^j given in (5.4) and (2.2), respectively. It is of interest that, since the characteristic times for droplet vaporization and droplet heating are comparable to the droplet acceleration time, the Stokes number St^j characterizes not only the coupling of the droplet motion with the gas flow in (5.16) and (5.17) but also their vaporization and heating, as can be seen in (5.18) and (5.19). As previously anticipated, α^j/St^j measures in (5.22)–(5.25) the coupling of the gas flow with the droplets. Since for all liquid fuels the mass of air S needed to burn the unit mass of fuel is always a large quantity, fairly small values of $\alpha \ll 1$ are sufficient to generate a robust spray flame. For these dilute conditions, the direct effects of droplet vaporization, heating, and acceleration on the gas motion are negligible, as can be inferred from observation of the droplet source terms in (5.22)–(5.25), although significant interphase coupling still exists associated with the strong exothermicity of the chemical reaction.

The boundary conditions (5.27) introduce only one additional parameter in the description, namely, the free-stream temperature ratio T_A. An attractive characteristic of the formulation given here for low-inertia sprays which burn in the mixing layer is that the boundary conditions for the liquid phase are independent of the injection conditions, whose effects are reflected mainly on α^j through the value of the apparent number density n_m^j.

5.4.4 The Burke-Schumann formulation of counterflow spray flames

The above formulation can be used to compute reacting sprays and also purely vaporizing sprays, the latter requiring the introduction of $\omega_{\mathrm{F}} = 0$ in (5.24)–(5.26). Reactive solutions depend on the competition of the chemical reaction rate with the transport rates of heat of species and also with the interphase

exchange rates. The solution can be simplified in the Burke-Schumann limit of infinitely fast reaction rate, when the chemical reaction is seen to occur in an infinitesimally thin flame located at $z = z_f$ separating a region for $z > z_f$ where $\hat{Y}_{\mathrm{O}} = 0$ from a region for $z < z_f$ where $Y_{\mathrm{F}} = 0$, whereas at the flame both reactant concentrations are simultaneously zero.

As indicated elsewhere [28, 29], to handle the Dirac-delta character of the reaction term associated with the limit of infinitely fast reaction one may follow the general procedure suggested by Shvab [31] and Zeldovich [32] for gaseous diffusion flames, appropriately extended to account for the nonunity Lewis number of the fuel vapor [33–35]. Thus, subtracting (5.26) from (5.25) times S leads to

$$\begin{aligned}\frac{\mathrm{d}}{\mathrm{d}z}[\rho u(SY_{\mathrm{F}} - \hat{Y}_{\mathrm{O}})] + \rho A(SY_{\mathrm{F}} - \hat{Y}_{\mathrm{O}}) \quad &= \\ \frac{\mathrm{d}}{\mathrm{d}z}\left[T^{\sigma}\frac{\mathrm{d}}{\mathrm{d}z}(SY_{\mathrm{F}}/L_{\mathrm{F}} - \hat{Y}_{\mathrm{O}})\right] \quad &+ \quad \frac{2S}{3\mathrm{Pr}}\sum_{j=1}^{N_c}\frac{\alpha^j}{\mathrm{St}^j}n^j a^j T^{\sigma}\lambda^j, \end{aligned} \tag{5.29}$$

which can be written in the alternative form

$$\frac{\mathrm{d}}{\mathrm{d}z}(\rho u Z) + \rho A Z = \frac{S/L_{\mathrm{F}} + 1}{S+1}\frac{\mathrm{d}}{\mathrm{d}z}\left(T^{\sigma}\frac{\mathrm{d}\tilde{Z}}{\mathrm{d}z}\right) + \frac{2}{3\mathrm{Pr}}\sum_{j=1}^{N}\frac{\alpha^j}{\mathrm{St}^j}n^j a^j T^{\sigma}\lambda^j, \tag{5.30}$$

involving a diffusion-weighted mixture-fraction variable

$$\tilde{Z} = \frac{SY_{\mathrm{F}}/L_{\mathrm{F}} - \hat{Y}_{\mathrm{O}} + 1}{S/L_{\mathrm{F}} + 1} \tag{5.31}$$

in addition to the classical mixture-fraction variable

$$Z = \frac{SY_{\mathrm{F}} - \hat{Y}_{\mathrm{O}} + 1}{S+1}. \tag{5.32}$$

A similar manipulation of (5.24) and (5.26) yields

$$\begin{aligned}\frac{\mathrm{d}}{\mathrm{d}\eta}\left[\rho u\left(T + q\hat{Y}_{\mathrm{O}}/S\right)\right] \quad &+ \quad \rho A\left(T + q\hat{Y}_{\mathrm{O}}/S\right) = \frac{\mathrm{d}}{\mathrm{d}\eta}\left[T^{\sigma}\frac{\mathrm{d}}{\mathrm{d}\eta}\left(T + q\hat{Y}_{\mathrm{O}}/S\right)\right] \\ &+ \quad \frac{2}{3\mathrm{Pr}}\frac{\alpha}{\mathrm{St}}naT^{\sigma}\lambda\left(T_d - \frac{T - T_d}{(e^{\lambda} - 1)}\right), \end{aligned} \tag{5.33}$$

which can be written in the form

$$\frac{\mathrm{d}}{\mathrm{d}z}(\rho u H)+\rho A H=\frac{\mathrm{d}}{\mathrm{d}z}\left(T^{\sigma}\frac{\mathrm{d}H}{\mathrm{d}z}\right)+\frac{2}{3\mathrm{Pr}}\sum_{j=1}^{N}\frac{\alpha^{j}}{\mathrm{St}^{j}}n^{j}a^{j}T^{\sigma}\lambda^{j}\left(H_{d}^{j}-\frac{1}{q/S}\frac{T-T_{d}^{j}}{e^{\lambda^{j}}-1}\right) \tag{5.34}$$

involving the excess enthalpy

$$H=\frac{T-T_{A}}{q/S}+\hat{Y}_{\mathrm{O}}-1. \tag{5.35}$$

In the sum over droplet classes, $H_{d}^{j}=(T_{d}^{j}-T_{A})/(q/S)-1$ represents the excess-enthalpy value for the vaporizing fuel vapor of each droplet class. In this case, since the Lewis number of oxygen is assumed to be unity, the coupling functions emerging in the diffusion and convective terms in (5.34) are identical, thereby simplifying the formulation. The boundary conditions for (5.30) and (5.34) are given by

$$Z-Z_{st}=\tilde{Z}-\tilde{Z}_{st}=0\quad\text{and}\quad H=(T_{s}-T_{A})/(q/S)-1\quad\text{as}\quad z\rightarrow\infty \tag{5.36}$$

$$Z-0=\tilde{Z}-0=0\quad\text{and}\quad H=0\quad\text{as}\quad z\rightarrow-\infty, \tag{5.37}$$

where $Z_{st}=1/(1+S)$ and $\tilde{Z}_{st}=1/(1+S/L_{\mathrm{F}})$.

In the description of the limit of infinitely fast reaction, the three conservation equations for the energy and the reactants (5.24)–(5.26) are replaced with the chemistry-free equations (5.30) and (5.34), together with the condition

$$Y_{\mathrm{F}}\hat{Y}_{\mathrm{O}}=0 \tag{5.38}$$

of non coexistence of the reactants. The flame is located where both the vapor fuel Y_{F} and the oxygen $\hat{Y}_{\mathrm{O}}$ are simultaneously zero, corresponding to values of the mixture fraction $Z=Z_{st}$ or $\tilde{Z}=\tilde{Z}_{st}$. For $Z\geq Z_{st}$ no oxidizer is found $\hat{Y}_{\mathrm{O}}=0$ and

$$Y_{\mathrm{F}}=\frac{Z-Z_{st}}{1-Z_{st}}=\frac{\tilde{Z}-\tilde{Z}_{st}}{1-\tilde{Z}_{st}}\quad\text{and}\quad T=T_{A}+\frac{q}{S}(H+1), \tag{5.39}$$

whereas for $Z\leq Z_{st}$, $Y_{\mathrm{F}}=0$ and

$$\hat{Y}_{\mathrm{O}}=1-\frac{Z}{Z_{st}}=1-\frac{\tilde{Z}}{\tilde{Z}_{st}}\quad\text{and}\quad T=T_{A}+\frac{q}{S}\left(H+\frac{Z}{Z_{st}}\right). \tag{5.40}$$

These relationships link the values of Z, $\tilde{Z}$, and H and provide the mass frac-

tions of reactants and the temperature in terms of the coupling functions across the mixing layer. If needed, source-free conservation equations that determine the product concentrations can be obtained from linear combinations accounting for non-unity Lewis numbers of CO_2 and H_2O [29].

5.4.5 Sample numerical results

The above formulation can be used to investigate different aspects of strained spray diffusion flames for the two limiting regimes of zero and infinitely fast reaction rates. In the sample integrations shown below, the values $c_p/c_l = 0.543$, $M_{\mathrm{N}_2}/M_{\mathrm{F}} = 0.165$, $L_{\mathrm{F}} = 2.62$, $L_v/(c_p T_s) = 1.005$, $T_B/T_s = 1.63$, and $q = 123.6$ are employed, as corresponds to dodecane with $T_s = 300$ K and with a constant mean value $c_p = 1200$ J/(kg K) assumed for the specific heat of the gas mixture. Also, since the air is often preheated in fuel-spray applications, an elevated air-to-inert temperature ratio $T_A = 2$ is considered.

Solutions corresponding to chemically frozen flow, obtained by removing the chemical source terms in (5.24)–(5.26), are investigated first. Sample profiles obtained for a monodisperse dodecane spray with $\alpha = 0.2$ and $\mathrm{St} = 0.2$ are shown in Fig. 5.4, where the axial distance is measured with respect to the stagnation plane, which was found to lie at $z_0 = -0.69$. Due to their inertia, the droplets are seen to accumulate, as can be seen in the profile of n. The droplet radius remains constant until the surrounding gas temperature increases to values sufficiently close to the boiling temperature as the droplets approach the stagnation plane. The large residence time associated with the limited axial velocities found as the droplets approach $z = z_0$ facilitates droplet vaporization, so that the radius a is seen to decrease rapidly across a thin vaporization region adjacent to the stagnation plane. Rapid droplet vaporization generates fuel vapor that accumulates near $z = z_0$ and then diffuses to both sides of the mixing layer, mixing with the oxygen of the air.

The limit of infinitely fast reaction is considered in Fig. 5.5, with all parameters being identical to those of Fig. 5.4. The computation makes use of (5.30) and (5.34) as a replacement for (5.24)–(5.26). The profiles of Z, $\tilde{Z}$, and H, scaled with their characteristic values $Z \sim \tilde{Z} \sim \alpha$ and $H \sim q/S$, are given in the lower plot, and the associated profiles of Y_{F}, $\hat{Y}_{\mathrm{O}}$, and T, calculated from (5.39) and (5.40), are shown in the upper plot, along with the profiles of u, u_d, a, and n. As can be seen, in the fast-reaction limit the gradients of temperature and mass fractions have jumps at the flame sheet, while the gradients of $\tilde{Z}$ and H are continuous. The gradient of the classical mixture fraction Z also jumps at the flame, as corresponds to a localized chemical source.

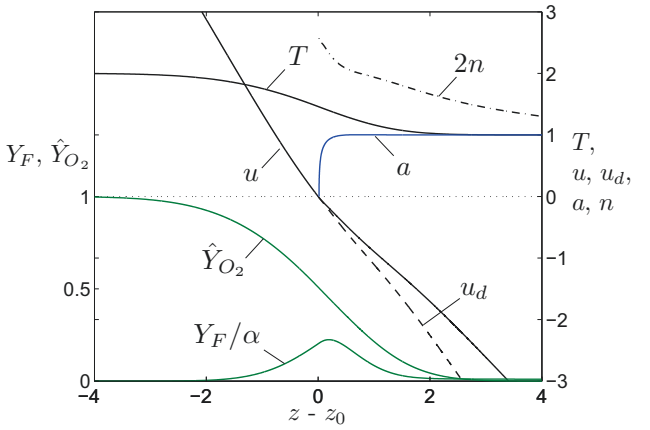

Figure 5.4. Structure of a vaporizing monodisperse dodecane spray in a counterflow mixing layer for [illegible]

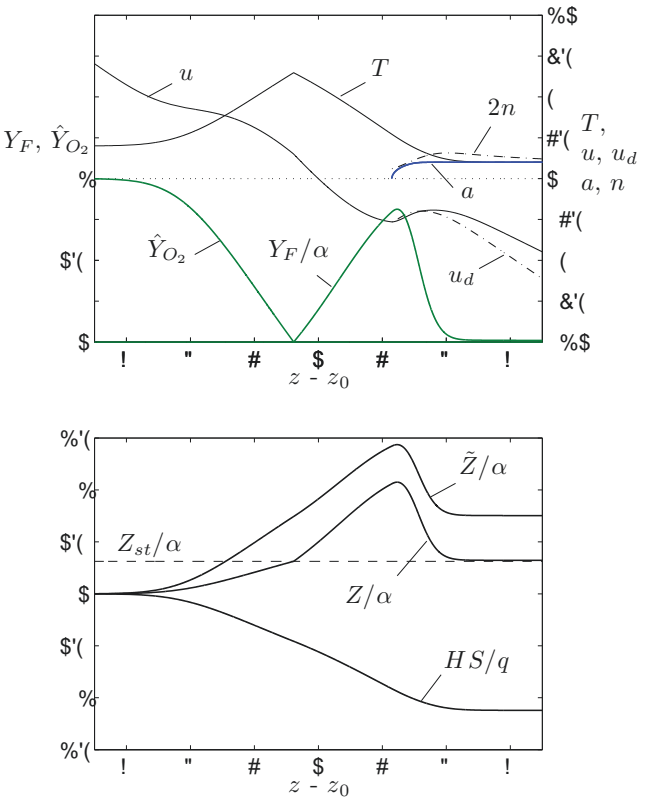

Figure 5.5. Structure of a monodisperse dodecane spray flame in a counterflow mixing layer for $\alpha = 0.2$ and $\mathrm{St} = 0.2$.

The comparison of Figs. 5.4 and 5.5 clearly shows how thermal expansion modifies significantly the velocity field in the presence of combustion, as can be seen by observation of the profile of axial velocity. As a result, the stagnation plane, located at $z_0 = -0.69$ for chemically frozen flow, is displaced to $z_0 = -2.75$ for infinitely fast reaction. The droplet behavior is also different when a spray diffusion flame is present, because the temperature increase associated with the chemical heat release enhances droplet vaporization, with the result that the droplets disappear far from the stagnation plane, at a relatively thin vaporization layer where the fuel vapor is seen to accumulate, with associated peak characteristic mass fractions $Y_{\mathrm{F}} \sim \alpha$ that are moderately small for the dilute sprays $\alpha \sim S^{-1} \ll 1$ considered here. The fuel vapor diffuses both upstream, against the incoming flow, and also downstream, to reach the diffusion flame and react with the oxygen of the air, arriving there by diffusion, with fluxes in stoichiometric proportions. Since $\alpha \sim S^{-1}$, the gradients of $\hat{Y}_{\mathrm{O}}$ and Y_{F}/α must take up comparable values at the flame. This is achieved when the flame sits not far from the stagnation plane, as shown in Fig. 5.5. For larger values of α, the flame tends to move into the air side of the mixing layer.

To enable the assessment of preferential diffusion effects, Fig. 5.6 exhibits the results obtained when the fuel-vapor Lewis number is set equal to unity in the integrations. Changing the fuel-vapor diffusivity modifies its transport rate across the mixing layer and also the solution for the local fuel-vapor profile in the vaporization region around the droplets. The latter modification has an impact on the spray flow through the perturbed droplet vaporization rate, as can be seen in (3.17), with λ being proportional to the reciprocal of L_{F}. The two separate phenomena have counteracting effects on the amount of fuel vapor present in the vaporization region. Thus, decreasing the Lewis number from $L_{\mathrm{F}} = 2.62$ to $L_{\mathrm{F}} = 1$ is expected to increase directly the production rate of fuel vapor as dictated by (3.17), and therefore the associated local value of Y_{F}. However, a smaller Lewis number promotes also the rate of fuel-vapor diffusion from the vaporization region, thereby decreasing the resulting peak value of Y_{F} there. As can be seen, both effects are approximately in balance for the case considered in Fig. 5.6, with the result that the peak value of Y_{F} is almost the same for both computations. The larger diffusivity of the fuel vapor for $L_{\mathrm{F}} = 1$ results in an increased transport rate from the vaporization region, leading to a wider Y_{F} profile and to a diffusion flame that lies farther into the air stream.

The local balance between the rate of heat loss from, and the rate of fuel diffusion into, the reaction sheet determines largely the peak temperature achieved at the flame. A decrease in L_{F} results in a reduction of the rate of

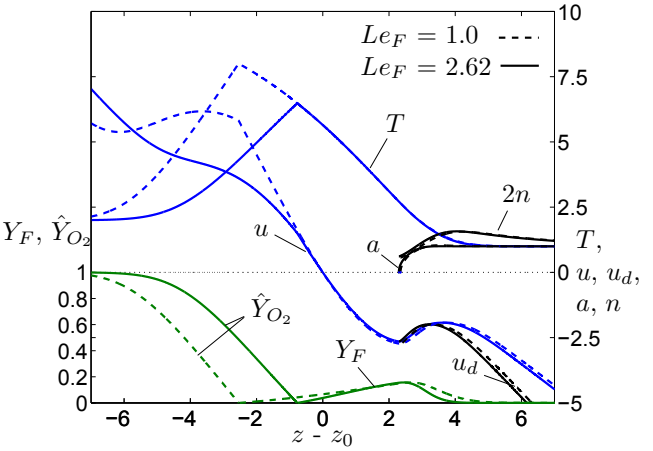

Figure 5.6. Structure of a monodisperse dodecane spray flame in a counterflow mixing layer for $\alpha = 0.2$ and $\mathrm{St} = 0.2$; besides the results obtained with the Lewis number of dodecane (i.e., $L_{\mathrm{F}} = 2.62$), shown in solid curves, the figure represents in dashed curves results obtained by setting the fuel Lewis number equal to unity. The black curves represent the liquid-phase properties a, n, and u_d in the region where droplets exist.

heat loss relative to that of fuel diffusion, and therefore causes an increase of the flame temperature, a well-known differential-diffusion effect observed for instance in hydrogen combustion [36]. This reasoning, based on the local molecular-transport balance at the flame, explains the results shown in Fig. 5.6, where the peak temperature found for $L_{\mathrm{F}} = 1$ is considerably larger than that corresponding to the heptane diffusivity.

5.5 Air-side vaporization and combustion of inertial sprays

The evolution of the droplets downstream from their injection location in high-Reynolds-number opposed-jet configurations, investigated above, indicates that, when the Stokes number is sufficiently large (i.e., $\mathrm{St} > 1/4$ for dilute sprays of nonvaporizing droplets), the droplets cross the stagnation plane to reach values of z of order z_I into the opposing air stream. The vaporization of the droplets and the reaction of the resulting fuel vapor with the oxygen of the air occur mainly, after crossing the mixing layer, in the air stream, without significant diffusion effects. The description will be simplified by considering that droplet injection occurs in the near-stagnation-point region, i.e., at distances z_I much larger than δ_m for the Reynolds number $(z_I/\delta_m)^2$ to be large, but small enough compared with R for the gas-phase solution (5.1) to apply. The

resulting formulation, which employes the length and velocity scales z_I and $A_s z_I$ associated with the injection distance, is delineated below and used to generate some illustrative results for the limiting cases of purely vaporizing sprays and infinitely fast reaction.

5.5.1 Conservation equations and boundary conditions

For the analysis, the conservation equations for the liquid and gas phases, given in (5.16)–(5.20) and in (5.22)–(5.26), respectively, must be rewritten by introducing the rescaled transverse coordinate z/z_I along with the rescaled variables $u/(A_s z_I)$, $u_d^j/(A_s z_I)$, and n^j/n_I^j, while the remaining nondimensional variables are those employed earlier in the mixing-layer analysis, i.e., A/A_s, A_d^j/A_s, T/T_s, ρ/ρ_s, a^j/a_I^j, and T_d^j/T_s. The resulting equations for the liquid phase can be seen to be equal to (5.16)–(5.20), but the boundary conditions (5.21) used in the mixing-layer analysis must be replaced now by

$$a^j - 1 = u_d^j + u_I^j/(A_s z_I) = A_d^j - A_I^j/A_s = T_d^j - T_I^j/T_s = n^j - 1 = 0 \quad \text{at} \quad z/z_I = 1, \tag{5.41}$$

involving the nondimensional injection velocity components $u_I^j/(A_s z_I)$ and A_I^j/A_s and the nondimensional injection temperature T_I^j/T_s.

Since the scales for the problem are based on the injection distance z_I, in the nondimensional equations for the gas flow the Reynolds number $(z_I/\delta_m)^2$ appears dividing the molecular transport terms in (5.23)–(5.26) (and also in equations (5.30) and (5.34) for the coupling functions of the fast-reaction limit). In the limit $z_I \gg \delta_m$, therefore, the equations reduce to the Euler equations. The integration for the spray side $z > 0$ must employ as boundary conditions $u = 0$ at $z = 0$ and $A - 1 = T - 1 = Y_{\mathrm{F}} = \hat{Y}_{\mathrm{O}} = 0$ as $z \to \infty$; whereas for $z < 0$ imposing $u = 0$ at $z = 0$ and $A - \sqrt{T_A} = T - T_A = Y_{\mathrm{F}} = \hat{Y}_{\mathrm{O}} - 1 = 0$ as $z \to -\infty$. The solution must allow for a discontinuity at the stagnation plane $z = 0$, with order-unity jumps in temperature, strain rate, and composition that are smoothed across the thin mixing layer, which is not described in the simplified diffusionless analysis given here.

The numerical computation with the multicontinua formulation requires the coupled solution of the gas and liquid phases in an iterative scheme that may start by solving the Euler form of the gas-phase equations (5.22)–(5.26) in the two separate domains $z > 0$ and $z < 0$, with an adequate starting guess used for the droplet properties. The resulting profiles of velocity, temperature, and reactant mass fractions are next used in computing for each droplet class the distributions of a, T_d, u_d, A_d, and n by integrating (5.16)–(5.20) from $z = z_I$.

The procedure is followed iteratively until convergence is achieved.

For dilute sprays with small values of the liquid mass-loading ratio α (now defined in terms of the droplet number density at injection n_I) of order $\alpha \sim S^{-1}$, there exists one-way coupling of the droplets with the gas flow in the spray stream $z > 0$, where only small departures in the gas are found, of order α, from the unperturbed properties $u + z/z_I = A - 1 = T - 1 = Y_{\text{F}} = \hat{Y}_{\text{O}} = 0$. For these dilute sprays, strong two-way coupling may appear on the air side if combustion occurs there. If the spray-carrier temperature T_s and the droplet injection temperature T_I are sufficiently smaller than the boiling temperature T_B for the condition $(T_B - T_d^j)/T_B \gg [L_v/(R_{\text{F}} T_B)]^{-1}$ to hold everywhere on the spray side of the counterflow, then droplet vaporization is entirely negligible on the spray stream. That is the case considered in the sample computations in Figs. 5.7 and 5.8 (to be discussed later), which correspond to dodecane sprays injected at normal atmospheric temperature.

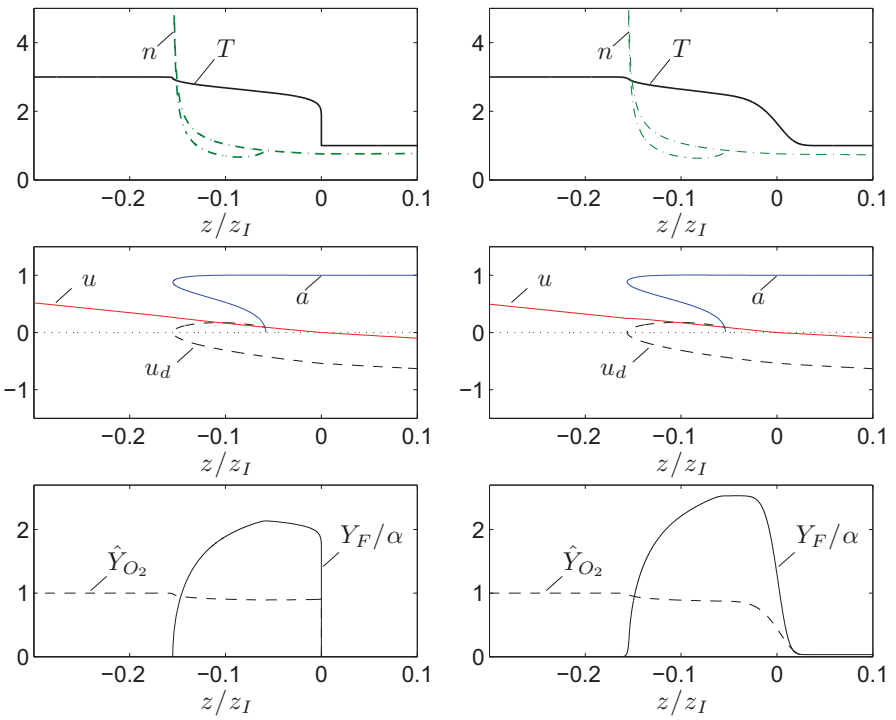

Figure 5.7. Structure of a vaporizing dodecane spray in a counterflow for $\alpha = 0.05$ and $\text{St} = 1.0$ with $u_I/(A_s z_I) = -1$, $A_I/A_s = 1$, $T_I/T_s = 1$, and $T_A/T_s = 3$; the profiles in the left-hand-side panel correspond to diffusionless results for $(z_I/\delta_m)^2 \gg 1$, whereas the right-hand-side plots are obtained with the complete equations of the mixing-layer formulation for $z_I/\delta_m = 85$.

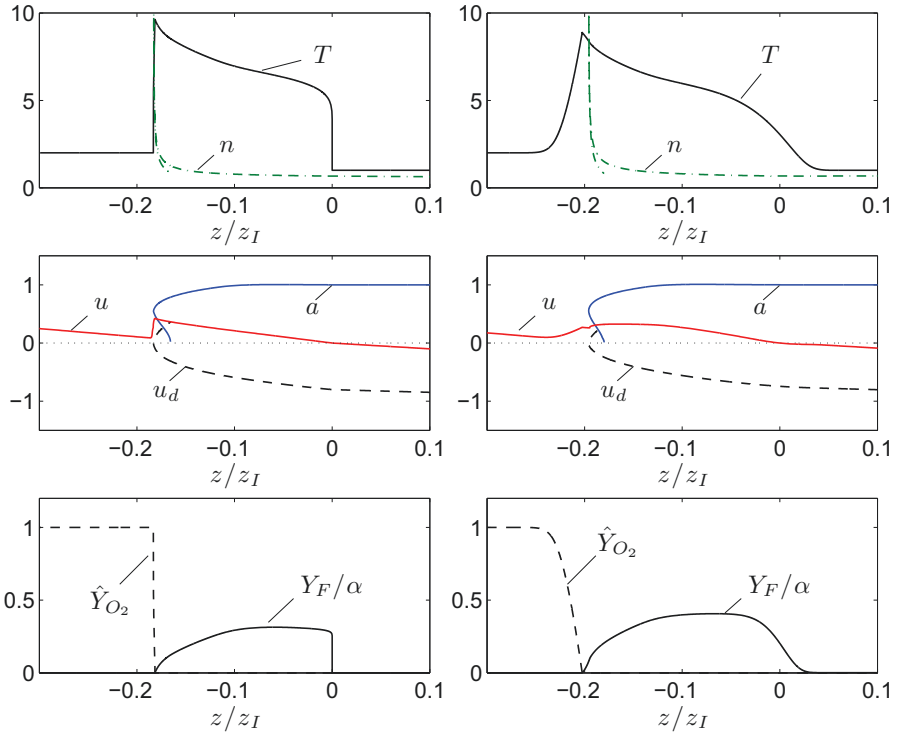

Figure 5.8. Structure of a dodecane spray flame in a counterflow for $\alpha = 0.05$ and $\mathrm{St} = 2.0$ with $u_I/(A_s z_I) = -1$, $A_I/A_s = 1$, $T_I/T_s = 1$, and $T_A/T_s = 2$; the profiles in the left-hand-side panel correspond to diffusionless results for $(z_I/\delta_m)^2 \gg 1$, whereas the right-hand-side plots are obtained with the complete equations of the mixing-layer formulation for $z_I/\delta_m = 85$.

5.5.2 Treatment of reversing droplets

For $\mathrm{St} > 1/4$, the droplets are seen to cross the stagnation plane and penetrate into the air side, a characteristic of sprays in counterflows noted in early work [5, 20]. In the presence of reverse droplet motion the solution for a given droplet class is no longer uniquely defined in terms of the distance to the stagnation plane, because it is possible to find advancing droplets and returning droplets at the same location z but with different values of a, T_d, u_d, and A_d. In the Eulerian description of the droplet dynamics, which is convenient for the self-similar analysis of the spray counterflow, this can be accounted for in the integrations, as proposed in [23], by introducing different "sheets of solutions" or, equivalently, by considering the advancing and returning droplets as belonging to different classes; so that an additional independent droplet class is added to the description when the droplets reverse their motion.

The implementation of the integration procedure for the turning droplets must account for the local description of the flow near the turning plane $z = z_t$, where $u_d^j = 0$. There, the integration of the advancing droplets provides nonzero finite values of $a^j = a_t^j$, $A_d^j = A_{d_t}^j$, and $T_d^j = T_{d_t}^j$. On the other hand, the local axial-velocity distribution

$$u_d^j = \mp \left(\frac{2T_t^\sigma u_t}{\mathrm{St}(a_t^j)^2} \right)^{1/2} (z - z_t)^{1/2}, \tag{5.42}$$

obtained from (5.16) in terms of the local values, at $z = z_t$, of the gas temperature T_t and gas velocity u_t (with the minus and plus signs corresponding to advancing and returning droplets, respectively), can be used in (5.20) to show that the droplet number density diverges at the turning plane in the form

$$n^j = C(z - z_t)^{-1/2}, \tag{5.43}$$

where the constant C is determined numerically. To avoid the existence of multivalued functions within a given droplet class, the droplets that have turned are assigned to a newly created droplet class, whose radius, velocity and temperature are determined by integrating (5.16)–(5.19) for increasing z with initial conditions $a^j = a_t^j$, $A_d^j = A_{d_t}^j$, $u_d^j = 0$, and $T_d^j = T_{d_t}^j$ at $z = z_t$, while the associated number of droplets is obtained from (5.20) with a boundary value $n^j = C(z - z_t)^{-1/2}$ evaluated near $z = z_t$.

5.5.3 Sample numerical results

The formulation delineated above was used to compute the diffusionless counterflow structure corresponding to a dodecane monodisperse spray with $\alpha = 0.05$, with results given in the left-hand-side panels of Figs. 5.7 and 5.8 for pure vaporization and infinitely fast reaction, respectively (the right-hand-side panels are to be discussed later). In the integrations, the thermochemical properties are those indicated earlier in Sec. 5.4.5 and the droplets are assumed to be injected with the local velocity and temperature of the gas flow.

The profiles given in Fig. 5.7 indicate that droplet vaporization is confined to the hot air side. Because of their significant inertia, the droplets cross the stagnation plane with a finite velocity, turning around at $z_t/z_I \simeq -0.156$. Droplet vaporization occurs at intermediate distances $-0.156 < z/z_I < 0$, resulting in a fuel mass fraction that peaks at an intermediate location $z/z_I = -0.05$. The accumulation of the droplets near the turning plane is visible in the profiles of droplet number density n. As can be inferred from the convection-vaporization

balance in (5.25), the local singularity (5.43) results in a fuel-vapor profile that increases rapidly from the turning point according to $Y_{\text{F}} \propto (z - z_t)^{1/2}$. Also of interest is that the returning droplets, whose radius decrease significantly after spending time on the hot side of the counterflow, disappear in this case before reaching the mixing layer. For larger values of the Stokes number, the droplets may have sufficient inertia to either cross the stagnation plane into the spray side of the counterflow, where they would undergo a second turning, or may approach the stagnation plane with a vanishing velocity and be trapped in the mixing layer, where they can continue to evolve.

Results corresponding to infinitely fast reaction are shown in Fig. 5.8. Because of the higher temperature associated with the chemical heat release, vaporization is more pronounced in this case, with the droplets disappearing soon after turning around at $z_t/z_I \simeq -0.183$. Since the mixture fraction begins to increase from the value $Z = 0$ only after the air stream meets the droplets at the turning point z_t, the flame surface $Z = Z_{st}$ is always at a location $z_f > z_t$, intermediate between the turning point and the stagnation plane, indicating that, in the diffusionless limit, the droplets necessarily cross the flame. Because of the rapid vaporization rate associated with the accumulation of the droplets at the turning point, the mixture fraction increases there according to $Z \propto (z - z_t)^{1/2}$. Since the value of Z_{st} is moderately small, the resulting diffusion flame appears very close to the turning point, i.e., at $z_f/z_I = -0.181$ in the computations of Fig. 5.8. Clearly, the flame would stand farther from the turning point in configurations with larger values of Z_{st}. Part of the heat released at the flame sheet by the chemical reaction is employed to vaporize the droplets, which explains the sharp decrease of the temperature profile on the fuel side of the flame.

Besides results of diffusionless computations, the figures also include, in the right-hand-side panels, results corresponding to a moderately large value of the Reynolds number $(z_I/\delta_m)^2$, computed by retaining in the gas-phase conservation equations the molecular transport terms, which are proportional to $(z_I/\delta_m)^{-2}$. The integrations use the boundary conditions (5.27). The diffusionless limit is seen to reproduce adequately the large-Reynolds-number results, with significant departures appearing mainly around the stagnation plane, where the jumps in temperature and composition predicted by the diffusionless approximation are smoothed out in the presence of diffusion. Molecular transport also has a noticeable effect on the profiles of temperature and oxygen on the air side of the flame sheet in Fig. 5.8, resulting in less pronounced gradients, to be taken into account when evaluating the flame-extinction conditions. Also of interest is that, unlike the diffusionless solution shown in the left-hand-side

panel, the droplets do not cross the flame in the finite-Reynolds-number computations of Fig. 5.8, where the flame stands to the left of, although very close to, the turning point. Outside the layers of rapid change mentioned above, the differences between corresponding profiles in the side-by-side panels of Figs. 5.7 and 5.8 are relatively small, with somewhat larger departures observed in the profiles of fuel-vapor mass fraction shown in Fig. 5.7, that being a result of the modified spray vaporization rate found in the mixing layer.

The sample computations given here serve to illustrate the structure of the resulting flow in this regime of air-side vaporization and combustion. The formulation should be exploited in future efforts to analyze the parametric dependence of the solution. The rapid transition regions identified also deserve specific attention. An example is the region, identified in the diffusionless computations, between the turning plane and the diffusion flame, corresponding in the left-hand-side panel Fig. 5.8 to the small intermediate range $-0.183 < z/z_I < -0.181$, where a large amount of droplets vaporizing in the presence of oxygen is found. This region has been described here in the limit of infinitely fast reaction, so that $Y_{\rm F} = 0$ there. Finite-rate effects would be needed in general for a more detailed description. Near the flame, the existing large temperature is expected to favor the rapid burning on the resulting fuel vapor in a distributed manner (or in flames enclosing the individual droplets, if their radii are large enough). Near the turning point, however, the temperature is close to that of the unperturbed air stream, and the fuel vapor would mix with the air, creating a reactant mixture that could burn in a premixed flame, upstream from the diffusion flame described here. Clearly, this and other aspects of the flow should be addressed to provide a more complete understanding of counterflow spray diffusion flames

5.6 Conclusions

We have given a compact formulation for the computation of vaporization and combustion of dilute inertial polydisperse sprays in high Reynolds number opposed-jet configurations, with attention focused on the self-similar region found near the stagnation plane. While the previous authors were concerned with formulations of the counterflow spray problem accounting simultaneously for detailed transport, thermochemistry, and chemical-kinetic descriptions together with advanced comprehensive models for the interphase exchange rates (see, for instance, [23]), we have used instead a simplified description based on a one-step fast-reaction model. Our approach allows us to identify the main scales and the key dimensionless parameters of the problem, based on these scales,

which are shown to exhibit in practical applications disparate values. We can thus identify distinguished regimes involving different physical phenomena. This methodology facilitates the derivation of simplified mathematical formulations, which readily enable parametric dependences to be investigated, and also the identification of distinguished behaviors, often obscured in numerical integrations accounting simultaneously for multiple physical phenomena.

The canonical formulations given for the two different regimes identified here, including their solution in the extreme limits of negligible and infinitely fast chemical reaction, can be used to investigate influences of spray dilution and droplet inertia on the flame structure. The formulation presented here, including the effects of nonunity Lewis numbers of the fuel vapor on the flame temperature and on the value of the scalar dissipation at the flame that determines the flame extinction, can be useful to generate valuable knowledge for flamelet modeling of turbulent spray reacting flows. It will be used in the next chapter to address diffusion-flame extinction.

References

[1] N. Peters, Turbulent combustion, Cambridge university press, 2000.

[2] W. A. Sirignano, Fluid dynamics and transport of droplets and sprays, 2nd edition, Cambridge University Press, Cambridge, UK., 2010.

[3] G. Corcos, F. Sherman, Vorticity concentration and the dynamics of unstable free shear layers, Journal of Fluid Mechanics 73 (02) (1976) 241–264.

[4] C. Edwards, R. Rudoff, Structure of a swirl-stabilized spray flame by imaging, laser doppler velocimetry, and phase doppler anemometry, in: Symposium (International) on Combustion, Vol. 23, Elsevier, 1991, pp. 1353–1359.

[5] I. K. Puri, P. A. Libby, Droplet behavior in counterflowing streams, Combustion science and technology 66 (4-6) (1989) 267–292.

[6] S. C. Li, P. A. Libby, F. A. Williams, Spray structure in counterflowing streams with and without a flame, Combustion and flame 94 (1) (1993) 161–177.

[7] S. C. Li, Spray stagnation flames, Progress in energy and combustion science 23 (4) (1997) 303–347.

[8] S. C. Li, F. A. Williams, Counterflow heptane flame structure, Proceedings of the Combustion Institute 28 (1) (2000) 1031–1038.

[9] G. Chen, A. Gomez, Counterflow diffusion flames of quasi-monodisperse electrostatic sprays, in: Symposium (international) on combustion, Vol. 24, Elsevier, 1992, pp. 1531–1539.

[10] M. Massot, M. Kumar, M. Smooke, A. Gomez, Spray counterflow diffusion flames of heptane: experiments and computations with detailed kinetics and transport, Proc. Combust. Inst. 27 (1998) 1975–1983.

[11] L. Gao, Y. D'Angelo, I. Silverman, A. Gome, M. Smooke, Quantitative comparison of detailed numerical computations and experiments in counterflow spray diffusion flames, in: Symposium (International) on Combustion, Vol. 26, Elsevier, 1996, pp. 1739–1746.

[12] V. S. Santoro, D. C. Kyritsis, A. Gomez, An experimental study of vortex-flame interaction in counterflow spray diffusion flames, Proceedings of the Combustion Institute 28 (1) (2000) 1023–1030.

[13] V. S. Santoro, A. Gomez, Extinction and reignition in counterflow spray diffusion flames interacting with laminar vortices, Proceedings of the Combustion Institute 29 (1) (2002) 585–592.

[14] G. Continillo, W. A. Sirignano, Counterflow spray combustion modeling, Combustion and Flame 81 (3) (1990) 325–340.

[15] D. Schlotz, E. Gutheil, Modeling of laminar mono-and bidisperse liquid oxygen/hydrogen spray flames in the counterflow configuration, Combustion science and technology 158 (1) (2000) 195–210.

[16] F. Laurent, M. Massot, Multi-fluid modelling of laminar polydisperse spray flames: origin, assumptions and comparison of sectional and sampling methods, Combustion theory and modelling 5 (4) (2001) 537–572.

[17] R. J. Kee, K. Yamashita, H. Zhu, A. M. Dean, The effects of liquid-fuel thermophysical properties, carrier-gas composition, and pressure, on strained opposed-flow non-premixed flames, Combustion and Flame 158 (6) (2011) 1129–1139.

[18] H. Zhu, R. J. Kee, L. Chen, J. Cao, M. Xu, Y. Zhang, Vaporisation characteristics of methanol, ethanol and heptane droplets in opposed stagnation flow at low temperature and pressure, Combustion Theory and Modelling 16 (4) (2012) 715–735.

[19] C. Wang, A. M. Dean, H. Zhu, R. J. Kee, The effects of multicomponent fuel droplet evaporation on the kinetics of strained opposed-flow diffusion flames, Combustion and Flame 160 (2) (2013) 265–275.

[20] N. Chen, B. Rogg, K. N. C. Bray, Modelling laminar two-phase counterflow flames with detailed chemistry and transport, in: Proceedings of the Combustion Institute, Vol. 24, Elsevier, 1992, pp. 1513–1521.

[21] A. Robinson, On the motion of small particles in a potential field of flow, Communications on pure and applied mathematics 9 (1) (1956) 69–84.

[22] D. La Mora, J. Fernández, P. Riesco-Chueca, Aerodynamic focusing of particles in a carrier gas, Journal of Fluid Mechanics 195 (1988) 1–21.

[23] E. Gutheil, W. A. Sirignano, Counterflow spray combustion modeling with detailed transport and detailed chemistry, Combustion and Flame 113 (1) (1998) 92–105.

[24] C. Hollmann, E. Gutheil, Diffusion flames based on a laminar spray flame library, Combustion science and technology 135 (1-6) (1998) 175–192.

[25] E. Gutheil, Structure and extinction of laminar ethanol/air spray flames, ZAMM-Journal of Applied Mathematics and Mechanics/Zeitschrift für Angewandte Mathematik und Mechanik 81 (S3) (2001) 533–536.

[26] H. Olguin, E. Gutheil, Influence of evaporation on spray flamelet structures, Combustion and Flame 161 (4) (2014) 987–996.

[27] F. A. Williams, Combustion Theory, Second ed., Benjaming Cummings, Menlo Park, CA., 1985.

[28] A. L. Sánchez, J. Urzay, A. Liñán, The role of separation of scales in the description of spray combustion, Proceedings of the Combustion Institute 35 (2) (2015) 1549–1577.

[29] J. Arrieta-Sanagustín, A. L. Sánchez, A. Liñán, F. A. Williams, Coupling-function formulation for monodisperse spray diffusion flames with infinitely fast chemistry, Fuel Processing Technology 107 (2013) 81–92.

[30] B. Abramzon, W. A. Sirignano, Droplet vaporization model for spray combustion calculations, International journal of heat and mass transfer 32 (9) (1989) 1605–1618.

[31] V. A. Shvab, Relation between the temperature and velocity fields of the flame of a gas burner, *Issledovanie protessov gorenia naturalnogo topliva*, Gos. Energ. izd.

[32] Y. B. Zeldovich, Teorii gorenia neperemeshannykh, *English translation*: On the theory of combustion of initially unmixes gases, NACA, Tech. Memo. 1296, 1951, Zhurnal Tekhnicheskoi Fiziki 19 (1949) 1199–1210.

[33] A. Liñán, The structure of diffusion flames, in: M. Onofri, A. Tesei (Eds.), Fluid dynamical aspects of combustion theory, Longman Scientific Technical Essex, 1991, pp. 11–19.

[34] A. Liñán, F. A. Williams, Fundamental aspects of combustion, Oxford University Press, New York, 1993.

[35] A. Liñán, M. Vera, A. L. Sánchez, Ignition, liftoff, and extinction of gaseous diffusion flames, Annual Review of Fluid Mechanics 47 (2015) 293–314.

[36] A. L. Sánchez, F. A. Williams, Recent advances in understanding of flammability characteristics of hydrogen, Progress in Energy and Combustion Science 41 (2014) 1–55.

CHAPTER

SIX

Strain-Induced Extinction of Spray Diffusion Flames

6.1 Introduction

As previously mentioned, the opposed-jet experimental configuration depicted in Fig. 5.1 has been widely used in studies of spray diffusion flames. Following the flame-structure investigation presented in Chapter 5 for these counterflow configurations we attempt now to account for finite-rate effects, the objective being the determination of the critical extinction conditions in spray diffusion flames. As before, the present analysis focuses on dilute sprays with liquid mass-loading ratios $\alpha \sim S^{-1}$ that are small enough for the droplets to exhibit one-way coupling with the gas flow in the spray feed stream and still sufficiently large to result in peak temperatures on the order of the stoichiometric adiabatic flame temperature, thereby leading to two-way interphase coupling when combustion is present. It will be assumed that the carrier gas is initially sufficiently cold for droplet vaporization in the spray stream outside the mixing layer to be entirely negligible. Furthermore, attention will be restricted to configurations with droplet Stokes numbers $\mathrm{St} < 1/4$, such that the droplets that have been injected in the spray stream approach the stagnation plane with a vanishing axial velocity, in which case the vaporization of the droplets and the subsequent chemical reaction of the resulting fuel vapor with the oxygen occur in the mixing layer separating the opposed streams, which displays a selfsimilar structure in the vicinity of the central stagnation point. As in the seminal analysis of gaseous-diffusion-flame extinction [1], a one-step irreversible reaction with a temperature-dependent Arrhenius rate is employed to model the chemistry, thereby enabling the use of large-activation-energy asymptotics for the theoretical description. While this chapter is devoted to spray diffusion flames, Appendix C presents an accompanying extinction analysis for gaseous diffusion flames, extending the work of [1] by accounting for nonunity Lewis numbers of the fuel and for variable density and variable transport properties of the gas, and by including comparisons with numerical computations em-

ploying finite values of the activation energy. A brief review of the previous results for gaseous flames is given now before we focus on the specific aspects of spray-diffusion-flame extinction.

As shown by Liñán [1], in diffusion flames with a strong temperature dependence of the rate-controlling chemical reactions, the nonlinear interactions of the flow with the chemical kinetics lead to the existence of distinguished regimes of ignition and extinction. His analysis pertains to gaseous fuels with unity Lewis numbers of the reactants. While in fuel-air systems that approximation is sufficiently accurate for oxygen, most hydrocarbon molecules are large, and their diffusivities, although of the order of thermal diffusivity of the gas mixture, are smaller, resulting in values of the fuel Lewis number L_{F} moderately larger than unity, the approximation $L_{\mathrm{F}} = 1$ being reasonably accurate only for methane. Hydrogen molecules, on the other hand, are small, and the associated Lewis number is $L_{\mathrm{F}} \simeq 0.3$. Clearly, therefore, both moderately large and moderately small values of L_{F} are of interest in applications.

Liñán's analysis [1] showed, in particular, that in the diffusion-flame regime the solution is in the first approximation that corresponding to chemical equilibrium, with the reaction layer appearing as a sheet separating a region without fuel from a region without oxidizer. The description of extinction requires consideration of nonequilibrium effects within the reaction layer. The solution involves a double-limit expansion in which the preexponential factor and the activation energy of the reaction-rate constant simultaneously take asymptotically large values, in such a way that the resulting temperature decrement from the Burke-Schumann value in the reaction layer becomes of the order of the Frank-Kamenetskii value, sufficient to decrease the reaction rate by a factor of order unity. The asymptotic procedure leads to a canonical boundary-value problem for the reaction-layer structure relating the small amount of reactants that leak through the flame with a reduced Damköhler number, proportional to the local strain time. These leaking reactants are transported out of the reaction layer, perturbing the Burke-Schumann solution in the outer regions, where the reaction is frozen because of the existing low temperatures. When the reactant Lewis numbers are taken to be unity the solution for the reaction-layer structure and the associated computation of the critical extinction conditions are independent of the nonequilibrium perturbations found outside, that being the case considered in the initial work [1]. In contrast, for nonunity Lewis numbers of the reactants the inner problem and the first-order corrections to the outer equilibrium solutions are coupled, thereby complicating the determination of the critical extinction conditions, which involves the integration of a set of linearized, chemically frozen transport equations for the leaking reactants in

the external streams (see, e.g., the online supplemental appendix of [2]).

Differential diffusion is known to alter the structure of diffusion flames [2]. Because of the strong temperature dependence of the chemical reaction, a fundamental change in connection with extinction is the resulting value of the flame temperature. For unity Lewis numbers of the reactants, regardless of the specific flow configuration the peak temperature of the Burke-Schumann solution is known to be equal to the adiabatic flame temperature of the gas mixture obtained by combining in stoichiometric proportions the air and fuel feed streams at their corresponding initial temperatures. By way of contrast, for nonunity Lewis numbers the peak temperature obtained in the Burke-Schumann limit, different from the adiabatic flame temperature, depends on the values of the Lewis numbers and also on the specific geometric configuration considered, so that, for instance, a counterflow and a coflow diffusion flame would yield different peak temperatures for the same reactant diffusivities. Correspondingly, in two-dimensional and three-dimensional configurations, the resulting peak temperature varies along the flame surface. While accounting for differential-diffusion effects in Burke-Schumann computations is a relatively simple task in one-dimensional steady configurations like the counterflow considered here, in time-dependent multi-dimensional flows the solution involves a free-boundary problem that is difficult to handle in numerical simulations. As explained in [3, 4], these computations can be facilitated by the use of formulations based on chemistry-free coupling functions, including a diffusion-weighted mixture fraction in addition to the traditional mixture fraction.

Different authors have attempted to solve the extinction problem with nonunity Lewis numbers [5–8], starting with Liñán [5], who addressed in particular the premixed-flame regime. Extinction in the diffusion-flame regime was studied by Chung and Law [6] for different one-dimensional configurations in the constant-density approximation. Their analysis, which correctly accounts for flame-temperature departures from the adiabatic value, showed how the reaction-layer structure is reducible to the canonical problem derived originally by Liñán [1] for the equidiffusional case, although in this case the matching procedure involves two terms in the expansion for the outer regions, which are perturbed as a result of the leakage of reactants through the flame. This aspect of the problem was also subsequently acknowledged by Kim and Williams [7], who specifically considered equal diffusivities of the two reactants in their counterflow extinction investigation. It is worth pointing out that the validity of a previous attempt [8] to describe differential-diffusion effects on extinction without accounting for these outer perturbations and for departures of peak temperatures from the adiabatic value is necessarily restricted to near-unity

Lewis number cases.

For fuels whose controlling chemical-kinetic rates have a strong temperature dependence, the structure of the spray diffusion flame near extinction is similar to that discussed above for gaseous fuels, in that we encounter also a near-equilibrium solution at leading order, including a thin reaction layer that is not affected directly by the presence of the droplets. We shall see that, if a one-step Arrhenius model is employed, then the solution for the inner-layer structure, determined by a balance between the chemical reaction and the diffusive transport of heat and chemical species, can be reduced to Liñán's canonical problem [1]. The main differences from the gaseous diffusion flames emerge in the outer chemically frozen regions, in that for spray flames the associated computation involves a two-phase problem with strong two-way coupling enhanced by the chemical heat release. As in the case of gaseous flames, the use of chemistry-free coupling functions facilitates the leading-order description, especially in time-dependent or multidimensional problems, although for spray flames the needed coupling functions are not passive scalars. For the counterflow, the required formulation was presented above in Sec. 5.4.4.

We address in this chapter the extinction problem for spray diffusion flames by describing small deviations from the Burke-Schumann solution in the limit of large activation energy of the controlling heat-release rate. The starting point in the description is the nondimensional counterflow formulation given above in (5.16)–(5.28). The chemical rate is modeled using the simple Arrhenius expression (3.21), which is written in the dimensionless form

$$\frac{\omega_{\mathrm{F}}}{\rho_s A_s} = (B/A_s)\rho e^{-T_a/T} Y_{\mathrm{F}} \hat{Y}_{\mathrm{O}}, \tag{6.1}$$

involving a dimensionless frequency factor B/A_s and a nondimensional activation temperature T_a. The procedure involves introduction of expansions for the different flow variables in terms of inverse powers of the Zeldovich number, defined below in (6.9). As in the case of gaseous flames with nonunity Lewis numbers, it is found that the determination of the inner flame structure requires two terms in the outer expansions, that is, the zeroth-order Burke-Schumann solution and the first-order perturbations associated with the leakage of the reactants. Previous attempts to extend the extinction analysis to the case of spray diffusion flames have been based on approximate descriptions that do not account for the needed first-order corrections in the outer streams (see, e.g., [9] and references therein). The purpose of the present work is that of providing, for the first time, the rigorous analysis of spray-diffusion-flame extinction in the limit of large activation energies through systematic use of matched asymptotic

expansions.

6.2 Summary of relevant equilibrium results

We begin now by revisiting the leading-order Burke-Schumann solution addressed in Sec. 5.4.5. This basic flame structure provides a number of key quantities needed for the extinction analysis, namely, the flame-sheet location z_f, its associated peak temperature T_f, the fuel and oxygen mass-consumption rates m_{F} and m_{O}, and the fraction of the chemical heat released at the flame that is conducted towards the fuel and oxidizer sides, γ_{F} and γ_{O}.

6.2.1 The Burke-Schumann structure

As previously mentioned, in the limit $B/A_s = \infty$ of infinitely fast reaction the reaction layer reduces to a sheet of infinitesimally small thickness located at $z = z_f$, with the Dirac-delta reaction terms acting as sinks for the reactants and as a heat source for the temperature, which peaks at the flame with a value $T = T_f$. The fuel vapor and the oxygen reach the flame sheet by diffusion from opposite sides in stoichiometric proportions, as can be seen by integrating (5.29) across the flame sheet to give

$$m_{\mathrm{F}} = \frac{1}{L_{\mathrm{F}}} \frac{\mathrm{d}Y_{\mathrm{F}}}{\mathrm{d}z}\bigg|_{z_f^+} = -\frac{1}{S} \frac{\mathrm{d}\hat{Y}_{\mathrm{O}}}{\mathrm{d}z}\bigg|_{z_f^-} = \frac{m_{\mathrm{O}}}{S}, \tag{6.2}$$

where m_{F} and $m_{\mathrm{O}} = S m_{\mathrm{F}}$ are appropriate nondimensional measures of the fuel and oxygen consumption rates (in dimensional form, the rate of fuel consumption per unit flame surface m''_{F} is given by $m''_{\mathrm{F}}/(\rho'_s \sqrt{D_{T_s} A'_s}) = T_f^{\sigma} m_{\mathrm{F}}$). The heat released at the flame is transported by conduction towards both sides of the flame according to

$$\frac{q}{S} m_{\mathrm{O}} = \frac{\mathrm{d}T}{\mathrm{d}z}\bigg|_{z_f^-} - \frac{\mathrm{d}T}{\mathrm{d}z}\bigg|_{z_f^+} \tag{6.3}$$

obtained by integration of (5.33).

For the counterflow, and also for other one-dimensional problems, the flame location z_f and the peak temperature at the flame T_f can be determined through a modified boundary-value problem in which (5.24) and (5.25) are integrated for $z_f \leq z < +\infty$ with boundary conditions $Y_{\mathrm{F}} = T - T_f = 0$ at $z = z_f$ while (5.24) and (5.26) are integrated for $-\infty < z \leq z_f$ with boundary conditions $\hat{Y}_{\mathrm{O}} = T - T_f = 0$ at $z = z_f$. The solution is uniquely determined

when the additional relationships (6.2) and (6.3) are employed.

Alternatively, one may use in the integrations the coupling-function formulation presented in Sec. 5.4.4, with the flame location z_f given directly by the point where the mixture-fraction variables achieve their stoichiometric values $Z = Z_{st}$ and $\tilde{Z} = \tilde{Z}_{st}$. The accompanying flame temperature can be easily evaluated from the value

$$H_f = \frac{T_f - T_A}{q/S} - 1 \tag{6.4}$$

of the excess enthalpy at the flame. While the gradients of the temperature and mass fractions (and also Z) have jumps at the flame sheet, those of the conserved scalars $\tilde{Z}$ and H are continuous there. Their values can be used to evaluate the oxygen consumption rate and the fuel-side temperature gradient according to

$$m_{\mathrm{O}} = -\left.\frac{\mathrm{d}Y_{\mathrm{O}}}{\mathrm{d}z}\right|_{z_f^-} = S m_{\mathrm{F}} = \left.\frac{S}{L_{\mathrm{F}}}\frac{\mathrm{d}Y_{\mathrm{F}}}{\mathrm{d}z}\right|_{z_f^+} = \left.\frac{1}{\tilde{Z}_{st}}\frac{\mathrm{d}\tilde{Z}}{\mathrm{d}z}\right|_{z_f} \tag{6.5}$$

and

$$\left.\frac{\mathrm{d}T}{\mathrm{d}z}\right|_{z_f^+} = \left.\frac{q}{S}\frac{\mathrm{d}H}{\mathrm{d}z}\right|_{z_f}. \tag{6.6}$$

The latter expression can be combined with (6.3) to yield

$$\gamma_{\mathrm{F}} = -\left.\frac{1}{qm_{\mathrm{O}}/S}\frac{\mathrm{d}T}{\mathrm{d}z}\right|_{z_f^+} = -\left.\frac{1}{m_{\mathrm{O}}}\frac{\mathrm{d}H}{\mathrm{d}z}\right|_{z_f} \tag{6.7}$$

for the fractional amount of chemical heat release that is conducted towards the fuel side of the flame, with $\gamma_{\mathrm{O}} = 1 - \gamma_{\mathrm{F}}$ correspondingly representing the fraction transported to the oxidizer side.

6.2.2 Discussion of results

Results of integrations are summarized in Fig. 6.1 for a fuel with $L_{\mathrm{F}} = 2.6$, and $M_{\mathrm{N}_2}/M_{\mathrm{F}} = 0.165$, as corresponds to dodecane. The properties of this fuel are also utilized to evaluate $q/S = 8.24$, $L_v/(c_p T_s') = 1.005$, $L_v/(R_{\mathrm{F}} T_B') = 15.05$, $c_p/c_l = 0.543$, and $T_B'/T_s' = 1.63$, with an average specific heat $c_p = 1200$ J/(kg K) and a boundary temperature $T_s' = 300$ K assumed in the evaluations. The results correspond to an elevated air-side temperature $T_A = T_A'/T_s' = 2$ for two different values of the Stokes number, represented by the thick curves (dashed: $\mathrm{St} = 0.05$; solid: $\mathrm{St} = 0.20$). The computations indicate that in the

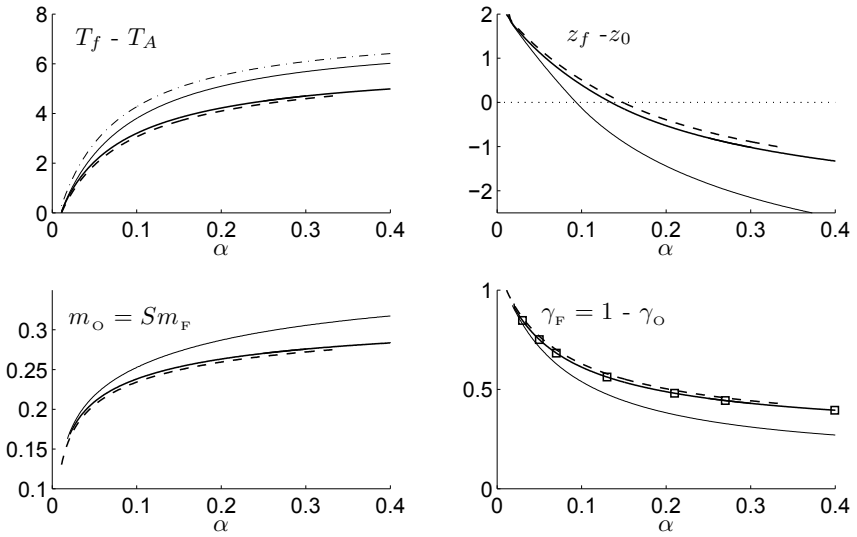

Figure 6.1. The variation with liquid mass-loading ratio of the Burke-Schumann flame properties for a dodecane spray flame ($S = 15$, $L_{\rm F} = 2.6$, $M_{\rm N_2}/M_{\rm F} = 0.165$, $q/S = 8.24$, $L_v/(c_p T_s') = 1.005$, $L_v/(R_{\rm F} T_B') = 15.05$, $c_p/c_l = 0.543$, and $T_B'/T_s' = 1.63$) with $T_A = 2$ for $\mathrm{St} = 0.05$ (thick dashed curves) and $\mathrm{St} = 0.20$ (thick solid curves), with the thin solid curves representing results obtained for $\mathrm{St} = 0.20$ with $L_{\rm F} = 1.0$. The dot-dashed temperature curve is the stoichiometric adiabatic temperature evaluated from (6.8). The squares on the curve of $\gamma_{\rm F}$ for $\mathrm{St} = 0.20$ mark the specific conditions to be investigated later in the extinction analysis.

range of Stokes numbers explored here the droplets always vaporize rapidly near the edge of the mixing layer, with the consequence that the differences in droplet inertia have only a minor effect on the resulting flow structure, thereby explaining the small differences observed in the four plots of Fig. 6.1 between the results corresponding to $\mathrm{St} = 0.05$ and $\mathrm{St} = 0.20$.

The upper plots display the variation of the peak temperature increment $T_f - T_A$ and flame location relative to the stagnation plane $z_f - z_0$. For completeness, the conditions in the plots include extremely small values of α associated with ultradilute sprays of limited practical interest, because their associated temperature increment is much too small to support significant reaction rates in hydrocarbon combustion applications *. For these values $\alpha \ll 1$, the flame

*When realistic chemical-kinetic schemes are used, hydrocarbon flames are known to display a limiting crossover pressure-dependent temperature $T_c' \sim 1500$ K. For the computations of Fig. 6.1, which assume boundary temperatures $T_s' = 300$ K and $T_A' = 600$ K, this crossover condition introduces a minimum nondimensional peak temperature $T_f - T_A \simeq 3$ below which the spray diffusion flame cannot exist.

is seen to appear at the edge of the mixing layer not far downstream from the vaporization region. As the fuel supply increases for increasing α, the flame temperature is seen to increase and the flame sheet migrates progressively towards the air side of the mixing layer, crossing the stagnation plane into the air side for $\alpha \simeq 0.15$. As previously discussed in connection with Fig. 5.5, the flame sheet is seen to remain in the vicinity of the stagnation plane for $\alpha \ll 1$, with a maximum standoff distance $z_f - z_0 \simeq -1.3$ achieved for the largest value $\alpha = 0.4$ of the liquid mass-loading ratio considered in Fig. 6.1. In this respect, the structure of diffusion flames for dilute sprays with $\alpha \sim S^{-1}$ differs fundamentally from that encountered in gaseous diffusion flames with undiluted fuel feed, for which the large value of S results in flames located on the air side of the mixing layer far from the stagnation plane [2].

As previously mentioned, for gaseous diffusion flames with unity Lewis numbers the peak temperature determined in the limit of infinitely fast reaction is always equal to the adiabatic temperature for the stoichiometric mixture formed by combining the unit mass of fuel stream with a mass S of the air stream, both with their initial temperatures [2]. To investigate the applicability of this result in the context of spray diffusion flames the plot of peak temperature in Fig. 6.1 includes a dot-dashed curve representing the adiabatic flame value

$$T_{ad} = 1 + \frac{q - L_v/(c_p T_s') + S(T_A - 1) - (c_l/c_p - 1)(T_B'/T_s' - 1)}{S + 1 + 1/\alpha} \tag{6.8}$$

for the stoichiometric mixture obtained by mixing a spray stream with liquid mass-loading ratio α and temperature T_s' with air at temperature T_A'. The result is seen to lie consistently above the peak temperature determined in the Burke-Schumann integrations. Part of the reason for this discrepancy is that the value given in (6.8) is based on a spray with droplet number density n_m', achieved in the spray stream at $z = \delta_m$ (i.e., $z = 1$) as a result of the accumulation of the droplets, as follows from (5.11). However, this apparent value n_m', corresponding to a nondimensional number density $n = 1$, is never reached in the integrations, because the droplets with $\mathrm{St} < 1/4$ vaporize for $z > 1$, in a region where $n < 1$, as can be seen in the sample profiles of Fig. 5.5. Hence, the value of the liquid mass loading for the spray in the vaporization region is somewhat smaller than α, so that the effective adiabatic flame temperature for the spray-air mixture is actually lower than that given in (6.8).

Differential diffusion effects can be also a source for the departures of T_f from T_{ad}. Flames with $L_{\mathrm{F}} > 1$ are know to exhibit subadiabatic peak tempera-

tures as a result of the relative decrease of the fuel diffusion rate into the flame sheet compared with the heat loss by conduction from the flame [2]. To assess this effect, the integrations for the dodecane spray with $\mathrm{St} = 0.20$ were repeated with the value $L_{\mathrm{F}} = 2.6$ replaced by $L_{\mathrm{F}} = 1$. The results are represented by the thin solid curves in Fig. 6.1. As can be seen, the resulting flame temperature lies much closer to T_{ad} in this case. The nonnegligible increment of T_f resulting from the increased fuel diffusivity, which is apparent by comparing the thick and thin solid curves in the plot, is a measure of the extent of the differential diffusion effects in spray diffusion flames. The resulting value of T_f still lies somewhat below the adiabatic flame temperature, the remaining difference being mainly attributable to the overestimated value of α present in the prediction (6.8), previously discussed.

The lower plots in Fig. 6.1 represent the variation of the burning rate $m_{\mathrm{O}} = Sm_{\mathrm{F}}$ and of the relative rate of heat loss towards the fuel and aire sides of the flame, measured by the parameters γ_{F} and $\gamma_{\mathrm{O}} = 1 - \gamma_{\mathrm{F}}$, respectively. As expected, the reactant consumption rate rises as more fuel becomes available for increasing α. The associated value of $\gamma_{\mathrm{F}} = 1 - \gamma_{\mathrm{O}}$ depends fundamentally on the flame position. Thus, for ultralean configurations with extremely small values of α the flame sheet sits on the spray side of the mixing layer and most of the heat released at the flame is transferred by conduction towards the spray side, resulting in values of γ_{F} close to unity and accompanying small values of γ_{O}. The parameter γ_{F} decreases rapidly as the flame moves towards the air side of the mixing layer for increasing α, reaching a value $\gamma_{\mathrm{F}} \simeq 0.40$ for $\alpha = 0.4$. It is noteworthy that over a large range of values of α associated with temperature increments of practical interest (i.e., $\alpha \gtrsim 0.05$), the flames are seen to remain in the vicinity of the stagnation plane and the heat release by chemical reaction is symmetrically distributed to both sides of the flame, giving values $\gamma_{\mathrm{F}} \sim \gamma_{\mathrm{O}} \simeq 0.5$. Because of the increased fuel diffusivity associated with the integrations using $L_{\mathrm{F}} = 1$, the resulting flames move closer to the air boundary, yielding smaller values of γ_{F}. As expected, the enhanced diffusive transport also results in a larger burning rate.

6.3 Extinction in the diffusion-flame regime

In the limit of large activation energy, arising for values of the activation temperature T_a much larger than the flame temperature T_f, flame extinction in the diffusion-flame regime [1] occurs for small departures from the equilibrium solution described above. Extinction is associated with small decrements of the temperature in the reaction layer from the peak value T_f of order T_f^2/T_a,

sufficient to reduce the reaction rate by a factor e, as can be inferred from the exponential temperature dependence present in (6.1). The ratio of this temperature decrement to the characteristic temperature increase by chemical reaction q/S defines the Zeldovich number

$$\beta = \frac{T_a}{T_f}\frac{q/S}{T_f}, \tag{6.9}$$

the relevant large parameter for the asymptotic description. The chemical reaction is confined to a thin layer of relative thickness β^{-1} around $z = z_f$, where small reactant mass fractions of order $Y_{\text{F}} \sim \beta^{-1}S^{-1}$ and $\hat{Y}_{\text{O}} \sim \beta^{-1}$ are found. These estimates, together with the condition that the inner structure of the reaction layer is given by a balance between reaction and diffusion, can be used to provide from (5.24) the order-of-magnitude estimate

$$\frac{A_s}{B} \sim \frac{\exp[-T_a/T_f]}{T_f^{1+\sigma}\beta^3}, \tag{6.10}$$

which applies near extinction in the diffusion-flame regime. This last expression reveals that the asymptotic limit $T_a/T_f \gg 1$ of large activation energies requires simultaneous consideration of exponentially large values of the nondimensional frequency factor B/A_s, resulting in the balance (6.10) that ensures temperature decrements of order T_f^2/T_a in the reaction layer.

To solve the problem in the limit $\beta \gg 1$, different expansions in increasing powers of β^{-1} must be introduced for the different variables in the inner reaction layer and in the outer regions. Determination of the critical strain rate at extinction requires consideration of the inner structure of the the reaction layer, given by a balance between reaction and diffusion, together with the first-order corrections to the flow in the outer regions, which satisfy chemically frozen conservation equations because of the existing low temperature. These first-order corrections are a consequence of the finite rate of reaction occurring in the reaction layer, which is not able to deplete the reactants, which therefore leak through the flame, resulting in nonzero boundary values for the outer reactant perturbations at $z = z_f^-$ and at $z = z_f^+$. As shown by Liñán [1], the amount of reactant leaking towards either side of the flame depends on the corresponding outer temperature gradients. Thus, values of $\gamma_{\text{F}} = 1 - \gamma_{\text{O}}$ approaching unity, corresponding to sharp temperature gradients at z_f^+, favor oxidizer leakage through rapid freezing of the chemical reaction on the fuel side of the flame. Conversely, the opposite limit $\gamma_{\text{F}} = 1 - \gamma_{\text{O}} \ll 1$ leads to augmented fuel leakage, that being the case most often encountered in gaseous diffusion

flames with $S \gg 1$, when the flame is located far on the oxidizer side. As seen in Fig. 6.1, in systems with $\alpha \sim S^{-1}$ the flames are located in the vicinity of the stagnation plane, such that $\gamma_{\mathrm{F}} \sim \gamma_{\mathrm{O}}$, correspondingly yielding reactant leakage of order β^{-1} towards both sides of the flame [1].

Besides perturbations associated with reactant leakage through the flame, in spray flows perturbations to the Burke-Schumann solution can also emerge on the air side when the droplets cross the flame. Since in the limit $\beta \gg 1$ the reaction rate is negligible outside the reaction layer, the droplets vaporizing on the air side of the flame sheet constitute a source of fuel vapor that modifies the equilibrium solution $Y_{\mathrm{F}} = 0$. Clearly, the extent of the perturbation depends on the amount of fuel transported to the air side by the crossing droplets.

The diffusion-flame regime, in which the Burke-Schumann solution arises as the leading-order representation of the flow, remains valid as long as the combined effects of the crossing droplets to the air side and the reactant leakage to either side of the flame lead to small perturbations to the outer equilibrium solution. Conversely, it ceases to be valid when these perturbations become of order unity and need to be accounted for in the leading-order description [1], ushering in either a premixed-flame regime (when only one of the reactants is present in significant amounts in the opposite stream) or a partial-burning regime (when both reactants are found in significant amounts on both sides of the flame). The numerical results presented above in Figs. 5.5 and 6.1 seem to suggest that the diffusion-flame regime prevails always in spray flames with $\mathrm{St} < 1/4$ and $\alpha \sim S^{-1}$, because the droplets vaporize before crossing the flame and because the flame is located not far from the stagnation plane, resulting in values of $\gamma_{\mathrm{F}} \sim \gamma_{\mathrm{O}}$ that do not cause excessive leakage. These findings indicate that the extinction of dilute spray diffusion flames occur predominantly in the diffusion-flame regime, thereby motivating the present analysis, focused on small perturbations to the outer equilibrium solution that are of order β^{-1}.

6.4 First-order corrections in the outer regions

When considering the outer solution, the reaction layer appears as a sheet located at z_f. Different expansions must be used for the different flow variables on each side of the flame sheet. In the following, the terms in the expansion on the fuel side of the reaction layer (i.e., for $z_f \leq z < +\infty$) will be denoted by the superscript $+$, while those on the air side (i.e., for $-\infty \leq z < z_f$) will be

denoted by the superscript $-$, giving for instance

$$\begin{array}{l} T = T_0^+ + \beta^{-1} T_1^+, \;\; Y_{\mathrm{F}} = Y_{\mathrm{F0}}^+ + \beta^{-1} Y_{\mathrm{F1}}^+, \;\; \hat{Y}_{\mathrm{O}} = \beta^{-1} \hat{Y}_{\mathrm{O1}}^+ \quad \text{for } z > z_f \\ T = T_0^- + \beta^{-1} T_1^-, \;\; Y_{\mathrm{F}} = \beta^{-1} Y_{\mathrm{F1}}^-, \;\; \hat{Y}_{\mathrm{O}} = \hat{Y}_{\mathrm{O0}}^- + \beta^{-1} \hat{Y}_{\mathrm{O1}}^- \quad \text{for } z < z_f \end{array} \tag{6.11}$$

for the first nontrivial terms in the expansions for the temperature and reactant mass fractions, with similar expansions introduced for ρ, u, and A. The zeroth-order terms in the expansions correspond to the Burke-Schumann solution described above. Note that the null leading-order terms $Y_{\mathrm{F0}}^- = 0$ on the air side and $\hat{Y}_{\mathrm{O0}}^+ = 0$ on the fuel side, resulting from the equilibrium condition $Y_{\mathrm{F}} \hat{Y}_{\mathrm{O}} = 0$, have been omitted for convenience in writing (6.11) .

The flame-extinction analysis addresses configurations such as that depicted in Fig. 5.5, for which no droplets cross the flame, so that the perturbations to the Burke-Schumann solution on the air side are only a result of the finite-rate effects occurring in the reaction layer. Furthermore, since droplet vaporization occurs far on the spray side of the mixing layer, the outer gas-phase perturbations on the fuel side of the flame, originating at the flame sheet as a result of the leakage of the oxidizer, become negligibly small by the time they reach the droplets, causing negligible changes to the source terms in (5.22)–(5.26). If these changes are neglected, as done below, then the perturbations to the gas phase become independent of the perturbations induced in the liquid phase, because the latter are negligibly small and therefore represent a higher-order correction to the outer solution. Correspondingly, in this one-way-coupling approximation the functions $Y_{\mathrm{F1}}^{\pm}$, $\hat{Y}_{\mathrm{O1}}^{\pm}$, $T_1^{\pm}$, $\rho_1^{\pm}$, $u_1^{\pm}$, and $A_1^{\pm}$ that describe the perturbation to the gas flow can be determined by integrating

$$\frac{\mathrm{d}}{\mathrm{d}z}(\rho_0^{\pm} u_1^{\pm}) + \frac{\mathrm{d}}{\mathrm{d}z}(\rho_1^{\pm} u_0^{\pm}) + \rho_1^{\pm} A_0^{\pm} + \rho_0^{\pm} A_1^{\pm} = 0 \tag{6.12}$$

$$\frac{\mathrm{d}A_1^{\pm}}{\mathrm{d}z} + \left(\frac{\rho_1^{\pm}}{\rho_0^{\pm}} + \frac{u_1^{\pm}}{u_0^{\pm}} \right) \frac{\mathrm{d}A_0^{\pm}}{\mathrm{d}z} + \frac{\rho_1^{\pm}}{\rho_0^{\pm}} \frac{(A_0^{\pm})^2}{2u_0^{\pm}} + \frac{A_0^{\pm} A_1^{\pm}}{u_0^{\pm}} =$$

$$= \frac{\mathrm{Pr}}{\rho_0^{\pm} u_0^{\pm}} \frac{\mathrm{d}}{\mathrm{d}z} \left[(T_0{}^{\pm})^{\sigma} \left(\frac{\mathrm{d}A_1^{\pm}}{\mathrm{d}z} + \sigma \frac{T_1^{\pm}}{T_0^{\pm}} \frac{\mathrm{d}A_0^{\pm}}{\mathrm{d}z} \right) \right] \tag{6.13}$$

$$\frac{\mathrm{d}T_1^{\pm}}{\mathrm{d}z} + \left(\frac{\rho_1^{\pm}}{\rho_0^{\pm}} + \frac{u_1^{\pm}}{u_0^{\pm}} \right) \frac{\mathrm{d}T_0^{\pm}}{\mathrm{d}z} = \frac{1}{\rho_0^{\pm} u_0^{\pm}} \frac{\mathrm{d}}{\mathrm{d}z} \left[(T_0{}^{\pm})^{\sigma} \left(\frac{\mathrm{d}T_1^{\pm}}{\mathrm{d}z} + \sigma \frac{T_1^{\pm}}{T_0^{\pm}} \frac{\mathrm{d}T_0^{\pm}}{\mathrm{d}z} \right) \right] \tag{6.14}$$

$$\frac{\mathrm{d}Y_{\mathrm{F1}}^{\pm}}{\mathrm{d}z} + \left(\frac{\rho_1^{\pm}}{\rho_0^{\pm}} + \frac{u_1^{\pm}}{u_0^{\pm}} \right) \frac{\mathrm{d}Y_{\mathrm{F0}}^{\pm}}{\mathrm{d}z} = \frac{1}{\rho_0^{\pm} u_0^{\pm} L_F} \frac{\mathrm{d}}{\mathrm{d}z} \left[(T_0{}^{\pm})^{\sigma} \left(\frac{\mathrm{d}Y_{\mathrm{F1}}}{\mathrm{d}z} + \sigma \frac{T_1^{\pm}}{T_0^{\pm}} \frac{\mathrm{d}Y_{\mathrm{F0}}}{\mathrm{d}z} \right) \right] \tag{6.15}$$

$$\frac{\mathrm{d}\hat{Y}_{\mathrm{O1}}^{\pm}}{\mathrm{d}z} + \left(\frac{\rho_1^{\pm}}{\rho_0^{\pm}} + \frac{u_1^{\pm}}{u_0^{\pm}} \right) \frac{\mathrm{d}\hat{Y}_{\mathrm{O0}}}{\mathrm{d}z} = \frac{1}{\rho_0^{\pm} u_0^{\pm}} \frac{\mathrm{d}}{\mathrm{d}z} \left[(T_0{}^{\pm})^{\sigma} \left(\frac{\mathrm{d}\hat{Y}_{\mathrm{O1}}}{\mathrm{d}z} + \sigma \frac{T_1^{\pm}}{T_0^{\pm}} \frac{\mathrm{d}\hat{Y}_{\mathrm{O0}}}{\mathrm{d}z} \right) \right] \tag{6.16}$$

$$\frac{\rho_1^{\pm}}{\rho_0^{\pm}} = -\frac{T_1^{\pm}}{T_0^{\pm}} + \frac{Y_{\mathrm{F1}}^{\pm}(1 - M_{\mathrm{N}_2}/M_{\mathrm{F}})}{\rho_0^{\pm} T_0^{\pm} [1 - Y_{\mathrm{F0}}^{\pm}(1 - M_{\mathrm{N}_2}/M_{\mathrm{F}})]^2} \tag{6.17}$$

obtained by linearizing (5.22)–(5.28) after neglecting the source and reaction

terms in (5.22)–(5.26). The boundary conditions

$$\left\{\begin{array}{l} A_1^- = T_1^- = Y_{\mathrm{F}1}^- = \hat{Y}_{\mathrm{O}1}^- = 0 \\ u_1^- - u_{1_f}^- = A_1^- - A_{1_f}^- = T_1^- - T_{1_f}^- = 0 \\ Y_{\mathrm{F}1}^- - Y_{\mathrm{F}1_f}^- = \hat{Y}_{\mathrm{O}1}^- - \hat{Y}_{\mathrm{O}1_f}^- = 0 \end{array}\right\} \begin{array}{ll} \text{as} & z \to -\infty \\ \text{at} & z = z_f \end{array} \tag{6.18}$$

and

$$\left\{\begin{array}{l} u_1^+ = A_1^+ = T_1^+ = Y_{\mathrm{F}1}^+ = \hat{Y}_{\mathrm{O}1}^+ = 0 \\ A_1^+ - A_{1_f}^+ = T_1^+ - T_{1_f}^+ = 0 \\ Y_{\mathrm{F}1}^+ - Y_{\mathrm{F}1_f}^+ = \hat{Y}_{\mathrm{O}1}^+ - \hat{Y}_{\mathrm{O}1_f}^+ = 0 \end{array}\right\} \begin{array}{ll} \text{as} & z \to +\infty \\ \text{at} & z = z_f \end{array} \tag{6.19}$$

include the five boundary perturbations $u_{1_f}^-, A_{1_f}^-$, $T_{1_f}^-$, $Y_{\mathrm{F}1}^-$, and $\hat{Y}_{\mathrm{O}1_f}^-$ on the air side and the four boundary perturbations $A_{1_f}^+$, $T_{1_f}^+$, $Y_{\mathrm{F}1}^+$, and $\hat{Y}_{\mathrm{O}1_f}^+$ on the fuel side. It is worth noting the lack of symmetry regarding the boundary conditions for the velocity on both sides of the flame, that being a consequence of the condition of zero spray-stream displacement employed in (5.27). Thus, in the computation procedure $u_{1_f}^+$ is part of the solution (i.e., it is obtained after integration of equation (6.12) on the spray side with the condition $u_1^+ = 0$ at $z \to \infty$), whereas the boundary value $u_{1_f}^-$ imposed on the fuel side of the flame is associated with a nonzero value of u_1^- at $z \to -\infty$, related to the small relative displacement of order β^{-1} of the stagnation plane.

The boundary values appearing in (6.18) and (6.19), as well as the accompanying values of the gradients of the different functions, satisfy a number of constraints. For instance, evaluating on both sides of the flame a first integral of the chemistry-free equations (5.29) and (5.33) with use made of the expansions (6.11) provides

$$\begin{aligned} \frac{\rho_f u_f}{T_f^\sigma}\left[\left(T_{1_f}^+ - T_{1_f}^-\right) + \frac{q}{S}\left(\hat{Y}_{\mathrm{O}1_f}^+ - \hat{Y}_{\mathrm{O}1_f}^-\right)\right] &= \\ \left.\frac{\mathrm{d}T_1^+}{\mathrm{d}z}\right|_{z_f} - \left.\frac{\mathrm{d}T_1^-}{\mathrm{d}z}\right|_{z_f} &+ \frac{q}{S}\left(\left.\frac{\mathrm{d}\hat{Y}_{\mathrm{O}1}^+}{\mathrm{d}z}\right|_{z_f} - \left.\frac{\mathrm{d}\hat{Y}_{\mathrm{O}1}^-}{\mathrm{d}z}\right|_{z_f}\right) \end{aligned} \tag{6.20}$$

$$\begin{aligned} \frac{\rho_f u_f}{T_f^\sigma}\left[S\left(Y_{\mathrm{F}1_f}^+ - Y_{\mathrm{F}1_f}^-\right) - \left(\hat{Y}_{\mathrm{O}1_f}^+ - \hat{Y}_{\mathrm{O}1_f}^-\right)\right] &= \\ \frac{S}{L_{\mathrm{F}}}\left(\left.\frac{\mathrm{d}Y_{\mathrm{F}1}^+}{\mathrm{d}z}\right|_{z_f} - \left.\frac{\mathrm{d}Y_{\mathrm{F}1}^-}{\mathrm{d}z}\right|_{z_f}\right) &- \left.\frac{\mathrm{d}\hat{Y}_{\mathrm{O}1}^+}{\mathrm{d}z}\right|_{z_f} + \left.\frac{\mathrm{d}\hat{Y}_{\mathrm{O}1}^-}{\mathrm{d}z}\right|_{z_f} \end{aligned}$$

where $\rho_f u_f / T_f^\sigma$ is evaluated from the leading-order solution, with $\rho_f = 1/T_f$ as follows from (5.28) with $Y_{\mathrm{F}} = 0$. Analogously, evaluation of first, second and

third integrals of the radial-momentum equation (5.23) lead to three additional conditions,

$$\begin{aligned}
&\mathrm{Pr}T_f^{\sigma}\left(\left.\frac{\mathrm{d}A_1^+}{\mathrm{d}z}\right|_{z_f}-\left.\frac{\mathrm{d}A_1^-}{\mathrm{d}z}\right|_{z_f}+\sigma\frac{T_{1_f}^+-T_{1_f}^-}{T_f}\left.\frac{\mathrm{d}A_0}{\mathrm{d}z}\right|_{z_f}\right)+\\
&\qquad+\rho_f u_f A_f\left(\frac{\rho_{1_f}^+}{\rho_f}-\frac{\rho_{1_f}^-}{\rho_f}+\frac{u_{1_f}^+}{u_f}-\frac{u_{1_f}^-}{u_f}+\frac{A_{1_f}^+}{A_f}-\frac{A_{1_f}^-}{A_f}\right)=0\\
&\mathrm{Pr}T_f^{\sigma}\left(A_{1_f}^+-A_{1_f}^-+\sigma\frac{T_{1_f}^+-T_{1_f}^-}{T_f}A_f\right)+\\
&\qquad+\frac{1}{2}\rho_f u_f^2\left(\frac{\rho_{1_f}^+}{\rho_f}-\frac{\rho_{1_f}^-}{\rho_f}+2\frac{u_{1_f}^+}{u_f}-2\frac{u_{1_f}^-}{u_f}\right)=0\\
&T_f^{\sigma}\left(u_{1_f}^+-u_{1_f}^-+\sigma\frac{T_{1_f}^+-T_{1_f}^-}{T_f}u_f\right)=0
\end{aligned}\tag{6.21}$$

where ρ_f, u_f, A_f and T_f are evaluated from the leading-order solution.

Since the problem is linear, the solution to (6.12)–(6.19) can be expressed as a linear combination of the elementary solutions arising by considering separately the flame-sheet values of each one of the perturbed variables. This strategy can be used in particular to generate the expressions

$$u_{1_f}^+ = a_{uA}^+A_{1_f}^+ + a_{uT}^+T_{1_f}^+ + a_{uF}^+Y_{\mathrm{F}1_f}^+ + a_{uO}^+\hat{Y}_{\mathrm{O}1_f}^+ \tag{6.22}$$

$$\left.\frac{\mathrm{d}A_1^{\pm}}{\mathrm{d}z}\right|_{z_f} = a_{Au}^-u_{1_f}^- + a_{AA}^{\pm}A_{1_f}^{\pm} + a_{AT}^{\pm}T_{1_f}^{\pm} + a_{AF}^{\pm}Y_{\mathrm{F}1_f}^{\pm} + a_{AO}^{\pm}\hat{Y}_{\mathrm{O}1_f}^{\pm} \tag{6.23}$$

$$\left.\frac{\mathrm{d}T_1^{\pm}}{\mathrm{d}z}\right|_{z_f} = a_{Tu}^-u_{1_f}^- + a_{TA}^{\pm}A_{1_f}^{\pm} + a_{TT}^{\pm}T_{1_f}^{\pm} + a_{TF}^{\pm}Y_{\mathrm{F}1_f}^{\pm} + a_{TO}^{\pm}\hat{Y}_{\mathrm{O}1_f}^{\pm} \tag{6.24}$$

$$\left.\frac{\mathrm{d}Y_{\mathrm{F}1}^{\pm}}{\mathrm{d}z}\right|_{z_f} = a_{Fu}^-u_{1_f}^- + a_{FA}^{\pm}A_{1_f}^{\pm} + a_{FT}^{\pm}T_{1_f}^{\pm} + a_{FF}^{\pm}Y_{\mathrm{F}1_f}^{\pm} + a_{FO}^{\pm}\hat{Y}_{\mathrm{O}1_f}^{\pm} \tag{6.25}$$

$$\left.\frac{\mathrm{d}\hat{Y}_{\mathrm{O}1}^{\pm}}{\mathrm{d}z}\right|_{z_f} = a_{Ou}^-u_{1_f}^- + a_{OA}^{\pm}A_{1_f}^{\pm} + a_{OT}^{\pm}T_{1_f}^{\pm} + a_{OF}^{\pm}Y_{\mathrm{F}1_f}^{\pm} + a_{OO}^{\pm}\hat{Y}_{\mathrm{O}1_f}^{\pm} \tag{6.26}$$

for the values of the velocity perturbation and gradients appearing in (6.20) and (6.21) in terms of the boundary values of the different functions. The 40 constant coefficients $a_{ij}^{\pm}$ in (6.22)–(6.26) are obtained from straightforward integrations of (6.12)–(6.17) with normalized boundary conditions at the flame. For instance, the coefficients a_{uA}^+, a_{AA}^+, a_{TA}^+, a_{FA}^+, and a_{OA}^+, correspond to the values of u_1^+, $\mathrm{d}A_1^+/\mathrm{d}z$, $\mathrm{d}T_1^+/\mathrm{d}z$, $\mathrm{d}Y_{\mathrm{F}1}^+/\mathrm{d}z$, and $\mathrm{d}\hat{Y}_{\mathrm{O}1}^+/\mathrm{d}z$ at $z=z_f$ when the boundary conditions at the flame sheet, given in (6.18), are replaced in the

integrations of (6.12)–(6.17) for $-\infty < z \leq z_f$ by the normalized boundary conditions $A_1^+ - 1 = T_1^+ = Y_{\mathrm{F}1}^+ = \hat{Y}_{\mathrm{O}1}^+ = 0$. Similarly, the coefficients a_{AT}^-, a_{TT}^-, a_{FT}^-, and a_{OT}^- correspond to the values of the different gradients when the alternative boundary conditions $A_1^- = T_1^- - 1 = Y_{\mathrm{F}1}^- = \hat{Y}_{\mathrm{O}1}^- = 0$ are utilized in the integrations. Once the different coefficients $a_{ij}^{\pm}$ are determined numerically for a given Burke-Schumann solution, the substitution of (6.22)-(6.26) into (6.20) and (6.21) generates five linear equations linking the nine boundary values $u_{1_f}^-$, $A_{1_f}^{\pm}$, $T_{1_f}^{\pm}$, $Y_{\mathrm{F}1}^{\pm}$, and $\hat{Y}_{\mathrm{O}1_f}^{\pm}$. The four additional equations that are needed to complete the solution follow from matching with the inner solution, as explained below.

6.5 The reactive layer

6.5.1 Basic formulation

In the inner reaction layer, the variables are rescaled to give the normalized variables of order unity $\zeta = \beta(z - z_f)$, $y_{\mathrm{F}} = S\beta Y_{\mathrm{F}}$, $y_{\mathrm{O}} = \beta\hat{Y}_{\mathrm{O}}$, and $\theta = \beta(T - T_f)/(q/S)$, with corresponding asymptotic expansions given by $y_{\mathrm{F}} = y_{\mathrm{F}_0} + \beta^{-1}y_{\mathrm{F}_1} + \cdots$, $y_{\mathrm{O}} = y_{\mathrm{O}_0} + \beta^{-1}y_{\mathrm{O}_1} + \cdots$, and $\theta = \theta_0 + \beta^{-1}\theta_1 + \cdots$. At the order pursued here, the determination of the extinction conditions involves only the zeroth-order terms in the above expansions, which are determined by integration of the corresponding reaction-diffusion equations

$$-\frac{\mathrm{d}^2\theta}{\mathrm{d}\zeta^2} = \frac{1}{L_{\mathrm{F}}}\frac{\mathrm{d}^2 y_{\mathrm{F}}}{\mathrm{d}\zeta^2} = \frac{\mathrm{d}^2 y_{\mathrm{O}}}{\mathrm{d}\zeta^2} = \frac{B\beta^{-3}}{A_s T_f^{1+\sigma}} e^{-T_a/T_f} y_{\mathrm{F}} y_{\mathrm{O}} e^{\theta} \tag{6.27}$$

obtained at leading order from (5.24)–(5.26), with the subscript 0 omitted to simplify the notation. The boundary conditions for integration of (6.27), given by

$$\left.\begin{array}{llll} \dfrac{\mathrm{d}\theta}{\mathrm{d}\zeta} = -\gamma_{\mathrm{F}} m_{\mathrm{O}}, & \dfrac{1}{L_{\mathrm{F}}}\dfrac{\mathrm{d}y_{\mathrm{F}}}{\mathrm{d}\zeta} = m_{\mathrm{O}}, & \dfrac{\mathrm{d}y_{\mathrm{O}}}{\mathrm{d}\zeta} = 0 & \text{as} \quad \zeta \to \infty \\ \dfrac{\mathrm{d}\theta}{\mathrm{d}\zeta} = \gamma_{\mathrm{O}} m_{\mathrm{O}}, & \dfrac{\mathrm{d}y_{\mathrm{F}}}{\mathrm{d}\zeta} = 0, & \dfrac{\mathrm{d}y_{\mathrm{O}}}{\mathrm{d}\zeta} = -m_{\mathrm{O}} & \text{as} \quad \zeta \to -\infty \end{array}\right\}, \tag{6.28}$$

follow from matching with the leading-order solution in the outer regions. In the intermediate matching region, the inner variables take the form

$$\left.\begin{array}{l} \theta = -\gamma_{\mathrm{F}} m_{\mathrm{O}}\zeta + \theta^+, \quad y_{\mathrm{F}} = m_{\mathrm{O}} L_{\mathrm{F}}\zeta + y_{\mathrm{F}}^+, \quad y_{\mathrm{O}} = y_{\mathrm{O}}^+ \quad \text{as} \quad \zeta \to \infty \\ \theta = \gamma_{\mathrm{O}} m_{\mathrm{O}}\zeta + \theta^-, \quad y_{\mathrm{F}} = y_{\mathrm{F}}^-, \quad y_{\mathrm{O}} = -m_{\mathrm{O}}\zeta + y_{\mathrm{O}}^- \quad \text{as} \quad \zeta \to -\infty \end{array}\right\}, \tag{6.29}$$

as corresponds to (6.28). These expressions involve six unknown constants, namely, the reactant leakages y_{O}^{+} and y_{F}^{-} and the apparent shifts y_{F}^{+}, θ^{+}, y_{O}^{-}, and θ^{-}, which are related to the reaction-sheet values of the first-order perturbations in the outer regions by

$$\theta^{\pm} = T_{1_f}^{\pm}/(q/S), \quad y_{\mathrm{F}}^{\pm} = SY_{\mathrm{F}1_f}^{\pm}, \quad \text{and} \quad y_{\mathrm{O}}^{\pm} = \hat{Y}_{\mathrm{O}1_f}^{\pm} \tag{6.30}$$

as required at this order to achieve the matching of (6.29) with the outer solution (6.11). The development continues by integrating the first two equations in (6.27) with the boundary conditions given in (6.28) to yield

$$\frac{\mathrm{d}\theta}{\mathrm{d}\zeta} + \frac{\mathrm{d}y_{\mathrm{O}}}{\mathrm{d}\zeta} = -\gamma_{\mathrm{F}} m_{\mathrm{O}} \quad \text{and} \quad \frac{1}{L_{\mathrm{F}}}\frac{\mathrm{d}y_{\mathrm{F}}}{\mathrm{d}\zeta} - \frac{\mathrm{d}y_{\mathrm{O}}}{\mathrm{d}\zeta} = m_{\mathrm{O}}, \tag{6.31}$$

followed by a second quadrature to provide the relationships

$$\theta = -y_{\mathrm{O}} - \gamma_{\mathrm{F}} m_{\mathrm{O}} \zeta + C_1 \quad \text{and} \quad \frac{y_{\mathrm{F}}}{L_{\mathrm{F}}} = y_{\mathrm{O}} + m_{\mathrm{O}}\zeta + C_2, \tag{6.32}$$

valid everywhere across the reaction layer. The two integration constants C_1 and C_2 are related to those in (6.29) by

$$C_1 = y_{\mathrm{O}}^{+} + \theta^{+} = y_{\mathrm{O}}^{-} + \theta^{-} \quad \text{and} \quad C_2 = \frac{y_{\mathrm{F}}^{+}}{L_{\mathrm{F}}} - y_{\mathrm{O}}^{+} = \frac{y_{\mathrm{F}}^{-}}{L_{\mathrm{F}}} - y_{\mathrm{O}}^{-}, \tag{6.33}$$

as can be obtained by substitution of (6.29) into (6.32). The interpretation of these constants becomes more evident when the two relations (6.32) are written in terms of the excess enthalpy and generalized mixture fraction, respectively, to give the expressions

$$H - H_f = \left.\frac{\mathrm{d}H}{\mathrm{d}z}\right|_{z_f} (z - z_f) + \beta^{-1} C_1 \quad \text{and} \quad \tilde{Z} - \tilde{Z}_{st} = \left.\frac{\mathrm{d}\tilde{Z}}{\mathrm{d}z}\right|_{z_f} (z - z_f) + \beta^{-1}\tilde{Z}_{st} C_2, \tag{6.34}$$

which indicate that C_1 and C_2 are apparent shifts of order β^{-1} in the level of H and $\tilde{Z}$ at the flame from their Burke-Schumann values H_f and $\tilde{Z}_{st}$.

6.5.2 The canonical problem

Using (6.32) to write the reaction rate in terms of y_{O} reduces the last equation in (6.27) to

$$\frac{\mathrm{d}^2 y_{\mathrm{O}}}{\mathrm{d}\zeta^2} = \frac{B\beta^{-3} L_{\mathrm{F}}}{A_s T_f^{1+\sigma}} e^{-T_a/T_f} y_{\mathrm{O}} \left(y_{\mathrm{O}} + m_{\mathrm{O}}\zeta + C_2\right) \exp\left(-y_{\mathrm{O}} - \gamma_{\mathrm{F}} m_{\mathrm{O}}\zeta + C_1\right). \tag{6.35}$$

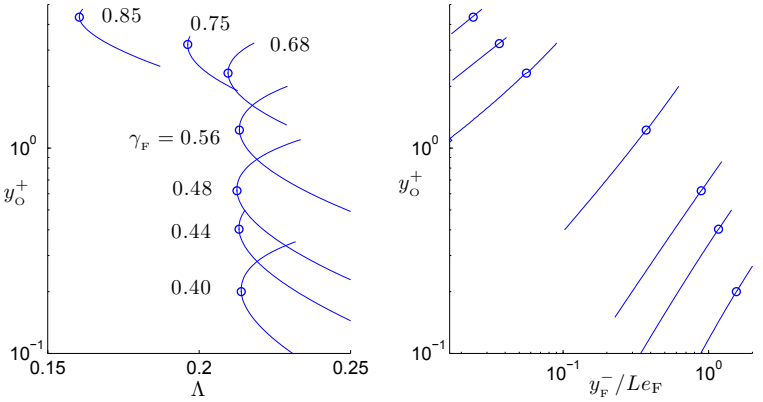

Figure 6.2. The solution of the canonical problem (6.36) for the values of the heat-loss parameter γ_F indicated by the squares in Fig. 6.1. The circles denote the conditions at the minimum value of Λ for each γ_F.

Introducing the normalized coordinate $\xi = m_O\zeta + C_2$ enables the problem to be written in the canonical form

$$\frac{d^2y_O}{d\xi^2} = \Lambda y_O(y_O + \xi)e^{-y_O-\gamma_F\xi} \begin{cases} y_O = y_O^+ & \text{as} \quad \xi \to +\infty \\ y_O + \xi = y_F^-/L_F & \text{as} \quad \xi \to -\infty \end{cases} \tag{6.36}$$

in terms of the reactant leakages y_O^+ and y_F^-. The balance between chemical reaction and diffusion is measured in (6.36) by the parameter

$$\Lambda = \mathcal{D}\exp(C_1 + \gamma_F C_2), \tag{6.37}$$

involving the relevant Damköhler number

$$\mathcal{D} = \frac{B}{A_s}\frac{L_F\beta^{-3}}{m_O^2 T_f^{1+\sigma}}e^{-T_a/T_f}, \tag{6.38}$$

a nondimensional measure of the strain time A_s^{-1} at extinction that embodies the correct balance between B and E associated with the double asymptotic limit implied by (6.10).

For a given value of γ_F, determined from the outer solution, the integration of (6.36) provides the inner structure of the reaction layer for different values of Λ, including the reactant leakages. For the values $0 < \gamma_F < 1$ that apply to most conditions of practical interest, two solutions are found for Λ above a critical value Λ_E and no solution exists for $\Lambda < \Lambda_E$. To handle effectively the

resulting multiplicity and determine accurately the solution near the turning point, instead of solving (6.36) for a known value of Λ, it is convenient to pose the problem as that of finding the solution for a given oxygen leakage y_{O}^{+}. The value of Λ is correspondingly determined as the eigenvalue that satisfies the boundary condition $\mathrm{d}y_{\mathrm{O}}/\mathrm{d}\xi = -1$ as $\xi \to -\infty$. Increasing the value of y_{O}^{+} in successive integrations provides the evolution of Λ with y_{O}^{+} as well as the accompanying value of $y_{\mathrm{F}}^{-}/L_{\mathrm{F}}$, obtained by evaluating $y_{\mathrm{O}} + \xi$ for $\xi \to -\infty$, giving the results shown in Fig. 6.2. The integrations cover seven different values of γ_{F}, corresponding to representative values of α selected for the previous heptane computations, as indicated by the squares in the lower right plot of Fig. 6.1.

6.6 Evaluation of the extinction conditions

As explained above, given the properties of the fuel, the boundary temperatures, and the spray parameters St and α, one may solve the counterflow spray problem in the limit of infinitely fast reaction (using the coupling-function formulation or otherwise) to determine the flame location z_f, the peak temperature T_f, the reactant consumption rates m_{O} and $m_{\mathrm{F}} = m_{\mathrm{O}}/S$, and the heat-loss parameters $\gamma_{\mathrm{F}} = 1 - \gamma_{\mathrm{O}}$. The associated outer profiles appear in the coefficients of the linear equations (6.12)–(6.17), which can be therefore integrated to determine the values of the factors $a_{ij}^{\pm}$ in (6.22)–(6.26) for a given Burke-Schumann solution. Also, the heat-loss parameter γ_{F} can be used when solving the canonical problem (6.36), which gives the variation of Λ and y_{F}^{-} with y_{O}^{+}.

The critical value of the strain rate is determined by the minimum value of $\mathcal{D}$ for which a solution exists, associated with an intermediate value of the oxygen leakage y_{O}^{+}. Since the constants C_1 and C_2 appearing in (6.37) are in general nonzero, this minimum value cannot be evaluated directly from the turning point in Fig. 6.2, but rather from the turning point of the associated curve of $\mathcal{D}$ as a function of y_{O}^{+}, determined from (6.37) once the value of $C_1 + \gamma_{\mathrm{F}} C_2$ is computed for a given value of y_{O}^{+}.

The calculation of C_1 and C_2 involves the simultaneous determination of the fourteen additional unknowns $u_{1_f}^{-}$, $A_{1_f}^{\pm}$, $T_{1_f}^{\pm}$, $Y_{\mathrm{F}1}^{\pm}$, $\hat{Y}_{\mathrm{O}1_f}^{\pm}$, $\theta^{\pm}$, $y_{\mathrm{F}}^{\pm}$, and y_{O}^{-}. The sixteen equations required to determine the solution include the five equations generated by substituting the expressions (6.22)-(6.26) into (6.20) and (6.21), the six matching conditions (6.30), the four identities (6.33), and the relationship between y_{F}^{-} and y_{O}^{+} displayed in the right-hand-side plot of Fig. 6.2. Once the system is solved for C_1 and C_2 as a function of y_{O}^{+}, it is straightforward to evaluate from (6.37) the Damköhler number $\mathcal{D} = \Lambda \exp(C_1 + \gamma_{\mathrm{F}} C_2)$ using the

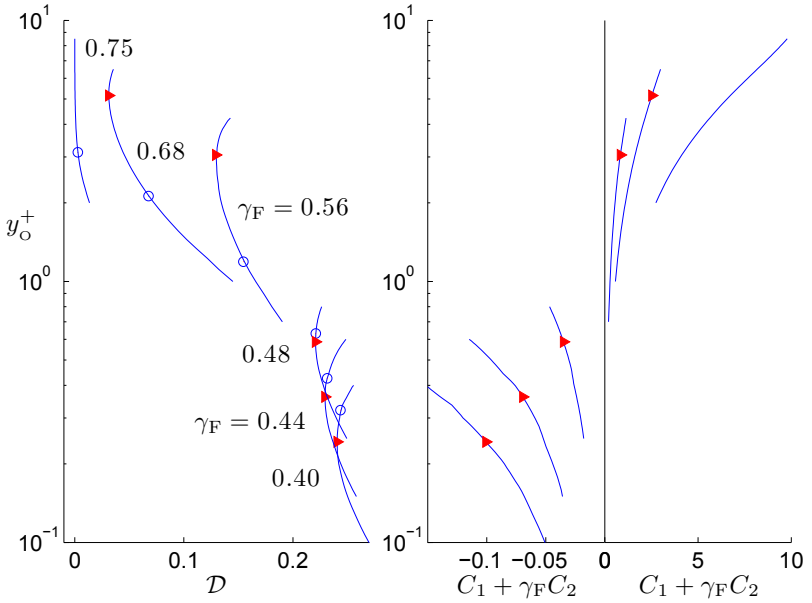

Figure 6.3. The variation of $\mathcal{D}$ with y_{O}^+ for the seven flames indicated by the squares in Fig. 6.1.

function $\Lambda(y_{\mathrm{O}}^+)$ shown in the left-hand-side plot of Fig. 6.2.

Sample results corresponding to the conditions indicated by the squares in Fig. 6.1 are shown in Fig. 6.3, where extinction curves for increasing γ_{F} correspond to increasing spray dilution (smaller values of α). A triangle is used to mark the turning points characterizing the extinction conditions. Also, a circle is placed along the curves in Fig. 6.3 to denote the oxygen leakage corresponding to the turning point of the canonical solution represented in Fig. 6.2.

For the range of values of α investigated, the results reveal a monotonic dependence of the critical extinction conditions on the spray dilution. As can be seen in Fig. 6.1 for decreasing values of α (i.e., increasing values of γ_{F}) the flame moves towards the spray side of the mixing layer, resulting in weaker flames with smaller consumption rates and smaller temperature increments. Larger values of the spray-side temperature gradient γ_{F} promote the freezing of the chemical reaction, leading to significant oxygen leakage, a result clearly visible in Fig. 6.3. As a consequence, the value of the constant $C_1 + \gamma_{\mathrm{F}} C_2$, which carries the influence of the reactant-leakage perturbations in the outer streams on the extinction process, is found to increase significantly for increasing values

of γ_{F}.

Thus, for $\gamma_{\mathrm{F}} < 0.56$, corresponding to values of $\alpha > 0.1$ in Fig. 6.1, the value of $C_1 + \gamma_{\mathrm{F}} C_2$ is sufficiently small that the associated extinction conditions can be evaluated with reasonably accuracy with (6.37) written in the approximate form $\Lambda \simeq \mathcal{D}$ by using the definition (6.38) together with the critical conditions given by the canonical problem (i.e., the turning points in Fig. 6.2). This simplified evaluation procedure, independent of the first-order corrections in the outer regions, requires only the leading-order information provided by the Burke-Schumann solution, displayed in Fig. 6.1.

On the other hand, for very dilute spray flames with $\alpha < 0.1$, the corrections associated with the nonzero value of $C_1 + \gamma_{\mathrm{F}} C_2$ become quantitatively important and can no longer be neglected when evaluating the critical value of $\mathcal{D}$. The correction is so large for $\gamma_{\mathrm{F}} = 0.75$ that the corresponding extinction curve does not display a turning point up to the largest value of y_{O}^{+} considered in the figure. Clearly, since the associated leakage becomes so pronounced, the diffusion-flame regime is no longer applicable near extinction, so that in addressing these dilute flames one should consider instead the premixed-flame regime, including at leading order oxygen leakage of order unity and frozen flow, rather than equilibrium flow, on the spray side of the flame. Nevertheless, the practical relevance of these extremely dilute spray flames is questionable in view of the limited associated heat release, which would lead to peak temperatures below the minimum crossover temperature required for hydrocarbon oxidation, as can be inferred from the plot in Fig. 6.1.

6.7 Conclusions

We have used the two-continua formulation to investigate strain-induced extinction of counterflow spray diffusion flames, with a one-step Arrhenius reaction adopted to model the chemical reaction. Although the formal asymptotic description of the critical extinction conditions in the limit of large activation energy requires consideration of two terms in the outer frozen regions, including the perturbations associated with reactant leakage, it is found that the quantitative effect of these perturbations is limited as long as the spray is not too dilute, so that the information provided by the leading-order Burke-Schumann solution combined with the leading-order solution for the inner reaction layer (whose reaction-diffusion structure is independent of the flow configuration) enables sufficiently accurate quantitative predictions to be made in many instances. The results further indicate that, since the occurrence of extinction depends critically on the reaction-layer temperature through the

exponential term in the Damköhler-number definition (6.38), computations of spray diffusion flames based on source-free mixture-fraction variables that do not account for fuel-production associated with droplet vaporization or for differential diffusion of the fuel vapor are doomed because of their anticipated inability to predict correctly peak temperatures.

References

[1] A. Liñán, The asymptotic structure of counterflow diffusion flames for large activation energies, Acta Astronautica 1 (7) (1974) 1007–1039.

[2] A. Liñán, M. Vera, A. L. Sánchez, Ignition, liftoff, and extinction of gaseous diffusion flames, Annual Review of Fluid Mechanics 47 (2015) 293–314.

[3] A. Liñán, The structure of diffusion flames, in: M. Onofri, A. Tesei (Eds.), Fluid dynamical aspects of combustion theory, Longman Scientific Technical Essex, 1991, pp. 11–19.

[4] A. Liñán, Diffusion-controlled combustion, in: H. Aref, J. W. Phillips (Eds.), Mechanics for a New Millenium, Kluwer Acad. Dordrecht, Holland, 2001, pp. 487–502.

[5] A. Liñán, in: J. Jiménez (Ed.), The Role of Coherent Structures in Modelling Turbulence and Mixing, 1981, pp. 333–339.

[6] S. H. Chung, C. K. Law, Structure and extinction of convective diffusion flames with general lewis numbers, Combustion and Flame 52 (1983) 59–79.

[7] J. S. Kim, F. A. Williams, Extinction of diffusion flames with nonunity lewis numbers, Journal of engineering mathematics 31 (2-3) (1997) 101–118.

[8] S. Cheatham, M. Matalon, A general asymptotic theory of diffusion flames with application to cellular instability, Journal of Fluid Mechanics 414 (2000) 105–144.

[9] J. Greenberg, A. Dvorjetski, Opposed flow polydisperse spray diffusion flames: steady state and extinction analysis, Combustion Theory and Modelling 7 (1) (2003) 145–162.

CHAPTER
SEVEN

Concluding remarks and future prospects

This final chapter summarizes the main conclusions of this dissertation and suggests future research lines in the field of spray combustion.

7.1 Conclusions and summary of the results

As explained above, remarkable progress has been made over the past fifty years regarding the mathematical description of reactive spray flows by exploiting judiciously the disparity of length and time scales present in the problem. Reasons for the validity and limitations of the continuum description of the gas and liquid phases in the vaporization and combustion of sprays in diesel engines and liquid-fueled gas turbines have been indicated in Chapter 2. The resulting homogenized description, given in Chapter 3, can be used for the direct numerical simulation of turbulent reacting sprays and also as starting point for Reynolds-averaged representations of these flows. We have aimed to show in this dissertation how consideration of canonical model problems can be instrumental for the analysis of spray-combustion phenomena. In particular, we have tried to illustrate, with the examples of the coflow and counterflow mixing-layer configurations, how by the careful nondimensional formulation of the problems they can become a tool to gain understanding of the dynamics of sprays. The main results pertaining to the canonical problems are presented in Chapters 4–6. Besides, three separate appendixes are included containing additional results corresponding to the spherical droplet cloud, the canonical configuration preferred by the early researchers, and also complementary investigations of different aspects of coflow and counterflow flames.

The laminar coflow mixing-layer configuration is used in Chapter 4 to investigate spray autoignition processes. Different ignition modes have been identified depending on the thermochemical properties of the liquid fuel and the type of spray-carrier gas (inert or oxidizer, as shown in Fig. 4.3). For nonpremixed configurations in which a spray of heptane droplets is carried by an inert gas, ignition is seen to occur as a precipitous temperature increase at

a localized ignition kernel that serves to anchor a tribrachial flame structure with rich and lean premixed branches and a trailing diffusion flame. By way of contrast, when the properties of methanol are used in the nonpremixed integrations, ignition is seen to occur more gradually, in the form of a a deflagration originating on the air side that travels towards the spray side. The occurrence of gradual or abrupt ignition is controlled by the fuel availability in the ignition region and the associated temperature increase due to the chemical reaction; these in turn depend on the volatility and diffusivity of the fuel and on its heat of combustion, leading to the criterion (4.40) for the occurrence of a thermal runaway. As seen in Fig. 4.9, an asymptotic analysis based on the large value of the activation temperature provides reasonably accurate predictions of ignition distances for configurations where ignition occurs as a thermal runaway.

Two different ignition regimes are also encountered when we analyze the partially premixed configuration corresponding to sprays introduced into the combustion chamber by air. The main differences with respect to the case when the spray is carried by an inert gas pertain to the downstream flame development. Depending on the fuel thermochemical properties, the numerical integrations of partially premixed spray systems give either solutions including a lean deflagration propagating into the spray followed by a region of distributed reaction, as occurs predominantly when the methanol properties are employed in the integrations because of its limited volatility, or a double-flame configuration including a rich deflagration and a diffusion flame bounding an intermediate oxygen-free region where the droplets vaporize to generate a large fuel-vapor pocket, as occurs in our computations when the heptane properties are considered.

A second canonical configuration, useful in addressing effects of strain on spray diffusion flames, is the self-similar counterflow mixing layer between a spray stream of fuel droplets carried by an inert gas and an opposite stream of hot air. This is investigated in Chapter 5 on the basis of the two-continua spray formulation in the two limiting cases of frozen gas-phase reactions and infinitely fast reaction. For the moderately large values of the Reynolds number typically found in experimental counterflow-spray configurations, the mixing between the air and the spray streams is confined to a separating mixing layer of thickness δ_m, small compared with the radius R of the supply stream and the distance H between the injectors. As often occurs in experiments, the droplets are assumed to be injected in the outer nearly inviscid region, at distances $z_I \gg \delta_m$. For small values of the initial liquid mass-loading ratio α, there is only one-way coupling between the droplets and the gas in the spray stream outside the mixing layer, so that the gas velocity can be determined independently

of the liquid phase, and then used to compute the droplet motion from the injection plane towards the stagnation plane before the edge of the mixing layer. Because of their diverging radial motion, only the droplets initially located near the axis eventually enter the self-similar region of the mixing-layer around the stagnation point, so that the computation of the droplet evolution can be restricted to the near-axis region. The analysis, which provides the droplet velocity and droplet number density as the stagnation plane is approached, leads to identification of two different regimes depending on the value of the droplet Stokes number St, defined as the ratio of the droplet deceleration time to the strain time in the nearly inviscid gas flow on the spray side of the stagnation point. For $\mathrm{St} < 1/4$, the droplet axial velocity in the spray stream vanishes at the stagnation plane, indicating that these droplets enter the mixing layer where they can vaporize, producing fuel vapor that can react there with the oxygen that diffuses from the air side. By way of contrast, for $\mathrm{St} > 1/4$ the droplets cross the stagnation plane with a velocity smaller than, although comparable to, the injection velocity, penetrating large distances of order $z_I \sim H \gg \delta_m$ into the air stream, where they can vaporize. For the case of fast reaction rates, this second regime gives a diffusion flame standing far on the air side of the counterflow, outside the mixing layer.

The counterflow configuration is also analyzed in Chapter 6 to examine strain-induced extinction of spray diffusion flames with a one-step Arrhenius model for the chemical reaction. We focus on dilute configurations with small initial values of the liquid mass-loading ratio α of the order of or only moderately large compared with S^{-1}, where $S \simeq 15$ is the mass of air needed to burn the unit mass of fuel vapor, enough to generate flame temperatures on the order of the stoichiometric adiabatic flame temperature. Attention is restricted to droplets with Stokes number $\mathrm{St} < 1/4$, for which the flame lies in the mixing layer separating the spray stream from the air stream. The analysis, which includes variable density and variable transport properties, extends the large-activation-energy analysis of extinction of gaseous diffusion flames [1] by accounting for the presence of the droplets as well as the limited molecular diffusivity of the fuel vapor. The Burke-Schumann analysis of Chapter 5 provides the basic flame structure, including the flame location, its associated peak temperature, the reactant mass consumption rates, and the fraction of heat release transferred to each side of the flame. The determination of the critical extinction conditions requires consideration of finite-rate perturbations, which, although small for large activation energies under near-extinction conditions, cause a lowering of the flame temperature below the Burke-Schumann value, sufficient to freeze the reaction on the outer sides of the reaction layer, thereby resulting in

leakage of the reactants. The flame structure is finally obtained by matching the inner reaction layer with two terms in the expansions for the outer chemically frozen transport regions; extinction corresponding to a bending bifurcation in the curve representing the fuel leakage as a function of an appropriately reduced Damköhler number (the ratio of the relevant flame chemical time to the strain time). Evaluation of the results reveals that for $\alpha \gtrsim S^{-1}$ extinction occurs in the diffusion-flame regime with limited reactant leakage, such that the associated corrections to the extinction predictions resulting from the first-order nonequilibrium perturbations in the outer regions remain small. For extremely small values of α, however, the flame is seen to migrate from the stagnation plane towards the spray side of the mixing layer, developing a pronounced temperature gradient on the spray side of the flame that freezes the chemical reaction and promotes significant oxygen leakage. Closed-form evaluation of extinction conditions for those extremely dilute spray flames would require consideration of the premixed-flame regime with oxygen leakage of order unity and frozen flow, rather than equilibrium flow, at leading order on the spray side of the flame.

7.2 Future prospects

Finite-rate effects, controlling the transition from the non-reacting mode to the diffusion-controlled mode, have been limited here to an Arrhenius reaction for the computation of ignition and extinction in mixing-layer configurations. These results should be extended in future work to more realistic chemical schemes, needed for reliable predictions of finite-rate chemical effects in spray flames, including ignition distances and critical conditions for strain-induced extinction, the latter considered earlier [2]. It is anticipated that, although the associated detailed chemistry involves typically hundreds of intermediate species and a few thousand elementary reactions [3], systematic chemical-kinetic reduced mechanisms based on steady-state approximations for intermediates [4] should suffice to describe accurately most finite-rate aspects of spray flames, including pollutant emissions.

Despite the significant progress made in recent years, our understanding of spray-combustion phenomena is far from complete. Improved descriptions of the hydrodynamic instabilities leading to liquid-jet atomization and of droplet breakup and coalescence processes occurring in the secondary atomization region are needed. Although investigations focused on the dynamics of momentum transfer in particle-laden turbulent flows have contributed valuable understanding of the essential mechanisms leading to droplet dispersion in

spray jets, including effects associated with turbulent kinetic-energy modulation by the solid phase as well preferential concentration [5] (both having important implications for subgrid-scale modeling [6–9]), the needed extension to spray turbulent combustion necessitates the additional consideration of two-way mass and thermal-energy transfer processes.

The current trends that gear designs of diesel engines towards higher compression ratios promote increasing interest in spray combustion under supercritical conditions [10]. Since the liquid fuel is seldom preheated before injection, the presence of both subcritical and supercritical conditions in the combustion chamber is warranted. This requires simultaneous consideration of the liquid phase, which may contain droplets and ligaments, in addition to the gas phase and the supercritical mixture, with the spatial location of the transcritical conditions being determined by the capabilities of the hot environment to heat up the liquid fuel to its critical temperature. Clearly, the different simplifications stemming in our analysis from the condition $\rho_l/\rho \gg 1$ do not apply to the description of the supercritical fluid. Although analyses of droplet vaporization and combustion have addressed supercritical conditions [11], including transient effects associated with shorter life times [12, 13], more work is needed to provide reliable droplet submodels.

Considerable advances have been made in recent years in understanding the onset and development of thermoacoustic instabilities in gaseous combustion [14–16]. Extension to spray combustion of predictive capabilities developed for gaseous combustion instabilities requires the consideration of finite inertia of the liquid phase, which responds to pressure oscillations with a characteristic delay that depends on the Stokes number [17, 18]. In this regard, recent investigations have been carried out to model spray-flame transfer functions using numerical simulations [19] and experiments [20–22], of interest for the development of reduced-order models. Use of reduced chemical-kinetic mechanisms may facilitate quantitative predictions, in particular in connection with $\mathrm{LOx/H_2}$ systems, for which sufficiently accurate chemistry models are available [23].

A number of modeling issues remain to be resolved. For example, the direct extension to spray combustion of flamelet approaches for the modeling of turbulent reacting flows appears to be nontrivial. Since both premixed and non-premixed flames can coexist in liquid-fueled burners [24–30], the accuracy of modeling strategies based on either premixed or non-premixed flamelets is necessarily limited, so that the use of hybrid models must be considered in spray-combustion applications. In contrast to gaseous flamelets, in which the local strain rate is often sufficient to parametrize the entire manifold of solutions, spray flamelets display a richer parametric dependence, as can be in-

ferred from the counterflow results presented above. On the other hand, the gas mixture fraction, which provides a one-to-one mapping between physical and mixture-composition spaces in gaseous combustion, becomes non-monotonic in spray flames because of droplet vaporization [31, 32]. This, in turn, prevents straightforward tabulation of the flamelet variables, and introduces additional difficulties for modeling the scalar dissipation rate, which strongly departs from its gaseous counterpart. Alternative definitions of mixture-fraction variables incorporating the liquid fuel have been proposed [33], but those appear to become more effective for numerical simulations that resolve the spray down to droplet scales including the liquid-gas interface. A different approach that parallels the treatment of gaseous combustion involves the use of a mixture fraction that satisfies a source-free transport equation [34], thereby simplifying greatly the numerical integration. Such a mixture fraction cannot be derived, however, from the original conservation equations, a shortfall of the formulation that necessarily limits its descriptive capability (e.g., the location of the stoichiometric mixture fraction in physical space is not related in any way to the flame position). Clearly, many of these modeling difficulties are not present when the droplets are so small that they heat up and vaporize very fast while following closely the gaseous streamlines, under which conditions a quasi-gaseous flamelet formulation based on the counterflow configuration may be used, including modified boundary conditions on the fuel side that account for the enthalpy loss required for droplet vaporization [35].

References

[1] A. Liñán, The asymptotic structure of counterflow diffusion flames for large activation energies, Acta Astronautica 1 (7) (1974) 1007–1039.

[2] E. Gutheil, W. A. Sirignano, Counterflow spray combustion modeling with detailed transport and detailed chemistry, Combustion and Flame 113 (1) (1998) 92–105.

[3] Z. Luo, S. Som, S. M. Sarathy, M. Plomer, W. J. Pitz, D. E. Longman, T. Lu, Development and validation of an n-dodecane skeletal mechanism for spray combustion applications, Combustion theory and modelling 18 (2) (2014) 187–203.

[4] N. Peters, B. Rogg, Reduced kinetic mechanisms for applications in combustion systems, Lecture notes in Physics 15, Springer-Verlag, 1993.

[5] S. Balachandar, J. K. Eaton, Turbulent dispersed multiphase flow, Annual Review of Fluid Mechanics 42 (2010) 111–133.

[6] W. R. Michałek, J. G. M. Kuerten, J. C. H. Zeegers, R. Liew, J. Pozorski, B. J. Geurts, A hybrid stochastic-deconvolution model for large-eddy simulation of particle-laden flow, Physics of Fluids (1994-present) 25 (12) (2013) 123302.

[7] G. Jin, J. Zhang, G.-W. He, L.-P. Wang, Assessment of large-eddy simulation in capturing preferential concentration of heavy particles in isotropic turbulent flows, Physica Scripta 2010 (T142) (2010) 014061.

[8] P. Fede, O. Simonin, P. Villedieu, K. Squires, Stochastic modeling of the turbulent subgrid fluid velocity along inertial particle trajectories, Proceeding of the Summer Program Center for Turbulence Research Stanford University, Stanford, CA, July (2006) 247–258.

[9] M. Moreau, O. Simonin, B. Bédat, Development of gas-particle euler-euler les approach: a priori analysis of particle sub-grid models in homogeneous isotropic turbulence, Flow, turbulence and combustion 84 (2) (2010) 295–324.

[10] R. N. Dahms, J. Manin, L. M. Pickett, J. C. Oefelein, Understanding high-pressure gas-liquid interface phenomena in diesel engines, Proceedings of the Combustion Institute 34 (1) (2013) 1667–1675.

[11] C. Sánchez Tarifa, A. Crespo Martínez, E. Fraga, A theoretical model for the combustion of droplets in supercritical conditions and gas pockets, Acta Astronautica 17 (1972) 685–692.

[12] W. A. Sirignano, Fluid dynamics and transport of droplets and sprays, 2nd edition, Cambridge University Press, Cambridge, UK., 2010.

[13] J. Shuen, V. Yang, C. Hsiao, Combustion of liquid-fuel droplets in supercritical conditions, Combustion and Flame 89 (3) (1992) 299–319.

[14] D. Veynante, T. Poinsot, Theoretical and numerical combustion, Philadelphia: Edwards.

[15] T. C. Lieuwen, V. Yang, Combustion instabilities in gas turbine engines(operational experience, fundamental mechanisms and modeling), Progress in astronautics and aeronautics.

[16] Y. Huang, V. Yang, Dynamics and stability of lean-premixed swirl-stabilized combustion, Progress in Energy and Combustion Science 35 (4) (2009) 293–364.

[17] P. CLAVIN, J. SUN, Theory of acoustic instabilities of planar flames propagating in sprays or particle-laden gases, Combustion science and technology 78 (4-6) (1991) 265–288.

[18] C. Clanet, G. Searby, P. Clavin, Primary acoustic instability of flames propagating in tubes: cases of spray and premixed gas combustion, Journal of Fluid Mechanics 385 (1999) 157–197.

[19] C. Pera, J. Reveillon, Direct numerical simulation of spray flame/acoustic interactions, Proceedings of the Combustion Institute 31 (2) (2007) 2283–2290.

[20] E. Mastorakos, Ignition of turbulent non-premixed flames, Progress in Energy and Combustion Science 35 (1) (2009) 57–97.

[21] P. Gajan, A. Strzelecki, B. Platet, R. Lecourt, F. Giuliani, Investigation of spray behavior downstream of an aeroengine injector with acoustic excitation, Journal of propulsion and power 23 (2) (2007) 390–397.

[22] T. Providakis, L. Zimmer, P. Scouflaire, S. Ducruix, Characterization of the acoustic interactions in a two-stage multi-injection combustor fed with liquid fuel, Journal of Engineering for Gas Turbines and Power 134 (11) (2012) 111503.

[23] A. L. Sánchez, F. A. Williams, Recent advances in understanding of flammability characteristics of hydrogen, Progress in Energy and Combustion Science 41 (2014) 1–55.

[24] S. C. Li, F. A. Williams, Experimental and numerical studies of two-stage methanol flames, in: Symposium (International) on Combustion, Vol. 26, Elsevier, 1996, pp. 1017–1024.

[25] S. Marley, E. Welle, K. Lyons, W. Roberts, Effects of leading edge entrainment on the double flame structure in lifted ethanol spray flames, Experimental thermal and fluid science 29 (1) (2004) 23–31.

[26] J. Reveillon, L. Vervisch, Analysis of weakly turbulent dilute-spray flames and spray combustion regimes, Journal of Fluid Mechanics 537 (2005) 317–347.

[27] M. Mikami, Y. Mizuta, Y. Tsuchida, N. Kojima, Flame structure and stabilization of lean-premixed sprays in a counterflow with low-volatility fuel, Proceedings of the Combustion Institute 32 (2) (2009) 2223–2230.

[28] K. Luo, H. Pitsch, M. G. Pai, O. Desjardin, Direct numerical simulations and analysis of three-dimensional n-heptane spray flames in a model swirl combustor, Proc. Comb. Inst. 89 (2011) 1447–1460.

[29] D. Martínez-Ruiz, J. Urzay, A. L. Sánchez, A. Liñán, F. A. Williams, Dynamics of thermal ignition of spray flames in mixing layers, Journal of Fluid Mechanics 734 (2013) 387–423.

[30] B. Franzelli, B. Fiorina, N. Darabiha, A tabulated chemistry method for spray combustion, Proceedings of the Combustion Institute 34 (1) (2013) 1659–1666.

[31] C. Hollmann, E. Gutheil, Modeling of turbulent spray diffusion flames including detailed chemistry, in: Symposium (international) on combustion, Vol. 26, Elsevier, 1996, pp. 1731–1738.

[32] C. Hollmann, E. Gutheil, Diffusion flames based on a laminar spray flame library, Combustion science and technology 135 (1-6) (1998) 175–192.

[33] R. Bilger, A mixture fraction framework for the theory and modeling of droplets and sprays, Comb. Flame 158 (2011) 191–202.

[34] N. Peters, Turbulent combustion, Cambridge university press, 2000.

[35] Y. Baba, R. Kurose, Analysis and flamelet modelling for spray combustion, Journal of Fluid Mechanics 612 (2008) 45–79.

APPENDIX

A

Vaporization of fuel-spray clouds

A.1 The continuum, homogenized description of droplet-cloud vaporization

Let us consider the temporal evolution of a spherical cloud of radius R_o containing air and N_o uniformly distributed droplets of radius a_o and initial temperature T_I. An unbounded atmosphere of hot air with temperature $T_A > T_I$ and density ρ_A surrounds the cloud. The initial number of droplets per unit volume in the cloud, $n_o = N_o/[(4/3)\pi R_o^3]$, defines the interdroplet distance $l_d = n_o^{-1/3}$, which is assumed to be in the range $R_o \gg l_d \gg a_o$, so that the condition (2.7) is satisfied. The droplet number density together with the droplet radius and the gas density defines the liquid mass-loading ratio, $\alpha = (4\pi/3)a_o^3 n_o \rho_l/\rho_A$; when $\alpha \sim 1$ we can expect two-way coupling between the phases. The cloud evolution is mainly determined by the competition of droplet vaporization with heat conduction across the droplet cloud. The rate of the former is measured by the characteristic droplet vaporization time t_v, given in (3.26) as a function of the initial values of the droplet radius a_o and air density and thermal diffusivity ρ_A and D_{T_A}, whereas the heat conduction time based on the cloud radius $t_c = R_o^2/D_{T_A}$ characterizes gas-phase heat conduction from the surrounding atmosphere. Another significant parameter is T_A/T_B.

The description of the problem delineated above requires integration of (3.6), (3.7), and (3.10) for the gas phase together with (3.1)–(3.5) for the liquid phase, supplemented with the equation of state and with additional equations for the droplet source terms $\mathbf{f}$, $\dot{m}$, and $\dot{q}_d$. Since the heat needed to heat up and vaporize the equilibrium droplet cloud must come from the surrounding hot air, it is appropriate to use the heat conduction time t_c to scale the problem. Introducing the dimensionless variables $\hat{t} = t/t_c$, $\hat{r} = r/R_o$, $\hat{v} = v_r/(D_{T_A}/R_o)$, $\hat{T} = T/T_A$, $\hat{\rho} = \rho/\rho_A$, $\hat{n} = n/n_o$, $\hat{a} = a/a_o$, $\hat{T}_d = T_d/T_A$, and $\hat{v}_d = v_{d_r}/(D_{T_A}/R_o)$, reduces

the conservation equations for the gas phase to

$$\frac{\partial\hat{\rho}}{\partial\hat{t}}+\frac{1}{\hat{r}^2}\frac{\partial}{\partial\hat{r}}\left(\hat{r}^2\hat{\rho}\hat{v}\right)=\alpha\frac{t_c}{t_v}\hat{n}\hat{a}\hat{T}^{\sigma}\lambda \tag{A.1}$$

$$\frac{\partial\hat{\rho}Y_{\mathrm{F}}}{\partial\hat{t}}+\frac{1}{\hat{r}^2}\frac{\partial}{\partial\hat{r}}\left(\hat{r}^2\hat{\rho}\hat{v}Y_{\mathrm{F}}\right)-\frac{1}{\hat{r}^2}\frac{\partial}{\partial\hat{r}}\left(\frac{\hat{r}^2\hat{T}^{\sigma}}{\mathrm{Le}_{\mathrm{F}}}\frac{\partial Y_{\mathrm{F}}}{\partial\hat{r}}\right)=$$

$$\alpha\frac{t_c}{t_v}\hat{n}\hat{a}\hat{T}^{\sigma}\lambda, \tag{A.2}$$

$$\frac{\partial\hat{\rho}\hat{T}}{\partial\hat{t}}+\frac{1}{\hat{r}^2}\frac{\partial}{\partial\hat{r}}\left(\hat{r}^2\hat{\rho}\hat{v}\hat{T}\right)-\frac{1}{\hat{r}^2}\frac{\partial}{\partial\hat{r}}\left(\hat{r}^2\hat{T}^{\sigma}\frac{\partial\hat{T}}{\partial\hat{r}}\right)=$$

$$-\alpha\frac{t_c}{t_v}\hat{n}\hat{a}\hat{T}^{\sigma}\left[(\hat{T}-\hat{T}_d)\frac{\lambda}{e^{\lambda}-1}-\hat{T}_d\lambda\right], \tag{A.3}$$

to be supplemented with $\hat{\rho}\hat{T}=[1-(1-M_A/M_{\mathrm{F}})Y_{\mathrm{F}}]^{-1}$, where M_A/M_{F} denotes the air-to-fuel molecular-mass ratio. A simple power law with exponent $\sigma=0.7$ has been adopted for the temperature dependence of the transport coefficients. Radiative heat transfer has been neglected in writing (A.3), along with changes in specific heat. The source terms in (A.1)–(A.3) are proportional to $\hat{n}$, which satisfies the conservation law

$$\frac{\partial\hat{n}}{\partial\hat{t}}+\frac{1}{\hat{r}^2}\frac{\partial}{\partial\hat{r}}\left(\hat{r}^2\hat{n}\hat{v}_d\right)=0, \tag{A.4}$$

involving the droplet velocity $\hat{v}_d$. This parabolic system of equations must be complemented with the simultaneous Lagrangian description of the variation of the droplet properties $\hat{a}$, $\hat{T}_d$, $\hat{v}_d$, given by

$$\frac{\mathrm{d}\hat{a}^3}{\mathrm{d}\hat{t}}=-\frac{t_c}{t_v}\hat{a}\hat{T}^{\sigma}\lambda \tag{A.5}$$

$$\hat{a}^3\frac{\mathrm{d}\hat{T}_d}{\mathrm{d}\hat{t}}=\frac{t_c}{t_v}\frac{c_p}{c_l}\hat{a}\hat{T}^{\sigma}\left[(\hat{T}-\hat{T}_d)\frac{\lambda}{e^{\lambda}-1}-\frac{L_v}{c_pT_A}\lambda\right], \tag{A.6}$$

$$\hat{a}^3\frac{\mathrm{d}\hat{v}_d}{\mathrm{d}\hat{t}}=\frac{3Pr}{2}\frac{t_c}{t_v}\hat{a}\hat{T}^{\sigma}(\hat{v}-\hat{v}_d), \tag{A.7}$$

along the droplet paths $\hat{r}_d(\xi,\hat{t})$, given by the solution of $\mathrm{d}\hat{r}_d/\mathrm{d}\hat{t}=\hat{v}_d$ in terms of its initial radial location $\hat{r}_d=\xi$. The source terms in the above equations, which are proportional to $\dot{m}$ and $\dot{q}_d$, have been written using (3.13) and (3.16) in terms of λ, which is determined using (3.17), i.e., $\lambda=\mathrm{Le}_{\mathrm{F}}^{-1}\ln[(1-Y_{\mathrm{F}})/(1-Y_{\mathrm{F},S})]$, as a function of Y_{F} and Y_{F_s}. The latter is given by the Clausius-Clapeyron relation (3.18) in terms of $\hat{T}_d$, with $M_{\mathrm{F}}/M_s=Y_{\mathrm{F}_s}+(1-Y_{\mathrm{F}_s})M_{\mathrm{F}}/M_A$, thereby completing the formulation.

Different possible sets of initial conditions can be considered [1]. For example, one may assume that the droplets are suddenly placed in the unperturbed hot-air environment at the start of the integration, with the uniform gas temperature T_A everywhere at $t = 0$. Perhaps a more realistic initial condition, especially in connection with controlled experiments in which the spray is formed upstream from the injection section, follows from assuming that the spray is initially in equilibrium, so that $\lambda = 0$ and $T = T_d$ in the cloud, as is required for the right-hand side terms of (A.1)–(A.3), (A.5) and (A.6) to vanish. The associated initial conditions for (A.1)–(A.4) are $\hat{\rho} - \hat{\rho}_I = \hat{T} - \hat{T}_I = Y_{\text{F}} - Y_{\text{F}_I} = \hat{n} - 1 = 0$ for $\hat{r} \leq 1$ and by $\hat{\rho} - 1 = \hat{T} - 1 = Y_{\text{F}} = \hat{n} = 0$ for $\hat{r} > 1$, where $\hat{\rho}_I$ is the inter-droplet gas density associated with $\hat{T} = \hat{T}_I$ and Y_{F_I}, with Y_{F_I} determined from evaluating (3.18) at $T_d = T_I$. Correspondingly, the integration of (A.5)–(A.7) is initiated with $\hat{a} - 1 = \hat{v}_d = \hat{T}_d - \hat{T}_I = 0$. Boundary conditions for $\hat{t} > 0$, needed to integrate (A.1)–(A.3), are given by $\hat{v} = \partial\hat{T}/\partial\hat{r} = \partial Y_{\text{F}}/\partial\hat{r} = 0$ at $\hat{r} = 0$ and $\hat{T} - 1 = Y_{\text{F}} = 0$ as $\hat{r} \to \infty$.

Many of the early numerical investigations of spherical droplet-cloud vaporization [1–7] neglected the motion of the droplets induced by the gas expansion along with the resulting nonuniformities in $\hat{n}$, both having in general a non-negligible effect on the solution, as shown in [8, 9]. These effects are effectively handled in the multicontinua formulation outlined above. It is worth mentioning that, although the droplets in the interior of the cloud may conceivably accelerate to overtake those located farther outside, with the result that droplets originating at different ξ end up occupying the same radial location, such overtaking events were not observed in computations. If they occur, i.e., for initial conditions or parametric values different from those considered here, the associated duplicity should be taken into account when evaluating the droplet properties at a given location (e.g., by creating a new droplet class containing the droplets that have been overtaken, in a similar procedure as that employed in Chapter 5 for counterflow flames).

Before discussing further the solution, it is worth mentioning the modifications needed to generate additional model problems, useful for investigating different aspects of liquid-fueled systems. For example, the streamwise evolution of laminar spray jets generated by plain-orifice atomizers or issuing from round injectors can be investigated by using the boundary-layer approximation, leading to a set of equations that is fundamentally similar to (A.1)–(A.7), with the time being replaced by the axial distance and the spherical differential operator by its cylindrical counterpart [10]. The description of combustion would require consideration of additional chemical species, as well as inclusion of reaction terms in (A.2) and (A.3). The limit of infinitely fast reactions can be

addressed by formulating the problem in terms of coupling functions. Note that, if a unity Lewis number is assumed for the fuel vapor, as it is appropriate for methanol, then the resulting equation for the mixture fraction would be identical to (A.2), with the mixture-fraction variable Z replacing Y_{F}.

For numerical studies of vaporization and combustion of spray clouds in constant-volume or variable-volume chambers [9], of interest for diesel-engine applications, the term $\mathrm{d}p_o/\mathrm{d}t$ must be retained in writing (A.3) from (3.10), while the effect of the finite size of the combustion chamber could be effectively incorporated by introducing a moving or stagnant external wall at a finite radius $\hat{r} = R_w/R_o$. Since near stoichiometric conditions are of interest in diesel-engine combustion, values of $R_w/R_o \sim (\alpha S)^{1/3}$ should be considered in integrations. Such formulations could be employed to investigate autoignition by compression, providing the distributions of temperature and composition encountered immediately before ignition [11]. They would also be useful for studying the subsequent evolution of the diffusion flame generated upon ignition, which could be described in the limit of infinitely fast reaction.

A.2 Parameters controlling droplet-cloud vaporization

The solution depends on two fundamental independent parameters, the initial mass-loading ratio α, which modulates the extent of interphase coupling, and the characteristic time ratio t_c/t_v, which measures the competition of heat transfer from the surrounding atmosphere with droplet vaporization. The product $\alpha t_c/t_v$, which measures the extent of spray vaporization in (A.1)–(A.3), is essentially the group combustion number G introduced by Chiu and coworkers [2], variants of which were also used by other early investigators [1, 4, 6, 7]. Although $\alpha t_c/t_v$ can be expressed as $\alpha t_c/t_v = 4\pi n_o a_o R_o^2 = 3N_o a_o/R_o \sim N_o^{2/3} a_o/l_d$, involving either the initial droplet-number density n_o or the total number of droplets in the cloud N_o, the physical interpretation of the resulting expressions is not transparent. Besides, accounting separately for the two times involved in the problem facilitates consideration of the effect of enhanced heat transfer by turbulent transport, of interest in realistic applications. For instance, to characterize approximately the rate of heat transfer one could employ the gas-phase effective heat-transfer time $t_c^* = R_o^2/D_t$, defined by replacing the molecular diffusivity with a turbulent diffusivity D_t. Since exchanges between the two phases are still controlled by molecular transport in the immediate vicinity of the droplet, the resulting effective group combustion number $\alpha t_c^*/t_v$ would display a linear dependence on the ratio D_{T_A}/D_t, a function of the flow Reynolds number accounting approximately for the effect of turbulence.

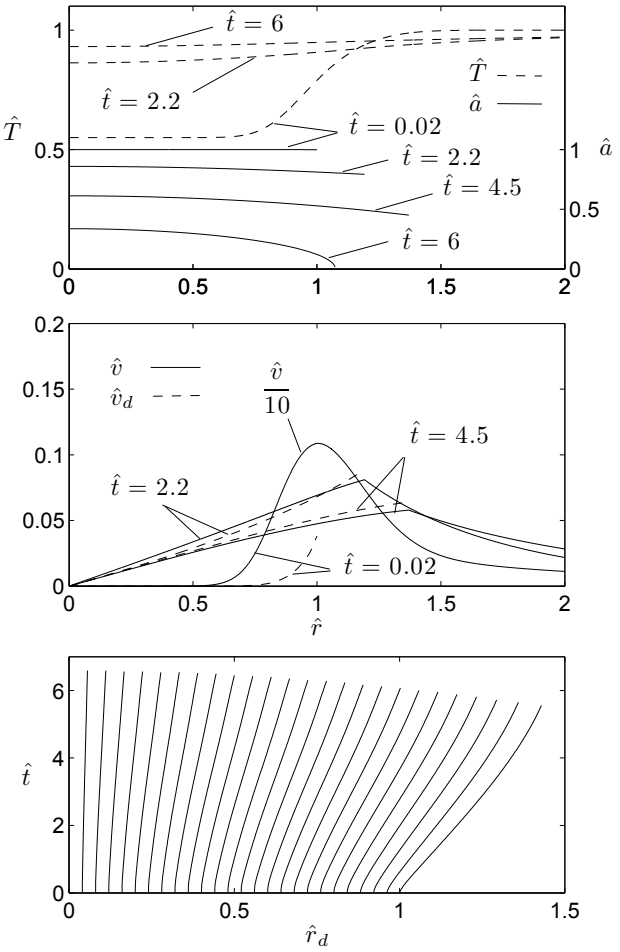

Figure A.1. The evolution of the vaporizing droplet cloud as obtained from integration of (A.1)–(A.7) for $\hat{T}_I = \hat{T}_B = 0.55$, $L_v/(c_p T_A) = 0.48$, $\mathrm{Le_F} = 2.6$, $Y_{\mathrm{F}_I} = 0$, $\alpha = 1.0$, and $t_c/t_v = 1$. The lower plot shows droplet trajectories, extended in time until the droplet disappears.

The distinguished limit $t_c/t_v = O(1)$ and $\alpha = O(1)$ of droplet-cloud vaporization with two-way coupling between the liquid and gas phases requires numerical integration of the complete problem (A.1)–(A.7). Simplifications arise when the initial droplet temperature $T_d = T_I$ is close to the boiling temperature T_B, the case considered in the sample results of Fig. A.1, for which

$\hat{T}_d \simeq \hat{T}_B = T_B/T_A$ at all times, with the result that the evolution equation (A.6) is no longer needed. The expansion of the gas, which is initially very strong at the separating interface, is seen to induce significant droplet motion, as can be seen in the droplet trajectories shown in the bottom plot, which are extended in time until the droplet disappears. The slip velocity $\hat{v} - \hat{v}_d$, which is very large in the beginning, decays for $\hat{t} \sim 1$. Once the thermal wave reaches the center, vaporization occurs throughout the cloud, so that when the boundary droplet disappears for $\hat{t} \simeq 5.6$ the radius of the central droplet has decreased already to $\hat{a} \simeq 0.19$.

Consideration of extreme values of α help to identify limiting solutions. For example, one-way coupling exists for $\alpha \ll 1$, with the solution for the gas evolving independently of the droplets. Since the resulting fuel-vapor mass fraction is negligible, the equation of state reduces to $\hat{\rho}\hat{T} = 1$, which can be used in (A.3) to give $\hat{v} = \hat{T}^\sigma \partial\hat{T}/\partial\hat{r}$. Substitution of this result into (A.1) reduces the computation of $\hat{T}$ to a nonlinear heat problem, with σ and $\hat{T}_I$ entering as the only parameters. Once the gas-phase properties are determined, the evolution of the droplets follows from integration of (A.5)–(A.7) in terms of t_c/t_v.

The limit of sheath vaporization [7] arises for $\alpha t_c/t_v \gg 1$, as can be seen from (A.1) and (A.2), which lead in this limit to the condition $\hat{a}\lambda = 0$, indicating the existence of a thin vaporization front located at $\hat{r} = \hat{r}_s(\hat{t})$ separating and outer region for $\hat{r} > \hat{r}_s$ where no droplets are found and an inner region for $\hat{r} < \hat{r}_s$ where the vaporization rate is identically zero. Inside the cloud, where $\lambda = 0$, the temperature must satisfy $\hat{T} = \hat{T}_d$, as follows from (A.3) in this limit. The vaporization front bounding the shrinking cloud moves slowly with a characteristic time that can be seen to be of order αt_c, so that if $\alpha \gg 1$ the solution evolves in a quasi-steady fashion for $\hat{t} = t/t_c \gg 1$. The near-equilibrium stagnant solution in the cloud and the outer droplet-free, quasisteady solution for $\hat{r} > \hat{r}_s$ must satisfy appropriate jump conditions at the vaporization layer, providing an equation for $\mathrm{d}\hat{r}_s/\mathrm{d}\hat{t}$ that yields a prediction for the cloud life time, $\sim \alpha t_c$, upon integration (see the parallel analysis given in [10] for the cylindrical droplet cloud). Note that the sheath solution is somewhat more complex in the alternative limiting case $t_c/t_v \gg 1$ with $\alpha = O(1)$, corresponding also to large values of $\mathrm{G} = \alpha t_c/t_v \gg 1$, because in that case the cloud life time is of order t_c and the solution outside the vaporization layer remains unsteady during the vaporization process.

References

[1] M. Yang, M. Sichel, Spherical droplet clouds, AIAA paper (1990) 90–3060.

[2] T. Suzuki, H. H. Chiu, Multi-droplet combustion of liquid propellants, Proceedings of 9th International on Space Technology Science (1971) 145–153.

[3] H. H. Chiu, T. Liu, Group combustion of liquid droplets, Combust. Sci. Tech. 17 (1977) 127–142.

[4] M. Labowsky, D. E. Rosner, Group combustion of droplets in fuel clouds, i. quasi-steady predictions, in: J. T. Zung (Ed.), Evaporation-Combustion of Fuels, Americal Chemical Society, 1978, pp. 63–79.

[5] H. H. Chiu, H. Kim, E. J. Croke, Internal group combustion of liquid droplets, Proc. Combust. Inst. 19 (1982) 971–980.

[6] S. M. Correa, M. Sichel, The group combustion of a spherical cloud of monodisperse fuel droplets, Proc. Combust. Inst. 19 (1982) 981–991.

[7] S. M. Correa, M. Sichel, The boundary layer structure of a vaporizing fuel cloud, Combust. Sci. Tech. 28 (1982) 121–130.

[8] S. K. Aggarwal, W. A. Sirignano, Unsteady spray flame propagation in a closed volume, Combustion and flame 62 (1) (1985) 69–84.

[9] G. Continillo, W. A. Sirignano, Numerical study of multicomponent fuel spray flame propagation in a spherical closed volume, in: Symposium (International) on Combustion, Vol. 22, Elsevier, 1989, pp. 1941–1949.

[10] J. Arrieta-Sanagustín, A. L. Sánchez, A. Liñán, F. A. Wiliams, The sheath vaporization of a monodisperse fuel-spray jet, J. Fluid Mech. 675 (2011) 435–464.

[11] A. Liñán, F. A. Williams, Autoignition of nonuniform mixtures in chambers of variable volume, Combustion science and technology 105 (4-6) (1995) 245–263.

APPENDIX

B

Spray diffusion flames in coflow mixing layers

B.1 Unsteady unstrained spray mixing-layers

As seen in Figs. 4.3(a) and 4.4, when the spray is carried by an inert gas, the coflow mixing layer downstream from the ignition kernel includes a thin diffusion flame separating a region without oxygen from a region without gaseous fuel. The time evolution of this diffusion flame can be described for times moderately large after ignition by considering the limit of infinitely fast chemical reaction as applicable from $x = 0$. The computation is facilitated by writing the species and energy equations in terms of the mixture-fraction variables Z and $\tilde{Z}$ and accompanying excess enthalpy H introduced in Section 4.7.1. For simplicity, attention will be restricted to the isovelocity case $u = u_d = 1$. As discussed above, the resulting mathematical problem provides also the temporal evolution of the mixing layer formed by putting into contact at a given time a semi-infinite space of hot air with a semi-infinite spray suspension, with x being equivalent in that case to the dimensionless time $\hat{t} = t/t_v$.

The resulting equations for the liquid phase include the conservation of droplets

$$\frac{\partial n}{\partial \hat{t}} + \frac{\partial (n v_d)}{\partial y} = 0, \tag{B.1}$$

along with equations for the evolution of the droplet radius and droplet transverse velocity

$$\frac{\partial \hat{a}^3}{\partial \hat{t}} + v_d \frac{\partial \hat{a}^3}{\partial y} = -\dot{m}_d, \tag{B.2}$$

$$\hat{a}^3 \left(\frac{\partial v_d}{\partial \hat{t}} + v_d \frac{\partial v_d}{\partial y} \right) = f_y, \tag{B.3}$$

where the expressions for the exchange rates between phases are $\dot{m}_d = \hat{a} \ln[1 + (\hat{T} - \hat{T}_B)/l_v]$ and $f_y = (3/2)\mathrm{Pr} T^\sigma \hat{a}(v - v_d)$. The accompanying gas-phase

conservation equations are

$$\frac{\partial \rho}{\partial \hat{t}} + \frac{\partial (\rho v)}{\partial y} = \alpha n \dot{m}_d, \tag{B.4}$$

$$\frac{\partial (\rho Z)}{\partial \hat{t}} + \frac{\partial (\rho v Z)}{\partial y} = \frac{S/L_{\mathrm{F}} + 1}{S+1} \frac{\partial}{\partial y} \left(T^{\sigma} \frac{\partial \tilde{Z}}{\partial y} \right) + \alpha n \dot{m}_d, \tag{B.5}$$

$$\frac{\partial (\rho H)}{\partial \hat{t}} + \frac{\partial (\rho v H)}{\partial y} = \frac{\partial}{\partial y} \left(T^{\sigma} \frac{\partial H}{\partial y} \right) - \alpha n \left[\dot{m}_d \left(\frac{q}{S} + l_v - T_{\scriptscriptstyle B} + 1 \right) \right]. \tag{B.6}$$

The above equations, supplemented with the equation of state (4.10) and with the coupling-function expressions (4.50), are to be integrated with the initial conditions at $\hat{t} = 0$ (or $x = 0$) defined by the step distributions $Z = \tilde{Z} = H = 0$ for $y > 0$ and $n - 1 = \hat{a} - 1 = v_d = Z - Z_{st} = \tilde{Z} - \tilde{Z}_{st} = H - H_{\scriptscriptstyle S} = 0$ for $y < 0$ and associated boundary conditions given by $Z = \tilde{Z} = \hat{H} = 0$ as $y \to +\infty$ and by $Z - Z_{st} = \tilde{Z} - \tilde{Z}_{st} = H - H_{\scriptscriptstyle S} = 0$ as $y \to -\infty$. Here, $H_{\scriptscriptstyle S} = -[q/S + c_p(T_A - T_B)]$ is the value of the excess enthalpy on the spray side, whose initial temperature is assumed to be equal to the boiling temperature T_B, so that droplet vaporization begins immediately after the spray is put in contact with the air, at temperature $T_A > T_B$.

Sample integrations of the Burke-Schumann spray flame are shown in Figs. B.1 and B.2 for $L_{\mathrm{F}} = 1$, a simplification that applies with sufficient accuracy to methanol combustion. For simplicity in the integrations, changes of density and transport properties are neglected along with the motion induced by droplet vaporization. The evolution in time associated with the presence of droplet vaporization is adequately represented by rescaling in the two figures the transverse coordinate with the characteristic value of the instantaneous mixing-layer thickness according to $y/\sqrt{D_T t}$. Profiles of reactants, temperature, and dimensionless vaporization rate are shown in Fig. B.1 at four different times. The distribution of droplet radius is indicated by shaded contours, whose boundary mark the edge of the spray. Corresponding profiles of Z are shown in Fig. B.2, with indication of the diffusion-flame location.

The four instants of time selected for the plots are representative of the four different regimes that emerge during the evolution of the diffusion flame, corresponding to the four regimes identified by Chiu [1–3] in his analyses of droplet-cloud combustion. As can be seen in Fig. B.2, the effect of vaporization on the mixture-fraction distribution is negligible for $t \ll t_v$, so that the mixture fraction effectively behaves as a passive scalar, with small departures of order t/t_v from the self-similar mixing-layer solution $Z/Z_{st} = \frac{1}{2}\mathrm{erfc}[y/(2\sqrt{D_T t})]$. Since Z remains below Z_{st} all across the mixing layer in this early stage, in this

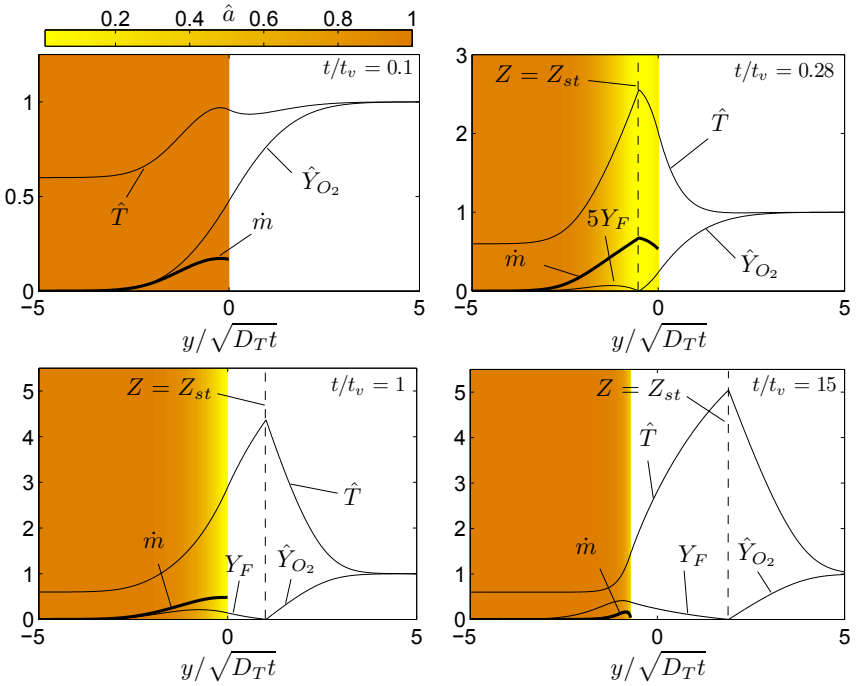

Figure B.1. Transient evolution of the unstrained mixing layer obtained for $\alpha = 1$, $L_F = 1$, $Pr = 0.7$, $q/(c_p T_A) = 36.19$, $L_v/(c_p T_A) = 1.95$, $S = 6.46$, and $T_B/T_A = 0.6$. In this figure, $\dot{m}$ denotes the dimensionless vaporization rate $\hat{a}\ln[1 + (\hat{T} - \hat{T}_B)/l_v]$, whose distribution is represented with thick curves in the plots, while the dimensionless radius a is represented by shaded contours. The dashed lines indicate the location of the diffusion flame.

limit of infinitely fast chemistry the fuel vapor that is initially generated burns rapidly in a distributed fashion, without producing a spray flame, giving a solution with $Y_F = 0$ in which the effect of the distributed chemical heat release on the temperature distribution is clearly apparent, as seen in the profile of $\hat{T} = T/T_A$. If the droplets were sufficiently large, then in this initial stage the fuel vapor would burn instead in a spherical flame around each individual droplet, that being the single-droplet combustion mode identified by Chiu [1–3].

For the parametric values selected in Figs. B.1 and B.2, a spray diffusion flame is first observed at $t/t_v \simeq 0.2$ near the spray side, giving rise to a period of internal group combustion in which the flame lies within the spray, the case shown for $t/t_v = 0.28$ in Figs. B.1 and B.2, with the droplets found between the flame and the outer edge of the spray vaporizing in an oxidizer atmosphere with distributed fuel oxidation (or in spherical flames surrounding the droplets

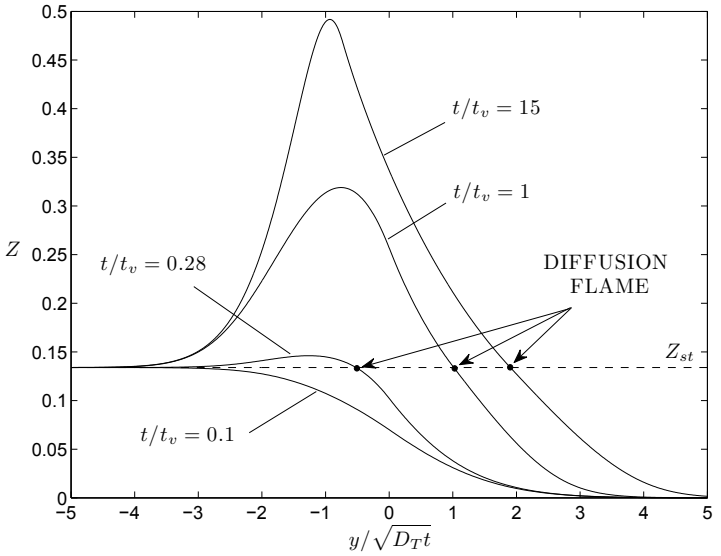

Figure B.2. Profiles of Z corresponding to the four computations shown in Fig. B.1.

if their radii are sufficiently large). As the fuel vapor is further accumulated, the flame moves towards the air side, leaving the spray domain at $t/t_v \simeq 0.35$. External group combustion is observed for later times, with the flame sitting outside the spray at an increasingly large distance from its edge, a configuration clearly observed in the profiles for $t/t_v = 1.0$. For $t \gg t_v$, the vaporization layer, of characteristic thickness $\sqrt{D_T t_v}$, becomes much thinner than the mixing-layer thickness $\sqrt{D_T t}$, so that for large times a sheath combustion regime emerges, including a thin vaporization layer on the outer edge of the spray, visible in the results given for $t/t_v = 15$ in Fig. B.1. In the limit $t/t_v \to \infty$, the resulting solution is again selfsimilar when expressed in the dimensionless variable $y/\sqrt{D_T t}$ [4].

The Burke-Schumann solution given in Figs. B.1 and B.2 can be used to describe the evolution of the diffusion flame that is formed after ignition takes place in nonpremixed spray mixing layers with $\Delta = O(1)$. In using the results of the Burke-Schumann analysis to represent the post-ignition solution, introduction of a virtual origin would be in general necessary to account for the existence of an ignition stage. Since ignition tends to occur near the air-side edge of the mixing layer, as seen in Fig 4.3, the diffusion flame typically originates at a location outside the spray, giving an external-group-combustion solution that eventually evolves for $t \gg t_v$ to develop a vaporization sheath. Consequently,

solutions involving internal group combustion and/or distributed fuel-vapor oxidation (or single-droplet combustion), which arise during a short initial period in the limit of infinitely fast chemical reactions, as seen in Figs. B.1 and B.2, are unlike to be observed in igniting mixing layers with $\Delta = O(1)$.

Before closing this section, it is worth mentioning that the transient solution given in Fig. B.2 for the spray-flame mixture fraction Z is fundamentally different from the profile that appears in gaseous combustion. In that case, the mixture-fraction variable Z shows a monotonic distribution that varies from the value $Z = 1$, assigned by convention on the fuel side of the mixing layer, to vanish on the air side. For the unsteady unstrained flamelet, the solution is selfsimilar, reducing for $L_{\mathrm{F}} = 1$ to the well-known distribution $Z = \frac{1}{2}\mathrm{erfc}[y/(2\sqrt{D_T t})]$ when the thermo-diffusive approximation is employed in the description [5]. At the flame location $Z = Z_{st}$, the peak temperature of equidiffusive gaseous diffusion flames equals the adiabatic flame temperature of the stoichiometric mixture of air and oxidizer T_{ad}. By way of contrast, the profile of Z shown in Fig. B.2 becomes non-monotonic as the solution develops at a finite time a maximum within the vaporization region. This peak becomes more pronounced for larger times, as can be seen in Fig. B.2. Correspondingly, the peak temperature evolves as t/t_v increases. The value for $t \gg t_v$ approaches the adiabatic flame temperature

$$T_{ad} = T_B + \frac{(q - L_v)/c_p + S(T_A - T_B)}{S + 1 + 1/\alpha}, \tag{B.7}$$

resulting from burning the spray stream and the air in stoichiometric proportions ($T_{ad} \simeq 4.95$ for the conditions of Fig. B.1). For finite values of $t \sim t_v$, however, the peak temperature can be seen in Fig. B.1 to remain significantly below T_{ad}. Effects of preferential diffusion of the gaseous fuel and of preferential droplet concentration further modify the peak value, as shown in Chapter 5 in connection with the counterflow computations.

References

[1] T. Suzuki, H. H. Chiu, Multi-droplet combustion of liquid propellants, Proceedings of 9th International on Space Technology Science (1971) 145–153.

[2] H. H. Chiu, T. Liu, Group combustion of liquid droplets, Combust. Sci. Tech. 17 (1977) 127–142.

[3] H. H. Chiu, H. Kim, E. J. Croke, Internal group combustion of liquid droplets, Proc. Combust. Inst. 19 (1982) 971–980.

[4] D. Martínez-Ruiz, J. Urzay, A. L. Sánchez, A. Liñán, F. A. Williams, Dynamics of thermal ignition of spray flames in mixing layers, Journal of Fluid Mechanics 734 (2013) 387–423.

[5] N. Peters, Turbulent combustion, Cambridge university press, 2000.

APPENDIX

C

The Large-Activation-Energy Analysis of Strain-Induced Extinction of Counterflow Diffusion Flames with Nonunity Lewis Numbers of the Fuel

Our literature survey on differential-diffusion effects on strain-induced extinction of gaseous diffusion flames indicated that, although a basic understanding of the process is available, including the additional technical difficulties that arise when attempting a large-activation-energy treatment [1–4], some aspects of the problem have not been addressed in previous work. For instance, we found that all analytical studies were conducted in the thermodiffusive approximation, thereby neglecting influences of variable density on extinction. In addition, to the best of our knowledge, no comparisons have ever been made between activation-energy asymptotic predictions of critical extinction conditions and results of direct numerical simulations using finite chemistry. Therefore, although spray flow is the main subject of this dissertation, it appeared to be desirable to revisit the classical problem of extinction of a gaseous nonpremixed flame in a counterflow configuration, that being the purpose of the present appendix. As in the classical work [7], a one-step Arrhenius model will be adopted for the chemistry, accounting in our analysis for nonunity values of the fuel Lewis number and for variable density and variable transport properties and including comparisons of the asymptotic results with sample numerical integrations for large but finite values of the activation energy. The associated asymptotic treatment parallels that given in the online supplemental appendix of [1] for constant density, modified here to incorporate the additional complications arising from the consideration of a more realistic flow description.

C.1 Diffusion flames in counterflow mixing layers

C.1.1 Chemistry model

We give below the equations and boundary conditions for the description of non-premixed flames in counterflow mixing layers separating a stream of air from a stream containing a gas mixture of fuel and inert (e.g. N_2). As in the finite-rate analyses of spray combustion given in Chapters 4 and 6, the reaction between the fuel and the oxygen of the air is assumed to occur according to the global irreversible step

$$\mathrm{F} + s\mathrm{O}_2 \rightarrow (1+s)\mathrm{P} + q', \tag{C.1}$$

expressed in terms of the mass of oxygen consumed s and the amount of heat released q' per unit mass of fuel burnt. As noted in [1], these two quantities differ only by a small amount for hydrocarbons that share the same molecular structure, [e.g., $s = (3.65, 3.58)$ and $q' = (50.03, 49.53)$ kJ/g for propane and butane, respectively]. It is also of interest that, although the associated values are quite different for hydrogen, for which $s = 8$ and $q' \simeq 120$ kJ/g, the value of the heat release referred to the unit mass of oxygen burnt $q'/s \simeq 15$ kJ/g is very similar to the values $q'/s \simeq 14$ kJ/g corresponding to hydrocarbon combustion.

To facilitate investigations of systems with dilute fuel feed the Arrhenius reaction rate (mass of fuel consumed per unit volume per unit time)

$$\omega_{\mathrm{F}} = B\rho' e^{-E_a/(R^o T')} \hat{Y}_{\mathrm{F}} \hat{Y}_{\mathrm{O}}. \tag{C.2}$$

includes the normalized fuel mass fraction $\hat{Y}_{\mathrm{F}} = Y_{\mathrm{F}}/Y_{\mathrm{F}_0}$, where Y_{F_0} is the mass fraction of the fuel in its feed stream. Two different rate parameters appear in (C.2), namely, the preexponential frequency factor B and the activation energy E_a, which defines the activation temperature E_a/R^o when divided by the universal gas constant R^o.

C.1.2 Conservation equations and boundary conditions

We shall consider the steady axisymmetric counterflow diffusion flame established in a steady mixing layer separating opposed streams of fuel, coming from $z' = \infty$, and air, coming from $z' = -\infty$. In the stagnation-point region the flow is known to be selfsimilar in terms of the transverse coordinate z', with the solution depending on the strain rate imposed on the mixing layer by the growing radial velocities. The strain rates on the air and fuel sides A_A and

A_0 are in general different, their values being related to the fuel-to-air density ratio ρ_0/ρ_A by the equation $A_0 = A_A\sqrt{\rho_A/\rho_0}$, resulting from the condition of negligible pressure variations across the mixing layer.

While the properties of the spray stream were used in Chapters 4 and 5 to scale the counterflow problem, for gaseous diffusion flames it is more convenient to employ the airstream values, to give for instance $\rho = \rho'/\rho_A$ and $T = T'/T_A$ for the dimensionless density and temperature. Furthermore, following common practice in formulating the gaseous counterflow problem, we introduce a nondimensional density-weighted transverse coordinate

$$\eta = \left(\frac{A_A}{D_{T_A}}\right)^{1/2} \int_0^{z'} \rho \mathrm{d}\tilde{z}, \tag{C.3}$$

where D_{T_A} is the thermal diffusivity in the airstream, along with a nondimensional stream function $F(\eta)$, defined to give radial and axial velocity components v' and u' satisfying

$$\frac{v'}{A_A r} = \frac{1}{2}\frac{\mathrm{d}F}{\mathrm{d}\eta} \quad \text{and} \quad \frac{u'}{(A_A D_{T_A})^{1/2}} = -\frac{F}{\rho}. \tag{C.4}$$

In terms of these nondimensional variables, the radial component of the momentum equation simplifies to

$$\mathrm{Pr}\frac{\mathrm{d}}{\mathrm{d}\eta}\left(\rho T^\sigma \frac{\mathrm{d}^2 F}{\mathrm{d}\eta^2}\right) + F\frac{\mathrm{d}^2 F}{\mathrm{d}\eta^2} + \frac{1}{2}\left[\frac{1}{\rho} - \left(\frac{\mathrm{d}F}{\mathrm{d}\eta}\right)^2\right] = 0 \tag{C.5}$$

while the conservation equations for energy and reactants become

$$\frac{\mathrm{d}}{\mathrm{d}\eta}\left(\rho T^\sigma \frac{\mathrm{d}T}{\mathrm{d}\eta}\right) + F\frac{\mathrm{d}T}{\mathrm{d}\eta} = -q\frac{B}{A_A}\hat{Y}_{\mathrm{F}}\hat{Y}_{\mathrm{O}}e^{-T_a/T}, \tag{C.6}$$

$$\frac{1}{L_{\mathrm{F}}}\frac{\mathrm{d}}{\mathrm{d}\eta}\left(\rho T^\sigma \frac{\mathrm{d}\hat{Y}_{\mathrm{F}}}{\mathrm{d}\eta}\right) + F\frac{\mathrm{d}\hat{Y}_{\mathrm{F}}}{\mathrm{d}\eta} = \frac{B}{A_A}\hat{Y}_{\mathrm{F}}\hat{Y}_{\mathrm{O}}e^{-T_a/T} \tag{C.7}$$

$$\frac{\mathrm{d}}{\mathrm{d}\eta}\left(\rho T^\sigma \frac{\mathrm{d}\hat{Y}_{\mathrm{O}}}{\mathrm{d}\eta}\right) + F\frac{\mathrm{d}\hat{Y}_{\mathrm{O}}}{\mathrm{d}\eta} = S\frac{B}{A_A}\hat{Y}_{\mathrm{F}}\hat{Y}_{\mathrm{O}}e^{-T_a/T}. \tag{C.8}$$

A Fickian description is adopted for the species diffusion velocities, with a unity value assumed for the Lewis number of O_2 and a general Lewis number L_{F} utilized for the fuel. A simple power-law with exponent σ is adopted for the temperature variation of the viscosity and thermal conductivity, giving

a constant Prandtl number Pr in (C.5) when changes in the specific heat at constant pressure c_p are neglected. At the same level of approximation, the product of the species diffusivity and the density is also assumed to vary with T^σ in (C.7) and (C.8). As can be seen, the reaction rate involves two dimensionless rate parameters, namely, the dimensionless frequency factor (B/A_A) and the nondimensional activation temperature $T_a = E_a/(R^o T_A)$.

The formulation displays the two main thermochemical parameters that are known to determine the structure of gaseous diffusion flames [1], namely, the mass of air $S = sY_{\mathrm{F}_0}/Y_{\mathrm{O}_{2\mathrm{A}}}$ needed to burn the fuel contained in the unit mass of fuel stream and the dimensionless heat release per unit mass of fuel $q = q'Y_{\mathrm{F}_0}/(c_p T_A)$. Although the stoichiometric ratio S is a fairly large quantity in undiluted fuel-air combustion (e.g., $S \simeq 15$ and $S \simeq 34.5$ for dodecane-air and hydrogen-air systems, respectively), values of order unity can also be found in systems including dilution of the fuel stream, so that values $S \gtrsim 1$ appear to be of general interest. The ratio $q/(S+1)$ defines the dimensionless temperature increment associated with the adiabatic isobaric combustion of the gas mixture generated by mixing in stoichiometric proportions the fuel and air streams, a relevant quantity in nonpremixed diffusion flames with unity reactant Lewis numbers [1].

Equations (C.5)–(C.8), supplemented with the equation of state

$$\rho T = 1 \tag{C.9}$$

written here for simplicity with the variations of the density with the mixture composition neglected, must be integrated with the boundary conditions

$$\begin{cases} \mathrm{d}F/\mathrm{d}\eta - \sqrt{\rho_A/\rho_0} = T - T_0 = \hat{Y}_{\mathrm{F}} - 1 = \hat{Y}_{\mathrm{O}} = 0 & \text{as} \quad \eta \to +\infty \\ F - \eta = T - 1 = \hat{Y}_{\mathrm{F}} = \hat{Y}_{\mathrm{O}} - 1 = 0 & \text{as} \quad \eta \to -\infty. \end{cases} , \tag{C.10}$$

where T_0 represents the fuel-to-air temperature ratio. The boundary condition for the rescaled radial velocity $\mathrm{d}F/\mathrm{d}\eta$ on the fuel side follows from the condition $A_0 = A_A\sqrt{\rho_A/\rho_0}$, where the density ratio can be expressed as $\rho_A/\rho_0 = T_0$ by means of (C.9). An arbitrary zero stream displacement is assumed on the air side when writing $F - \eta = 0$ as $\eta \to -\infty$, thereby removing the translational invariance present in the counterflow mixing-layer problem. This selection is inconsequential, in that a different choice would just amount to a translation of the resulting profiles. In our computations, the location $\eta = \eta_0$ of the stagnation plane, where $F = 0$, will be obtained as part of the integration and the profiles of temperature and reactant mass fraction will be plotted

using the distance to the stagnation plane $\eta - \eta_0$. It is worth mentioning that, if the assumption of constant density and constant transport properties is employed, then integration of (C.5) provides $F = \eta$, a result that can be used to simplify (C.6)–(C.8), giving the starting equations used in previous analyses [2–4, 7].

C.1.3 Sample computations

Results of integrations corresponding to dilute fuel feed ($S = 2$) and equal feed temperatures ($T_0 = 1$) are given in Fig. C.1, which includes solid curves representing temperature and reactant mass fractions for $L_{\mathrm{F}} = 0.3$ (upper plot) and $L_{\mathrm{F}} = 2$ (lower plot) along with dashed curves representing results for infinitely fast reaction, to be discussed later. For both flames in Fig. C.1, the rate parameters selected place the system moderately far from extinction.

The Lewis numbers selected are representative of hydrogen ($L_{\mathrm{F}} = 0.3$) and large hydrocarbon ($L_{\mathrm{F}} = 2$) molecules, respectively. Because of its higher diffusivity, the hydrogen reaction layer, where the temperature peaks, sits farther from the stagnation plane than that of the hydrocarbon flame. Preferential diffusion is seen to have a noticeable effect on the resulting temperature increment $T - 1$, which is referred in the plots to the value $q/(S + 1)$ corresponding to adiabatic stoichiometric combustion. As can be seen, the temperature profile for $L_{\mathrm{F}} = 2$ displays a peak value well below the adiabatic flame temperature, whereas a superadiabatic peak temperature $T - 1 > q/(S + 1)$ is found when the diffusivity of hydrogen is employed.

C.1.4 Coupling functions for diffusion flames

For the following development, it is convenient to derive from (C.6)–(C.8) chemistry-free conservation equations by eliminating the reaction terms through appropriate linear combinations. For instance, multiplying (C.8) by q/S and adding (C.6) leads to

$$\frac{\mathrm{d}}{\mathrm{d}\eta}\left[T^{\sigma-1}\frac{\mathrm{d}}{\mathrm{d}\eta}\left(T + q\hat{Y}_{\mathrm{O}}/S\right)\right] + F\frac{\mathrm{d}}{\mathrm{d}\eta}\left(T + q\hat{Y}_{\mathrm{O}}/S\right) = 0, \tag{C.11}$$

which can be written in the compact form

$$\frac{\mathrm{d}}{\mathrm{d}\eta}\left(T^{\sigma-1}\frac{\mathrm{d}H}{\mathrm{d}\eta}\right) + F\frac{\mathrm{d}H}{\mathrm{d}\eta} = 0 \tag{C.12}$$

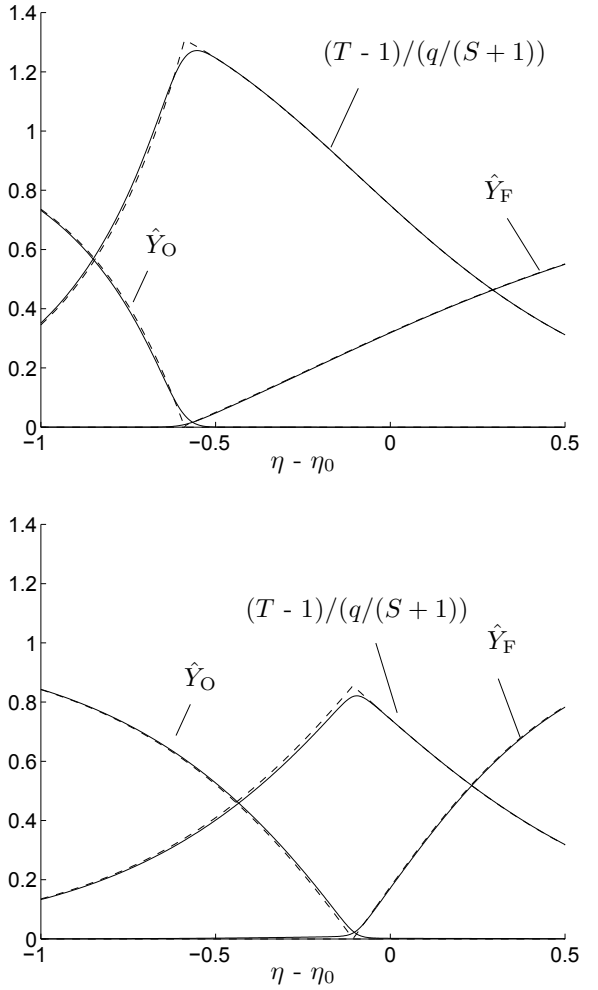

Figure C.1. The variation of the temperature and reactant mass fractions with the distance to the stagnation plane $\eta - \eta_0$ as obtained from integrations of (C.5)–(C.8) (solid curves) and from integrations of (C.5), (C.12), and (C.15) (dashed curves) for $T_0 = 1$, $q = 20$, and $S = 2$ (i.e., $q/S = 10$) with $L_{\rm F} = 0.3$ (upper plot) and $L_{\rm F} = 2$ (lower plot). The values of the rate parameters in the finite-rate chemistry computations are $T_a = 282.9$ and $B/A_A = 5.97 \times 10^{17}$ for $L_{\rm F} = 0.3$ and $T_a = 336.5$ and $B/A_A = 6.08 \times 10^{26}$ for $L_{\rm F} = 2$, which correspond to points in the extinction curve of $\mathcal{D} = 0.73$ and $\mathcal{D} = 0.29$ respectively.

in terms of the excess enthalpy

$$H = \frac{T-1}{q/S} + \hat{Y}_{\mathrm{O}} - 1. \tag{C.13}$$

The reaction term can also be eliminated by subtracting (C.8) from (C.7) times S to give

$$\frac{\mathrm{d}}{\mathrm{d}\eta}\left[T^{\sigma-1}\frac{\mathrm{d}}{\mathrm{d}\eta}\left(\frac{S\hat{Y}_{\mathrm{F}}}{L_{\mathrm{F}}} - \hat{Y}_{\mathrm{O}}\right)\right] + F\frac{\mathrm{d}}{\mathrm{d}\eta}(S\hat{Y}_{\mathrm{F}} - \hat{Y}_{\mathrm{O}}) = 0. \tag{C.14}$$

As can be seen, different linear combinations appear in the convective and diffusion terms when the fuel Lewis number L_{F} is taken to be different from unity. The resulting equation can be written in the compact form

$$\frac{S/L_{\mathrm{F}}+1}{S+1}\frac{\mathrm{d}}{\mathrm{d}\eta}\left(T^{\sigma-1}\frac{\mathrm{d}\tilde{Z}}{\mathrm{d}\eta}\right) + F\frac{\mathrm{d}Z}{\mathrm{d}\eta} = 0, \tag{C.15}$$

involving a diffusion-weighted mixture-fraction variable

$$\tilde{Z} = \frac{S\hat{Y}_{\mathrm{F}}/L_{\mathrm{F}} - \hat{Y}_{\mathrm{O}} + 1}{S/L_{\mathrm{F}}+1} \tag{C.16}$$

in addition to the classical mixture-fraction variable

$$Z = \frac{S\hat{Y}_{\mathrm{F}} - \hat{Y}_{\mathrm{O}} + 1}{S+1}. \tag{C.17}$$

Using (C.10) together with the definitions given in (C.13), (C.16), and (C.17) yields

$$\begin{gathered} Z-1 = \tilde{Z}-1 = 0 \quad \text{and} \quad H = H_0 \quad \text{as} \quad \eta \to \infty \\ Z = \tilde{Z} = 0 \quad \text{and} \quad H = 0 \quad \text{as} \quad \eta \to -\infty, \end{gathered} \tag{C.18}$$

as boundary conditions for integration of (C.12) and (C.15), where $Z_{st} = 1/(1+S)$, $\tilde{Z}_{st} = 1/(1+S/L_{\mathrm{F}})$, and $H_0 = (T_0-1)/(q/S) - 1$.

In computing the reactive mixing layer, one can in general replace two of the three equations (C.6)–(C.8) by the chemistry-free equations (C.12) and (C.15). As seen below, this replacement is particularly useful in the limit of infinitely fast reaction, for which the integration of (C.5), (C.12), and (C.15) together with the equilibrium condition $\hat{Y}_{\mathrm{F}}\hat{Y}_{\mathrm{O}} = 0$ and the definitions given in (C.13), (C.16),

and (C.17) suffice to determine the solution.

C.2 The limit of infinitely fast reaction

C.2.1 General considerations

The dimensionless rate emerging on the left-hand side of (C.6)–(C.8) involves the ratio B/A_A as a factor, with the limiting case of infinitely fast reaction emerging for $B/A_A = \infty$ [1]. The form of the reaction terms in (C.6)–(C.8) implies the non coexistence

$$\hat{Y}_{\mathrm{F}}\hat{Y}_{\mathrm{O}} = 0 \tag{C.19}$$

of the reactants. The reaction layer reduces in this case to a sheet of infinitesimally small thickness located at $\eta = \eta_f$, with the Dirac-delta reaction terms acting as sinks for the reactants and as a heat source for the temperature, which peaks at the flame with a value $T = T_f$. The fuel vapor and the oxygen reach the flame sheet by diffusion from opposite sides in stoichiometric proportions, as can be seen by integrating (C.14) across the flame sheet to give

$$m_{\mathrm{F}} = \frac{1}{L_{\mathrm{F}}}\frac{\mathrm{d}\hat{Y}_{\mathrm{F}}}{\mathrm{d}\eta}\bigg|_{\eta_f^+} = -\frac{1}{S}\frac{\mathrm{d}\hat{Y}_{\mathrm{O}}}{\mathrm{d}\eta}\bigg|_{\eta_f^-} = \frac{m_{\mathrm{O}}}{S}, \tag{C.20}$$

where m_{F} and $m_{\mathrm{O}} = Sm_{\mathrm{F}}$ are appropriate nondimensional measures of the fuel and oxygen consumption rates (in dimensional form, the rate of fuel consumption per unit flame surface m''_{F} is given by $m''_{\mathrm{F}}/(\rho_A\sqrt{D_{T_A}A_A}) = T_f^{\sigma+1}m_{\mathrm{F}}$). The heat released at the flame qm_{F} is transported by conduction towards both sides of the flame according to

$$qm_{\mathrm{F}} = \frac{\mathrm{d}T}{\mathrm{d}\eta}\bigg|_{\eta_f^-} - \frac{\mathrm{d}T}{\mathrm{d}\eta}\bigg|_{\eta_f^+} \tag{C.21}$$

obtained by integration of (C.11).

For the counterflow, and also for other one-dimensional problems, the flame location η_f and the peak temperature at the flame T_f can be determined through a modified boundary-value problem in which (C.5), (C.6), and (C.7) are integrated for $\eta > \eta_f$ (where $\hat{Y}_{\mathrm{O}} = 0$) while (C.5), (C.6) and (C.8) are integrated for $\eta < \eta_f$ (where $\hat{Y}_{\mathrm{F}} = 0$), with the chemical-reaction term removed in the species and energy equations. At the flame sheet, we use the condition $\hat{Y}_{\mathrm{F}} = \hat{Y}_{\mathrm{O}} = 0$ resulting from the equilibrium equation (C.19) along with the conditions of continuity of T, F, F', and F''. The solution is uniquely determined when the additional relationships (C.20) and (C.21) are employed. These equations

relate the jumps in the gradients of temperature and reactant mass fractions at the flame sheet, resulting from the Dirac-delta nature of the chemical-reaction term in the limit $B/A_A \to \infty$.

Sample solutions of the Burke-Schumann problem are included in Fig. C.1 for comparison with the finite-rate results. As can be seen, the infinitely fast reaction limit provides the general flame structure. The profiles of reactant mass fractions and temperature approximate well those of finite chemistry, except in the thin reaction layer. For the rate parameters selected, the equilibrium condition (C.19) applies with good approximation outside the reaction layer, in that reactant leakage is not noticeable in the plots with finite chemistry.

C.2.2 Solution in terms of coupling functions

Handling the limit of infinitely fast reaction becomes considerably more difficult in unsteady or multidimensional situations, for which the determination of the flame location poses a complicated free-boundary problem. For those configurations, the integration is significantly facilitated by using the coupling-function equations defined in (C.13), (C.16), and (C.17), which satisfy chemistry-free transport equations [5, 6], given for the counterflow problem in (C.12) and (C.15). In the integration, the flame surface, where $\hat{Y}_{\mathrm{F}}$ and $\hat{Y}_{\mathrm{O}}$ are simultaneously zero, corresponds to the iso-surface $Z = Z_{st} = 1/(1+S)$ and $\tilde{Z} = \tilde{Z}_{st} = 1/(1+S/L_{\mathrm{F}})$. For $Z \geq Z_{st}$

$$\hat{Y}_{\mathrm{O}} = 0 \quad \text{and} \quad \hat{Y}_{\mathrm{F}} = \frac{Z - Z_{st}}{1 - Z_{st}} = \frac{\tilde{Z} - \tilde{Z}_{st}}{1 - \tilde{Z}_{st}}, \quad \frac{T-1}{q/S} = H + 1, \tag{C.22}$$

whereas for $Z \leq Z_{st}$

$$\hat{Y}_{\mathrm{F}} = 0 \quad \text{and} \quad \hat{Y}_{\mathrm{O}} = 1 - \frac{Z}{Z_{st}} = 1 - \frac{\tilde{Z}}{\tilde{Z}_{st}}, \quad \frac{T-1}{q/S} = H + \frac{Z}{Z_{st}}. \tag{C.23}$$

Equations (C.22) and (C.23) provide a relation, piece-wise linear, between Z and $\tilde{Z}$. In addition, they enable the evaluation of Y_{F}, $\hat{Y}_{\mathrm{O}}$, and T in terms of Z (or $\tilde{Z}$) and H to be performed.

The computation of the counterflow diffusion flame using coupling functions provides the flame location η_f, where $Z = Z_{st}$ and $\tilde{Z} = \tilde{Z}_{st}$, as well as the flame temperature, which is evaluated from the value

$$H_f = \frac{T_f - 1}{q/S} - 1 \tag{C.24}$$

of the excess enthalpy at the flame. While the gradients of the temperature and mass fractions (and also Z) have jumps at the flame sheet, those of the conserved scalars $\tilde{Z}$ and H are continuous there, as follows from (C.20) and (C.21). Their values can be used to evaluate the fuel and oxygen consumption rates per unit flame surface

$$m_{\mathrm{F}} = m_{\mathrm{O}}/S = \frac{1}{L_{\mathrm{F}}}\frac{\mathrm{d}\hat{Y}_{\mathrm{F}}}{\mathrm{d}\eta}\bigg|_{\eta_f^+} = \frac{S^{-1}}{\tilde{Z}_{st}}\frac{\mathrm{d}\tilde{Z}}{\mathrm{d}\eta}\bigg|_{\eta_f} \tag{C.25}$$

and the fuel-side temperature gradient

$$\frac{\mathrm{d}T}{\mathrm{d}\eta}\bigg|_{\eta_f^+} = \frac{q}{S}\frac{\mathrm{d}H}{\mathrm{d}\eta}\bigg|_{\eta_f}. \tag{C.26}$$

The latter expression can be combined with (C.21) to yield

$$\gamma_{\mathrm{O}} = 1 + \frac{1}{qm_{\mathrm{F}}}\frac{\mathrm{d}T}{\mathrm{d}\eta}\bigg|_{\eta_f^+} = 1 + \frac{1}{m_{\mathrm{O}}}\frac{\mathrm{d}H}{\mathrm{d}\eta}\bigg|_{\eta_f} \tag{C.27}$$

for the fractional amount of chemical heat release that is conducted towards the air side of the flame, with $\gamma_{\mathrm{O}} = 1 - \gamma_{\mathrm{F}}$ correspondingly representing the fraction transported to the oxidizer side.

The problem simplifies when $L_{\mathrm{F}} = 1$, in which case the solution reduces to the integration of the momentum equation (C.5) together with an equation for the passive scalar $H/H_0 = Z = \tilde{Z}$. In particular, the peak temperature evaluated from (C.24) with $H_f = H_0 Z_{st}$ and $H_0 = (T_0 - 1)/(q/S) - 1$ reduces to

$$T_f - 1 = T_{st} - 1 = \frac{q}{S+1} + \frac{(T_0 - 1)}{S+1}, \tag{C.28}$$

the adiabatic flame temperature resulting from burning the stoichiometric mixture formed by combining the air and fuel streams at their corresponding initial temperatures. As previously mentioned, with $L_{\mathrm{F}} \neq 1$ the Burke-Schumann peak temperature T_f differs in general from T_{st}, as seen in the computations of Fig. C.1,

C.2.3 Variation of flame properties with fuel diffusivity and fuel-feed dilution

The solution in the limit of infinitely fast reaction provides the values of η_f, T_f, m_{F}, and γ_{O}, which are known [7] to be necessary when assessing the occurrence of extinction. With constant density and constant transport properties, the equilibrium profiles of reactant and temperature on both sides of the reaction

sheet can be written in terms of error functions, which can be used in the jump conditions (C.20) and (C.21) to generate the solution, enabling evaluations of the different flame properties to be made through algebraic implicit expressions. The resulting parametric dependences are given in the supplemental online material of [1].

Numerical integration is needed to evaluate the different flame properties when variable density and variable transport properties are accounted for. Besides the Prandtl number Pr and the exponent σ for the temperature dependence of the transport properties, the formulation in the limit $B/A_A = \infty$ involves as main parameters S, q, L_{F}, and the fuel-to-air temperature ratio T_0. The numerical integrations presented below in Fig. C.2 employ the realistic values $\mathrm{Pr} = 0.7$ and $\sigma = 0.7$ and are restricted to the case of equal feed temperature ($T_0 = 1$). In selecting the other parameters we note that, since the values of S and q vary linearly with Y_{F_0}, their ratio $q/S = q' Y_{\mathrm{O_2A}}/(c_p T_A s)$ is independent of the degree of dilution of the fuel stream. In fuel-air systems the resulting value is very similar for different fuels, including hydrocarbons and hydrogen, for which $q'/s \simeq 14 - 15 \times 10^6$ J/kg yielding $q/S \simeq 10$ when $Y_{\mathrm{O_2A}} = 0.232$, $c_p = 1200$ J/(kg K), and $T_A = 300$ K are used in the evaluations. This invariance is used in selecting the parameters in the computations below, so that for each value of S the accompanying heat-release parameter q is computed from the condition $q/S = 10$, representative of all fuel-air systems of interest here. When this is implemented, only the two parameters L_{F} and S, measuring the diffusivity of the fuel and the dilution of the fuel feed, need to be considered in evaluating the main flame properties in the limit of infinitely fast reaction.

Results of numerical calculations of the equilibrium flame parameters η_f, T_f, m_{F} and γ_{O} are shown in Fig. C.2. The plot allows us to evaluate the dependences of the different flame properties on the fuel diffusivity and on the fuel-feed dilution. To facilitate the representation, the stoichiometric ratio S is replaced in the plots by the stoichiometric value of the modified mixture fraction $\tilde{Z}_{st} = (1 + S/L_{\mathrm{F}})^{-1}$. The range of values of the fuel Lewis number considered $0.3 \leq L_{\mathrm{F}} \leq 2.5$ covers adequately the conditions encountered in typical combustion applications.

The plots reveal the significant influence of the preferential-diffusion effects on flame temperatures. While the temperature increment $T_f - 1$ with $L_{\mathrm{F}} = 1$ remains always equal to the adiabatic value $q/(S+1)$, subadiabatic peak temperatures $T_f - 1 < q/(S+1)$ are found for $L_{\mathrm{F}} > 1$ while superadiabatic flame temperatures $T_f - 1 > q/(S+1)$ emerge for $L_{\mathrm{F}} < 1$. The trends observed are therefore consistent with classical reasoning according to which for $L_{\mathrm{F}} > 1$ the rate at which the fuel diffuses into the reaction layer is smaller than the

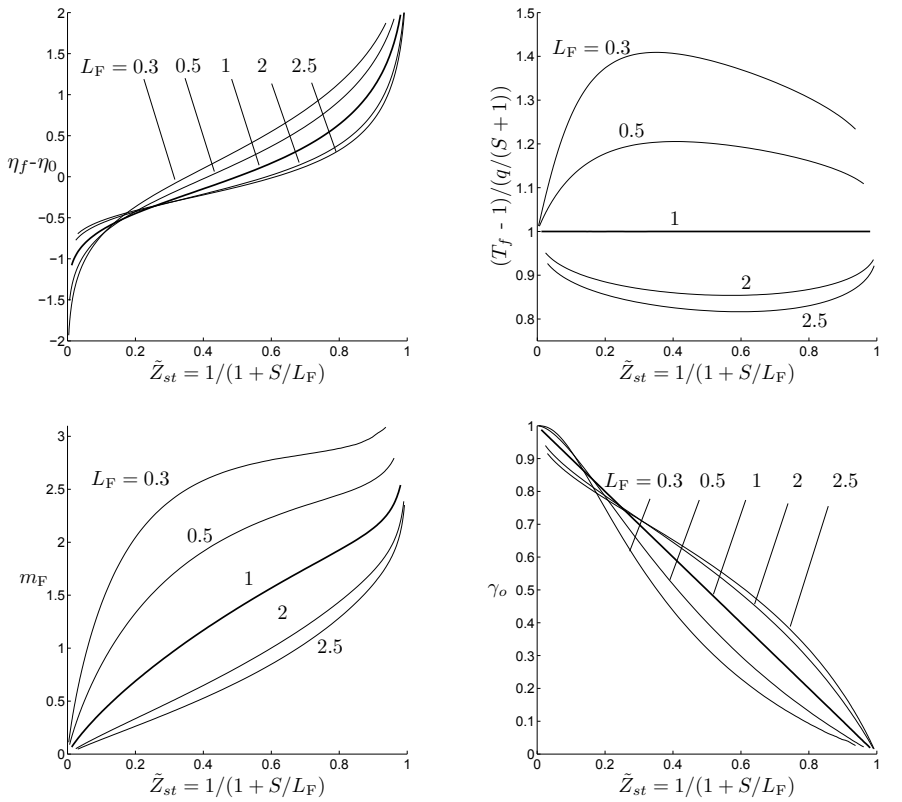

Figure C.2. Burke-Schumann computations for varying oxygen-to-fuel mass-consumption ratio S, showing the influence on; flame position η_f, peak temperature T_f, fuel-mass consumption m_F, and fractional amount of heat of combustion towards the oxidizer γ_O. Calculations made for $L_F = 0.3, 0.5, 1, 2, 2.5$, $\Pr = 0.7$, $\sigma = 0.7$, $q/S = 10$, and $T_0 = 1$.

rate at which the heat is removed, thereby resulting in a temperature decrease, while the opposite behavior is found for $L_F < 1$. It is also of interest that this effect is more pronounced for moderately dilute flames that sit close to the stagnation plane, as can be seen by observing the accompanying plots of flame location $\eta_f - \eta_0$. It is worth pointing out that caution should be exerted when extrapolating the quantitative results presented here, in that the values given are specific to the counterflow and cannot be extrapolated directly to other configurations.

C.3 Extinction in the diffusion-flame regime

C.3.1 Finite-rate effects for large activation energy

In the limit of large activation energy, arising for values of the activation temperature T_a much larger than the flame temperature T_f, flame extinction in the diffusion-flame regime [7] occurs for small departures from the equilibrium solution described above. Extinction is associated with small decrements of the temperature in the reaction layer from the peak value T_f of order T_f^2/T_a, sufficient to reduce the reaction rate by a factor e, as can be inferred from the exponential temperature dependence present in (C.2). The ratio of this temperature decrement to the characteristic temperature increase by chemical reaction $q/(S+1)$ defines the Zeldovich number

$$\beta = \frac{T_a}{T_f^2}\frac{q}{S+1}, \tag{C.29}$$

the relevant large parameter for the asymptotic description. The chemical reaction is confined to a thin layer, of relative thickness β^{-1}, where we find small reactant mass fractions of order $\hat{Y}_{\mathrm{F}} \sim \beta^{-1}$ and $\hat{Y}_{\mathrm{O}} \sim \beta^{-1}$. These estimates, together with the condition that the inner structure of the reaction layer is given by a balance between reaction and diffusion, can be used to provide from (C.6) the near-extinction order-of-magnitude estimate

$$\frac{A_A}{B} \sim T_f^{1-\sigma}(S+1)\beta^{-3}\exp(-T_a/T_f). \tag{C.30}$$

This last expression reveals that the asymptotic limit $T_a/T_f \gg 1$ of large activation energies requires simultaneous consideration of asymptotically large values of the preexponential factor, resulting in the balance (C.30) that ensures temperature decrements of order $T_f^2/T_a = \beta^{-1}q/(S+1)$ in the reaction layer.

To solve the problem in the limit $\beta \gg 1$, different expansions in increasing powers of β^{-1} must be introduced for the different variables in the inner reaction layer and in the outer regions. Determination of the critical strain rate at extinction requires consideration of the leading-order solution in the reaction layer, given by a balance between reaction and diffusion, together with two terms for the outer regions, which are chemically frozen because of the existing low temperature. Matching provides relationships for the boundary values of the different variables, needed to close the solution.

C.3.2 Solution in the outer chemically frozen regions

When considering the outer solution, the reaction layer appears as a sheet located at η_f. Different expansions must be used for the different flow variables on each side of the flame sheet. In the following, the terms in the expansion on the fuel side of the mixing layer (i.e., for $\eta_f \leq \eta < +\infty$) will be denoted by the superscript $+$, while those on the air side (i.e., for $-\infty < \eta \leq \eta_f$) will be denoted by the superscript $-$, giving for instance

$$\begin{aligned} T = T_0^+ + \beta^{-1} T_1^+,\ \hat{Y}_{\mathrm{F}} = Y_{\mathrm{F}0}^+ + \beta^{-1} Y_{\mathrm{F}1}^+, \ \text{ and } \quad \hat{Y}_{\mathrm{O}} = Y_{\mathrm{O}0}^+ + \beta^{-1} Y_{\mathrm{O}1}^+ \\ \text{for} \quad \eta_f \leq \eta < +\infty \\ T = T_0^- + \beta^{-1} T_1^-,\ \hat{Y}_{\mathrm{F}} = Y_{\mathrm{F}0}^- + \beta^{-1} Y_{\mathrm{F}1}^-, \ \text{ and } \quad \hat{Y}_{\mathrm{O}} = Y_{\mathrm{O}0}^- + \beta^{-1} Y_{\mathrm{O}1}^- \\ \text{for} \quad -\infty < \eta \leq \eta_f \end{aligned} \tag{C.31}$$

for the first two terms in the expansions for the temperature and reactant mass fractions, with similar expansions introduced for the stream function $F = F_0^{\pm} + \beta^{-1} F_1^{\pm}$. The zeroth-order terms in the expansions correspond to the Burke-Schumann solution described above, giving for instance $Y_{\mathrm{F}0}^- = 0$ for $\eta < \eta_f$ and $Y_{\mathrm{O}0}^+ = 0$ for $\eta > \eta_f$, as follows from (C.19). The resulting zeroth-order solution, which corresponds to that depicted in Fig. C.1 (dashed profiles), determines in particular the reaction-sheet location η_f along with the additional flame properties shown in Fig. C.2.

The first-order corrections appear due to finite-rate effects in the reaction layer, leading in particular to nonzero boundary values $Y_{\mathrm{F}1_f}^-$ and $Y_{\mathrm{O}1_f}^+$ for the functions $Y_{\mathrm{F}1}^-$ and $Y_{\mathrm{O}1}^+$ at $\eta = \eta_f$, associated with reactant leakage of order β^{-1} across the flame. The functions $Y_{\mathrm{F}1}^{\pm}$, $Y_{\mathrm{O}1}^{\pm}$, $T_1^{\pm}$, $F_1^{\pm}$ and $\mathrm{d}F_1^{\pm}/\mathrm{d}\eta$ can be determined by integrating

$$\mathrm{Pr}\frac{\mathrm{d}}{\mathrm{d}\eta}\left[(T_0{}^{\pm})^{\sigma-1}\left(\frac{\mathrm{d}^2F_1^{\pm}}{\mathrm{d}\eta^2} + (\sigma-1)\frac{T_1^{\pm}}{T_0^{\pm}}\frac{\mathrm{d}^2F_0^{\pm}}{\mathrm{d}\eta^2}\right)\right] + F_0^{\pm}\frac{\mathrm{d}^2F_1^{\pm}}{\mathrm{d}\eta^2} + \\ + F_1^{\pm}\frac{\mathrm{d}^2F_0^{\pm}}{\mathrm{d}\eta^2} + \frac{1}{2}\left(T_1^{\pm} - 2\frac{\mathrm{d}F_0^{\pm}}{\mathrm{d}\eta}\frac{\mathrm{d}F_1^{\pm}}{\mathrm{d}\eta}\right) = 0 \tag{C.32}$$

$$\frac{\mathrm{d}}{\mathrm{d}\eta}\left[(T_0{}^{\pm})^{\sigma-1}\left(\frac{\mathrm{d}T_1^{\pm}}{\mathrm{d}\eta} + (\sigma-1)\frac{T_1^{\pm}}{T_0^{\pm}}\frac{\mathrm{d}T_0^{\pm}}{\mathrm{d}\eta}\right)\right] + F_0^{\pm}\frac{\mathrm{d}T_1^{\pm}}{\mathrm{d}\eta} + F_1^{\pm}\frac{\mathrm{d}T_0^{\pm}}{\mathrm{d}\eta} = 0 \tag{C.33}$$

$$\frac{1}{L_{\mathrm{F}}}\frac{\mathrm{d}}{\mathrm{d}\eta}\left[(T_0{}^{\pm})^{\sigma-1}\left(\frac{\mathrm{d}Y_{\mathrm{F}1}^{\pm}}{\mathrm{d}\eta} + (\sigma-1)\frac{T_1^{\pm}}{T_0^{\pm}}\frac{\mathrm{d}Y_{\mathrm{F}0}^{\pm}}{\mathrm{d}\eta}\right)\right] + F_0^{\pm}\frac{\mathrm{d}Y_{\mathrm{F}1}^{\pm}}{\mathrm{d}\eta} + F_1^{\pm}\frac{\mathrm{d}Y_{\mathrm{F}0}^{\pm}}{\mathrm{d}\eta} = 0 \tag{C.34}$$

$$\frac{\mathrm{d}}{\mathrm{d}\eta}\left[(T_0{}^{\pm})^{\sigma-1}\left(\frac{\mathrm{d}Y_{\mathrm{O}1}^{\pm}}{\mathrm{d}\eta} + (\sigma-1)\frac{T_1^{\pm}}{T_0^{\pm}}\frac{\mathrm{d}Y_{\mathrm{O}0}^{\pm}}{\mathrm{d}\eta}\right)\right] + F_0^{\pm}\frac{\mathrm{d}Y_{\mathrm{O}1}^{\pm}}{\mathrm{d}\eta} + F_1^{\pm}\frac{\mathrm{d}Y_{\mathrm{O}0}^{\pm}}{\mathrm{d}\eta} = 0 \tag{C.35}$$

obtained by linearizing (C.5)–(C.8) after neglecting the reaction terms. The

boundary conditions

$$\left\{\begin{array}{l} F_1^- = \mathrm{d}F_1^-/\mathrm{d}\eta = T_1^- = Y_{\mathrm{F}1}^- = Y_{\mathrm{O}1}^- = 0 \\ \mathrm{d}F_1^-/\mathrm{d}\eta - (\mathrm{d}F_1^-/\mathrm{d}\eta)_f = T_1^- - T_{1_f}^- = 0 \\ Y_{\mathrm{F}1}^- - Y_{\mathrm{F}1_f}^- = Y_{\mathrm{O}1}^- - Y_{\mathrm{O}1_f}^- = 0 \end{array}\right\} \begin{array}{l} \mathrm{as} \quad \eta \to -\infty \\ \\ \mathrm{at} \quad \eta = \eta_f \end{array} \tag{C.36}$$

and

$$\left\{\begin{array}{l} \mathrm{d}F_1^+/\mathrm{d}\eta = T_1^+ = Y_{\mathrm{F}1}^+ = Y_{\mathrm{O}1}^+ = 0 \\ F_1^+ - F_{1_f}^+ = \mathrm{d}F_1^+/\mathrm{d}\eta - (\mathrm{d}F_1^+/\mathrm{d}\eta)_f = 0 \\ T_1^+ - T_{1_f}^+ = Y_{\mathrm{F}1}^+ - Y_{\mathrm{F}1_f}^+ = Y_{\mathrm{O}1}^+ - Y_{\mathrm{O}1_f}^+ = 0 \end{array}\right\} \begin{array}{l} \mathrm{as} \quad \eta \to +\infty \\ \\ \mathrm{at} \quad \eta = \eta_f \end{array} \tag{C.37}$$

include nine flame-sheet parameters, namely, the four boundary perturbations $(\mathrm{d}F_1^-/\mathrm{d}\eta)_f$, $T_{1_f}^-$, $Y_{\mathrm{F}1_f}^-$, and $Y_{\mathrm{O}1_f}^-$ on the air side and the five boundary perturbations $F_{1_f}^+$, $(\mathrm{d}F_1^+/\mathrm{d}\eta)_f$, $T_{1_f}^+$, $Y_{\mathrm{F}1_f}^+$, and $Y_{\mathrm{O}1_f}^+$ on the fuel side (note that this asymmetry is related to the boundary condition used in (C.10) for the momentum equation). These boundary values, as well as the accompanying values of the gradients of the different functions, satisfy a number of constraints. For instance, evaluating on both sides of the flame a first integral of the chemistry-free equations (C.11) and (C.14) with use made of the expansions (C.31) provides

$$\begin{aligned} \frac{F_f}{T_f^{\sigma-1}}\left[\left(T_{1_f}^+ - T_{1_f}^-\right) + \frac{q}{S}\left(Y_{\mathrm{O}1_f}^+ - Y_{\mathrm{O}1_f}^-\right)\right] \quad &+ \\ + \left(\left.\frac{\mathrm{d}T_1^+}{\mathrm{d}\eta}\right|_{\eta_f} - \left.\frac{\mathrm{d}T_1^-}{\mathrm{d}\eta}\right|_{\eta_f}\right) \quad &+ \quad \frac{q}{S}\left(\left.\frac{\mathrm{d}Y_{\mathrm{O}1}^+}{\mathrm{d}\eta}\right|_{\eta_f} - \left.\frac{\mathrm{d}Y_{\mathrm{O}1}^-}{\mathrm{d}\eta}\right|_{\eta_f}\right) = 0, \end{aligned} \tag{C.38}$$

$$\begin{aligned} \frac{F_f}{T_f^{\sigma-1}}\left[S\left(Y_{\mathrm{F}1_f}^+ - Y_{\mathrm{F}1_f}^-\right) - \left(Y_{\mathrm{O}1_f}^+ - Y_{\mathrm{O}1_f}^-\right)\right] \quad &+ \\ + \frac{S}{L_{\mathrm{F}}}\left(\left.\frac{\mathrm{d}Y_{\mathrm{F}1}^+}{\mathrm{d}\eta}\right|_{\eta_f} - \left.\frac{\mathrm{d}Y_{\mathrm{F}1}^-}{\mathrm{d}\eta}\right|_{\eta_f}\right) \quad &- \quad \left(\left.\frac{\mathrm{d}Y_{\mathrm{O}1}^+}{\mathrm{d}\eta}\right|_{\eta_f} + \left.\frac{\mathrm{d}Y_{\mathrm{O}1}^-}{\mathrm{d}\eta}\right|_{\eta_f}\right) = 0, \end{aligned}$$

where $F_f/T_f^{\sigma-1}$ is evaluated from the leading-order solution. On the other hand, since the chemical reaction has no direct effect on the momentum balance equation, the jump conditions for the stream function and its derivatives are easily obtained from successive integrations of (C.5) across the flame, thereby

yielding three additional relationships

$$\begin{aligned}
&\mathrm{Pr}T_f^{\sigma-1}\left[\left.\frac{\mathrm{d}^2F_1^+}{\mathrm{d}\eta^2}\right|_{\eta_f}-\left.\frac{\mathrm{d}^2F_1^-}{\mathrm{d}\eta^2}\right|_{\eta_f}+(\sigma-1)\frac{T_{1_f}^+-T_{1_f}^-}{T_f}\left.\frac{\mathrm{d}^2F_0}{\mathrm{d}\eta^2}\right|_{\eta_f}\right]+\\
&\quad+F_f\left(\left.\frac{\mathrm{d}F_1^+}{\mathrm{d}\eta}\right|_{\eta_f}-\left.\frac{\mathrm{d}F_1^-}{\mathrm{d}\eta}\right|_{\eta_f}\right)+\left.\frac{\mathrm{d}F_0}{\mathrm{d}\eta}\right|_{\eta_f}\left(F_{1_f}^+-F_{1_f}^-\right)=0,\\
&\mathrm{Pr}T_f^{\sigma-1}\left[\left.\frac{\mathrm{d}F_1^+}{\mathrm{d}\eta}\right|_{\eta_f}-\left.\frac{\mathrm{d}F_1^-}{\mathrm{d}\eta}\right|_{\eta_f}+(\sigma-1)\frac{T_{1_f}^+-T_{1_f}^-}{T_f}\left.\frac{\mathrm{d}F_0}{\mathrm{d}\eta}\right|_{\eta_f}\right]+F_f\left(F_{1_f}^+-F_{1_f}^-\right)=0,\\
&T_f\left(F_{1_f}^+-F_{1_f}^-\right)+(\sigma-1)\left(T_{1_f}^+-T_{1_f}^-\right)F_f=0.
\end{aligned}\tag{C.39}$$

Since the problem is linear, the solution to (C.32)–(C.37) can be expressed as a linear combination of the elementary solutions arising by considering separately the flame perturbations to each one of the variables. This strategy can be used in particular to generate the expressions

$$F_{1_f}^- = \alpha_{01}^-\left.\frac{\mathrm{d}F_1^-}{\mathrm{d}\eta}\right|_{\eta_f}+\alpha_{0T}^-T_{1_f}^-+\alpha_{0F}^-Y_{\mathrm{F}1_f}^-+\alpha_{0O}^-Y_{\mathrm{O}1_f}^-,\tag{C.40}$$

$$\left.\frac{\mathrm{d}^2F_1^\pm}{\mathrm{d}\eta^2}\right|_{\eta_f} = \alpha_{20}^\pm F_{1_f}^+ + \alpha_{21}^\pm\left.\frac{\mathrm{d}F_1^\pm}{\mathrm{d}\eta}\right|_{\eta_f}+\alpha_{2T}^\pm T_{1_f}^\pm+\alpha_{2F}^\pm Y_{\mathrm{F}1_f}^\pm+\alpha_{2O}^\pm Y_{\mathrm{O}1_f}^\pm,\tag{C.41}$$

$$\left.\frac{\mathrm{d}T_1^\pm}{\mathrm{d}\eta}\right|_{\eta_f} = \alpha_{T0}^\pm F_{1_f}^+ + \alpha_{T1}^\pm\left.\frac{\mathrm{d}F_1^\pm}{\mathrm{d}\eta}\right|_{\eta_f}+\alpha_{TT}^\pm T_{1_f}^\pm+\alpha_{TF}^\pm Y_{\mathrm{F}1_f}^\pm+\alpha_{TO}^\pm Y_{\mathrm{O}1_f}^\pm,\tag{C.42}$$

$$\left.\frac{\mathrm{d}Y_{\mathrm{F}1}^\pm}{\mathrm{d}\eta}\right|_{\eta_f} = \alpha_{F0}^\pm F_{1_f}^+ + \alpha_{F1}^\pm\left.\frac{\mathrm{d}F_1^\pm}{\mathrm{d}\eta}\right|_{\eta_f}+\alpha_{FT}^\pm T_{1_f}^\pm+\alpha_{FF}^\pm Y_{\mathrm{F}1_f}^\pm+\alpha_{FO}^\pm Y_{\mathrm{O}1_f}^\pm,\tag{C.43}$$

$$\left.\frac{\mathrm{d}Y_{\mathrm{O}1}^\pm}{\mathrm{d}\eta}\right|_{\eta_f} = \alpha_{O0}^\pm F_{1_f}^+ + \alpha_{O1}^\pm\left.\frac{\mathrm{d}F_1^\pm}{\mathrm{d}\eta}\right|_{\eta_f}+\alpha_{OT}^\pm T_{1_f}^\pm+\alpha_{OF}^\pm Y_{\mathrm{F}1_f}^\pm+\alpha_{OO}^\pm Y_{\mathrm{O}1_f}^\pm,\tag{C.44}$$

for the gradients appearing in (C.38) and (C.39) in terms of the boundary values of the different functions. The 40 constant coefficients $\alpha_{ij}^\pm$ in (C.40)–(C.44) are obtained from straightforward integrations of (C.32)–(C.35) with normalized boundary conditions at the flame. For instance, the coefficients α_{01}^-, α_{21}^-, α_{T1}^-, α_{F1}^-, and α_{O1}^-, correspond to the values of F_1^-, $\mathrm{d}^2F_1^-/\mathrm{d}\eta^2$, $\mathrm{d}T_1^-/\mathrm{d}\eta$, $\mathrm{d}Y_{\mathrm{F}1}^-/\mathrm{d}\eta$, and $\mathrm{d}Y_{\mathrm{O}1}^-/\mathrm{d}\eta$ at $\eta=\eta_f$ when the boundary conditions at the flame, given in (C.36), are replaced in the integrations by the normalized boundary conditions $\mathrm{d}F_1^-/\mathrm{d}\eta-1=T_1^-=Y_{\mathrm{F}1}^-=Y_{\mathrm{O}1}^-=0$. Similarly, the coefficients α_{20}^+, α_{T0}^+, α_{F0}^+, and α_{O0}^+ correspond to the values of the different gradients when the alternative boundary conditions $F_1^+-1=\mathrm{d}F_1^+/\mathrm{d}\eta=T_1^+=Y_{\mathrm{F}1}^+=Y_{\mathrm{O}1}^+=0$ at the positive side of $\eta=\eta_f$ are utilized in the integrations. Once the different coefficients $\alpha_{ij}^\pm$ are determined numerically, the substitution of (C.40)–(C.44) into (C.38) and (C.39) generates five linear equations linking the nine boundary values $F_{1_f}^+$, $\mathrm{d}F_{1_f}^\pm/\mathrm{d}\eta$, $T_{1_f}^\pm$, $Y_{\mathrm{F}1}^\pm$, and $Y_{\mathrm{O}1_f}^\pm$. The four additional equations that are

needed to complete the solution follow from matching with the inner solution, as shown below.

C.3.3 The inner layer

In the inner reaction layer, the variables are rescaled to give normalized variables of order unity according to $\zeta = \beta(\eta - \eta_f)$, $y_{\mathrm{F}} = \beta\hat{Y}_{\mathrm{F}}$, $y_{\mathrm{O}} = \beta\hat{Y}_{\mathrm{O}}$, and $\theta = \beta(T - T_f)/[q/(S+1)]$, with corresponding asymptotic expansions given by $y_{\mathrm{F}} = y_{\mathrm{F}_0} + \beta^{-1}y_{\mathrm{F}_1} + \cdots$, $y_{\mathrm{O}} = y_{\mathrm{O}_0} + \beta^{-1}y_{\mathrm{O}_1} + \cdots$, and $\theta = \theta_0 + \beta^{-1}\theta_1 + \cdots$. At the order pursued here, the determination of the extinction conditions involves only the leading-order terms in the above expansions, which are determined by integration of the corresponding reaction-diffusion equations

$$-\frac{S}{S+1}\frac{\mathrm{d}^2\theta}{\mathrm{d}\zeta^2} = \frac{\mathrm{d}^2 y_{\mathrm{O}}}{\mathrm{d}\zeta^2} = \frac{S}{L_{\mathrm{F}}}\frac{\mathrm{d}^2 y_{\mathrm{F}}}{\mathrm{d}\zeta^2} = \frac{B\beta^{-3}S}{A_s T_f^{\sigma-1}} e^{-T_a/T_f} y_{\mathrm{F}} y_{\mathrm{O}} e^{\theta} \tag{C.45}$$

obtained from (C.6)–(C.8), with the subscript 0 omitted to simplify the notation. The boundary conditions for integration of (C.45), given by

$$\left.\begin{aligned} \frac{\mathrm{d}\theta}{\mathrm{d}\zeta} = -(1-\gamma_{\mathrm{O}})(S+1)m_{\mathrm{F}}, \quad \frac{1}{L_{\mathrm{F}}}\frac{\mathrm{d}y_{\mathrm{F}}}{\mathrm{d}\zeta} = m_{\mathrm{F}}, \quad \frac{\mathrm{d}y_{\mathrm{O}}}{\mathrm{d}\zeta} = 0 \qquad \text{as} \quad \zeta \to \infty \\ \frac{\mathrm{d}\theta}{\mathrm{d}\zeta} = \gamma_{\mathrm{O}}(S+1)m_{\mathrm{F}}, \quad \frac{\mathrm{d}y_{\mathrm{F}}}{\mathrm{d}\zeta} = 0, \quad \frac{\mathrm{d}y_{\mathrm{O}}}{\mathrm{d}\zeta} = -Sm_{\mathrm{F}} \qquad \text{as} \quad \zeta \to -\infty \end{aligned}\right\}, \tag{C.46}$$

follow from matching with the leading-order solution in the outer regions. In the intermediate matching region, the inner variables take the form

$$\left.\begin{aligned} \theta = -(1-\gamma_{\mathrm{O}})(S+1)m_{\mathrm{F}}\zeta + \theta^{+}, \quad y_{\mathrm{F}} = m_{\mathrm{F}}L_{\mathrm{F}}\zeta + y_{\mathrm{F}}^{+}, \quad y_{\mathrm{O}} = y_{\mathrm{O}}^{+} \\ \text{as} \quad \zeta \to \infty \\ \theta = \gamma_{\mathrm{O}}(S+1)m_{\mathrm{F}}\zeta + \theta^{-}, \quad y_{\mathrm{F}} = y_{\mathrm{F}}^{-}, \quad y_{\mathrm{O}} = -Sm_{\mathrm{F}}\zeta + y_{\mathrm{O}}^{-} \\ \text{as} \quad \zeta \to -\infty \end{aligned}\right\}, \tag{C.47}$$

as corresponds to (C.46). These expressions involve six unknown constants, namely, the reactant leakages y_{O}^{+} and y_{F}^{-} and the apparent shifts y_{F}^{+}, θ^{+}, y_{O}^{-}, and θ^{-}, which are related to the flame values of the first-order perturbations in the outer regions by

$$\theta^{\pm} = \frac{T_{1_f}^{\pm}}{q/(S+1)}, \quad y_{\mathrm{F}}^{\pm} = Y_{\mathrm{F}1_f}^{\pm}, \quad \text{and} \quad y_{\mathrm{O}}^{\pm} = Y_{\mathrm{O}1_f}^{\pm} \tag{C.48}$$

as required at this order to achieve the matching of (C.47) with the outer solution (C.31).

The derivation continues by integrating the first two equations in (C.45) with the boundary conditions given in (C.46) to yield

$$\frac{S}{S+1}\frac{\mathrm{d}\theta}{\mathrm{d}\zeta}+\frac{S}{L_{\mathrm{F}}}\frac{\mathrm{d}y_{\mathrm{F}}}{\mathrm{d}\zeta}=\gamma_{\mathrm{O}}Sm_{\mathrm{F}} \quad \text{and} \quad \frac{S}{L_{\mathrm{F}}}\frac{\mathrm{d}y_{\mathrm{F}}}{\mathrm{d}\zeta}-\frac{\mathrm{d}y_{\mathrm{O}}}{\mathrm{d}\zeta}=Sm_{\mathrm{F}}, \tag{C.49}$$

followed by a second quadrature to provide the relationships

$$\frac{S}{S+1}\theta=-\frac{S}{L_{\mathrm{F}}}y_{\mathrm{F}}+\gamma_{\mathrm{O}}Sm_{\mathrm{F}}\zeta+C_1 \quad \text{and} \quad \frac{S}{L_{\mathrm{F}}}y_{\mathrm{F}}=y_{\mathrm{O}}+Sm_{\mathrm{F}}\zeta+C_2, \tag{C.50}$$

valid everywhere across the reaction layer. The two integration constants C_1 and C_2 are related to those in (C.47) by

$$C_1=\frac{S}{L_{\mathrm{F}}}y_{\mathrm{F}}^{+}+\frac{S}{S+1}\theta^{+}=\frac{S}{L_{\mathrm{F}}}y_{\mathrm{F}}^{-}+\frac{S}{S+1}\theta^{-} \quad \text{and} \quad C_2=\frac{S}{L_{\mathrm{F}}}y_{\mathrm{F}}^{+}-y_{\mathrm{O}}^{+}=\frac{S}{L_{\mathrm{F}}}y_{\mathrm{F}}^{-}-y_{\mathrm{O}}^{-}, \tag{C.51}$$

obtained by substitution of (C.47) into (C.50). The interpretation os these constants becomes more evident when the two relations (C.50) are written in terms of the excess enthalpy and generalized mixture fraction to give the expressions

$$H-H_f=\left.\frac{\mathrm{d}H}{\mathrm{d}\eta}\right|_{\eta_f}(\eta-\eta_f)+\beta^{-1}(C_1-C_2) \quad \text{and} \quad \tilde{Z}-\tilde{Z}_{st}=\left.\frac{\mathrm{d}\tilde{Z}}{\mathrm{d}\eta}\right|_{\eta_f}(\eta-\eta_f)+\beta^{-1}\tilde{Z}_{st}C_2, \tag{C.52}$$

which indicate that C_1-C_2 and C_2 are apparent shifts of order β^{-1} in the level of H and $\tilde{Z}$ at the flame from their Burke-Schumann values H_f and $\tilde{Z}_{st}$.

C.3.4 The canonical problem

Using (C.50) to write the reaction rate in terms of y_{F} reduces the last equation in (C.45) to

$$\begin{aligned}\frac{\mathrm{d}^2y_{\mathrm{F}}}{\mathrm{d}\zeta^2}=\frac{B\beta^{-3}L_{\mathrm{F}}}{A_AT_f^{\sigma-1}}e^{-T_a/T_f}y_{\mathrm{F}}\left(\frac{S}{L_{\mathrm{F}}}y_{\mathrm{F}}-Sm_{\mathrm{F}}\zeta-C_2\right)\times\\ \times\exp\left[\frac{S+1}{S}\left(-\frac{S}{L_{\mathrm{F}}}y_{\mathrm{F}}+\gamma_{\mathrm{O}}Sm_{\mathrm{F}}\zeta+C_1\right)\right].\end{aligned} \tag{C.53}$$

Introducing the normalized coordinate $\xi=(S+1)m_{\mathrm{F}}\zeta+C_2(S+1)/S$ and the rescaled fuel variable $y=y_{\mathrm{F}}(S+1)/L_{\mathrm{F}}$ enables the problem to be written in the canonical form

$$\frac{\mathrm{d}^2y}{\mathrm{d}\xi^2}=\Lambda y(y-\xi)e^{-y+\gamma_{\mathrm{O}}\xi}\begin{cases}y-\xi=y_{\mathrm{O}}^{+}(S+1)/S & \text{as} \quad \xi\to+\infty\\ y=y_{\mathrm{F}}^{-}(S+1)/L_{\mathrm{F}} & \text{as} \quad \xi\to-\infty\end{cases} \tag{C.54}$$

in terms of the reactant leakages y_{O}^{+} and y_{F}^{-}. The balance between chemical reaction and diffusion is measured in (C.54) by the parameter

$$\Lambda = \mathcal{D} \exp\left(\frac{S+1}{S} (C_1 - \gamma_{\mathrm{O}} C_2) \right), \tag{C.55}$$

involving the relevant Damköhler number

$$\mathcal{D} = \frac{B}{A_A} \frac{S \beta^{-3} L_{\mathrm{F}} T_f^{1-\sigma}}{(S+1)^3 m_{\mathrm{F}}^2} e^{-T_a/T_f}, \tag{C.56}$$

a nondimensional measure of the strain time A_A^{-1} at extinction that embodies the correct balance between B and E associated with the double asymptotic limit implied by (C.30).

For a given value of γ_{O}, determined from the outer solution, the integration of (C.54) provides the inner structure of the reaction layer for different values of Λ, including the reactant leakages. For the values $0 < \gamma_{\mathrm{O}} < 1$ that apply to most conditions of practical interest, two solutions are found for Λ above a critical value Λ_E and no solution exists for $\Lambda < \Lambda_E$. To handle effectively the resulting multiplicity and determine accurately the solution near the turning point, instead of solving (C.54) for a known value Λ, it is convenient to pose the problem as that of finding the solution for a given fuel leakage y_{F}^{-}. Increasing the value of y_{F}^{-} in successive integrations provides the evolution of Λ and y_{O}^{+} shown in Fig. C.3. Note that the value of Λ defined in (C.55) is in general different from the relevant Damköhler number $\mathcal{D}$, with the constants C_1 and C_2 carrying the influence of the outer solution on the extinction process.

C.3.5 Evaluation of the extinction conditions

Given the properties of the fuel and the boundary temperatures, one may solve the counterflow problem in the limit of infinitely fast reaction (using the coupling-function formulation or otherwise) to determine the flame location η_f, the peak temperature T_f, the reactant consumption rates m_{O} and $m_{\mathrm{F}} = m_{\mathrm{O}}/S$, and the heat-loss parameters $\gamma_{\mathrm{O}} = 1 - \gamma_{\mathrm{F}}$. The associated outer profiles appear in the coefficients of the linear equations (C.32)–(C.35), which can be therefore integrated to determine the values of the factors $\alpha_{ij}^{\pm}$ in (C.40)–(C.44) for a given Burke-Schumann solution. Also, the heat-loss parameter γ_{O} can be used when solving the canonical problem (C.54), which gives the variation of Λ and y_{O}^{+} with y_{F}^{-}.

The critical value of the strain rate at extinction is determined by the mini-

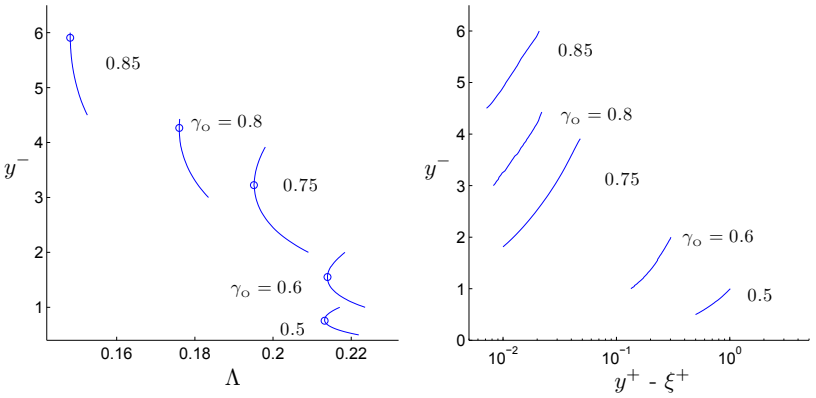

Figure C.3. Evolution of Λ through the integration of the canonical problem as a function of the fuel leakage y^- is shown on the left plot for different values of γ_O. The minimum value or critical Λ is marked with a red circle. The relation found for the previous integrations of reactant leakages, $y^- = y_F^-(S+1)/L_F$ and $y^+ - \xi^+ = y_O^+(S+1)/S$, is depicted on the right plot.

mum value of $\mathcal{D}$ for which a solution exists, associated with an intermediate value of the fuel leakage y_F^-. Since the constants C_1 and C_2 appearing in (C.55) are in general nonzero, this minimum value cannot be evaluated directly from the turning point in Fig. C.3, but rather from the turning point of the associated curve of $\mathcal{D}$ as a function of y_F^-, determined from (C.55) once the values of C_1 and C_2 are computed for a given value of y_F^-. The computation is not straightforward, in that it involves the simultaneous determination of the sixteen unknowns C_1, C_2, $F_{1_f}^+$, $(\mathrm{d}F_1^\pm/\mathrm{d}\eta)_f$, $T_{1_f}^\pm$, $Y_{F1_f}^\pm$, $Y_{O1_f}^\pm$, $\theta^\pm$, $y_F^\pm$ and y_O^-.

The sixteen equations required to determine the solution include the five equations generated by substituting the expressions (C.40)–(C.44) into (C.38) and (C.39), the six matching conditions (C.48), the four identities (C.51), and the relationship between y_F^- and y_O^+ displayed in the right-hand-side plot of Fig. C.3. Once the system is solved for C_1 and C_2 as a function of y_F^-, it is straightforward to evaluate from (C.50) the inner expansions of the oxidizer and temperature variables as a function of the solution of the canonical-problem variable $y = y_F(S+1)/L_F$.

C.4 Sample computations

This final section presents finite-rate results corresponding for nonunity values of the fuel Lewis number L_F. In particular, Fig. C.4 illustrates the matching of the outer solution with the inner reaction layer. Besides the peaked profiles

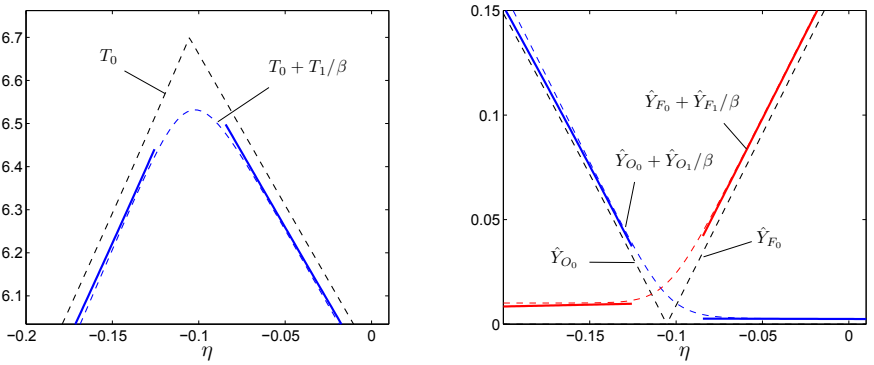

Figure C.4. Profiles corresponding to $S = 2$ and $L_{\rm F} = 2$ ($\gamma_{\rm O} = 0.57$). Besides the leading-order Burke-Schumann solution (black-dashed curves), the plot includes the first-order corrections for the outer expansions (thick-solid lines) as well as the inner-layer solution (dashed-color curves) for $\beta = 100$.

obtained with infinitely fast chemistry for $S = 2$ and $L_{\rm F} = 2$, the figure includes as color curves results corresponding to the inner-layer solution for $\beta = 100$ along with the corresponding outer two-term expansion at the reaction sheet. As expected, the inner solution matches with the asymptotes of the outer solution for $\eta - \eta_f \sim O(\beta^{-1})$ and start to diverge at larger distances as the effect of convection curves the outer profiles.

The effect of the outer perturbations on the critical extinction conditions is illustrated in Fig. C.5, which displays the extinction curves corresponding to the canonical problem together with that of the corrected Damköhler number $\mathcal{D}$ for $S = 2$ and two different values of $L_{\rm F}$. The differences, associated with the nonzero values of $C_1 - \gamma_{\rm O} C_2$ are seen to be fairly small for $L_{\rm F} = 2$ but considerably larger for $L_{\rm F} = 0.3$. Also of interest is that the correction goes in different directions, giving turning points on different sides of the canonical curve.

The variation of the extinction curves with dilution for $L_{\rm F} = 2$ is shown in Fig. C.6. In this case, the corrections associated with the perturbations to the outer flow are seen to be negligible, in that the resulting values of $C_1 - \gamma_{\rm O} C_2$ at extinction are smaller than 0.1 for all dilutions considered. Also of interest is the non-monotonicity of the resulting critical Damköhler number, which first increases and then decreases for increasing dilutions.

The original set of conservation equations (C.5)–(C.8) was employed to compute the extinction curves for finite values of the activation energy. The integrations employed continuation methods to capture the turning point of

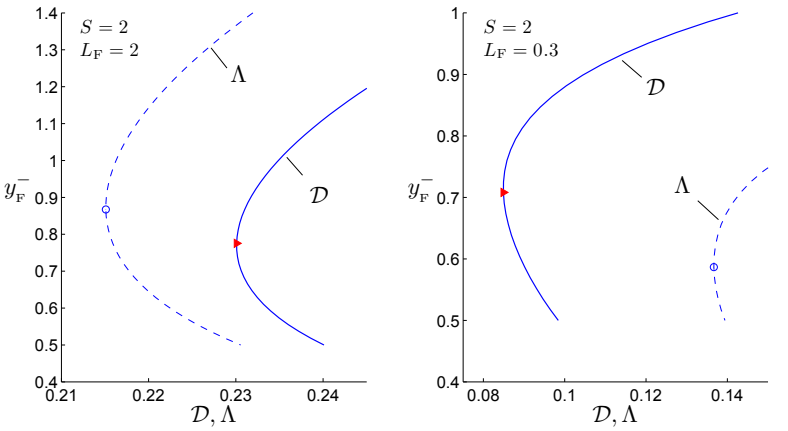

Figure C.5. Comparison of extinction curves. Representation of fuel leakage versus Λ given by the canonical problem (dashed) and the relevant Damköhler number $\mathcal{D}$ obtained after consideration of outer solution perturbations (solid).

the extinction curve. To facilitate the comparisons with the results of the asymptotic analysis, the one-step reaction rate given in (C.2) was rewritten in non-dimensional form with use made of the definition of $\mathcal{D}$ as follows,

$$\frac{\omega_F}{\rho' A_A} = \mathcal{D}\frac{(S+1)^3 m_{\text{F}}^2}{S L_{\text{F}}} T_f^{\sigma-1} \beta^3 \hat{Y}_{\text{F}} \hat{Y}_{\text{O}} \exp\left(\beta \frac{T - T_f}{T} T_f \frac{S+1}{q}\right). \qquad \text{(C.57)}$$

For given values of q, S and L_{F}, the Burke-Schumann solution was computed first to obtain the equilibrium values T_f and m_{F}. Then, the finite-chemistry numerical simulations were carried out for a fixed value of the Zeldovich number β for different values of $\mathcal{D}$ and the resulting curves were compared against the predictions of the asymptotic analysis for $\beta = \infty$, giving the results shown in Fig. C.7.

For dilute configurations with $S \sim 1$ the numerical integrations tend to approach the asymptotic curves as the value of β increases. The convergence is not achieved, however, for $S = 10$, when we observe significant departures even for the largest value of $\beta = 200$ employed in the numerical integrations, thereby suggesting that for these conditions of small dilution and significant fuel leakage extinction occurs in the premixed-flame regime rather than in the diffusion-flame regime investigated here.

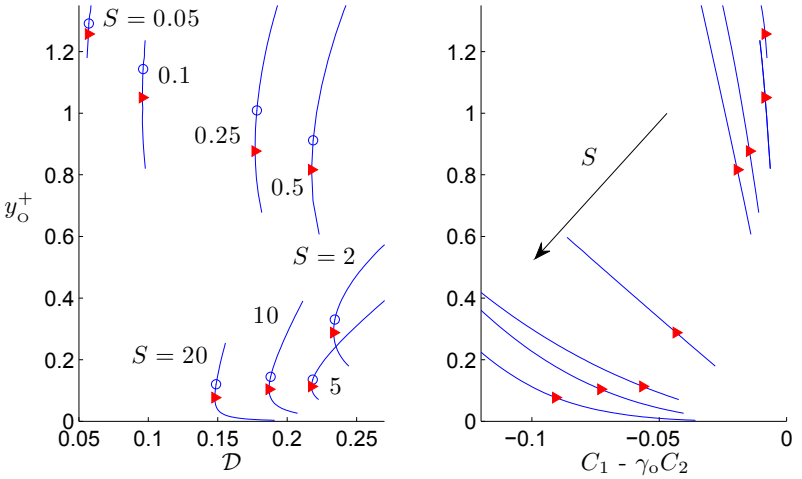

Figure C.6. Extinction curves and values of correction factors $C_1 - \gamma_{\mathrm{O}} C_2$ for different dilutions.

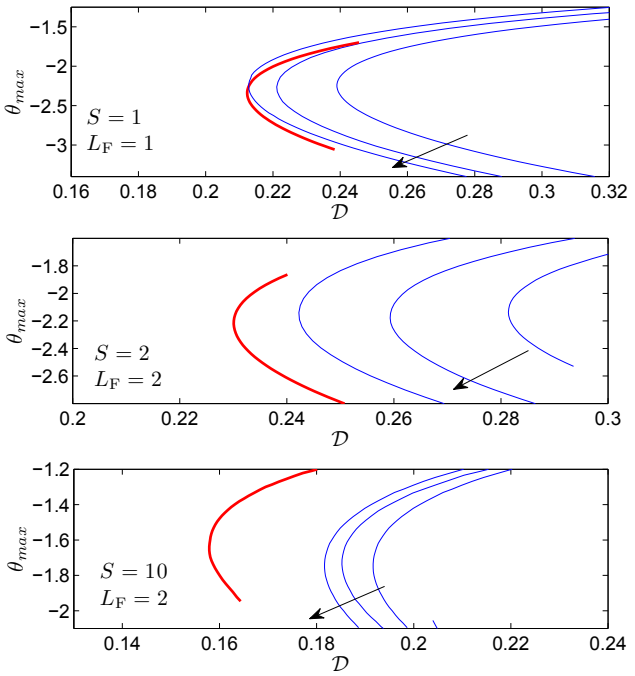

Figure C.7. Extinction curves for $q/S = 10$. Numerical results are shown in blue for growing succesive values of $\beta = 50, 100, 150$, in addition to the asymptotic prediction depicted with a thick red line.

References

[1] A. Liñán, M. Vera, A. L. Sánchez, Ignition, liftoff, and extinction of gaseous diffusion flames, Annual Review of Fluid Mechanics 47 (2015) 293–314.

[2] A. Liñán, in: J. Jiménez (Ed.), The Role of Coherent Structures in Modelling Turbulence and Mixing, 1981, pp. 333–339.

[3] S. H. Chung, C. K. Law, Structure and extinction of convective diffusion flames with general lewis numbers, Combustion and Flame 52 (1983) 59–79.

[4] J. S. Kim, F. A. Williams, Extinction of diffusion flames with nonunity lewis numbers, Journal of engineering mathematics 31 (2-3) (1997) 101–118.

[5] A. Liñán, The structure of diffusion flames, in: M. Onofri, A. Tesei (Eds.), Fluid dynamical aspects of combustion theory, Longman Scientific Technical Essex, 1991, pp. 11–19.

[6] A. Liñán, Diffusion-controlled combustion, in: H. Aref, J. W. Phillips (Eds.), Mechanics for a New Millenium, Kluwer Acad. Dordrecht, Holland, 2001, pp. 487–502.

[7] A. Liñán, The asymptotic structure of counterflow diffusion flames for large activation energies, Acta Astronautica 1 (7) (1974) 1007–1039.